THE MICROWAVE THERMAL THRUSTER
AND ITS APPLICATION TO THE LAUNCH
PROBLEM

Thesis by

Kevin L.G. Parkin

In Partial Fulfillment of the Requirements

for the Degree of

Doctor of Philosophy

CALIFORNIA INSTITUTE OF TECHNOLOGY

Pasadena, California

2006

(Defended 26 May 2006)

ii

Acknowledgements

To Mum and Jay

Abstract

Nuclear thermal thrusters long ago bypassed the 50-year-old specific impulse (I_{sp}) limitation of conventional thrusters, using nuclear powered heat exchangers in place of conventional combustion to heat a hydrogen propellant. These heat exchanger thrusters experimentally achieved an I_{sp} of 825 seconds, but with a thrust-to-weight ratio (*T/W*) of less than ten they have thus far been too heavy to propel rockets into orbit.

This thesis proposes a new idea to achieve both high I_{sp} and high *T/W*: The Microwave Thermal Thruster. This thruster covers the underside of a rocket aeroshell with a lightweight microwave absorbent heat exchange layer that may double as a re-entry heat shield. By illuminating the layer with microwaves directed from a ground-based phased array, an I_{sp} of 700–900 seconds and *T/W* of 50–150 is possible using a hydrogen propellant. The single propellant simplifies vehicle design, and the high I_{sp} increases payload fraction and structural margins. These factors combined could have a profound effect on the economics of building and reusing rockets.

A laboratory-scale microwave thermal heat exchanger is constructed using a single channel in a cylindrical microwave resonant cavity, and new type of coupled electromagnetic-conduction-convection model is developed to simulate it. The resonant cavity approach to small-scale testing reveals several drawbacks, including an unexpected oscillatory behavior. Stable operation of the laboratory-scale thruster is nevertheless successful, and the simulations are consistent with the experimental results.

In addition to proposing a new type of propulsion and demonstrating it, this thesis provides three other principal contributions: The first is a new perspective on the launch problem, placing it in a wider economic context. The second is a new type of ascent trajectory that significantly reduces the diameter, and hence cost, of the ground-based phased array. The third is an eclectic collection of data, techniques, and ideas that constitute a Microwave Thermal Rocket as it is presently conceived, in turn selecting and motivating the particular experimental and computational analyses undertaken.

Table of Contents

List of Figures

List of Tables

CHAPTER 1

INTRODUCTION

Lastly, there is a third and most attractive method of acquiring velocity. This consists in the transmission of energy from the outside, from Earth.

The projectile itself need not carry "material" energy, i.e., extra weight, in the form of explosives or fuel. This energy could be transmitted to it from the planet in the form of a parallel beam of shortwave electromagnetic rays.

...This method of imparting velocity raises quite a few difficult problems, the solution of which I shall leave to the future.

K.E. Tsiolkovsky, *The Spaceship* (1924)

1.1 The Launch Problem and the Need for Nonchemical Propulsion

In the year 2006 payloads are launched into orbit the same way they were in 1966; by chemical rockets. Traditional expendable multistage rockets achieve payload fractions of less than 4.2%. As described by the rocket equation, this is due partly to the structural limits of existing materials, and partly to the limited specific impulse (I_{sp}) of chemical propellants, which have reached a practical limit of 460 seconds.[i] The structural economies made to preserve these minute payload fractions result in fragile rockets that are expensive to build. Despite 40 years of incremental rocket development, materials improvements have made little difference to price (Fig. 1-1), novel propellants have proven impractical, reliability is still variable, and the price of launch has remained around $10,000 per kilogram of payload delivered to low earth orbit. In contrast, the energy cost of launch ($/Joule of energy expended) is around $100 per kilogram.

---

[i] For H_2/O_2 systems at high pressure. The highest chemical I_{sp} achieved was 523 sec in vacuum using a $Li/H_2/F_2$ tripropellant combination (Arbit *et al.*, 1970), but this and other combinations have all proven to be highly impractical, volatile, and economically infeasible for mass production.

The ongoing high cost of launch arises for both technical and economic reasons. On the economic side, market models predict an essentially flat elasticity of demand for space launch until the payload cost is reduced below $1000 per kilogram (NASA, 1994), implying that the primary economic benefits of space cannot be realized without an order of magnitude reduction in launch costs. With modest price reductions only weakly affecting the present market size, any reduction in launch price simply reduces revenue for launch providers.

Fig. 1-1, which is compiled using price data is from Astronautix.com, shows the price that the unchanging users of the international launch market will bear; prices that have remained relatively constant since the dawn of the space age, and have proven insensitive to incremental technology improvements over the years. To complete the overall picture, the launch vehicle reliability diagrams of Chang (2000) are included at the bottom. Note that launch *price* is different to launch *cost*, which is modestly lower but in most cases proprietary. Aside from the vehicle cost itself, insurance costs, range costs and a number of other economic factors can form a significant fraction of the launch price. These costs decrease as the flight rate increases.

Small market size and a small revenue stream relative to development costs undermine the commercial incentive for investment in space launch technology. Many improvements have been funded in good faith by government launch customers; unfortunately, it might be concluded from Fig. 1-1 that either these improvements have been ineffective, or that the cost savings have not been reflected in the launch price, which is consistent with the market view of launch economics.

In contrast, with increasing flight rate, a stable cycle of increasing revenue, launcher improvement, and decreasing payload cost can exist, and is depicted on the right of Fig. 1-1. A key question is how to bridge the gap between the present high-cost low-flight rate regime and the desired high-flight rate low-cost regime. Forty years of trial and error suggest that the two regimes are separate, without an incremental evolutionary path between them. Whether or not the initial price reduction can be achieved via non-

incremental technological improvements or by government-generated demand for existing launch systems is presently the subject of informal and heated debate within some sections of the rocket science community. The key question in this regard is how the monetary cost of the initial artificial boost in demand varies as a function of the monetary cost of new technology.
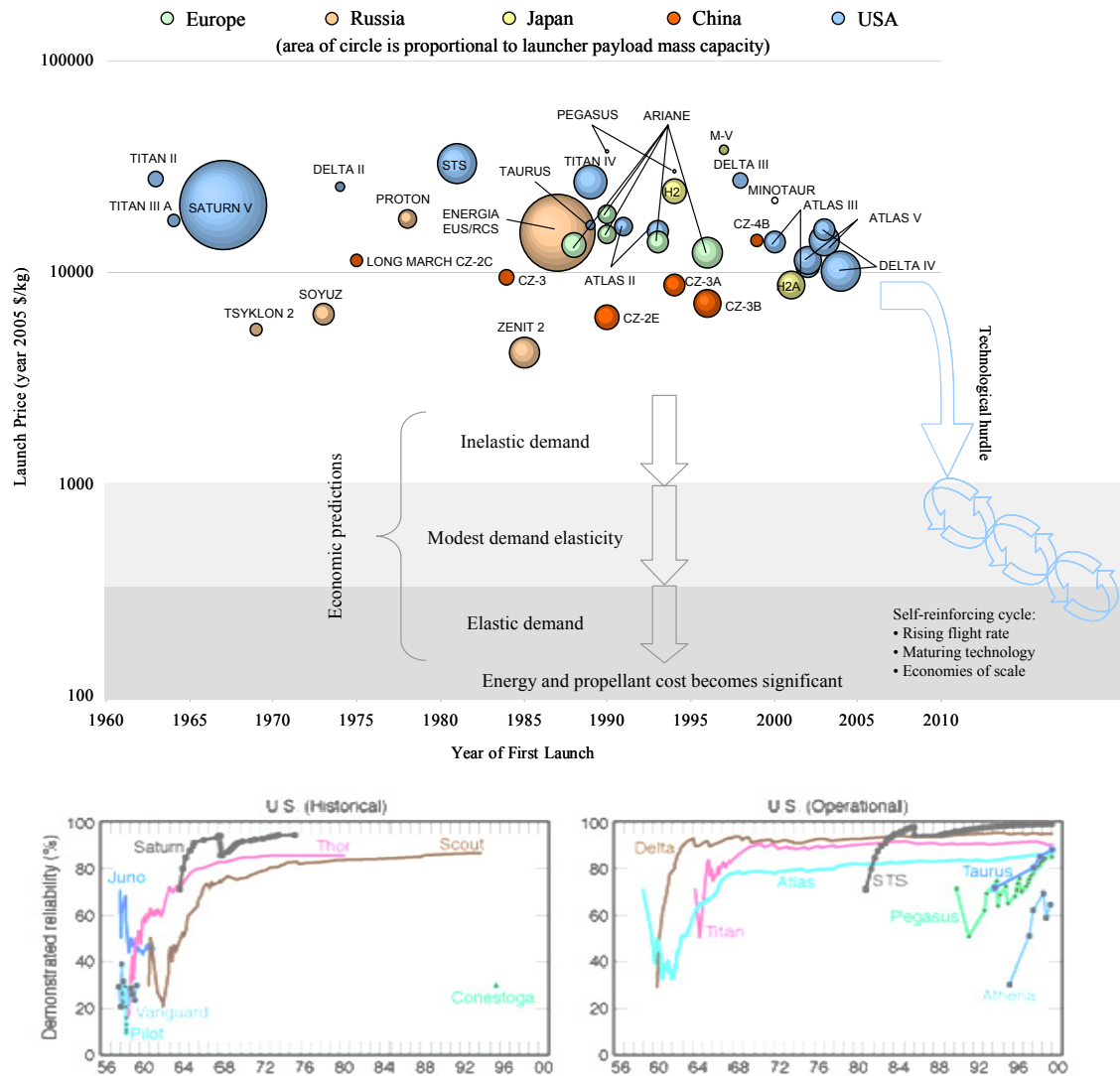
Fig. 1-1: Economics of the launch problem. Reliability data (bottom) is from Chang (2000).

On the technical side there are significant and fundamental limitations in chemical propulsion–the energy density of propellants is limited by the energy of chemical bonds, and hence the energy density of the best chemical reaction known. For all intents and purposes that is the H_2/O_2 reaction, which at high pressure has an I_{sp} of 460 seconds.

Low energy density translates to low I_{sp}; at least a factor of two increase is needed, since the energy density of all known chemical propellants is barely enough to carry their own weight into space, let alone the structure of the rocket and a payload on top of that. Engineers have shaved structural margins to their limits and resorted to multiple stages so that a payload can be carried into space at all, and even then, only 1–4.2% of the wet mass can be spared. The result is that to make a rocket that can reach orbit, elaborate and expensive construction techniques to remove every possible kilogram must be used.

Small structural margins not only increase the cost of conventional expendable rockets, they impede them from evolving toward reusability: Launch is a violent process and a structure operating near its design tolerance is more susceptible to fatigue. The Space Shuttle as a reusable vehicle needs extensive refurbishment and testing between launches, to the extent that the launcher is disassembled, inspected, refurbished and rebuilt before every launch. For example, a hydrogen tank used for the on-board fuel cell is manufactured to burst at 1.5 times its usual operating pressure in order to save mass, but this safety factor of 1.5 means the tank may last only 100 cycles. Such a failure-prone component must have a more regular inspection regime, so operational costs go up. In contrast, the fuselage of a pressurized civil aircraft has a safety factor of two, and for that relatively little extra mass will last tens of thousands of pressurization cycles.

This nonlinear relationship between margins and reusability is shown in Fig. 1-2. On the left is an example cumulative plot of load (L) and strength (S) cases for a structural member common to a family of vehicles. Due to the standard deviation of the loads and strengths there exists a small possibility that the load exceeds the strength where the two curves overlap, leading to failure. On the right, the probability of failure is plotted vs. the safety factor $SF_{00} = S_{avg}/L_{avg}$. A better safety factor estimate SF_{03} takes into account the

variability of the load, in this case three standard deviations. Given known distributions for loads and strengths, the corresponding safety factor and failure rate can be estimated. Referring to the right hand figure, note that a small increase in safety factor (*y*-axis) from perhaps 1.2 to 1.5 can decrease the failure rate (*x*-axis) by orders of magnitude and reduce the accuracy with which the loads and strengths for each part must be known. For reusable launchers this increase translates into less frequent inspections and faster turnaround between flights, lower maintenance costs, easier construction and greater reliability.
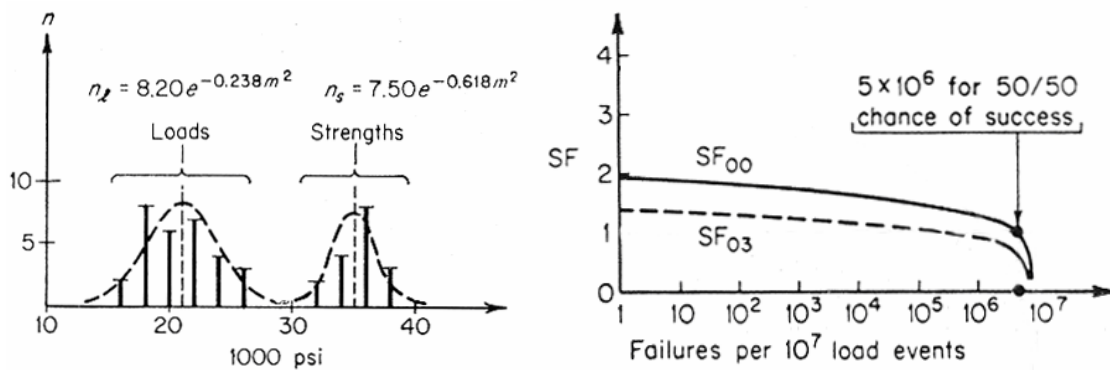
Fig. 1-2: Relationship between structural margins and reusability (Koelle, 1961).

The Space Shuttle is unique in that it is the only craft routinely brought back to earth and inspected for damage and fatigue. Though the overall utility of the Space Shuttle is still debated, the flight and maintenance history of the program since its first flight in 1981 has yielded valuable lessons in the true cost of running a vehicle with overly tight margins. Twenty years of experience with Space Shuttle ground maintenance has failed to produce efficiencies that reduce cost without reducing reliability. Indeed, the outcome of each launcher development effort yields another data point suggesting that every chemically propelled reusable rocket suffers from the problems of fragility and reusability, and that these problems are inherent to the structural and propulsive performance regime within which chemical rockets are feasible. A truly low-cost launch system must be reusable, because without reusability there is a price floor below which launch costs cannot go (Hickman, 2004).

Changing the balance between the propulsive, structural and payload performance is essential to increase structural margins and achieve cheap construction and reusability. This balance is depicted graphically in Fig. 1-3 based on the rocket equation. A 2.5% payload fraction is achieved with an I_{sp} of 450 seconds (nearly the 460 second limit for chemical propellants) and a structural mass fraction of 0.1. Alternatively, the same payload fraction of 2.5% can be achieved using an I_{sp} of 900 seconds and a structural mass fraction of 0.3, meaning that the vehicle structure should be cheaper to manufacture and be orders of magnitude more reliable than for the previous case. In this simplistic sense the I_{sp} (propulsive performance) and structural mass fraction (fragility) can be traded off against one another to provide a given payload fraction, and clearly a structural mass budget three times larger allows for higher margins at lower cost, rather than low margins at high cost.
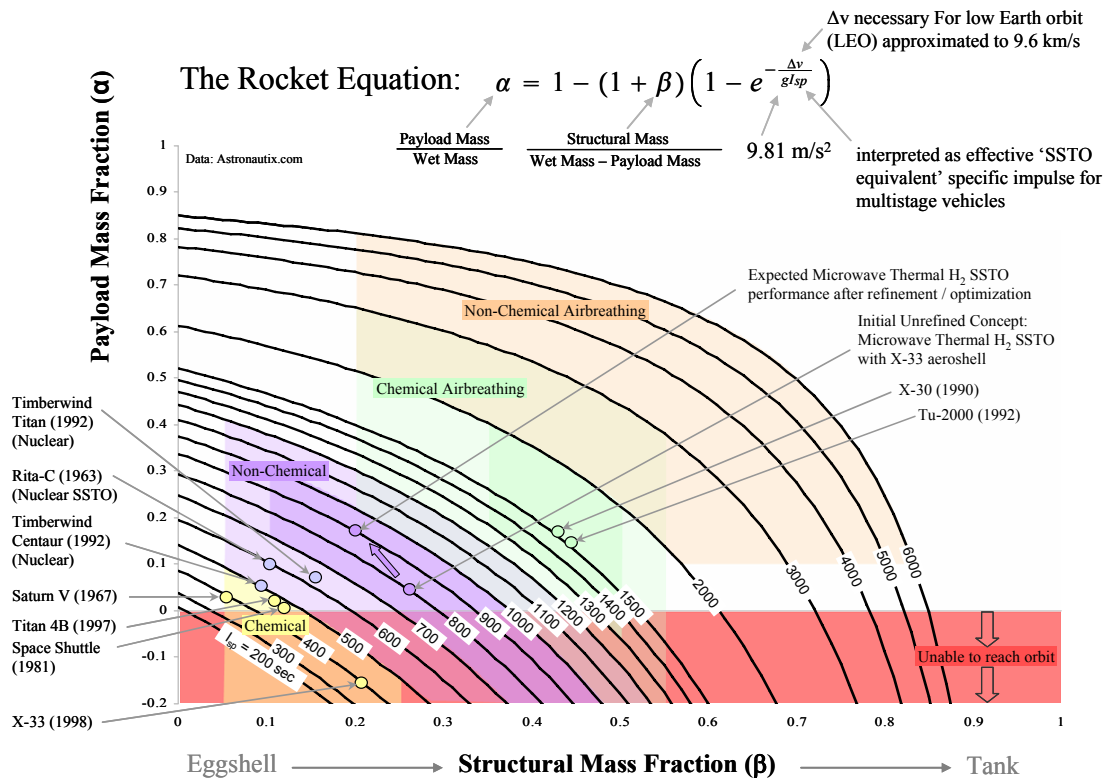
Fig. 1-3: Single stage to orbit (SSTO) equivalent propulsive, structural, and payload performance of launchers. Multistage launchers are compared in this diagram on the basis of an "effective" I_{sp} or structural mass fraction.

Past concept studies, particularly RITA-C nuclear SSTO and the X-33, provide bounds on the likely balance between propulsion, structure, and payload for microwave thermal rockets. Assuming the structural inefficiency of the X-33 combined with an average propulsive performance (I_{sp}) of 720 seconds, Fig. 1-3 can be used graphically to predict a payload fraction of 5%–15% from a launcher with the propulsive capabilities expected for a microwave thermal rocket.

To increase the I_{sp} of the propellant past the practical chemical limit of 460 seconds, the energy given to each kilogram of propellant must be increased. There are only two ways (using existing physics) to do this: The first is to increase the energy density of the launcher power source. The second way is to supply that energy from outside the rocket, thereby avoiding the chemical energy density limit.

Table 1-1 is a sample of the various concepts that have been proposed to bypass the limitations of conventional rockets. In each category, a present constraint is suggested. Some constraints are fundamental, whereas others are resolvable. The approaches themselves may be judged as near-term or more long term, though this distinction is left to the reader. Some approaches have proven to be promising, others not so. Of the promising concepts, perhaps the greatest drawback to all of them is that they have not been brought to the point where they may considered serious alternatives to chemical rockets.

The following sections detail some of the concepts from Table 1-1, and some that are not in the table (yet). Several elements of the systems described were considered at various stages and add context to the microwave thermal rocket concept, which is presented in detail in the next chapter.

Energy Source / Propellant	Chemical	Nuclear	Elementary	External	Present Constraints
Air+other products	Chemical Airbreathing (Curran and Murthy, 2000; Hunt and Martin, 2001) (§ 1.1.8)	Fusion (Adams and Landrum, 2002; Bussard and Jameson, 1995), Nuclear Isomer (Johnson, 2004)	Antimatter Thermal (Vulpetti and Pecchioli, 1989)		Accelerating to near orbital velocity within the atmosphere causes fundamental thermal and propulsion issues.
Combustion Products (e.g., H_2O)	Chemical Rocket (Humble *et al.*, 1995; Sutton and Biblarz, 2001)			Balloon (Rand, 1997)	High molecular weight of combustion products leads to low I_{sp}; low mass fraction.
Elementary Particles (e.g., photons, neutrons)		Nuclear Pulsed (Schmidt *et al.*, 2002)			Low recoil for kinetic energy invested.
Solid Object (e.g., the earth or a tether)				Space elevator (Bradley C. Edwards, 2003), tether (Bogar, 2000), gun launch (Gilreath *et al.*, 1998)	LEO environment lifetime of tethers and elevators. Tether atmospheric heating and grappling. Space elevator material strength. Payload size, acceleration and market elasticity for gun launch.
Non-combusted products, including decomposition products (e.g., H_2, N_2)		Nuclear Thermal (Bussard and DeLauer, 1958), Nuclear Isomer (Johnson, 2004) (§ 1.1.1)	Antimatter Thermal (Vulpetti and Pecchioli, 1989)	Microwave & Laser Thermal (§ 1.1.2) / Ablative (§ 1.1.7), solar thermal.	
Present Constraint	Limited energy density of known chemical combinations.	Public perceptions. Nuclear thermal thrust-to-weight ratio. Production and X-ray de-excitation of nuclear isomers.	Antimatter storage, energy cost of generating antimatter (Schmidt *et al.*, 2000).	Availability of high power sources for microwave and laser systems.	

Table 1-1: Launch vehicle propulsion methods admitted by existing physics, with the possible exception of nuclear isomers, which await further experimental and theoretical verification (Johnson, 2004).

1.1.1 Nuclear Rockets

Solid core nuclear thermal propulsion has been technologically possible since the 1950s and was developed to an advanced level by the Atomic Energy Commission ROVER and NERVA programs between 1954 and 1971 (Gunn, 2001). Fig. 1-4a shows one such hour-long endurance test in Jackass Flats, Nevada. The stability and transient behavior of the nuclear reactors was an early concern, and the destructive test in Fig. 1-4b was conducted as part of the KIWI program that preceded NERVA in order to better understand this. In Russia, a similar development program brought the RD-0410 nuclear thermal thruster to operational status during the 1980s (Haeseler, 1993).

| (a) | (b) | (c) |
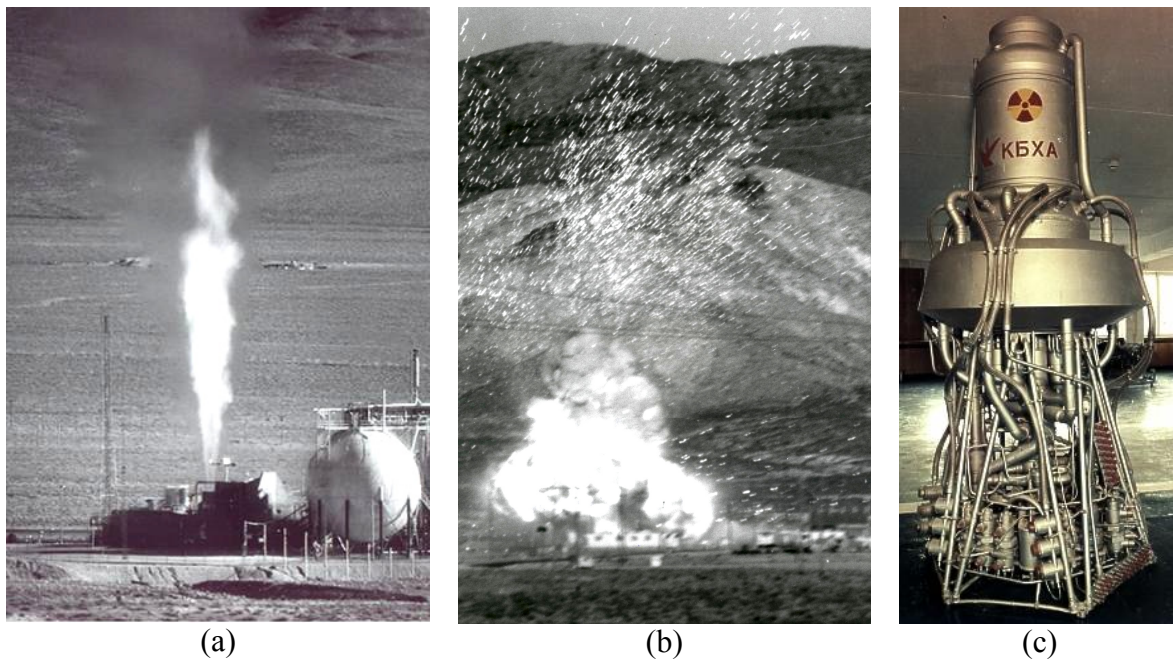
Fig. 1-4: (a) NERVA nuclear thermal rocket test. (© National Air and Space Museum, Smithsonian Institution photo SI 75-13750). In December 1967, an experimental version of NERVA completed a 60-minute endurance test at 2270 K and 1100 MW. (b) Launch accident simulation using a modified Kiwi Nuclear Rocket in January 1965. A sudden increase in power output was imposed, causing the reactor to explode. (NASA Image No. 65-H-49). (c) The RD-0410 Nuclear Thermal Engine (© Dietrich Haeseler).

In place of a conventional combustion chamber, the hydrogen propellant is passed through a reactor core within a number of small channels, forming a heat exchanger like the one shown in Fig. 1-5.
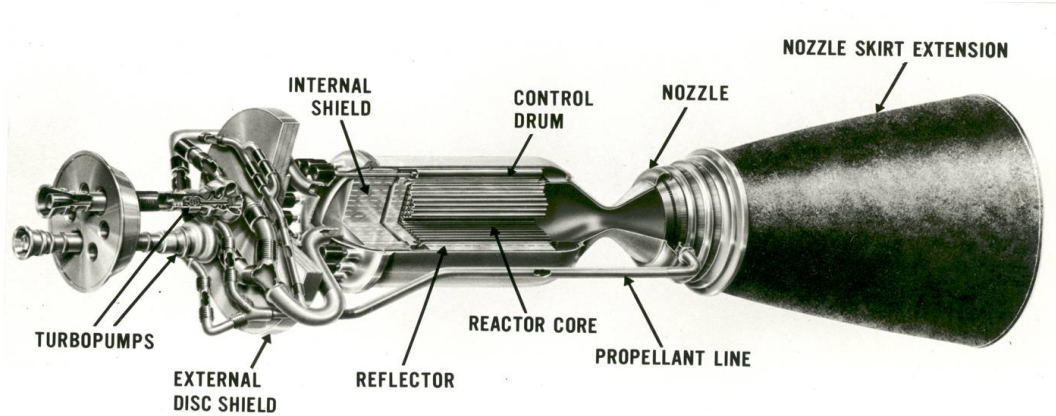
Fig. 1-5: A 1970 schematic of the NERVA nuclear thermal rocket engine (NASA Image No. NPO-70-15803).

As the hydrogen passes through the channels it is heated to the thermal limits of the refractory materials from which the core is made. This temperature limit in turn limits the I_{sp} in a way that can be deduced by considering the conservation of enthalpy as the propellant travels from the combustion chamber (or equivalent) and expands through the nozzle to ambient atmospheric conditions. Since I_{sp} is related to the exhaust velocity by (Humble *et al.*, 1995)

$$I_{sp} = gU_e, \tag{1.1}$$

this can be substituted into the enthalpy conservation equation and rearranged using well-known perfect gas relations to give,

$$I_{sp} = \frac{1}{g}\sqrt{2h} = \frac{1}{g}\sqrt{2c_pT_c} = \frac{1}{g}\sqrt{2R_u\frac{\gamma}{\gamma-1}\frac{T_c}{M_r}}. \tag{1.2}$$

The I_{sp} is therefore proportional to the square root of the propellant temperature T_c prior to nozzle expansion.

Hydrogen is the optimum propellant for a propulsion system whose peak temperature is limited by the melting and softening points of materials, because the enthalpy at any given temperature is higher than any other gases and liquids that could be used for propulsion. That is to say it has the highest enthalpy at the maximum material temperature of the heat exchanger, and therefore the most energy per unit mass to convert into kinetic energy, hence exhaust velocity, hence I_{sp}.

The nuclear fuel itself is often in the form of uranium carbide (UC) pellets coated with zirconium carbide (ZrC), a hydrogen resistant refractory metal. A thin ZrC layer can withstand high temperature hydrogen corrosion for many hours at 2500 K, corresponding to a vacuum I_{sp} of 850 seconds.

Aside from thermal and corrosion constraints, the chosen materials must also possess suitable neutronic properties. In practice, this constraint combined with the problem of high temperature uranium diffusion into the propellant kept the NERVA engine temperature down to around 2500 K. In contrast, the Space Shuttle main engine (SSME) uses an H_2/O_2 reaction to heat its propellant to 3588 K. Despite a higher propellant temperature, the SSME I_{sp} is 453 seconds, whereas the NERVA I_{sp} is 825 seconds, due to the high specific heat capacity of the hydrogen.

Despite the high I_{sp} of 700–950 seconds, solid core nuclear rockets to date still cannot reach orbit because the nuclear reactor is heavy and makes the thrust-to-weight ratio (T/W) too low. For example the 1990s Timberwind program increased the nuclear rocket I_{sp} to 900 seconds and its T/W from 2 to 10 (including shielding mass); but the T/W of the Space Shuttle main engine is around 70. The low T/W means that if the rocket can get off the ground at all, it spends a long time accelerating to orbital velocity. During this extra time, the ascent trajectory accumulates greater drag and gravity losses, which increase the total ΔV of the ascent, decreasing the payload fraction and greatly reducing the advantage of higher I_{sp}.

1.1.2 Laser Thermal Rockets

Laser thermal propulsion is similar to nuclear thermal propulsion in that a heat exchanger is used in place of a combustion chamber to heat a hydrogen propellant. The laser-propelled heat-exchanger (HX launcher) concept was suggested by Kare (1995) and is shown in Fig. 1-6.

FIGURE 1. Heat Exchanger rocket concept
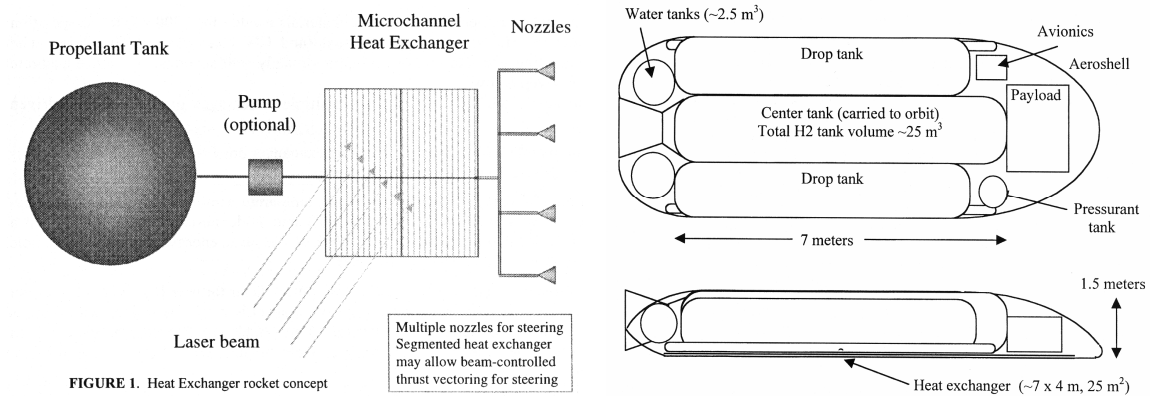
Fig. 1-6: HX Laser Heat Exchange Concept of Kare (1995).

The heat exchanger operates in a laminar regime by analogy to designs used for integrated circuit cooling. The heating channels are 200 μm wide by 2 mm deep and 3 cm long, raising the hydrogen propellant temperature to 1300 K; corresponding to an I_{sp} of ~ 600 s. Kare estimates the heat-exchanger mass to be 125 kg for a 5.4 ton vehicle carrying a 122 kg payload, corresponding to a payload fraction of 2.26%.

The propagation of high power transatmospheric laser beams is discussed in § 1.1.6.

1.1.3 Electrothermal Rockets

Electrothermal propulsion, as opposed to thermal propulsion, uses the plasmadynamic breakdown of the propellant itself to absorb incoming radiation, thereby heating it to a very high temperature. Early experiments revealed that plasma forming in a propulsive duct has a tendency to propagate toward the source of radiation. This effect was first studied by Raizer (1972), who realized that the mechanism of this propagation is thermal

conduction.   He established an analogy between high-pressure discharges and combustion flames, leading to the terms "laser-supported combustion wave" and "microwave-supported combustion wave."   Following this work, a variety of plasma stabilization schemes were studied for application to electrothermal propulsion systems (Balaam and Micci, 1995; J. Mueller, 1992; Knecht and Micci, 1988).

A microwave electrothermal propulsion system can be built using a waveguide, as shown in Fig. 1-7. Incident microwaves enter through a dielectric window, forming a plasma absorption region by the electron inverse bremsstrahlung mechanism. Without a plasma stabilization scheme the plasma propagates toward the source and impinges on the window, causing damage.   In all schemes that employ plasmas for absorption it is important that the plasma, whose electron temperatures generally lie in the 10,000–13,000 K range, is confined away from any walls to minimize the energy losses and damage to internal surfaces.   For this purpose Power (1992) has discussed the use of magnetic nozzles.
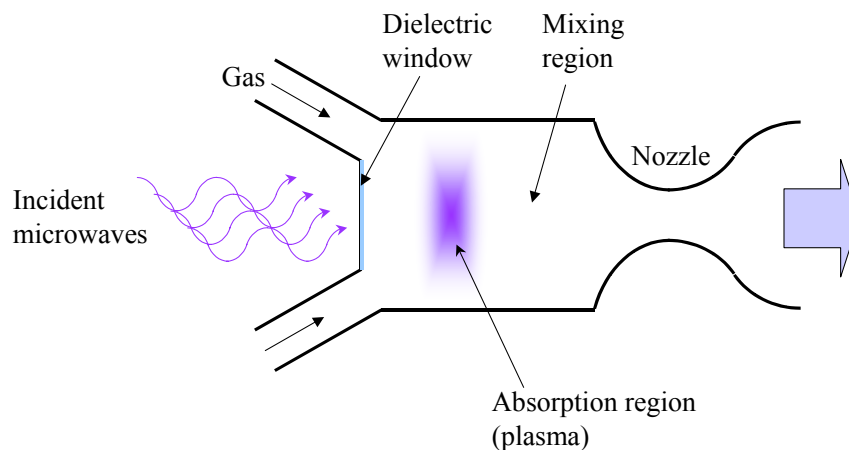
Fig. 1-7: Microwave-supported combustion wave in a waveguide.

Upon formation, the plasma mixes with the surrounding propellant as it enters the converging section of a converging-diverging nozzle. Ideally, collisions cause the mixture to reach thermal equilibrium before reaching sonic conditions at the nozzle, and

subsequent supersonic expansion from the diverging section of the nozzle, to produce a high exit velocity, and hence high I_{sp}. Mueller (1992) points out that coupling of microwave energy into gases at pressure on the order of atmospheric is extremely efficient, and that incident power absorption efficiencies in excess of 95% have been obtained experimentally.

Nevertheless, it should be noted that for absorption schemes involving plasmas there are important constraints: The plasma frequency $\omega_{p\sigma}$ is related to the number density of charged species by Eq. (1.3).

$$\omega_{p\sigma}^2 = \frac{n_{0\sigma}q_\sigma^2}{\varepsilon_0 m_\sigma} \tag{1.3}$$

As the plasma density $n_{0\sigma}$ increases, the plasma frequency described by Eq. (1.3) exceeds the frequency of incident microwaves, and reflection occurs. The net effect of the plasma density limitation is to constrain the maximum power absorbed by the propellant for a given pressure and mass flow rate. The frequency dependence of this constraint suggests that lasers may offer an advantage over microwaves in the context of electrothermal propulsion for application to launch.

Using microwaves at centimeter wavelengths enables the possibility of resonant cavity absorption. For example, microwaves at the industrial heating frequencies of 2.45 GHz and 915 MHz correspond to wavelengths of 12 cm and 33 cm, respectively. Resonant cavity techniques have been experimentally demonstrated to offer absorption efficiencies in excess of 95% (Power, 1992). In cylindrical cavities, the TM_{011} and TM_{012} modes shown in Fig. 1-8 are convenient for propulsion applications. Microwaves can be introduced into the cavity using a coaxial applicator or by coupling to a waveguide. For electron inverse bremsstrahlung absorption, areas with the strongest electric fields define the plasma discharge region.
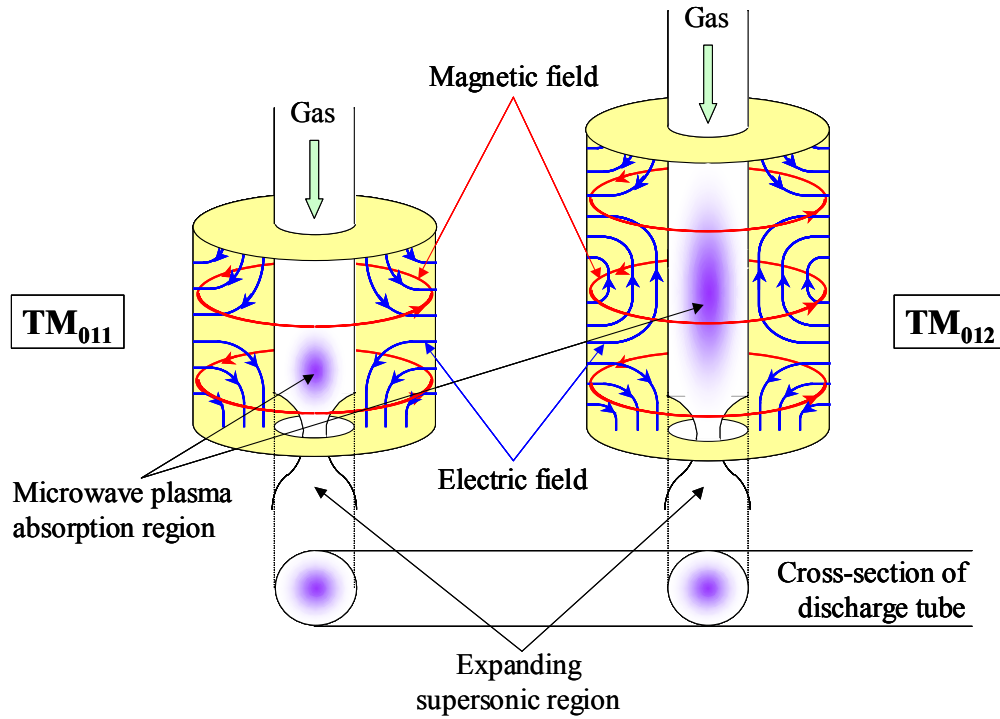
Fig. 1-8: Cylindrical resonant cavity modes suitable for propulsion.

The possibility of increasing the I_{sp} of electrothermal propulsion systems by introducing a second plasma absorption region in the expanding supersonic region of the nozzle flow was examined by Chiravalle *et al.* (2001). A resonant cavity thruster was simulated by solving the complete system of Maxwell and Navier-Stokes equations for argon flow in a realistic thruster geometry; however, the results suggest only modest increases in I_{sp} were possible in this particular case.

Thus far the majority of electrothermal propulsion work has focused on in-space propulsion, which operates at far lower pressures and mass flow rates than needed to produce a *T/W* ratio large enough for launch. The scalability of these techniques to the high pressure, high mass flow rate regime need for launch has yet to be demonstrated.

1.1.4 Molecular Absorption Propulsion

Molecular absorption of energy has recently been studied for application to laser propulsion (Chiravalle *et al.*, 1998) and can be employed in the microwave region too. In contrast to the electron inverse bremsstrahlung absorption of plasma formation, molecular absorption is achieved via excitation of an internal rotation or vibration mode. By acting on the propellant itself or a seed molecule, heating of the flow can be achieved in subsonic or supersonic flows without the use of plasmas. As shown in Fig. 1-9 this results in the possibility of energy addition throughout the length of a propulsive duct, (a), rather than concentrating energy in a particular region, (b), as with the waveguide and resonant cavity concepts shown in Fig. 1-7 and Fig. 1-8, respectively.

Fig. 1-9: Left: Combustion chamber energy addition. Right: Continuous energy addition. (Chiravalle *et al.*, 1998)

Because area variation along the flowpath can be used to offset temperature increases, more gradual addition of energy at lower temperatures could result in propulsion systems with less stringent cooling requirements and lower frozen-flow losses.

1.1.5 Rectenna-based Concepts

Rectennas (rectifying antennas), (Brown, 1984; Brown, 1992; East, 1992), are arrays of rectifying diodes arranged at scales similar to the wavelength of the incoming microwaves, typically at frequencies of 1–10 GHz, generating a DC current. Rectennas have been developed over a number of years in large part due to the efforts of Brown (1984; 1992), who demonstrated the flight of an helicopter using 2.45 GHz microwaves in 1964 (Fig. 1-10). Rectennas have also been used for demonstrations of wireless power transmission (WPT) and for the 1987 SHARP unmanned aerial vehicle (UAV), shown in Fig. 1-11.
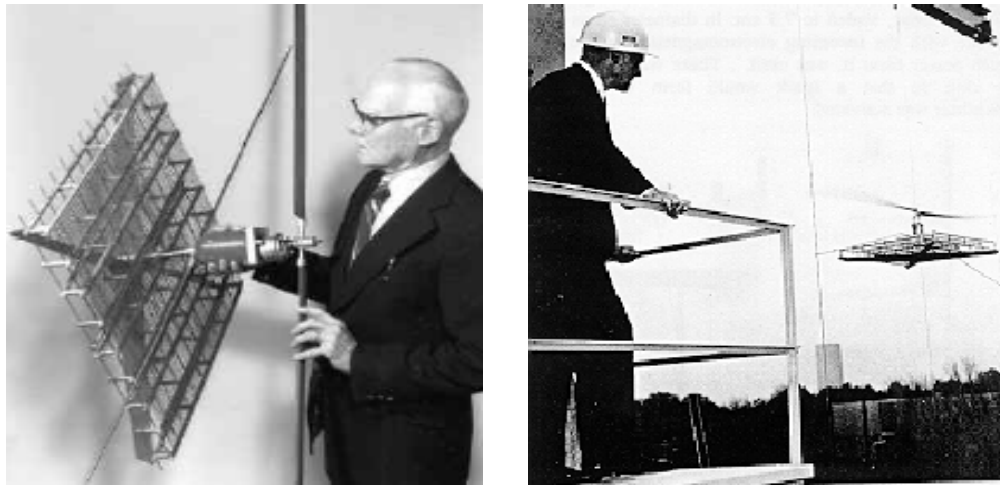
Fig. 1-10: W.C. Brown and the 200 Watt, 2.45 GHz microwave helicopter (1964) as described by Brown (1984).
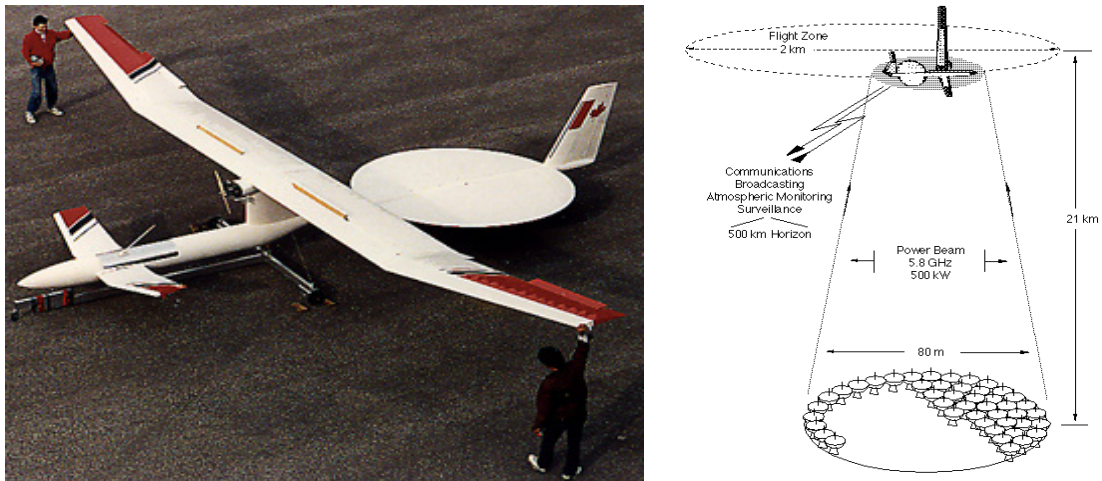
Fig. 1-11: The 10 kW, 2.45 GHz SHARP UAV (1987) as described by East (1992).

The microwave lightcraft concept of Myrabo (1995) shown in Fig. 1-12 uses rectennas to produce a DC current that drives a series of Lorentz force accelerators around the periphery of the craft. The 1400 kg helium-filled lenticular craft is 15 m in diameter and receives a 5.6 GW, 35 GHz microwave beam from above. A portion of the beam is reflected and focused ahead of the craft to form a microwave-induced aerospike that reduces heating and drag on the vehicle.
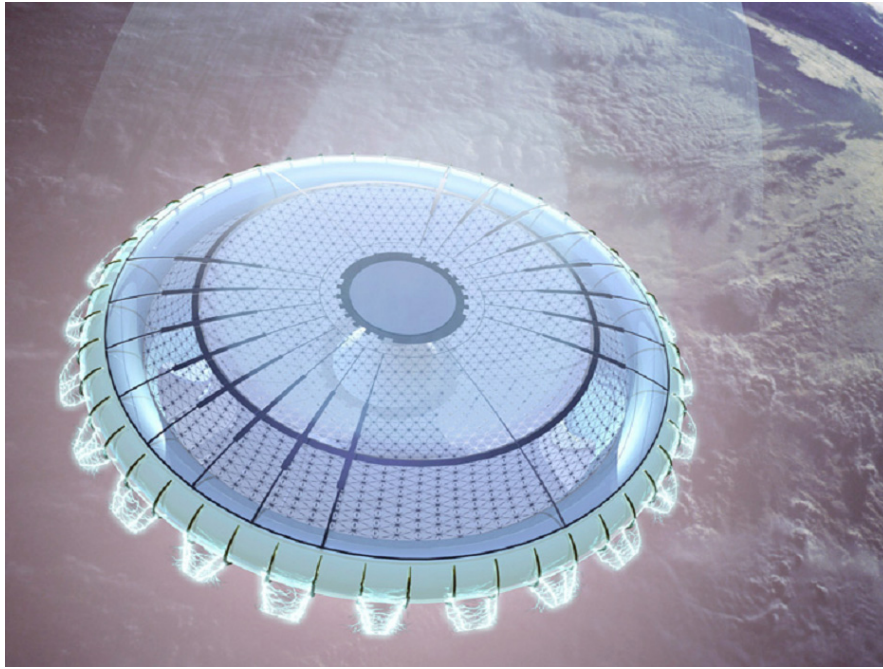
Fig. 1-12: The microwave lightcraft concept of Myrabo (1995).

However, rectennas are currently limited to power densities of less than 1 KW/m^2 at 2.45 GHz, which together with the high weight of ~1 kg/kW for DC power processing equipment, limits their use on highly energetic vehicles. Myrabo calculates that the microwave lightcraft requires a 35 GHz rectenna to operate at power densities 10,000 to 40,000 times higher than the present state of the art, and suggests a high-pressure helium-cooled silicon carbide rectenna array as a possible solution.

1.1.6   Transatmospheric Laser Propagation

Transatmospheric laser propagation has been studied for application to launch since the 1970s, and aside from cost, its use is constrained by three important factors: Water vapor absorption, scattering and thermal blooming.

Atmospheric turbulence causes small changes in the refractive index of air that bends the path of the laser beam. The majority of turbulence occurs in the lower 20 km of the atmosphere, shown in Fig. 1-13, and these lower layers of turbulence cause scintillation of the beam as seen from a target.
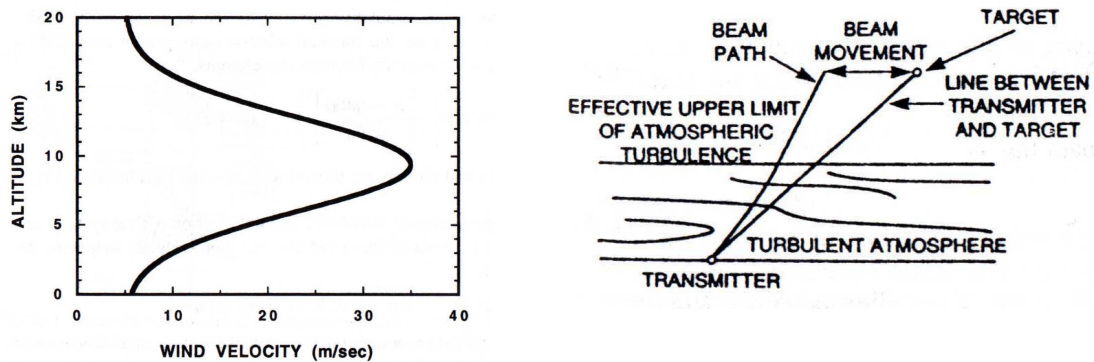
Fig. 1-13: Left: Atmospheric wind profile. Right: Effect of atmospheric turbulence on targeting. (Tyson, 2000)

Adaptive optics techniques developed to address similar problems with astronomical observations have been suggested to help combat the problem of scintillation. Alternatively, spacing multiple laser sources over a wide area combined with a relatively large vehicle as a target can avoid many of the downsides of atmospheric scintillation without the need for adaptive optics.

Thermal blooming occurs as heating of the atmosphere along the path of the laser beam causes the refractive index of the air to change. This nonlinearity of the air can self-focus or defocus the beam. As before, it has been suggested that this problem can be controlled using adaptive optics (Kanev *et al.*, 1998) or avoided to some extent by spacing the laser sources out over a wide area and combining the beams at the target. At laser wavelengths, the aperture diameter required is on the order of a meter and many such apertures can be used at modest power.

1.1.7   Ablative Laser & Microwave Propulsion

The use of lasers for propulsion was first suggested by Kantrowitz (1972) and independently by Minovich (1972) a short time later. Kantrowitz focused on lasers in his seminal paper because high power microwave sources at wavelengths practical for beamed- energy launch did not exist at that time (Kantrowitz, 2004). A history is given

by Brandstein & Levy (1998). Most of the attention thus far has focused on ablative laser propulsion (Pakhomov and Gregory, 2000).

The laser lightcraft (Wang *et al.*, 2002) has a diameter of 12.2 cm and weighs roughly 50 grams. It is powered by a 10 kW CO_2 laser. A parabolic mirror on the underside of the craft, shown in Fig. 1-14, focuses the beam into the engine air or propellant. The pulsed laser heats the air, causing it to break down into a plasma. The plasma strongly absorbs the incoming pulse, heating to roughly 18,000 K before exploding from the annular underside region, generating thrust.
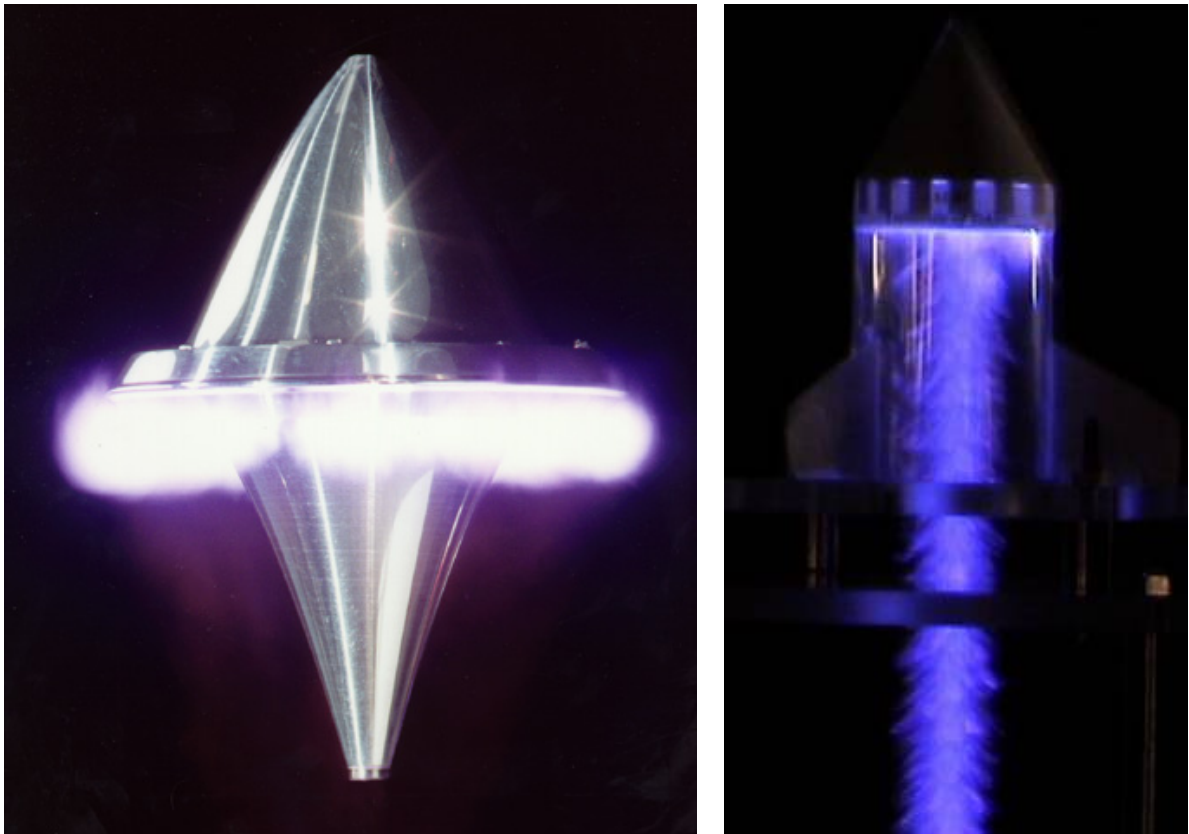
Fig. 1-14: Ablatively propelled craft. Left: Myrabo's laser lightcraft (Wang *et al.*, 2002) (1987–2000, 50 g, 150 kW). Right: Microwave ablative rocket of Oda *et al.* (2003); (140 GHz, 1 MW).

The ablative microwave lightcraft concept of Myrabo and Benford (1994) shown in Fig. 1-15 uses microwaves rather than lasers. The concept is airbreathing but switches to an on-board hydrogen supply for the later stages of ascent (in vacuum). Because of the optics, the beam must point roughly down the axis of the vehicle, so the ascent trajectory is constrained to be flat initially, and an HPM relay satellite can be used to complete the orbital insertion.
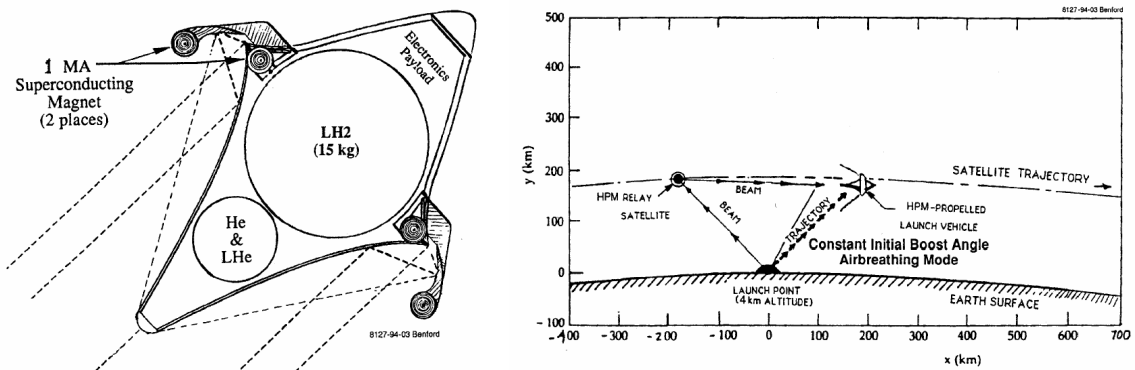
Fig. 1-15: Left: Ultralight microwave-boosted microsatellite (liftoff mass 30 to 50 kg). Right: Airbreathing ascent of the microwave lightcraft. (Myrabo and Benford, 1994)

In 2003 ablative propulsion using a 1 MW 140 GHz gyrotron was demonstrated, and is shown on the right of Fig. 1-14. At present, ablative propulsion converts only a few percent of the incident energy to thrust; however, propulsive cycles using double pulses appear to offer efficiencies as high as 40% (Pakhomov *et al.*, 2002).

1.1.8   Hypersonic Airbreathing Propulsion

Some chemical-energy and beamed-energy concepts use an airbreathing ascent. Conventional airbreathing propulsion has a greater I_{sp} (often greater than 1000 seconds) because oxidizer does not need to be carried. Although the I_{sp} degrades with increasing Mach number, as in Fig. 1-16, it can outperform conventional rocket propulsion provided there is enough air intake to provide sufficient thrust. Numerous different propulsion modes are required to progress from Mach 0–15, as seen in Fig. 1-16, with transition to rockets taking place at roughly 100,000 ft (30 km). These multiple modes of propulsion

significantly increase the engineering difficulty of practical airbreathing launch vehicles. Nevertheless, the Hyper-X program has recently flight tested the X-43 vehicle to demonstrate airframe-integrated scramjet propulsion (Bahm *et al.*).
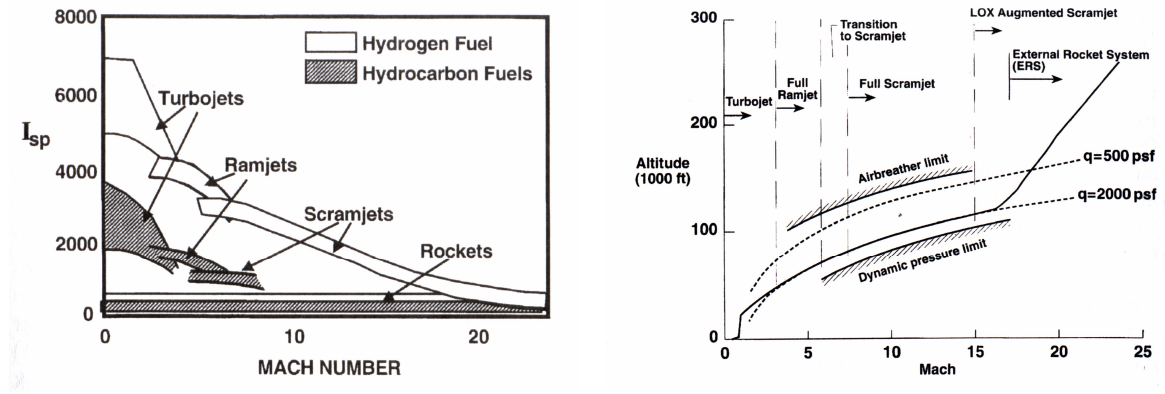
Fig. 1-16: The airbreathing ascent regime. Left: High Mach number propulsion performance (Maurice *et al.*, 2001). Right: The airbreathing ascent corridor (Hunt and Martin, 2001).

For ideal beamed-energy airbreathing propulsion the launcher does not expend an on-board propellant of any kind, so the mass of the launcher remains unchanged and the effective I_{sp} is infinite. However, the airbreathing regime of propulsive performance brings with it other constraints: From a fundamental point of view, an airbreathing launch vehicle must accelerate to a reasonable fraction of orbital velocity *within the atmosphere*, unlike rockets, which need no air intake and therefore accelerate outside the atmosphere.

Broadly speaking the engine air mass flow rate increases with velocity, vehicle drag with velocity squared, and surface heating with velocity cubed. As this velocity increases, the engineering difficulties of reconciling thrust, drag, and thermal loads within manageable limits become extreme. To deal with surface heating heavy thermal protection systems are required. To overcome the drag and maximize propulsion system performance the airbreathing launch vehicle must appear to the oncoming flow as mostly inlet. Should the engine fail, the tremendous net force could result in catastrophic deceleration. If it were

possible to overcome the aforementioned problems, an airbreathing beamed-energy launch vehicle in particular would be formidable, carrying little or no propellant.

1.2 Why Microwave Thermal Propulsion? Summary and References

In the field of propulsion, there are many technologies that could solve the launch problem, and each has its particular advantages and drawbacks. This thesis sets forth the new approach of microwave thermal propulsion, which belongs to the wider class of heat exchanger-based propulsion techniques that includes nuclear thermal and laser thermal propulsion.

As described in the introduction, the launch problem is both a technological and economic problem in nature, and all developments in the launch market since 1960, technological or otherwise, have had little or no effect on the launch price because they do not affect the market size or the price the market will bear. The past 40 years of launch prices (Fig. 1-1) suggest that the elasticity of demand is locally flat at the present launch price of $10,000 per kilogram of payload, in essence a metastable level, and that an evolutionary path to a lower launch price does not exist.

It is unclear whether or not a transition to a lower price at which the market size increases is possible with present technology given that the next lowest stable price is thought to be less than $1,000 per kilogram of payload delivered to LEO. With present technology, such a tenfold reduction in cost is achieved by economies of scale, and these economies are in turn supported by a boost in demand, artificial or otherwise. Furthermore, this boost in demand must be sustained until new markets can develop to support the increased volume of launches.

This thesis offers a technological solution to the problem above: The Launch Problem. Using a nonchemical circumvents the specific impulse (I_{sp}) limitation of 460 seconds for convectional rockets by using a heat-exchanger. This heat-exchanger approach is used for nuclear thermal propulsion, which achieved an I_{sp} of 825 seconds using the technology of the 1960s. As described by the rocket equation, doubling the I_{sp}

approximately triples the structural mass fraction of the launcher, sparing a large amount of extra mass that can be used to increase the payload fraction and increase structural margins, leading to lower cost construction.

The highly nonlinear relationship between structural margins and probability of failure (Fig. 1-2) raises the possibility of reusability, leaving a vehicle with mass to spare for an increased payload fraction using only a single stage. The combined effect of lower structural cost, greater payload fraction and higher flight rate can profoundly alter the economics of launch, minimizing the need to boost launch demand in order to solve the launch problem.

Although there are alternatives to microwave thermal propulsion, summarized in Table 1-1, these alternatives appear less attractive for various reasons. This is not to say that the problems cited in Table 1-1 are insurmountable, even with modest investment, simply that the microwave thermal approach appears more practical to implement in the near-term. Airbreathing launch generally requires a complex series of elements in the propulsion flow path, and the problem of thermal protection has yet to be fully resolved. Gun launch imposes extreme conditions on the payload that limit its utility. Tethers, skyhooks and space elevators await solutions to several materials science problems relating to high strength threads combined with atmospheric heating and/or longevity in the space micrometeoroid environment. Laser directed energy launch awaits a substantial reduction in the cost ($/W) of suitable lasers, and finally, antimatter and nuclear thermal approaches carry power sources that are presently so heavy that their thrust-to-weight ratio (T/W) is too low for launch, limiting their utility to in-space applications.

Aside from public perception of all nuclear issues, T/W is the key factor that precludes nuclear thermal thrusters being used for launch. On the other hand, the microwave thermal thruster does not require many of the heaviest elements of the nuclear thermal thruster, and it is a key finding of Chapter 2 that for microwave thermal rockets a propulsion system T/W of 50–150 is possible; comparable to conventional rockets.

Chapter 2 begins with an explanation of how the microwave thermal idea arose. It is perhaps the *raison d'être* for this unusual thesis, giving some further context for the work as a whole and the motivations that shaped it. Chapter 2 then goes on to describe the unique elements of a microwave thermal launch system. Unlike conventional launch systems, microwave thermal launch has the peculiar constraints of atmospheric absorption and high power breakdown that affect propagation of the microwave beam, which can be generated by a ground-based array of high power gyrotron sources. The finite diameter of the phased array constrains the maximum useful beam range, leading to a particular new type of ascent trajectory that minimizes the downrange distance traveled during orbital insertion by using unusually high acceleration. A simplistic model of the microwave thermal thruster performance and ascent trajectory is given.

Given the description of a microwave thermal rocket and an examination of its general characteristics and expected performance in Chapter 2, Chapter 3 places such a system as the end goal and begins the process of constructing a series of practical steps toward it. Back-of-the-envelope calculations are used to define the parameters of an initial theoretical and experimental investigation of microwave thermal heat exchange. It is determined that a low-cost initial demonstration of the microwave thermal heat exchange process is feasible at laboratory-scale using resonant microwave cavities at low frequency and low power, as opposed to free-space beams at high frequency and high power.

At its core, the resonant cavity approach to a laboratory-scale microwave thermal thruster harbors a highly nonlinear coupled electromagnetic-conduction-convection problem whose dynamics are in many ways more complex than anticipated from a free-space (non resonant cavity) experimental test. Great care is needed to capture the dominating affect that material temperature has on the distribution of microwave absorption throughout the single tube heat exchanger. Chapter 4 and Chapter 5 therefore develop the electromagnetic, conduction and convection aspects of this model separately, combining them in Chapter 6 to produce a fully coupled simulation of the laboratory-scale microwave thermal system. This is the first time such a coupled simulation has been attempted, and in addition to predicting the expected performance of the laboratory-scale

system, the results show unexpected time-dependent dynamics that depend on propellant flow rate and are specific to the resonant cavity approach.

An experimental examination of this 200 watt single tube thruster is presented in Chapter 7. The microwave thermal thruster principle is demonstrated and measurements of thruster surface temperature are compared to the theoretical predictions of Chapter 6. Aside from verifying the basic operational parameters of such a thruster, the measured or calculated temperature distribution of the heat exchanger forms the starting point for several further analyses. Also observed is a time-dependent oscillation similar to that predicted in Chapter 6, though given practical constraints, a direct comparison between theory and experiment is deferred to later study.

Chapter 8 explores future analyses that are important to the design of a microwave thermal thruster and that become possible with the heat exchanger temperature model set forth in Chapter 6. Given the lessons learned from the present work, all the expected engineering challenges in reducing a microwave thermal rocket to practice are summarized.

Adams, R.B. and Landrum, D.B. (2002). *Analysis of a fusion-electric airbreathing earth to orbit launch vehicle*. Journal of Propulsion and Power **18**(4): p. 933–942.

Arbit, H.A., Clapp, S.D. and Nagai, C.K. (1970). *Investigation of the Lithium-Fluorine-Hydrogen Trimonellant System*. J. Spacecraft **7**(10).

Bahm, C., Baumann, E.*, et al. The X-43A Hyper-X Mach 7 Flight 2 Guidance, Navigation, and Control Overview and Flight Test Results*.

Balaam, P. and Micci, M.M. (1995). *Investigation of Stabilized Resonant-Cavity Microwave Plasmas for Propulsion*. Journal of Propulsion and Power **11**(5): p. 1021–1027.

Bogar, T.J., et. al. (2000). *Hypersonic Airplane Space Tether Orbital Launch System - Phase 1 Final Report*. NASA Institute for Advanced Concepts.

Bradley C. Edwards, E.A.W. (2003). *The Space Elevator: A Revolutionary Earth-to-Space Transportation System*.

Brandstein, A. and Levy, Y. (1998). *Laser propulsion for space vehicles*. Journal of Propulsion and Power **12**(12).

Brown, W.C. (1984). *The history of power transmission by radio waves*. IEEE Transactions on Microwave Theory and Techniques **MTT-32**(9).

Brown, W.C. (1992). *Beamed microwave power and its application to space*. IEEE Transactions on Microwave Theory and Techniques **40**(6).

Bussard, R.W. and DeLauer, R.D. (1958). *Nuclear rocket propulsion*. McGraw-Hill series in missile and space technology, New York. McGraw-Hill.

Bussard, R.W. and Jameson, L.W. (1995). *Inertial-Electrostatic-Fusion Propulsion Spectrum – Air-Breathing to Interstellar Flight*. Journal of Propulsion and Power **11**(2): p. 365–372.

Chang, I. (2000). *Overview of world space launches*. Journal of Propulsion and Power **16**(5): p. 853–866.

Chiravalle, V.P., Miles, R.B. and Choueiri, E.Y. (1998). *Laser propulsion using a molecular absorber*.

Chiravalle, V.P., Miles, R.B. and Choueiri, E.Y. (2001). *Numerical simulation of microwave-sustained supersonic plasmas for application to space propulsion*, in 39th AIAA Aerospace Sciences Meeting and Exhibit. Reno, NV.

Curran, E.T. and Murthy, S.N.B. (2000). *Scramjet propulsion*. Progress in astronautics and aeronautics; v. 189., Reston, VA. American Institute of Aeronautics and Astronautics.

East, T.W.R. (1992). *A Self-Steering Array for the Sharp Microwave-Powered Aircraft*. IEEE Transactions on Antennas and Propagation **40**(12): p. 1565–1567.

Gilreath, H., Driesman, A.*, et al.* (1998). *The Feasibility of Launching Small Satellites with a Light Gas Gun*, in 12th AIAA/USU Conference on Small Satellites.

Gunn, S. (2001). *Nuclear propulsion – a historical perspective*. Space Policy **17**: p. 291–298.

Haeseler, D. (1993). *Informational material from Chemical Automatics Design Bureau, Voronezh*. Private Communication to M. Wade.

Hickman, R. (2004). *The Space Shuttle and the Future of Space Launch Vehicles*. Testimony to the science, technology and space subcommittee of the Senate committee on commerce, science and transportation on behalf of The Aerospace Corporation.

Humble, R.W., Henry, G.N. and Larson, W.J. (1995). *Space propulsion analysis and design*. 1st ed. Space technology series, New York. McGraw-Hill.

Hunt, J.L. and Martin, J.G. (2001). *Rudiments and methodology for design and analysis of hypersonic air-breathing launch vehicles*. Progress in Astronautics and Aeronautics **189**: p. 939–978.

J. Mueller, M.M.M. (1992). *Microwave waveguide helium plasmas for electrothermal propulsion*. Journal of Propulsion and Power **8**(5): p. 1017-1022.

Johnson, B.L. (2004). *Isomer Energy Source for Space Propulsion Systems*. Wright-Patterson Air Force Base, Air Force Institute of Technology.

Kanev, F., Lukin, V. and Lavrinova, L. (1998). *Analysis of algorithms for adaptive control of laser beams in a nonlinear medium*. Applied Optics **37**(21).

Kantrowitz, A. (1972). *Propulsion to orbit by ground-based lasers*. Astronautics and Aeronautics **10**(74-76).

Kantrowitz, A. (2004). *Regarding 1972 paper.* Private Communication to K. Parkin.

Kare, J.T. (1995). *Laser-Powered Heat-Exchanger Rocket for Ground-to-Orbit Launch*. Journal of Propulsion and Power **11**(3): p. 535–543.

Knecht, J.P. and Micci, M.M. (1988). *Analysis of a microwave-heated planar propagating hydrogen plasma*. AIAA Journal **26**(2).

Koelle, H.H. (1961). *Handbook of Astronautical Engineering*. McGraw-Hill.

Maurice, L., Edwards, T. and Griffiths, J. (2001). *Liquid hydrocarbon fuels for hypersonic propulsion*. Progress in astronautics and aeronautics **189**: p. 939–978.

Minovich, M.A. California Institute of Technology (1972). *The laser rocket – A rocket engine design concept for achieving a high exhaust thrust with high I_{SP}.*

Myrabo, L.N. (1995). *Hyper-energetic manned aerospacecraft propelled by intense pulsed microwave beam*. SPIE **2557** p. 193–208.

Myrabo, L.N. and Benford, J. (1994). *Propulsion of Small Launch Vehicles Using High Power Millimeter Waves*. SPIE 2154: p. 198.

NASA (1994). *Commercial Space Transportation Study*.

Oda, Y., Nakagawa, T.*, et al.* (2003). *An observation of plasma inside of microwave boosted thruster*, in Second International Symposium on Beamed Energy Propulsion. Sendai, Japan: Conf. Proc. AIP.

Pakhomov, A.V. and Gregory, D.A. (2000). *Ablative laser propulsion: An old concept revisited*. AIAA Journal **38**(4): p. 725–727.

Pakhomov, A.V., Gregory, D.A. and Thompson, M.S. (2002). *Specific impulse and other characteristics of elementary propellants for ablative laser propulsion*. AIAA Journal **40**(5): p. 947–952.

Power, J.L. (1992). *Microwave electrothermal propulsion for space*. IEEE Transactions on Microwave Theory and Techniques **40**(6).

Raizer, Y.P. (1972). *Propagation of a high-pressure microwave discharge*. Soviet Physics JETP **34**(Jan): p. 114–120.

Rand, J.L. (1997). *Balloon assisted launch to orbit – An historical perspective*, in 33rd AIAA/ASME/SAE/ASEE Joint Propulsion Conference and Exhibit, Seattle, WA, July 6–9.

Schmidt, G.R., Bonometti, J.A. and Irvine, C.A. (2002). *Project Orion and future prospects for nuclear pulse propulsion*. Journal of Propulsion and Power **18**(3): p. 497–504.

Schmidt, G.R., Gerrish, H.P.*, et al.* (2000). *Antimatter Requirements and Energy Costs for Near-Term Propulsion Applications*. Journal of Propulsion and Power **16**(5).

Sutton, G.P. and Biblarz, O. (2001). *Rocket propulsion elements*. 7th ed, New York. John Wiley & Sons.

Tsiolkovsky, K.E. (1924). *Spaceship, 1924, in Izbrannye Trudy, Compiled by Vorob'ev, B.N., Sokol'skii, V.N., General Editor Acad. Blagonravov, Izdatel'stvo Akademii Nauk SSSR, Moscow, Russia, 1962, 222 (in Russian). Edited Machine Translation prepared by Translation Division, Foreign Technology Division, WP-AFB, Ohio, on May 5th, 1966, 307.*

Tyson, R.K. (2000). *Adaptive optics engineering handbook.*

Vulpetti, G. and Pecchioli, M. (1989). *Considerations About the Specific Impulse of an Antimatter-Based Thermal Engine*. Journal of Propulsion and Power **5**(5): p. 591–595.

Wang, T.S., Chen, Y.S.*, et al.* (2002). *Advanced performance modeling of experimental laser lightcraft*. Journal of Propulsion and Power **18**(6): p. 1129–1138.

CHAPTER 2
ELEMENTS OF MICROWAVE THERMAL ROCKETRY

2.1   A Personal Note on the Origin of This Work

In order to understand this thesis it helps to understand what it is and where it came from. Herein lies the documentation of a new idea, the Microwave Thermal Rocket, for which a patent has recently been issued (Parkin, 2006).   Much of the intellectual input that underlies this body of work, perhaps even the majority, lies not in the experimental or theoretical problems but in the largely unwritten evolution of an understanding of what a microwave thermal rocket is, should be, and where its inherent advantages lie.   It was a necessary process in order to arrive at the important questions, the kernel of the problem, to which I devote the analytical chapters of this thesis.

A great deal of work has gone into bringing together often simple techniques and understanding from an eclectic group of fields: Economics, propulsion, fluid mechanics, electromagnetics, plasmadynamics, trajectory analysis, microwave sintering, particle accelerators (resonant cavities), materials science and system engineering. This has been a long process of convergence and learning, where many parts of a puzzle have fallen into place as research and feedback has enabled me to discard less promising avenues of inquiry and design possibilities one by one.

The microwave thermal rocket concept, its manner of operation and the thruster that powers it arose over time from the intersection of several ideas. The process leading up to the initial idea began when I read "*The Way to Go in Space*" (Beardsley, 1999), a Scientific American article that in part discusses Dr. Leik Myrabo's ideas on the future of space launch.   The article mentions a trip to Russia in which experts suggest that microwaves are a more practical energy source than lasers. I began to wonder which type of source made sense from the perspective of a beamed-energy propulsion system, and what type of absorption and propulsion process might best capitalize on that.

In 2001 I was able to examine the plasmadynamic options as part of a short eight week study on plasmadynamic options for an AJAX-like space transportation system, made possible by a gift from Blue Operations LLC. During the study I constructed a taxonomy listing all the propulsion options compatible with beamed-energy on a blackboard, and I held a meeting with Dr. Fred Culick and Dr. Joel Sercel to discuss them. Dr. Sercel suggested that I include heat exchangers on the list, which he had previously examined for application to in-space propulsion using lasers. At the time my thoughts were still very much occupied with plasmadynamic methods, and it was several months before I judged the plasmadynamic approach to be more complex than the alternatives.

Those alternatives to plasmadynamic propulsion boiled down to two approaches, the first was the use of molecular absorption (§ 1.1.4). A molecular absorber such as ammonia could be used to absorb microwaves directly, thereafter being expanded though a nozzle to produce thrust. The alternative was an absorber plate that was thermally coupled to a propellant flow. A key question in both cases was how to integrate a high power microwave window into a rocket structure that could focus an incoming beam into a "combustion chamber," and how to do so using the minimum possible mass. In the molecular absorber case, the poor microwave absorption of many possible propellants suggested that a resonant cavity would be needed also.

The first mental leap, which seems trivial in hindsight, was to shift from the airbreathing approach of AJAX, to a rocket approach, and to realize that no window or focusing method is needed if the absorber is attached to the outside of the rocket, for which most acceleration is above the atmosphere in vacuum. At that stage, I set aside the molecular absorption approach because it appeared that a resonant cavity would be needed for a high performance propellant like hydrogen.

Thereafter followed a sequence of leaps and deductions that formed the microwave thermal rocket concept as it is described shortly. The first was to draw an analogy with nuclear thermal rockets (§ 1.1.1) and begin with the approach to high temperature heat exchange used in that field. The second was to understand how a surface could be made

to strongly absorb microwaves. The graduate student diet led me to research the susceptor approach used in microwave food packing, and this in turn led to the formulation of a stratified layer model (§ 2.2.1). Experimentation with the material properties of that model gave rise to a more attractive semiconductor approach using silicon carbide (§ 2.2.3).

Analysis of the microwave beam facility began with the assumption of a monolithic microwave integrated circuit (MMIC) phased array; however, this approach was economically unattractive because MMICs are expensive on a $/W basis, and high power output is limited to relatively low frequencies, implying kilometer-scale arrays. Further research brought a revelation from Benford (1995) that contrary to standard transmissivity charts, atmospheric microwave transmission above 35 GHz is both possible and efficient up into the 100 GHz plus range using high altitude sites (§ 2.2.6), and that a phased array may be constructed in this frequency range using parabolic dishes (§ 2.2.5) and commercially available gyrotron microwave sources (§ 2.2.4). This profoundly reduced the necessary size and cost of a microwave beam facility.

The final prohibitive factor for microwave thermal launch was overcome when verifying the payload performance predictions based on the rocket equation (Fig. 1-3) using an ascent trajectory model (§ 2.3.2). It very quickly became clear that a regular ascent trajectory would place the launcher thousands of kilometers downrange before cutoff, implying a very large phased array. This problem was solved by using a high acceleration trajectory at the lowest possible altitude before cutoff in order to stay within a few hundred kilometers of the microwave source.

Finally, with all these elements established, it was then possible to estimate how much the hardware cost of a beam facility could add to the payload launch cost (§ 2.3.4). With the overall concept defined, the detailed study of the key technical issues is begun in Chapters 3–7 to provide a starting point for reducing microwave thermal rockets to practice (Chapter 8). These relatively involved experimental and numerical investigations do not stand alone, as they are shaped and chosen with a particular design,

purpose, and set of questions in mind. Therefore, the remainder of this chapter details as briefly as possible an entire launch system, which the later chapters implicitly pertain to, and specific examples are presented to give insight into how this new approach translates into simpler, cheaper and higher performance rockets.

2.2   Concept of the Microwave Thermal Rocket

The microwave thermal rocket, shown in Fig. 2-1, is an adaptation of the nuclear thermal propulsion principle to use a ground-based microwave energy source rather than an on-board nuclear reactor. Using an array of high power microwave sources directed at the rocket underside, propellant is heated within hundreds of small channels running through a microwave absorbent coating. Microwave thermal launch is possible due to the recent advent of high power microwave sources in the millimeter wavelength range for which microwave launch is economically feasible.

Until recently, it was believed that the size and cost of the ground based beam facility would be prohibitive; however, it is shown in this chapter that in addition to using millimeter wavelengths, a new type of short range, high acceleration ascent trajectory significantly reduces the diameter of aperture needed. Beam diffraction determines this minimum diameter, and by moving to shorter wavelengths and shorter beam ranges, § 2.3.6 shows it is now plausible that the hardware cost of the beam facility, measured in the payload terms of $/kg to orbit, is similar to the energy cost of launch (the cost of generating and distributing the energy required to place the payload into orbit).

By dispensing with the uranium fuel, neutron shielding, reflectors and moderators of a nuclear reactor, the microwave thermal thruster is predicted to achieve an I_{sp} of 700–900 seconds and T/W of 50–150 using a hydrogen propellant. In contrast, nuclear thermal thrusters had an I_{sp} of 700–1000 seconds and a T/W of less than ten for the Timberwind particle bed reactors (Weglian *et al.*, 2001), and around unity for the NERVA reactors (Humble *et al.*, 1995). Chemical thrusters have a practical I_{sp} limit of 460 seconds using the H_2/O_2 reaction, and the T/W is in the range of 50–150.

40 kN Thruster Mass Budget	
Heat Exchanger	18 kg
Turbopump (~1 MW)	22 kg
Nozzle	6 kg
Feed and cooling pipes	15 kg
	61 kg

	Nerva (1960s)	Particle-Bed	Microwave Thermal	SSME (1970s)
Jet Power (MW)	1,570	1,945	165	4,621
Thrust (kN)	334	334	40	2,278
Propellant	H_2	H_2	H_2	O_2/H_2
Max. propellant temperature (K)	2,361	3,200	2,361	3,588
Chamber pressure (atm)	31	68	160	204
Mass (kg)	11,728	3,295	61	3,177
Vacuum I_{sp} (s)	825	971	825	453
T/W ratio	2.9	10.3	66	73.1

H_2, 1100K

Propellant tank

LH_2 3 atm

Turbopump

Heat exchanger

H_2

H_2

Regenerative nozzle

160 atm, LH_2

120 km

2 g's

20 g's

cutoff

microwave ceramic H_2 heat exchanger

140 GHz beam

0 km

0 km

100 km

200 km

Fig. 2-1: 40 kN design example for the microwave thermal rocket (MTR) system.

An example of a reusable single stage to orbit (SSTO) microwave thermal rocket is shown in Fig. 2-1, with mass and performance data derived using the methodology set forth by Humble *et al.* (1995). Prior attempts at SSTO vehicles met with failure because the I_{sp} of conventional rocket propulsion is too low to enable enough mass to be spared for a payload and robust structural margins without multiple stages. Because the microwave thermal rocket has roughly twice the I_{sp} of conventional rocket propulsion, it can afford a high payload fraction (up to 15% may be possible, depending upon scale) as well as higher structural margins. With higher structural margins, a robust, low-cost construction becomes possible.

By reducing the vehicle construction cost, increasing the payload fraction, reusing the vehicle and raising the launch rate, the economic and logistical constraints of space launch can be addressed, perhaps sufficiently to enable the launch mark to transition into a stable lower price regime, as discussed in § 1.1.

2.2.1 Thruster

The microwave thermal thruster is the enabling component of the microwave thermal rocket. It is fundamentally a hydrogen heat-exchanger (Turchi, 1998); being heated by microwaves directed from the ground and in turn heating a hydrogen propellant flowing through thousands of small channels within the layer. In this way, energy is added to a propellant by convection instead of combustion, single propellants such as hydrogen may be used, and much of the risk and complexity associated with an on-board power source is moved to the ground.

An example of this thruster is seen in Fig. 2-1; a segment of which is shown in Fig. 2-2. The hydrogen at a pressure of 140 atm flows through 1000 square channels, each 5 mm wide. The hydrogen channel flow is accelerated toward sonic velocity similarly to a Rayleigh flow, in which energy addition by convective heat transfer with the channel walls is the source of increasing kinetic and thermal energy. For a hydrogen propellant, the exit temperature must be around 2361 K to equal the vacuum I_{sp} of 825 seconds experimentally achieved by NERVA.
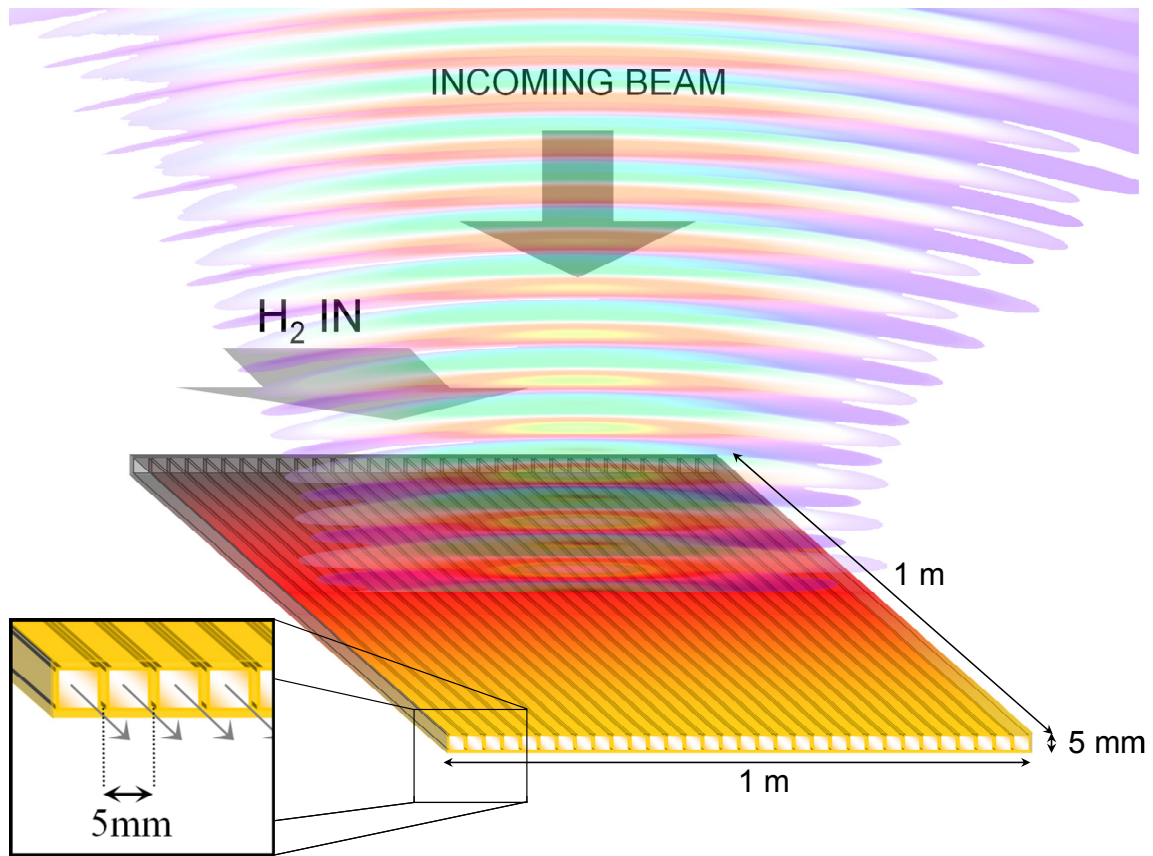
Fig. 2-2: A segment of the microwave thermal thruster shown in Fig. 2-1.

Worst-case radiative losses from the thruster are estimated by assuming that the entire thruster area is a black body radiating at peak wall temperature. With a surface area of 9 m^2 at a temperature of 2500 K, the thruster of Fig. 2-2 would lose approximately 10% of the power incident upon it, by radiation from the outer surface. Experiments and simulations presented in later chapters suggest that the thruster surface temperature reaches peak temperature only toward the channel exit, and that radiative losses should be lower.

In Fig. 2-2 and the vehicle in the lower left hand corner of Fig. 2-1, a single block heat exchanger is used to heat the hydrogen propellant. The channels run axially down the craft to a nozzle. In this configuration, the planar geometry of the heat exchanger would seem a natural fit to a linear aerospike nozzle (Korte *et al.*, 2001), as little piping would

be needed to take the heated propellant from the heat exchanger outlet to the nozzle inlet. This single block arrangement nevertheless has important hydrodynamic and manufacturing constraints, making it suitable only for the smallest of craft. The hydrodynamic constraints are discussed in § 2.3.4.

In a more practical system, hydrogen can pass though several heat exchanger segments fed through a pipe running underneath, as shown for the launcher on the upper right of Fig. 2-1. Smaller heat exchanger segments are easier to manufacture than a single block heat exchanger covering the same area. In this configuration, two sets of opposing exchanger segments are lined up in columns of four. Cold propellant enters the two opposing segments on the left and the right of the vehicle and proceeds towards the center, where the final peak temperature of the propellant (and wall material) is achieved. The heated propellant from the pair of segments then empties into a single pipe running underneath and passing down the axis of the vehicle to the nozzle.

To maintain high I_{sp} throughout the ascent trajectory, the heat exchanger needs to be tolerant to momentary beam interruptions, non-uniform illumination and to maintain its performance as the microwave beam incidence angle varies. The fraction of incident microwave energy absorbed or reflected by a planar thruster can be estimated analytically using a stratified layer model, given in Appendix D, which represents electromagnetic propagation within an idealized layered-structure thruster. In addition to predicting the optical performance of a thruster design, this model can be used to predict the layer thicknesses needed for optimal microwave absorption at the conceptual design stage.

The key parameter in microwave absorption is the product of material resistivity and layer thickness, because in essence the layer is impedance matched to free-space in order to maximize the power transfer (Buffler, 1991). One approach, called the susceptor approach, is to use a very thin layer of refractory metal to absorb the microwaves. This layer is deposited onto a dielectric substrate, and the optical performance of this approach is examined in Appendix D. The other approach is to use a thicker semiconducting layer, and the performance of this approach is described next.

Resonant Absorption: Silicon Carbide Thruster

Silicon carbide (SiC) is a wide band-gap semiconductor used as a microwave absorbent material in microwave furnaces. It is also a highly oxidation resistant refractory material used on the re-entry heat shield of the Space Shuttle. It can be doped to tailor resistivity over an eight order of magnitude range. This capability can be exploited at the design stage to "tune" the material plasma frequency to match the frequency of incoming microwaves, thereby maximizing absorption at this resonance.

The stratified layer model shown in Fig. 2-3 consists of a semiconductor layer with reflector underneath to maximize absorption. Reflection from the semiconducting layer is minimized by choosing the thickness to be a quarter wavelength, like an anti-reflection coating. Within the material, the wavelength is the free-space wavelength divided by the real part of the refractive index, which varies with resistivity. At 140 GHz, Fig. 2-4 (top) shows absorption of over 95% at a resistivity of 1.5 Ω.cm, corresponding to a layer thickness of 220 microns. For comparison, the thickness of an MgF_2 anti-reflection coating as found on binocular and camera lenses is about 100 nm; 2200 times thinner.

Because SiC is a semiconductor, a 1 mm layer of 1.5 Ω.cm resistivity absorbs 80% of the incident energy. The channel walls shown in Fig. 2-2 are layers of approximately this thickness. Absorption occurs within the first few hundred microns of the surface, and this is seen at the bottom of Fig. 2-4 for an angle of zero degrees. The absorption fraction of a TM-polarized wave increases with off-normal angle up to a maximum of over 95% at 70 degrees.

If a thinner layer must be used, an SiC layer 220 microns thick can be deposited onto a microwave transparent material that forms the load-bearing structure. Deposition directly onto an inner channel surface provides heat input directly next to the hydrogen flow; deposition on the top (outer) surface of the thruster provides oxidation resistance as well as heating.
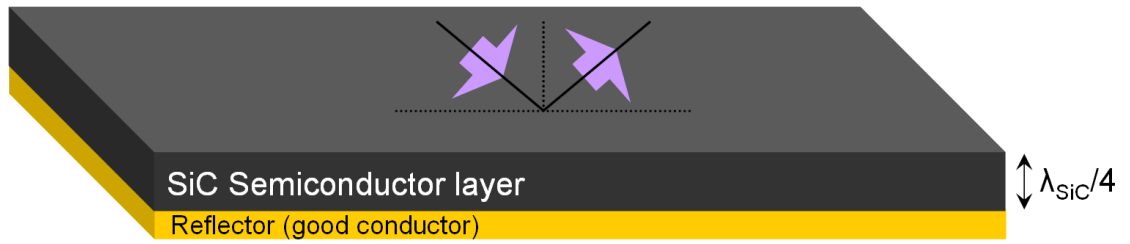
Fig. 2-3: An idealization of the SiC absorber layer structure, for simplicity neglecting the holes for heat exchanger channels.
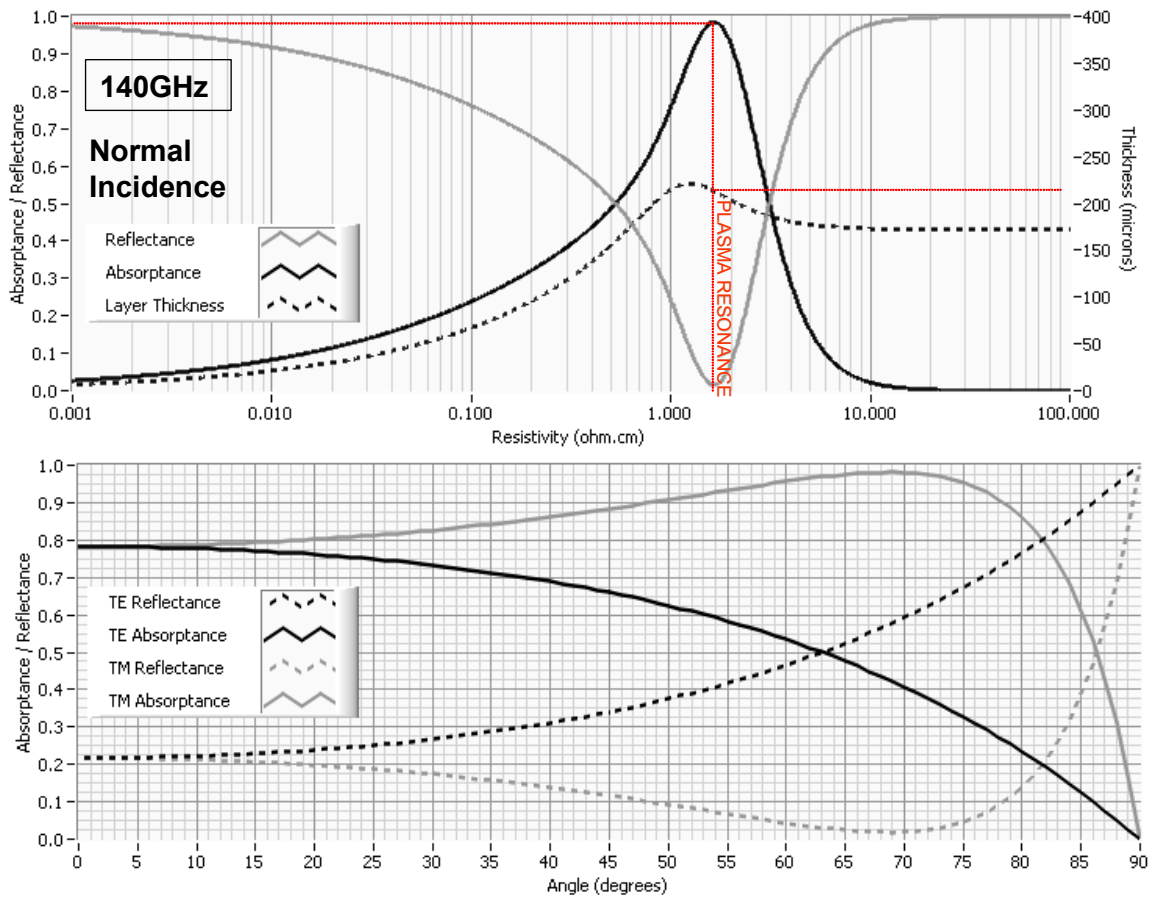
Fig. 2-4: Optical performance of the SiC microwave thermal channel, calculated from the stratified layer model presented in Appendix D. Top: SiC absorber performance at 140 GHz. Bottom: 1 mm thick SiC absorber off-normal response at 140 GHz, 1.5 Ω.cm.

A multimaterial thruster of this kind needs to avoid thermal expansion mismatches that could cause delamination of the layers. At 140 GHz, a single material thruster might be achieved using doped boron nitride, provided that suitable dopants (possibly magnesium) can be found. Depending on the dopant used, the entire material would be permeated with dopant, or just thin layers on the inner channel surfaces, where heating is most efficient. Indeed, the analysis presented here uses only room temperature material properties because high temperature data is not readily available; however, at 1670 K the resistivity of even undoped BN can drop by ten orders of magnitude (§ 2.2.3), bringing it close to the useful semiconducting range.

2.2.2   Nuclear Rocket Analogy

Fig. 2-5 shows that the microwave thermal thruster replaces the combustion chamber of a conventional rocket or the reactor core of a nuclear thermal rocket with a thin microwave absorbent refractory layer covering the underside of the aeroshell. Nuclear thermal thrusters operate on the hydrogen heat-exchange principle using nuclear reactions as an energy source, rather than microwaves.

From the 1950s to the 1970s a series of over 30 nuclear thermal thruster tests, conducted as part of the ROVER, KIWI and NERVA programs, demonstrated hydrogen heat exchangers approaching an I_{sp} of 825 seconds experimentally, operating at power levels exceeding 1 GW (for high thrust), and for durations of longer than an hour. Later particle bed designs constructed as part of the Timberwind program demonstrated heat exchanger exit temperatures of 3200 K, corresponding to an I_{sp} of around 900 seconds (Humble *et al.*, 1995; Weglian *et al.*, 2001).

Unlike nuclear rockets, which contain a neutron gas in a cylindrical heat exchange geometry using neutron reflective walls, the microwave rocket intersects a transatmospheric microwave beam, incident upon the underside of a lifting body aeroshell. This aeroshell imparts a cross-range of hundreds to thousands of miles upon re-entry, giving flexibility of landing sites and the option of gliding to a nearby landing site in the event of an aborted launch.
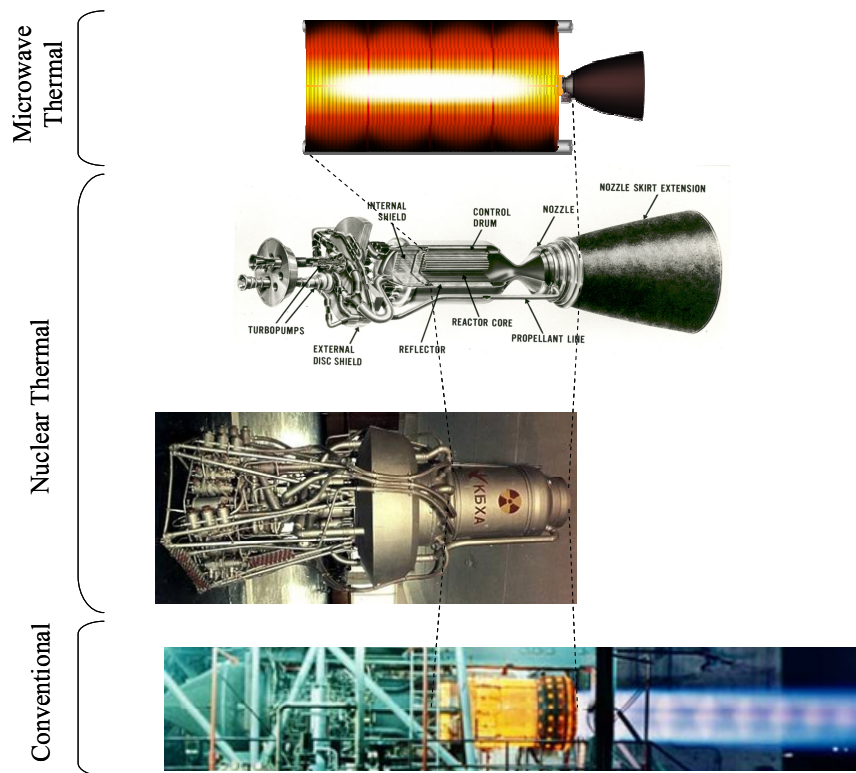
Fig. 2-5: A comparison of enthalpy addition stage for microwave, nuclear and conventional thrusters.

There are presently two performance-limiting factors for nuclear thermal rockets: The first is the thrust-to-weight ratio, which is limited by the need to carry uranium fuel, shields, reflectors and moderators. The second is the neutronic properties and hydrogen compatibility of refractory materials. For example, in particle bed designs the uranium carbide fuel pellets are sometimes coated with ZrC, which has a relatively low etch rate in a high pressure hydrogen flow even at temperatures of around 3000 K (Besmann, 1986; Knight and Anghaie, 1999). However, at such elevated temperatures uranium evaporation into the propellant becomes a limiting factor.

For the microwave thermal thruster, materials are constrained by microwave properties and hydrogen compatibility. Furthermore, the microwave thermal thruster uses no pressurized control drum, so the channel wall materials themselves must hold the propellant pressure against vacuum on the other side.

2.2.3 Materials and Fabrication

Moreover, the beam, with a temperature of several thousand degrees at the focal point, would instantaneously melt even the toughest parts of the spaceship.

K.E. Tsiolkovsky, *The Spaceship*, (1924)

Efficient use of materials is essential to maximize the thrust-to-weight ratio of the engine, and square channels may be packed more efficiently into the thickness of the layer than circular ones, although at the expense of greater stress concentrations. Channel pressure, mass flow rate and the high temperature material properties of resistivity, yield strength, and creep rate all drive the structural design of the heat exchanger channels.

The least stringent design requirement for the heat exchanger is that it must operate for a single ascent of around 200 seconds. Relative to a reusable heat exchanger, this enables the most ambitious combination of high temperature and high-pressure operation given the materials available. Provided the thruster begins operation in vacuum (upper stage), the outer surface of the thruster need not be oxidation resistant and can be sacrificed upon re-entry. Such an approach becomes advantageous if fabrication is inexpensive and thruster replacement is not labor intensive.

Given that nuclear thermal thrusters successfully operated at high I_{sp} for more than an hour (Gunn, 2001), it may be possible to fabricate a reusable microwave heat exchanger, perhaps lasting for tens of launches, after refinement. This reasuable approach minimizes the cost production, for example if expensive coating processes are required.

Metallic refractories such as W, WC, ZrC, HfC, TaC and TiB_2 are of interest for susceptor-based approaches and as load-bearing channel liners for high temperature designs, where ceramics such as silicon carbide (SiC) would soften and cause a rupture in the channel wall. For example, the flexural strength of SiC increases with temperature; however, so does the strain rate, whose variation with temperature is approximated by,

$$\frac{d\epsilon}{dt} = A\sigma^n e^{-\frac{E_{act}}{R_u T}}.$$

(2.1)

Beginning with a known strain rate at 1500 K and an activation energy E_{act} of 944 kg/mol (Munro, 1997), Eq. (2.1) can be used to predict a strain rate of 10^{-3}/s at 1900 K; roughly six orders of magnitude greater for a 300 K temperature increase. Over the course of a powered ascent lasting 200 seconds this corresponds to perhaps the largest acceptable deformation for the heat exchanger. If a purely SiC heat exchanger were to be built, its peak wall temperature would be ~ 100 K greater than the peak propellant temperature, giving an overall I_{sp} of around 720 seconds.

A higher performance version might still utilize SiC as an absorber and oxidation resistant coating, but load-bearing tungsten channels operating at much higher temperature could be used as channel liners.   For example, a W-SiC heat exchanger with a peak wall temperature of 2400 K and a peak flow temperature of 2300 K could produce an I_{sp} of 820 seconds, or a titanium diboride heat exchanger with a flexure creep rate of 3×10^{-9}/s at 100 MPa and 2300 K (Munro, 2000) could last for many launches. Propellant tanks utilize materials and alloys that are optimized for use at a given pressure and temperature, and the development of similarly optimized materials for the heat exchanger, though probably not essential as the SiC example suggests, has great potential to further increase I_{sp} performance.

Some of the strongest, purest forms of the materials shown in Table 2-2 are formed into custom structures by chemical vapor deposition (CVD) (Pierson, 1996), and it may eventually be possible to vapor deposit such a thin thruster directly onto the aeroshell, though this does not appear a near-term proposition. CVD materials also tend to possess the fullest anisotropy of a material's underlying crystal structure, and hexagonal boron nitride is a case in point. The anisotropy can sometimes be advantageous; for example, it can spread heat laterally across the heat exchanger channels but resist conduction along them.

	6H-SiC (Munro, 1997; Pierson, 1996)	W (Davis and Smith, 1996)	HfC (Pierson, 1996)	h-BN (Pierson, 1996)
Melting point	2818 K (1 atm) 3103 K (35 atm)	3683 K	4200 K (1 atm)	3273 K (1 atm, decomposes)
Evaporation rate		0.27 mg/cm^2/hr (2800 K) 0.12 mg/cm^2/min (3075 K)	0.3 mg/cm^2/min (2600 K) (Deadmore, 1965) 1.1 g/cm^2/hr (3030 K†)	
Density	3.21 g/cm^3	19.3 g/cm^3	12.67 g/cm^3	2.3 g/cm^3
Oxidation resistance	Forms protective SiO2 layer at 1500 K, layer is stable to 1900 K.	Rapid oxidation in air above 700 K	Oxidation begins in air above 770 K.	Oxidation above 1000 K, increases to 10 mg/cm^2/min at 2000 K; graphite oxidation similar.
Hydrogen resistance	H$_2$ reported to etch SiC at ~ nm/s	No reaction up to melting point	H$_2$ compatible up to melting point (Anon.)	H$_2$ compatible up to 1650 K
Thermal conductivity	25 W/m/K (293K) 11 W/m/K (1800K)	130 W/m/K (293 K); 105 W/m/K (2270 K)	20 W/m/K (293 K)	36 W/m/K (293 K) 15 W/m/K (1800K)
Dielectric constant	9.72 (300 K)			4.58 (ab) 4.15 (c)
Resistivity	10^{-2} to 10^6 Ω.cm, depending on dopant (B,N,Al)	5.5 μΩ.cm (293 K); 103 μΩ.cm (3273 K)	37–45 μΩ.cm (293 K)	>10^{14}Ω.cm (300 K) 10^7 Ω.cm (1300 K) 10^3–10^5 Ω.cm (1670 K)(Carpenter and Kirby, 1982)
Yield Stress	(tensile strength) 3.92 GPa (300 K) 1.5 GPa (2100 K)	(tensile) 50 MPa (2270K)	(tensile) 130 MPa (2310 K) (Wuchina et al., 2004)	(ultimate tensile) 40 MPa (300K). 130 MPa and rising (2500 K) 103 MPa (300 K)
Flexural strength	490 MPa (1500 K) 350 MPa (1700 K)	30 MPa at 2400 K using HfC-Re additives (Park and Lee, 1999)		
Strain Rate	10^{-9}/s (flexure, 200 MPa, 1500 K) 10^{-3}/s (flexure, 100 MPa, 1900 K†)	10^{-6}/s at 30 MPa, 2400 K using HfC-Re additives (Park and Lee, 1999)		
Notes	Can be vapor deposited up to 1" thick. Essentially creep resistant up to 1800 K	Metallic and therefore microwave reflector. Would be used as load-bearing channel lining.	Can be co-deposited with SiC (Pierson et al., 1989). 20% HfC 80% TaC alloy offers slower evaporation than W at T > 3000K.	Can be hot-pressed and vapor deposited. CVD form anisotropic; unusually large thermal expansion along c-axis.

Table 2-2: Candidate materials for the microwave thermal thruster.

---

† Extrapolation used.

An example of how these materials might be combined to make a thruster segment is shown in Fig. 2-6. Tungsten is used to line the inside of the channel due to its high melting point, high strength, low hydrogen etch rate at refractory temperatures. Silicon carbide is then used due to its microwave absorbent properties at the desired operating temperature. Since the operating temperature varies along the length of the channel, the SiC dopant (vanadium) concentration can be varied in successive coatings to give a graded resistivity; low on the inside and high on the outside. This ensures that regardless of the temperature, there is a depth at which the incident microwaves are strongly absorbed.
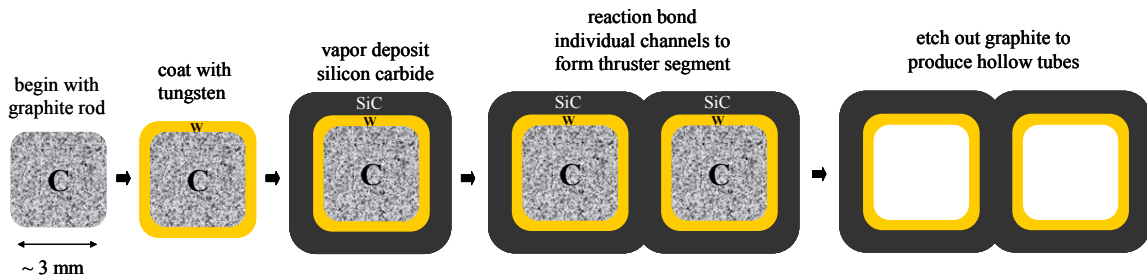
Fig. 2-6: Concept of how tungsten and silicon carbide could be combined to form a refractory heat exchanger channel.

The temperature variation of 6H-SiC:V resistivity can be calculated (Gradinaru *et al.*, 1997) and an example is plotted in Fig. 2-7. Note that the resistivity of optimal absorption in Fig. 2-4 is around 2 Ω.cm, which corresponds to a temperature of ~ 1600 K in Fig. 2-7. In principle, the vanadium concentration can be varied such that optimal absorption occurs at a given temperature; however, there is not yet experience in using vanadium-doped SiC at these temperatures. If there are problems with the approach, other materials such BN may be suitable; however, there is little experimental high temperature resistivity data for most of these materials and at present, these values are inferred.
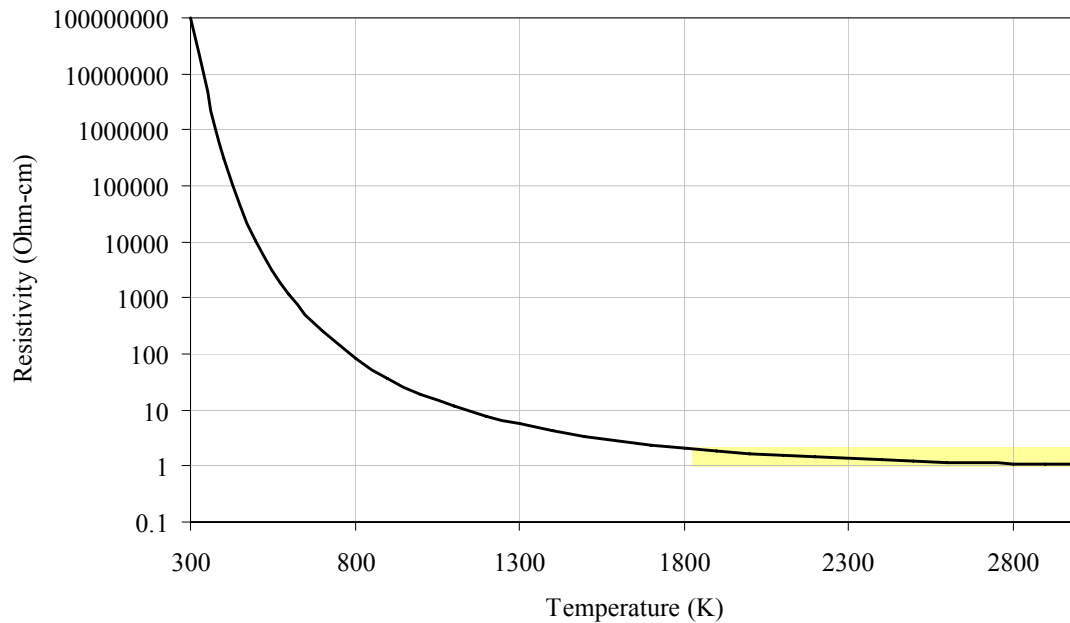
Fig. 2-7: Resistivity vs. temperature for vanadium-doped silicon carbide (V:SiC) calculated from the model of Gradinaru (1997).

Material reliability of the thruster need not be critical to the survival of a reusable craft. If a thruster channel ruptures, it could lead to propellant loss, local overheating and eventual melting of the relevant channel, which may or may not spread to neighboring channels. If ascent to orbit is essential, flow to the thruster segment could be halted and the corresponding segment allowed to melt, resulting in perhaps a 20% loss of thrust at the expense of undesirable microwave reflection from the damaged segment. If ascent to orbit is non-essential then the beam is turned off and the craft glides back to a designated landing site.

2.2.4   High Power Microwave Sources

For the most part the frequencies needed for microwave thermal launch are readily generated using gyrotron or gyroklystron microwave sources (Barker and Schamiloglu, 2001; Benford and Swegle, 1992), seen in the middle picture of Fig. 2-8. Gyrotron development has been spurred by its application to electron cyclotron heating systems in

fusion reactors, and in particular the recent goal of a 1 MW continuous wave (CW) gyrotron oscillator at 140 GHz. The advent of edge-cooled diamond windows in the late 1990s enabled these high power CW systems, and in March 2005 the commercially available 140 GHz CPI VGT-8141 gyrotron demonstrated 30 minute pulses of nearly 0.9 MW output power. This continues a trend shown in Fig. 2-8 that has seen time-average power output of millimeter wave source increase by *six orders of magnitude* over the past 40 years, seen on the left side of Fig. 2-8.
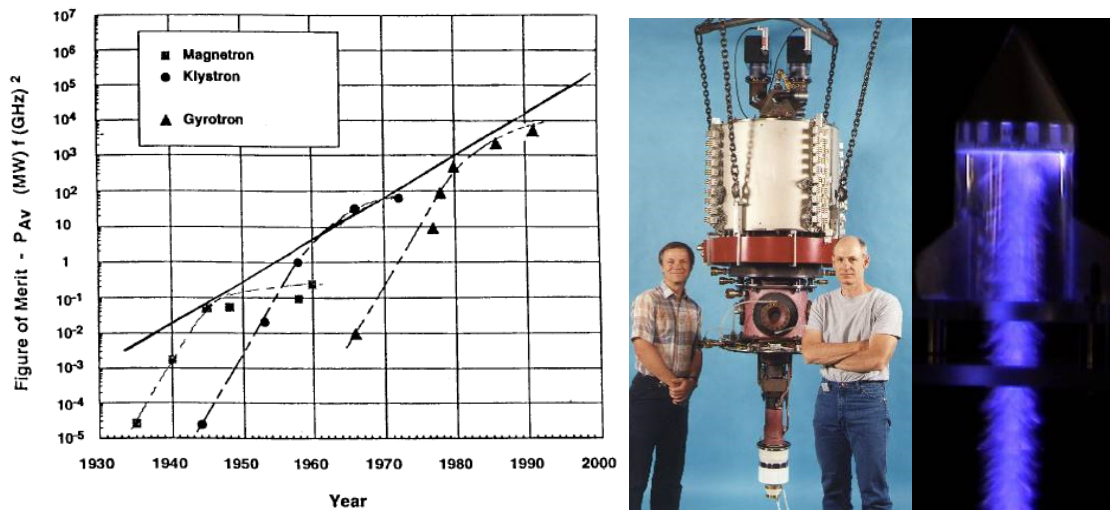
Fig. 2-8: Left: Average power density potential of single microwave tube vs. year. Middle: Dr. Kevin Felch and Dr. Pat Cahalan displaying their CPI 110 GHz gyrotron, capable of producing 1 MW of output power for 0.6 seconds, or 600 kW for 10 seconds. Right: 1 MW, 140 GHz gyrotron beam of ~ 3 cm diameter striking a microwave ablative rocket (Oda *et al.*, 2003).

The baseline microwave source is an array of phase-locked gyrotrons operating at a frequency of 140 GHz (wavelength of 2.14 mm) and a unit power level of order 1 MW. In principle, the power from any number of gyrotrons can be combined by the phase-locking technique, which has been used for oscillators since WWII and has reached powers exceeding 1 GW (Levine *et al.*, 1991). Phase locking of gyrotron oscillators is understood conceptually (Fliflet and Manheimer, 1989) and has been demonstrated experimentally (Guo *et al.*, 1995), although not yet at high power and with large numbers of oscillators.

A master oscillator feeding power amplifiers (Benford and Dickinson, 1995) is an alternative approach and is used at the Stanford Linear Accelerator, which has about 240 pulsed klystron amplifiers phased together, with each producing 67 MW in the S-band (Benford and Swegle, 1992). Using the master oscillator power amplifier approach, a near-term option for the microwave thermal beam facility is to use less powerful W-band (94 GHz) gyro-klystron amplifiers developed for radar applications.

For CW gyrotron oscillators (rather than amplifiers), the current state of the art wallplug-to-light efficiency is ~ 50% using depressed collector technology, although until recently design efforts have focused on high time-average power output for fusion applications rather than efficiency. The advent of single depressed collectors in the early 1990s raised practical gyrotron efficiencies from 30% to 50%, with a 62% predicted limit (Thumm, 2005). Multistage collectors offer further improvements but as yet are untried.

From a practical perspective cost estimates for the present generation of commercially available gyrotrons range from $2M/MW to $5M/MW depending mostly on how much of the supporting equipment (e.g., for cooling) is included in the cost. In low production quantities (1–10 units), the costs above include the gyrotron oscillator itself, a diamond output window (~$100K), a superconducting magnet system (~$0.5M), and a power supply (~$1M).

Although the present generation of gyrotrons are now commercially available[‡] they are still undergoing refinement for high reliability. In this regard the experiences of General Atomics with three different gyrotrons for fusion work give some indication of the present state of affairs: Of the three development gyrotrons, two repairable failures are described by Lohr *et al.* (1999). The first was a filament short that occurred after 5000 hours of operation, and the second was a braze failure causing a loss of vacuum. In both cases, the gyrotrons were repaired for about 10% of their original cost.

[‡] Albeit with a 2 year lead time and maximum production rate of 1 gyrotron/month using present facilities (Felch, 2003).

Aside from these early problems, there is little fundamental difference between gyrotrons and other high power microwave sources such as klystrons as far as reliability and lifetime are concerned, and a mean time between failures of 30,000 hours is a reasonable expectation as the production models mature. Lifetimes of only a few thousand hours were anticipated during the proposal to construct the Stanford Linear Accelerator; however, actual experience led to a mean time between failure now exceeding 50,000 hours, causing industry to lose interest in maintaining a production line for replacements. Consequently, the Stanford Linear Accelerator now handles all replacements through its internal shops (Panofsky, 1996).

Prospects for the long term are focused on increasing the CW power output of coaxial gyrotrons together with greater reliability and further efficiency enhancements beyond 50%. Present design efforts for "super-power" tubes aim to achieve 4–5 MW CW output power at frequencies of 95, 130, 140 and 170 GHz (Dumbrajs and Nusinovich, 2004). Diamond windows become a limiting factor at such high power levels, and future generations of devices are expected to use multiple diamond output windows.

2.2.5   Phased Array

This energy could be transmitted to it from the planet in the form of a parallel beam of shortwave electromagnetic rays. If the wavelength were not more than a few dozen centimeters, this electromagnetic "light" could be transmitted to the airplane in the form of a parallel beam by means of a large concave parabolic mirror and thus provide the energy needed to expel particles of air or a store of inert material and thus attain cosmic velocities while still in the atmosphere.

...The edge of the square parabolic reflector should be at least 12,600 meters or 12.6 kilometers (12 versts). This cannot be considered feasible at present.

...Moreover, how could the energy flux be continually trained on the moving projectile as it continually changed its position?

K.E. Tsiolkovsky, *The Spaceship* (1924)

The task of the phased array is to take *n* coherent gyrotron beams and transform them into a single Gaussian beam with the effective diameter of the phased array. A concept of the phased array built up from lifting and rotating segments of sub-arrays is shown in Fig. 2-10. Based on ascent trajectory analyses (§ 2.3.2) this single beam must converge at its waist upon a target of order 3 meters in diameter at a range of 80–120 km in the near field. For a reusable upper stage, the beam remains locked upon it through a slew angle of -40 to +40 degrees, at a peak slew rate of around 4 deg/sec.

Receive-only millimeter-wave phased arrays of steerable dishes have been demonstrated in radio astronomy. High power phased arrays with electronic steering and tracking are used in military radars; however, such a phased array has not yet been used to power or propel remote vehicles. The feasibility and design of a 30 MW, 245 GHz, ground-based beam facility using an array of parabolic dishes was examined by Benford, Myrabo, and Dickinson (Benford and Dickinson, 1995; Myrabo and Benford, 1994); this beam facility is shown in Fig. 2-9.
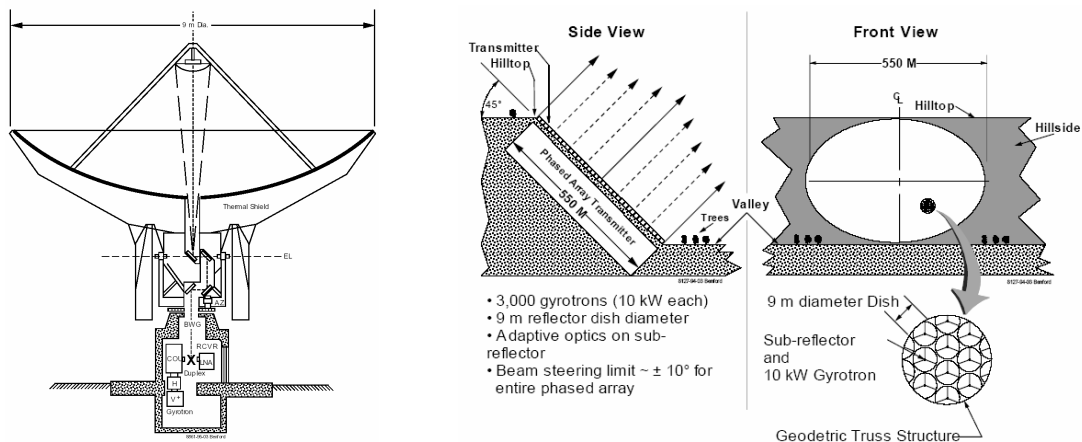
Fig. 2-9: Concept for a phased array element and 30 MW phased array (Benford and Dickinson, 1995). In the decade since this design was published the CW power output of gyrotrons has increased by two orders of magnitude.
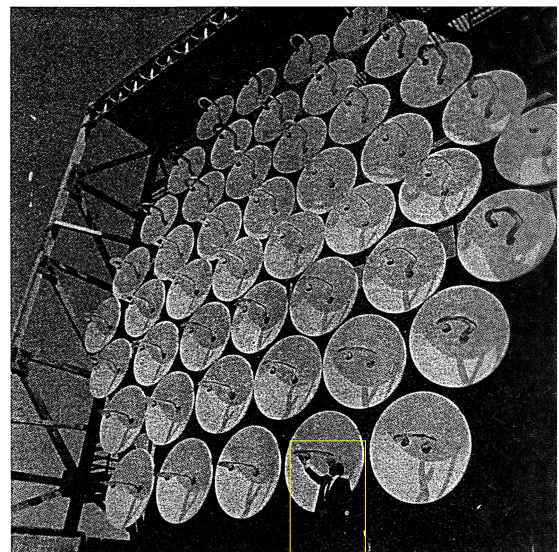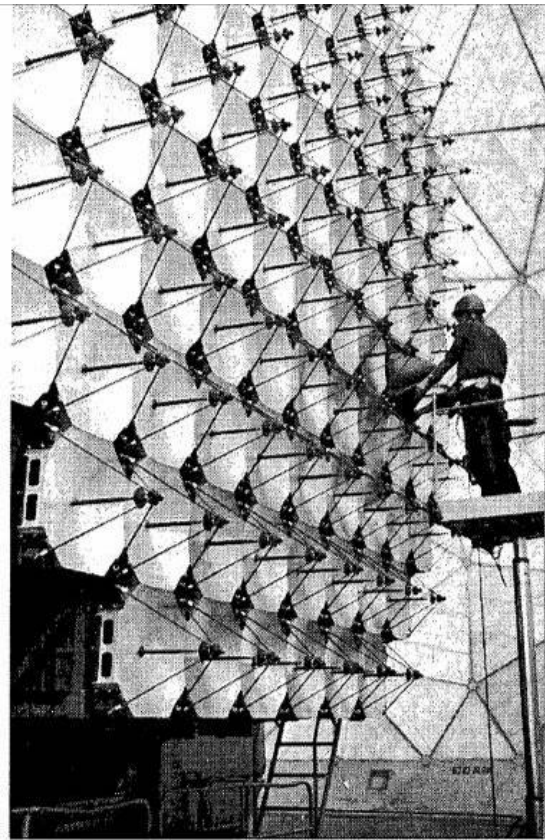
Fig. 2-10: Top left: Russian millimeter wave phased array (Tolkachev *et al.*, 2000). Top right: U.S. hexagonal close-packed array (maximum 93.7% fill factor) (Benford, 2004). Bottom: Concept for a large aperture millimeter-wave phased array.

beam facility as seen from target looking down

Zenith

rotating platform

100-200 m

Off-Zenith

lifting segments e.g. by hydraulics or pivot

Array appears compressed in one direction but segments still fully overlapping.

Individual antennas within a segment turned off as they go underneath others, or energy simply absorbed on the underside.
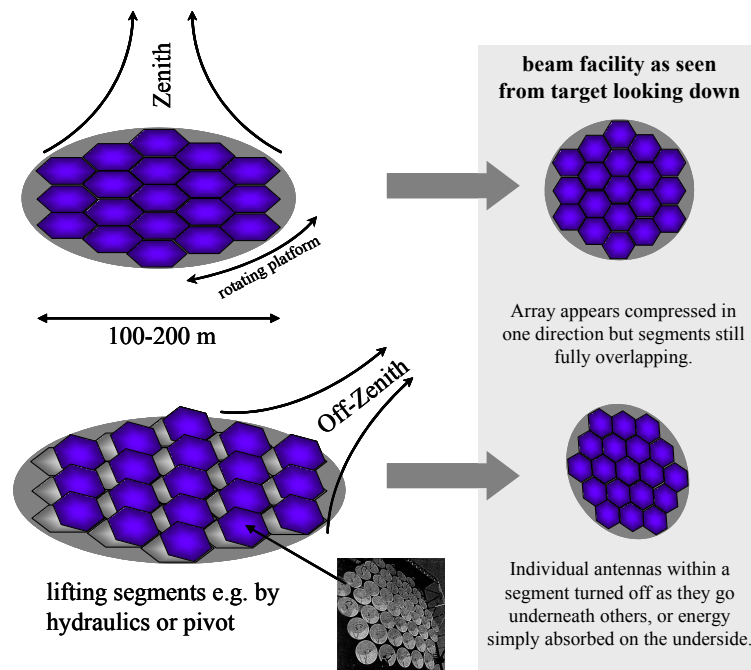
For the applications considered by Benford, the array uses relatively fixed dishes of 9 m diameter in a hexagonal close-packed formation, as sidelobe losses are proportional to the square of the packing fraction (Fourikis, 2000). In the decade since Benford & Dickinson's publication (1995), the time-average power output of gyrotrons has increased by one to two orders of magnitude, so that the 3,000 gyrotrons specified in Fig. 2-9 would now be 30 gyrotrons of 1 MW CW power output each. Such gyrotrons are now commercially available at a frequency of 140 GHz. If the 5 MW "super power" tubes come to fruition the number of gyrotrons needed for the array shown in Fig. 2-9 drops to six.

The effective diameter of the array may be estimated using simple diffraction formulae. It is simplest to imagine the time reversal of the situation in which the array illuminates the heat exchanger. Instead, imagine that the heat exchanger illuminates the phased array, implying a sinc function amplitude taper across the array such that the heat exchanger amplitude is uniform. In Eq. (2.2) a factor of 2.44 is used in place of the usual factor of 1.22 associated with the Rayleigh criterion for telescope resolution. The factor of 2.44 encompasses the entire diameter of the central Airy disc, corresponding to a 17% energy loss to sidelobes. To include both the central disk and the first bright ring a factor of 3.27 is used instead, implying only a 9% energy loss to sidelobes at the expense of a 34% greater array diameter (80% greater array area).

$$D = (2.44\lambda / \theta_{beam}) \big/ \sqrt{\cos(\theta_z)} \qquad\qquad (2.2)$$

The cosine term corrects for the along-track axis reduction in beamwidth when the vehicle is not directly overhead. A square root is used because the resulting elongation of the array only occurs along one axis, not two, as shown in Fig. 2-10. A maximum slew (zenith) angle of 45 degrees increases the array area required by 40% relative to normal pointing. High frequency operation above 90 GHz is preferable because array cost scales proportionally to array area and hence the inverse square of the array frequency.

Energy efficiencies are also importing in specifying the phased array. Feed systems are comparable to fusion experiment electron cyclotron heating feed systems (except for

rotary joints), and so losses are expected to be comparable. For example the electron cyclotron heating system on the D-IIID fusion experiment has waveguide losses of 2% per 40 m and 0.6% per dihedral (sharp) bend (Lohr *et al.*, 1996), so waveguide losses from the gyrotron to the antenna feed can be as small as a few percent provided the gyrotron is adjacent to the antenna.

Other losses arise from amplitude/phase errors of the parabolic dish surface and between array elements, non-uniform illumination of the dish by the feed system and the static fill factor of the array (including blockage effects if applicable). For example, for random phase errors of rms magnitude σ, the efficiency is $e^{-(2\pi\sigma/\lambda)^2}$; $\sigma = 0.036\ \lambda$ (a 13° phase error or a path length error of $\sim 80\ \mu m$), corresponds to 95% efficiency.

Feasibility studies for the Atacama Large Millimeter Array place aperture cost at $24K/m^2$ for dishes with diameters in the range of 8–12 m (Horne, 1982), and this is consistent with other figures. To optimize overall cost, Benford (1995) suggests that the optimum array size is determined by an economic analysis conforming to a correlation observed by Dickinson (1968). In this correlation, the minimum system cost is achieved when the cost of antenna gain (including pointing, acquisition and tracking) equals the cost of transmitter power (including the power generation, power supply, cooling and microwave sources).

2.2.6   Transatmospheric Microwave Beam Propagation

Beamed-energy concepts are limited to frequencies at which the atmosphere is transparent. Near total absorption by H_2O in a large portion of the far infrared spectrum divides viable beamed-energy concepts into two categories: Laser and microwave, as seen in the upper chart of Fig. 2-11. Beaming energy sufficient to propel a ton into LEO requires more than 100 MW of energy transmission through the atmosphere. Microwaves have two main advantages: First, at microwave wavelengths, atmospheric turbulence is not the major problem it is with lasers (§ 1.1.6). Second, commercially available microwave sources are already capable of generating this level power output whereas today's most powerful lasers are still an order of magnitude weaker.

The advent of submillimeter wavelength astronomy has highlighted the existence of locations with particularly low atmospheric water content, opening up new microwave transmission windows from 35 to 300 GHz and sometimes beyond. Since the atmospheric scale height of water vapor is only 1 to 2 km, sites such as the Caltech Submillimeter Observatory on Mauna Kea are at high altitude, where atmospheric water vapor levels permit transmission above 250 GHz, shown in Fig. 2-11.

Atmospheric propagation conditions are still better in parts of the Chilean Atacama desert, and Antarctica. Ongoing site surveys and millimeter wavelength projects, such as the CARMA array in eastern California, are revealing suitable locations for a beam facility on the U.S. mainland.

Microwave frequency determines the maximum beam energy density via the constraint of atmospheric breakdown. Free-space atmospheric breakdown is an electron avalanche process, a model for which is given in Appendix D. This model is used to generate the breakdown curves shown in the lower chart of Fig. 2-11, and predicts that breakdown occurs more easily at low frequencies, ionizing air into a plasma that can distort and reflect the incoming beam. The beam frequency has a disproportionate effect on the breakdown intensity; for example, a 300 GHz beam can achieve 1000 times the power density of a 3 GHz beam, assuming that it is constrained at the altitude of minimum breakdown intensity. By moving to higher frequency in this way, the energy density can enter the energetic regime needed for space launch.
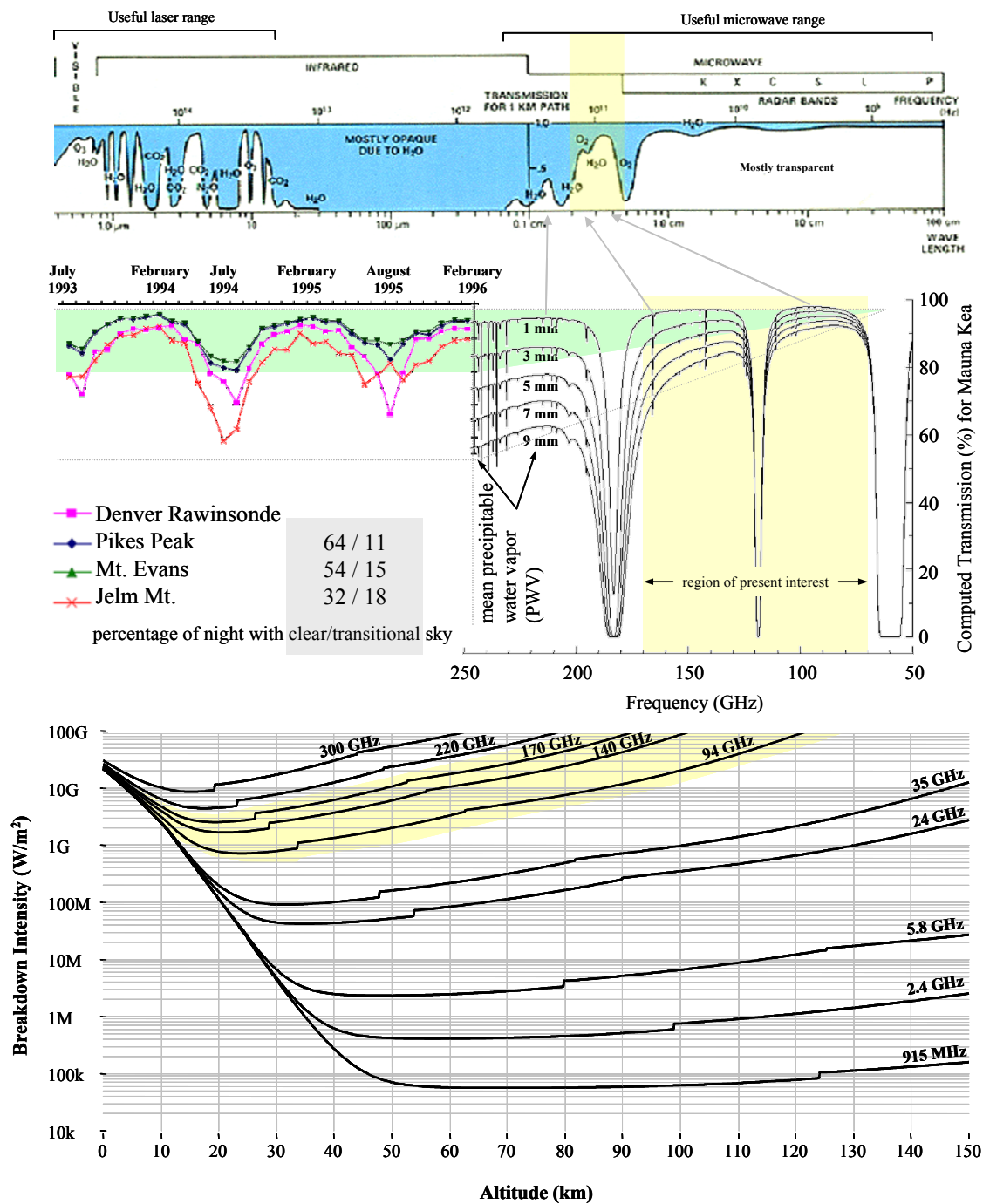
Fig. 2-11: Top: General atmospheric absorption. Middle left: Water vapor for example sites in the southwestern USA (Erasmus, 2000). Middle right: Calculated atmospheric transmission at Mauna Kea (Lis). Bottom: Atmospheric breakdown intensity by altitude and frequency, based on the semi-empirical model of Liu *et al.* (1997).

2.3 Sizing and Performance

2.3.1 A Note on Parametric Modeling

A rigorous, holistic performance analysis is an exercise in managing complexity that involves the convergence of hundreds of technology parameters and engineering choices into self-consistent system design (Sobieszczanski-Sobieski and Haftka, 1997). Each quantity an engineer must choose is a dimension of the "design space," and for launch systems the design space often has hundreds of dimensions to explore and optimize in order to minimize cost, risk and other top-level quantities.

The relatively straightforward process of connecting and solving many equations together produces point designs whose validity is difficult for others to assess, inevitably contain assumptions others will question, and can fall in an unstable region of the design space that is sensitive to variations in real-world performance such as structural mass fraction.

In particular, the key metrics of $/kg of payload, development cost, development risk and initial infrastructure cost are not only a function of payload size, they are probabilistic quantities that require a probabilistic treatment of design inputs and margins (Thunnissen, 2005) to be established with a known confidence, such as 10%, 50% and 90% confidence intervals.

Such an analysis is beyond the scope of the present work. Instead, the following simplified relations are used separately (rather than as an integrated model) to qualitatively highlight some key tradeoffs that are peculiar to microwave thermal rockets. The correct resolution of these key tradeoffs very much affects the overall system cost; however, the cost estimates here are confined to hardware acquisition costs intended only to give a sense of the scale of the numbers involved.

2.3.2 Ascent Trajectory

The rocket equation suggests the ideal payload capacity of a single stage to orbit (SSTO) microwave thermal rocket, and an ascent trajectory analysis is used to confirm this

finding by modeling the performance of a particular design example, in this case a launcher weighing 1 ton, and using an X-33 type aeroshell. Ascent trajectory equations are derived from a non-inertial control volume analysis in the radial coordinate system given in Appendix C. The resulting ODEs are coupled to a 1976 standard atmosphere and integrated using the Runge-Kutta method to yield Fig. 2-12.

On a planetary scale, the ascent trajectory is just visible at the top of Fig. 2-12. A ΔV of 523 m/s occurs at the transfer trajectory apoapsis, inserting the payload into a 1100 km circular orbit. This ΔV is similar to that imparted by rotation of the earth, and both are unaccounted for in the vehicle propellant budget. Depending on the mission, it may be sufficient to circularize only the payload and allow the craft to re-enter, saving the propellant mass of an orbital maneuvering system that may use conventional thrusters.
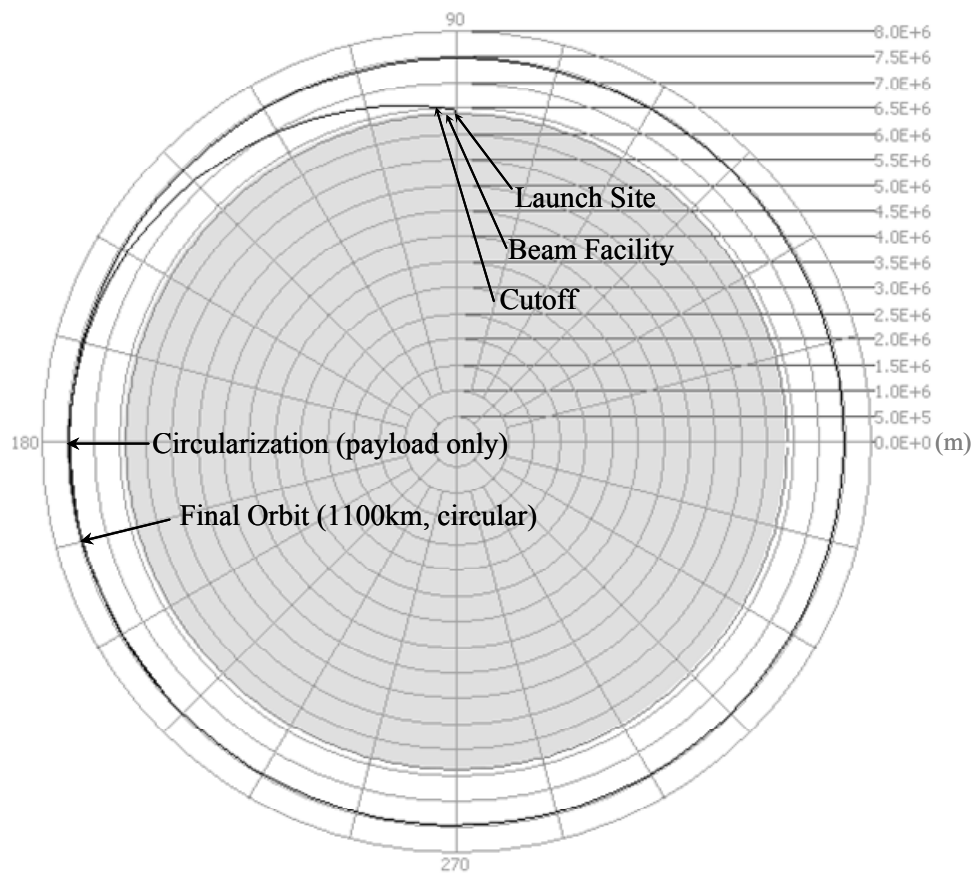
Fig. 2-12: Whole-earth view of the launcher ascent trajectory. Computed using the model given in Appendix C.

Taking into account atmospheric drag and gravity losses, the predicted payload is 10% for the baseline microsatellite launcher, characterized by:

- 1 ton vehicle wet mass: 100 kg payload, 180 kg structure, 720 kg LH_2
- 6 meter vehicle length. 5 m width at base excluding wings. 3 meter diameter beam footprint (on vehicle), 150 km maximum required beam range
- 100 kg payload to 1100 km circular orbit (with circularization burn)
- 275 MW jet power for 54 kN of thrust at an I_{sp} of 775–1030 seconds
- 210 second ascent from ground to cutoff, with H_2 Mass flow rate of 5 kg/s at 100% throttle
- 2 g's initial acceleration, 19 g's peak.
- 3m × 3m heat exchanger with average power density of 30 MW/m^2
- Average microwave beam intensity 65 times lower than 140 GHz atmospheric breakdown threshold at worst-case altitude
- Delta-V budget (integrated along direction of motion): Thrust +11044 m/s, drag -1513 m/s, gravity -2753 m/s, circularization burn +523 m/s. Total: 7031 m/s (equal to 1100 km circular orbit velocity).

The ascent trajectory itself consists of two segments: In the first, at the top left of Fig. 2-13, the vehicle is steered vertically ($\beta = 90°$) at 50% throttle to minimize drag losses during atmospheric ascent. The second segment of ascent begins when an altitude of 65 km is reached. The craft levels off, and accelerates horizontally ($\beta = 0°$) at 100% throttle. The acceleration of 9–19 g's during this segment of the ascent raises the craft velocity from 1.5 km/s to 8 km/s in only 60 seconds. Such acceleration precludes transporting humans as cargo, but enables the vehicle to achieve orbital velocity within 150 km of the beam source. The maximum beam range is chosen to be 200 km, corresponding to a point on the ground that is 150 km downrange of the launch point, as seen in Fig. 2-13.
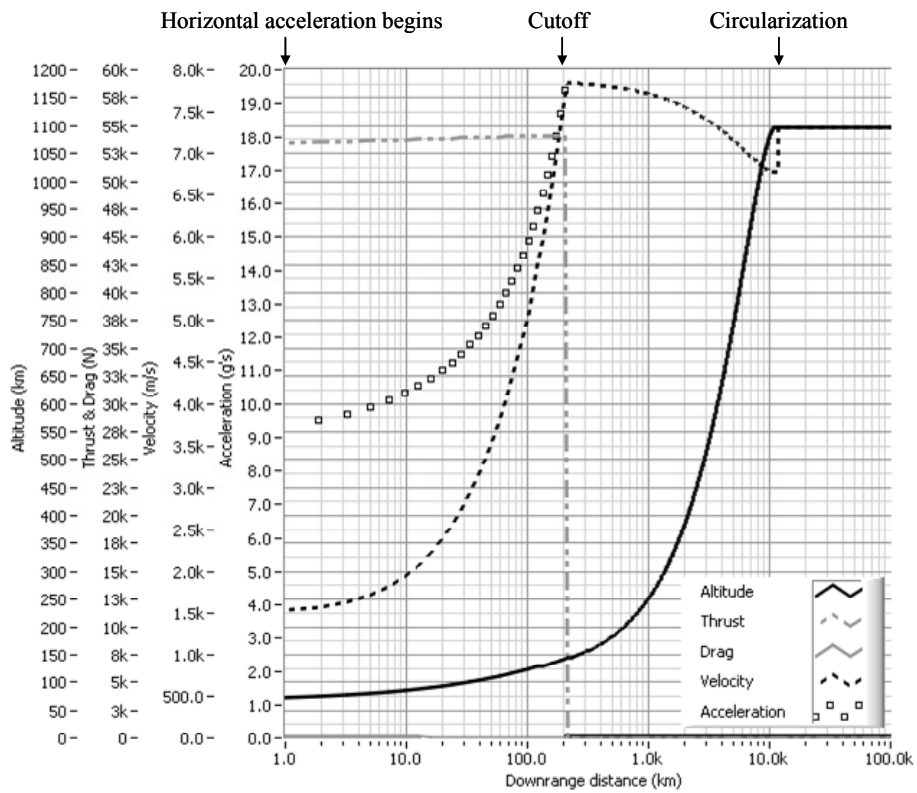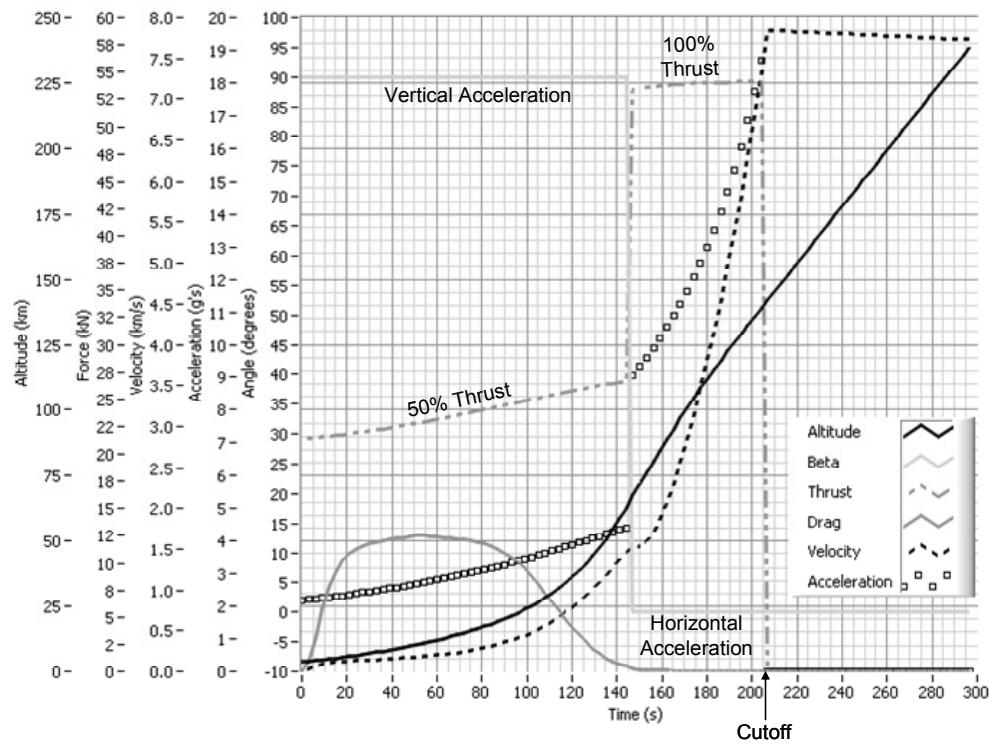
Fig. 2-13: Top: Ascent trajectory with time. Bottom: Ascent trajectory with downrange distance. Computed using the model given in Appendix C.

2.3.3 Heavy Launch

In the long term there is no particular reason why microwave thermal launch cannot be scaled to very heavy payloads, far heavier then yet launched by an order of magnitude. Table 2-3 shows the relationship between microwave frequency, the minimum scale of the heat exchanger as determined by atmospheric breakdown, and the optical quality needed of the beam site. Small payloads can use the 140 GHz frequency, or 35 GHz at a push if a small breakdown safety factor can be tolerated. For larger payloads a higher jet power is required, and the constraint of atmospheric breakdown leads to larger areas.

Frequency	CSO Zenith Transmission on a bad day	Breakdown altitude	Breakdown Intensity	Min beam/vehicle area at breakdown altitude (microsat, 100kg,100MW)	Min beam/vehicle area at breakdown altitude (Heavy launch, 100 ton, 100GW)
2.45 GHz	100%	60 km	300 kW/m^2	333 m^2	0.3 km^2
35 GHz	95%	32 km	90 MW/m^2	1.1 m^2	1100 m^2
140 GHz	85%	20 km	1.5 GW/m^2	0.07 m^2 or 667 cm^2	66.7 m^2
300 GHz	40%	15 km	8 GW/m^2	0.01 m^2 or 125 cm^2	12.5 m^2

Table 2-3: Ascent trajectory parameters of a microwave thermal launcher with a 100 ton payload vs. a 100 kg payload.

The minimum area implies a corresponding launcher volume, and so the frequency is chosen such that the volume of the launcher is consistent with its mass. For very heavy launch the frequency may be increased to 300 GHz; however, the larger atmospheric absorption at this frequency makes a launch site (or day) with high optical quality desirable. In the Antarctic, atmospheric transmission windows can open up all the way from microwave to infrared (Candidi and Lori, 2003).

Ascent trajectory results using the approach of the previous section are tabulated for launchers at many scales in Table 2-4. The simplistic analysis used for these ascent trajectory estimates shows that the heat exchanger microwave intensity is well below the breakdown threshold even at a wet mass of 10,000[§] tons, though sites of higher optical quality are beneficial to energy efficiency.

Wet mass (tons)	Payload (tons)	Payload fraction (%)	Destination altitude (km)	X-33 aeroshell base width (m)	Thruster throat temperature (K)	Jet Power (GW)	Peak microwave intensity (MW/m^2)	Breakdown intensity (MW/m^2)	Frequency (GHz)
1	0.1	10	220	5.1	2550	0.25	56	1500	140
10	1	10	200	11	2400	2.75	131	1500	140
100	15	15	220	23.6	2400	25	259	4200	220
1,000	170	17	260	49.5	2400	250	589	4200	220
10,000	2,000	20	280	106.5	2600	2500	1273	8500	300

Table 2-4: Heavy launch trajectory results using input parameters that are optimized by trial and error. The structural mass fraction is assumed to be 20% for all cases. A more accurate treatment is given in Appendix F.

For regular launchers the jet power is seldom explicitly listed; however, it is similar to the figures given here. The difference is that the energy expended in conventional launch is stored chemically over time and released quickly. There is no reason an equivalent

---

[§] For comparison, the Saturn V wet mass was 2,800 tons.

process should not occur on the ground to power the beam facility, and indeed Kare has suggested truck batteries as simple low-cost and mass-produced energy storage devices that are optimized to discharge over ~ 5 minutes, the duration a powered ascent.

2.3.4 Single Stage to Orbit Example

Using some of the design relations given in Appendix F and the methodology of Humble *et al.* (1995), a system analysis of the microwave thermal rocket is possible. In this idealized design example, the parameters in Table 2-5 are used to produce a 10 ton single stage to orbit (SSTO) vehicle point design.

An analysis of this kind tends to be an exercise in managing complexity, to converge many parameters and engineering judgments in order to form a self-consistent picture of the whole system. The primary intent is to give an idea of the kind of performance possible with a microwave thermal rocket and what demands the increasing I_{sp} places on the various subsystem components.

Not included in the analysis are masses for cooling, a thermal protection system, winglets, a landing system, or avionics. Because of the very significant effect that tank materials have on the payload fraction of SSTO vehicles, separate results are presented for Al-Li-2195 alloy tanks (Fig. 2-14), titanium tanks (Fig. 2-15), and carbon composite tanks (Fig. 2-16).

Al-Li alloys are used for the LH_2 tanks of the Space Shuttle and become stronger at cryogenic temperatures. However, there are a number of more promising tank materials that have emerged since the Space Shuttle was designed in the 1970s.

Titanium tanks have better structural performance, excellent fatigue characteristics (of interest for reusability) and can be used as part of a lightweight hot structures aeroshell (Johnson, 1998; Woods, 2003). Better yet for structural performance are carbon composite tanks, which provide good cryogenic insulation although questions remain over their fatigue characteristics.

Mission parameters

Mission Δv	9.6 km/s
Stages	1
Wet mass	10 tons
Acceleration at cutoff	20 g's (for short range ascent trajectory)

Vehicle parameters

Propellant	Hydrogen
Overhead for structural mounts	0.1 * propulsion system mass

Tank parameters

Material	Al-Li-2195 alloy (Fig. 2-14), titanium (Fig. 2-15), carbon composite (Fig. 2-16).
Geometry	Cylindrical, L/D ratio = 4, 2:1 ellipsoidal end caps.
Operating pressure	3 atm, autogenous (self-pressurized)
Ullage	10%
Structural safety factor	1.875 + 2.25 additional multiplier for welds etc.

Heat exchanger parameters

Material	Silicon carbide
Segments	2 sets of opposing segments, so that two outlets (peak temperatures) meet in the middle, as depicted on the upper right of Fig. 2-1.
Channel geometry	Square
Channel diameter	4 mm
Structural safety factor	5
Assumed stress concentration factor	8
Outlet Mach number	1 (sonic)
Feed system overhead	0.249 * heat exchanger mass
Length/Width ratio	1.5
Inlet temperature	300 K

Nozzle parameters

Material	Columbium alloy
Nozzle type	80% bell
Thrust efficiency	98.5%
Cone half angle	15 degrees
Safety factor	2.5
Outlet Mach	6

Table 2-5: Parameters for the 10 ton SSTO launcher point design.
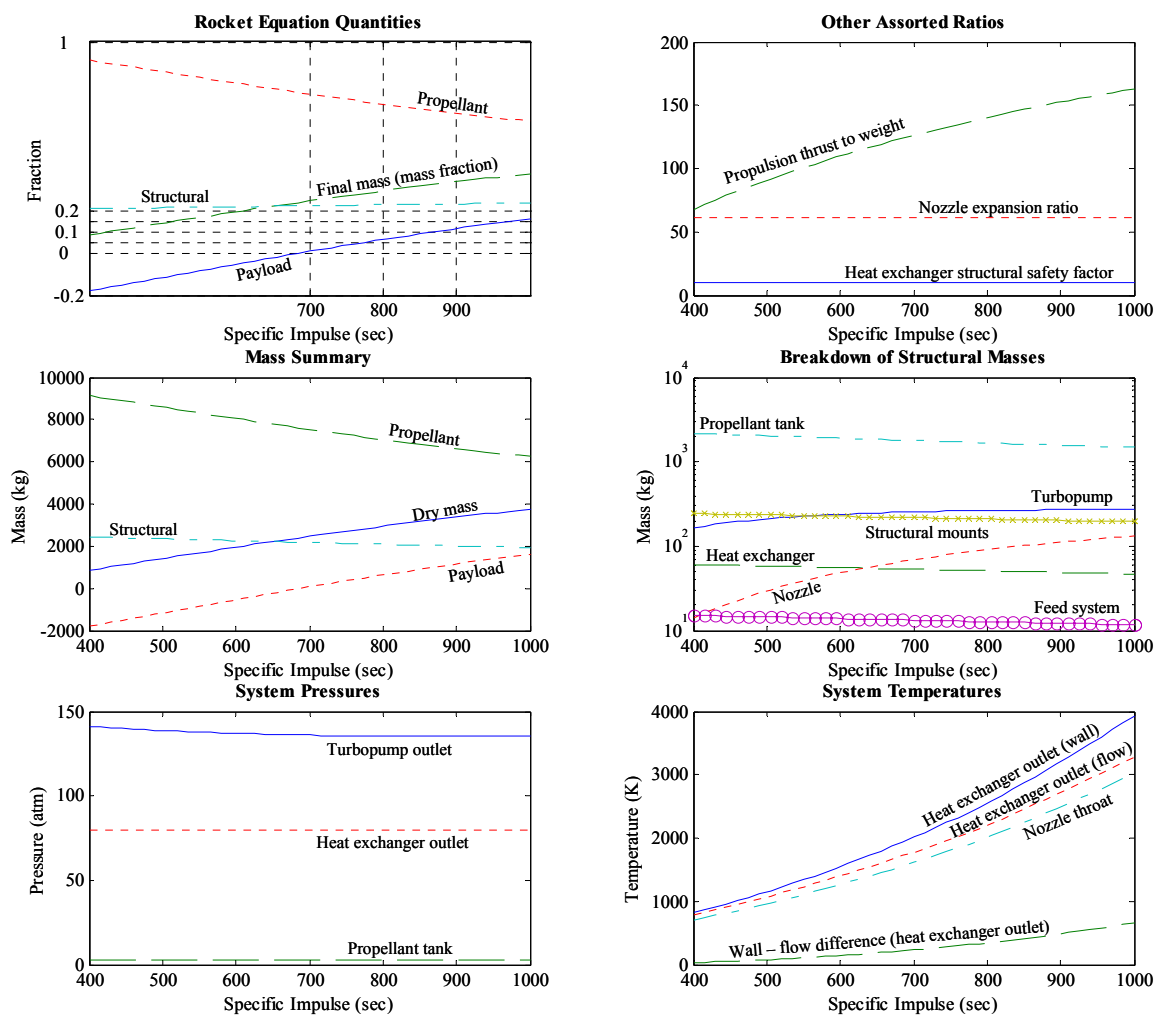
Fig. 2-14: System summary of the 10 ton SSTO launcher point design vs. I_{sp} using Al-Li-2195 alloy tanks.
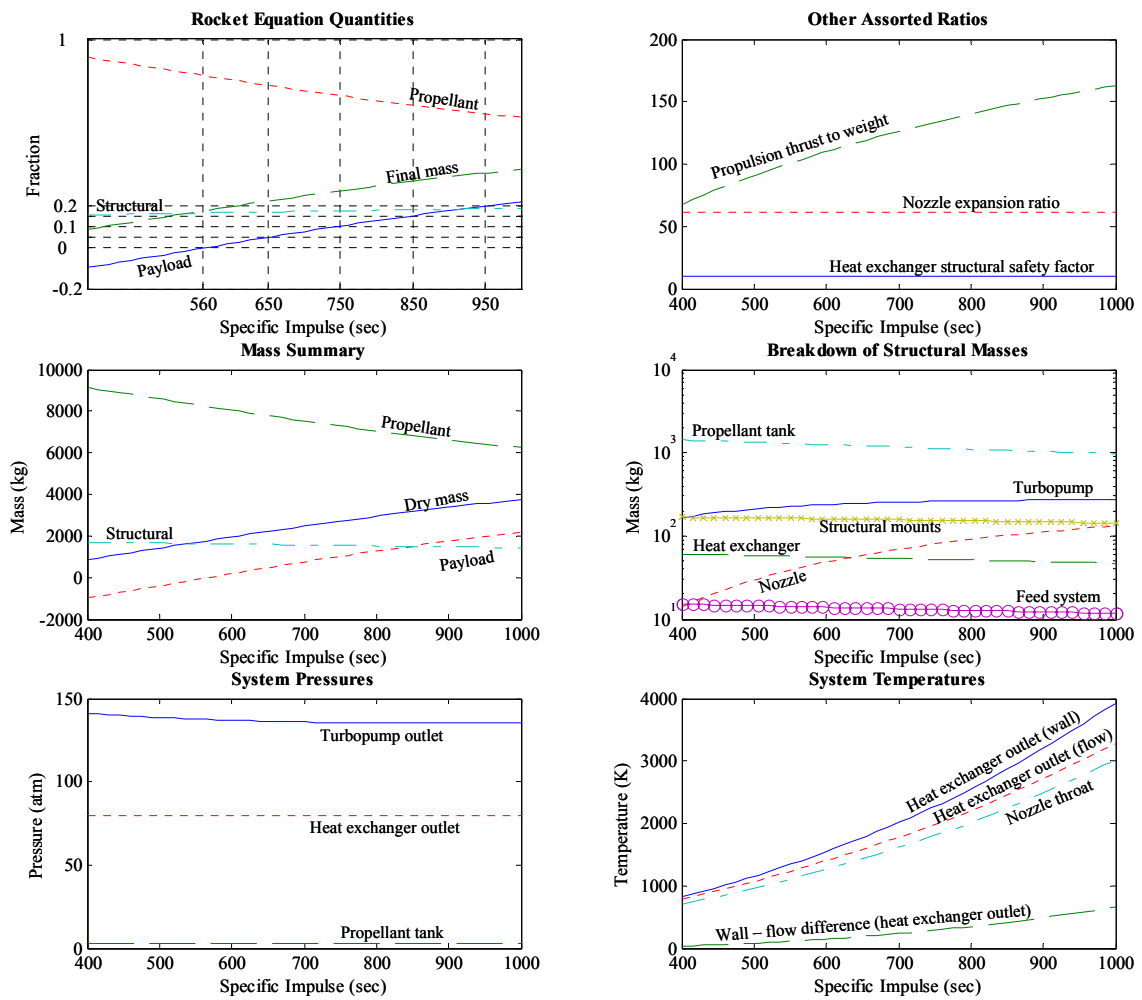
Fig. 2-15: System summary of the 10 ton SSTO launcher point design vs. I_{sp} using titanium tanks.
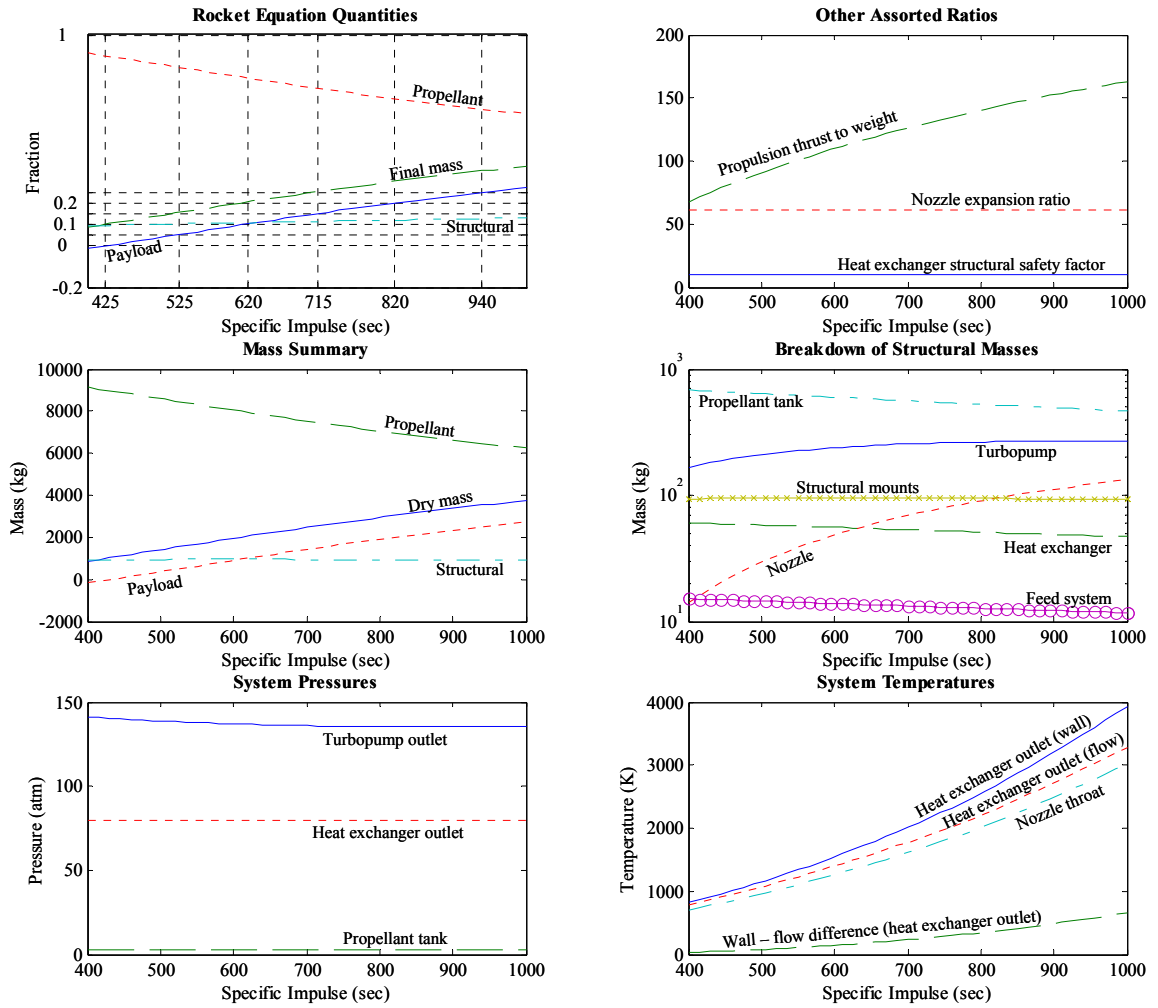
Fig. 2-16: System summary of the 10 ton SSTO launcher point design vs. I_{sp} using carbon composite tanks.

Clearly, the carbon fiber tanks are the most desirable from a payload performance point of view. Table 2-6 lists the key metrics for an SSTO with carbon composite tanks operating at an I_{sp} of 820 seconds. A key tradeoff is turbopump mass vs. specific impulse, and this occurs via the temperature difference between the wall and flow at the heat exchanger outlet. By switching from a single segment to opposing segments, the channel length is halved, reducing the pressure drop at the expense of lower I_{sp}, all other factors being equal. The net effect of the reduced pressure drop is to increase the T/W ratio by reducing the turbopump mass.

Payload fraction	20%
Structural mass fraction	11%
Propulsion *T/W* ratio	142
Tank diameter	3.17 m
Beam heating area	3.17 m wide by 4.75 m long
Heat exchanger channel length	1.6 m (half the width of the beam heating area)
Heat exchanger peak wall temperature	2680 K
Heat exchanger peak flow temperature	2300 K
Heat exchanger power absorbed	2500 MW (includes turbopump power requirement)
Turbopump power requirement	18 MW
Turbopump stages	1
Turbopump outlet pressure	135 atm

Table 2-6: Results for the 10 ton SSTO launcher point design. Taken from carbon composite tank dataset at I_{sp} = 820 seconds.

The model used to compute these results misses a key element of the channel flow dynamics in that it does not account for the maximum hydrodynamic channel length, as determined by the given set of problem parameters, which may appear perfectly rational yet correspond to a channel length longer than hydrodynamically allowed by the choking effect. This constraint is tested using the quasi-1D channel model given in § 5.1 and applied to a turbulent channel in § 5.1.4. The results of the quasi-1D analysis verify that the input parameters used here do not violate the hydrodynamic channel length limit.

2.3.5 Power Budget

Table 2-7 summarizes efficiencies from wallplug to expanded jet, and gyrotron beam to expanded jet. These efficiencies are collated from various sources in Table 2-8, and are important in gauging the scale of the system when starting with a vehicle of a given payload size. For example, a 100 kg payload launcher requires ~ 1 MW of jet power per kilogram of payload (i.e., 100 MW). In the medium case, tracing back the efficiencies with Table 2-7 to the gyrotron output implies that ~ 310 MW of microwave power output

is needed from the gyrotrons (310 * 1 MW gyrotrons). Further tracing back to the prime power requirement gives ~ 630 MW of wallplug power needed for the medium case.

	Individual efficiency			Wallplug to Jet cumulative			Gyrotron to Jet cumulative		
	Low	Med	High	Low	Med	High	Low	Med	High
Power supply	85%	92%	98%	85%	92%	98%			
Gyrotron	45%	54%	62%	38%	49%	61%			
Dish feed system	88%	92%	96%	34%	45%	58%	88%	92%	96%
Nonuniform illumination	80%	88%	95%	27%	39%	55%	70%	80%	91%
Surface accuracy	95%	98%	100%	26%	38%	55%	67%	78%	91%
Array fill factor loss	64%	76%	88%	16%	29%	48%	43%	59%	80%
Diffraction	84%	90%	95%	14%	26%	46%	36%	53%	76%
Atmospheric transmission	80%	89%	97%	11%	23%	45%	29%	47%	74%
Thruster absorption	80%	89%	98%	9%	21%	44%	23%	42%	72%
Convection	80%	88%	95%	7%	18%	42%	18%	37%	68%
Exchanger + Nozzle	80%	89%	97%	**6%**	**16%**	**40%**	**15%**	**32%**	**66%**

Table 2-7: Estimated end-to-end energy efficiencies for the microwave thermal system based on the efficiencies given in Table 2-8.

System	Basis of estimate	Efficiency range
Power supply	Based on solid state gyrotron power supply used by CPI (Gaudreau *et al.*, 1999)	85–98%
Gyrotron	As discussed in § 2.2.4	45–62%
Dish Feed system	By analogy with DIII-D ECH system (Lohr *et al.*, 1996). Quasi-optical beam launcher.	98% per 40 m of transmission line 99.4% per miter bend
Nonuniform illumination of individual dishes	Includes beam spillover. Dish diameter ~ 4000 wavelengths.	80–95%
Dish surface accuracy	Surface accuracy possible for millimeter-wave astronomical dishes (Cheng *et al.*, 1995; Walmsley, 2000)	95–100%
Array fill factor loss	Known fill factor of hexagonal close packing + margin	64–88%
Diffraction	Generalized power transmission analysis (Benford and Swegle, 2006 (in preparation); Brown, 1992)	84–95%
Atmospheric transmission	Includes path error (Cheng *et al.*, 1995). Cloud and water vapor for sites in the Southwestern USA (Erasmus, 2000); Fig. 2-11.	80–97%
Thruster absorption	Stratified layer analysis results shown in Fig. 2-4.	80–98%
Useful convective energy	Absorbed energy minus radiative and conductive losses.	80–95%
Nozzle	Includes frozen flow losses and turbopump losses (Humble *et al.*, 1995)	80–97%

Table 2-8: Basis of estimates and references for Table 2-7.

The uncertainty associated with the efficiencies seen in Table 2-7 has not been quantified, so in the absence of this data, the efficiencies at each level of confidence are multiplied. This almost certainly produces an over-pessimistic prediction in the low cases because it implies that everything is performing at the minimum expected efficiency simultaneously. A more reliable analysis awaits the investigation of a range of specific phased array designs.

All these powers are comparable with the power released in conventional airbreathing and rocket thrusters of a similar scale. If 630 MW of power is unavailable from the power grid, for example at an off-peak time, then Kare (2005a) has suggested the use of truck batteries for low duty cycle peak power operations, as truck batteries are very low-cost and optimized for maximum discharge over approximately the 3 minute duration of a powered ascent.

2.3.6 Cost

A full probabilistic cost estimate is beyond the scope of this work; however, it is instructive to make some simple calculations based on the information at hand. It is emphasized that the following is not a cost estimate, since it considers only the cost of key equipment without personnel, maintenance and other supporting infrastructure, which vary by organization and are highly uncertain at this stage.

Imagining the scale and complexity of engineering used to generate electricity at the present time, gas turbines, step-up transformers, a power distribution grid, step down transformers with maintenance and personnel all contribute to a present wallplug electricity cost on the order of 10 ¢/kWh (U.S. market spot price at time of writing is 5 ¢/kWh). Given the probable complexity of a beam facility, one can ask what it takes for a microwave beam facility to cost on the order of the energy cost of launch. Considering just the cost of relatively well-known major hardware elements in Table 2-9, such an estimate is possible.

System	Subsystem	Quantity considered	Est. 2006 unit cost $
Phased array	Dish area; 8–12 m diameter	1 dish	$22.800k / m^2
	Dish area; 3 m diameter	2500 dishes, 10% learning curve	$2.5k / m^2 (Horne, 1982)
Gyrotrons	1 MW Gyrotron + supporting equipment	1	$2M (Felch, 2003)– $5.5M (Kare, 2005b)
	1 MW Gyrotron + supporting equipment	200 gyrotrons, 15% learning curve	$580k–$1.6M (per Megawatt)

Table 2-9: Summary of hardware cost estimates.

Assuming:

- A wallplug energy cost of 10¢/kWh
- A 180 second powered ascent (§ 2.3.2)
- 2.5 MW of jet power required per kg of payload
- A jet power to wallplug power efficiency of 15%

The energy cost of launch including all inefficiencies is estimated to be $84/kg of payload.

Moving onto the beam facility, assuming in addition to the above:

- 300 kg payload
- 3 meter diameter beam waist and 150 km range with maximum azimuth angle of 45 degrees, corresponding to 300 m effective diameter circular phased array (§ 2.3.2)
- A jet power to microwave power efficiency of 30%
- 15% gyrotron cost learning curve
- 10% array cost learning curve

Then a total array microwave power output of 2.5 GW is required. Using present commercially available gyrotrons that corresponds to 2500 units at a unit cost of $350k, to give a total initial gyrotron cost of $880M. The phased array aperture requires 1400 dishes of 8 meters diameter, corresponding to a unit cost of $375k and total initial cost of

$570M.   Neglecting maintenance, personnel and supporting infrastructure costs, the gyrotron and dish contributions to the initial beam facility cost is around $1.5B.

With these estimates one can now ask how long on average the gyrotrons and dishes together must last (neglecting maintenance overheads) in order to contribute only the energy cost of launch ($84/kg) to the payload cost. Given

*No. launches * energy cost per launch = Array + Dish Cost*

The gyrotrons and dishes must last for 60,000 launches.   This is comparable to the number of takeoffs possible (every 3 minutes or so) from the runway of a busy airport in one year. Powered ascent for a microwave thermal launch also takes 3 minutes, meaning the gyrotrons and dishes must last for 3000 hours of operation, placing a total of 18,000 tons of payload into orbit over this lifetime. As discussed in § 2.2.4 some early development gyrotrons developed repairable faults after ~ 5,000 hours of (non-continuous) operation and more mature systems like the SLAC klystrons have lasted for 50,000 hours of operation so far, which is consistent with the lifetime of vacuum-type microwave sources generally.

Repeating the above calculation for 0% learning curves gives a $5.5Bn initial gyrotron cost and $1.7Bn initial aperture cost, corresponding to a required service life of 15,000 hours for the gyrotrons and dishes. Given the historical, present and projected increase in gyrotron performance, gyrotron cost in $/MW appears likely to fall even without a learning curve for economies of scale.

It is concluded that there is a plausible set of assumptions for which gyrotron and initial aperture costs alone contribute on the order of the energy cost to the overall cost of launch, equating in this example to a total of $170 per kilogram of payload on top of costs associated with other infrastructure, maintenance, personnel and the vehicle itself. For the latter, it is worth noting that even if the microwave thermal launcher construction costs the same as a conventional launcher, the greater I_{sp} allows a payload fraction roughly three times higher than a conventional launcher (10% vs. 3%). The scope for

larger structural safety factors (at the expense of payload fraction) favorably alters the economics and logistics of reusability.

2.4 Summary and References

The microwave thermal rocket draws upon the techniques and analyses of several fields to achieve an I_{sp} of 700–900 seconds. The turbopump is responsible for the majority of the propulsion subsystem mass, in part because hydrogen is relatively difficult to pressurize in this way. Nevertheless, a *T/W* of 50–150 is possible, which is essentially the some as the *T/W* range of chemical engines. A simplified system analysis predicts a payload fraction of 0–15% for a silicon carbide heat exchanger depending upon the choice of material for the propellant tanks. Other heat exchanger materials such as titanium diboride offer yet greater performance; however, they must be in good thermal contact with a second microwave absorbent material.

Ascent trajectory analysis reveals viable trajectories for microwave thermal rockets ranging from 1 ton to 10,000 tons wet mass. As payload increases so does heat exchanger area, and the intensity required changes little over several orders of magnitude of scale. For very heavy launch in the range of 10,000 tons wet mass, greater payload performance is attained by moving to higher frequency. It is shown that the atmospheric breakdown threshold is not exceeded even for very heavy payloads and that suitable beam facility sites with low atmospheric absorption exist in the southwestern United States, among other places.

The key question of cost is examined for the beam facility, and it is reasoned that the cost of the purely the beam facility hardware should correspond to $170/kg of the payload cost based on 0% learning curves and present commercially available hardware. If learning curves are included the hardware cost drops to $84/kg. The correct appraisal of personnel and maintenance costs, as well as vehicle costs, requires a probabilistic analysis that is beyond the scope of the present work.

There are no known fundamental reasons why a microwave thermal launch system should not be possible. There are two specific engineering reasons why a microwave thermal launch system might not be possible: The first is that a suitable way to construct a refractory hydrogen heat exchanger may not be found. Past experience with nuclear thermal rockets suggests otherwise, but in this case the pressure difference across channel walls is far greater. The second reason is that a suitable way to phase lock gyrotrons may not be found, but experience with every other class of vacuum-type microwave source suggests otherwise. In general, it is possible that the combined energy efficiencies of the various system elements could once again render the beam facility cost prohibitive, and a specific design for the phased array can reduce much of the uncertainty about this.

Given a feasible launch system and a specific concept for the microwave thermal thruster, the next step is to identify what can be done to begin the process of developing such a system. The key system component is the microwave absorbent heat exchanger, and the logical starting point is at the fundamental level. Therefore, the next chapter begins with the question of how to characterize the fundamental physics and behavior of a microwave absorbent heat exchanger.

Anon. U.S. Army Corps of Engineers (1990). *Electromagnetic Pulse (EMP) and Tempest Protection for Facilities.* Chapter 5 — Facility Design.

Barker, R.J. and Schamiloglu, E. (2001). *High-power microwave sources and technologies*. IEEE Press.

Beardsley (1999). *The Way to Go in Space*. Scientific American.

Benford, J. (2004). *Unpublished*. Private Communication to.

Benford, J. and Dickinson, R. (1995). *Space Propulsion and Power Beaming Using Millimeter Systems*, in Intense Microwave Pulses III. Also published in Space Energy and Transportation, 1, p. 211.

Benford, J. and Swegle, J.A. (1992). *High-power microwaves*. Artech House microwave library., Boston. Artech House.

Benford, J. and Swegle, J.A. (2006 (in preparation)). *High-power microwaves*. Artech House microwave library., Boston. Artech House.

Besmann, T.M. (1986). *Assessment of ceramic composites for multimegawatt space nuclear power systems*. Oak Ridge National Laboratory.

Brown, W.C. (1992). *Beamed microwave power and its application to space*. IEEE Transactions on Microwave Theory and Techniques **40**(6).

Buffler, C.R. (1991). *A Simple Approach to the Calculation of Microwave Absorption, Transmission and Reflection of Microwaves from a Susceptor Film*. Microwave World **12**(3): p. 5–7.

Candidi, M. and Lori, A. (2003). *Status of the Antarctic base at Dome C and perspectives for Astrophysics*. Memorie della Società Astronomica Italiana **74**: p. 29–37.

Carpenter, L.G. and Kirby, P.J. (1982). *The Electrical-Resistivity of Boron-Nitride over the Temperature-Range 700-Degrees-C to 1400-Degrees-C*. Journal of Physics D-Applied Physics **15**(7): p. 1143–1151.

Cheng, J., Emerson, D.T.*, et al.* (1995). *MMA Memo 145: Antennas for the Millimeter Wave Array*. National Radio Astronomy Observatory.

Davis, J.W. and Smith, P.D. (1996). *ITER material properties handbook*. Journal of Nuclear Materials **237**: p. 1593–1596.

Deadmore, D.L. (1965). *Vaporization of Tantalum Carbide-Hafnium Carbide Solid Solutions*. Journal of the American Ceramic Society **48**(7): p. 357.

Dickinson, R.M. (1968). *Cost Effectiveness of Spacecraft Pointing Antenna*. JPL Technical Memorandum 33-390.

Dumbrajs, O. and Nusinovich, G.S. (2004). *Coaxial gyrotrons: Past, present, and future (Review)*. IEEE Transactions on Plasma Science **32**(3): p. 934–946.

Erasmus, D.A. (2000). *A Satellite Survey of Water Vapor and Cloud Cover at Selected Existing and Potential Infrared Telescope Sites in the Southwestern U.S.A.* Rocky Mountain Observatories Consortium (RMOC).

Felch, K. (2003). *CPI Microwave Power Products: Gyrotron costs and lead time*. Private Communication to K. Parkin.

Fliflet, A.W. and Manheimer, W.M. (1989). *Nonlinear-Theory of Phase-Locking Gyrotron Oscillators Driven by an External Signal*. Physical Review A **39**(7): p. 3432–3443.

Fourikis, N. (2000). *Advanced array systems, applications and RF technologies*.

Gaudreau, M.P.J., Casey, J*., et al.* (1999). *Solid State Modulator for Klystron /Gyrotron Conditioning, Testing, and Operation*, in IEEE Pulsed Power Conference.

Gradinaru, G., Sudarshan, T.S*., et al.* (1997). *Electrical properties of high resistivity 6H-SiC under high temperature/high field stress*. Applied Physics Letters **70**(6): p. 735–737.

Gunn, S. (2001). *Nuclear propulsion – a historical perspective*. Space Policy **17**: p. 291–298.

Guo, H., Hoppe, D.J*., et al.* (1995). *Phase-locking of a second-harmonic gyrotron oscillator using a quasi-optical circulator to separate injection and output signals*. IEEE Transactions on Plasma Science **23**(5): p. 822–832.

Horne, W. (1982). *Millimeter Array Memo #5: Estimate antenna costs – millimeter array*. National Radio Astronomy Observatory.

Humble, R.W., Henry, G.N. and Larson, W.J. (1995). *Space propulsion analysis and design*. 1st ed. Space technology series, New York. McGraw-Hill.

Johnson, T.F. (1998). *Thermal Structures Technology Development for Reusable Launch Vehicle Cryogenic Propellant Tanks*. Springfield, VA: National Aeronautics and Space Administration; National Technical Information Service, distributor.

Kare, J. (2005a). *Private communication regarding energy storage for low duty-cycle beam facilities*.

Kare, J. (2005b). *Private communication regarding gyrotron cost estimates from General Atomics*.

Knight, T. and Anghaie, S. (1999). *Ternary Carbide Uranium Fuels For Advanced Reactor Design Applications*, in Proceedings of the 7th International Conference on Nuclear Engineering (ICONE-7).

Korte, J.J., Salas, A.O*., et al.* (2001). *Multidisciplinary approach to linear aerospike nozzle design*. Journal of Propulsion and Power **17**(1): p. 93–98.

Levine, J.S., Aiello, N*., et al.* (1991). *Design and Operation of a Module of Phase-Locked Relativistic Magnetrons*. Journal of Applied Physics **70**(5): p. 2838–2848.

Lis, D. (2005). *CSO Atmospheric Transmission Interactive Plotter*.

Liu, G., Liu, J*., et al.* (1997). *The study of high power microwave (HPM) air breakdown*. SPIE **3158**.

Lohr, J., Cahalan, P*., et al.* (1999). *The 110 GHz Gyrotron System on DIII-D: Gyrotron Tests and Physics*, in Fourth International Workshop on Strong Microwaves in Plasmas. Nizhny Novgorod, Russia.

Lohr, J., Ponce, D*., et al.* (1996). *Initial Tests and Operation of a 110 GHz, 1 MW Gyrotron with Evacuated Waveguide System on The DIII-D Tokamak*, in 3rd Int. Workshop on Strong Microwaves in Plasmas. Moscow/St. Petersburg, Russia: Also published as Technical Report GA-A22420, General Atomics, Inc., San Diego, CA, 1996.

Munro, R.G. (1997). *Material properties of a sintered alpha-SiC*. Journal of Physical and Chemical Reference Data **26**(5): p. 1195–1203.

Munro, R.G. (2000). *Material properties of titanium diboride*. Journal of Research of the National Institute of Standards and Technology **105**(5): p. 709–720.

Myrabo, L.N. and Benford, J. (1994). *Propulsion of Small Launch Vehicles Using High Power Millimeter Waves*. SPIE 2154: p. 198.

Oda, Y., Nakagawa, T*., et al.* (2003). *An observation of plasma inside of microwave boosted thruster*, in Second International Symposium on Beamed Energy Propulsion. Sendai, Japan: Conf. Proc. AIP.

Panofsky, W.K.H. (1996). *The Creation of SLAC Leading to 30 Years of Operation*, in XVIII International Linac Conference. Geneva, Switzerland.

Park, J.J. and Lee, J.D. (1999). *Formation of subgrains in tungsten-rhenium-hafnium carbide alloys during creep*. Journal of Materials Science Letters **18**(4): p. 273–275.

Parkin, K. (2006). *Microwave heat-exchange thruster and method of operating the same*, USPTO Patent 6993898. California Institute of Technology.

Pierson, H.O. (1996). *Handbook of Refractory Carbides and Nitrides*, Westwood, NJ. Noyes Publications.

Pierson, H.O., Sheek, J. and Tuffias, R. (1989). *Overcoating of Carbon-Carbon Composites*. Wright-Patterson AFB, OH.

Sobieszczanski-Sobieski, J. and Haftka, R.T. (1997). *Multidisciplinary aerospace design optimization: survey of recent developments*. Structural Optimization **14**(1): p. 1–23.

Thumm, M. (2005). *State-of-the-art of High Power Gyro-Devices and Free Electron Masers Update 2004*: Karlsruhe, Germany.

Thunnissen, D.P. (2005). *Propagating and mitigating uncertainty in the design of complex multidisciplinary systems*. Ph.D., Division of Engineering and Applied Science, California Institute of Technology.

Tolkachev, A.A., Levitan, B.A.*, et al.* (2000). *A megawatt power millimeter-wave phased-array radar*. Ieee Aerospace and Electronic Systems Magazine **15**(7): p. 25–31.

Tsiolkovsky, K.E. (1924). *Spaceship, 1924, in Izbrannye Trudy, Compiled by Vorob'ev, B.N., Sokol'skii, V.N., General Editor Acad. Blagonravov, Izdatel'stvo Akademii Nauk SSSR, Moscow, Russia, 1962, 222 (in Russian). Edited Machine Translation prepared by Translation Division, Foreign Technology Division, WP-AFB, Ohio, on May 5th, 1966, 307.*

Turchi, P.J. (1998). *Propulsion Techniques: Action and Reaction*. AIAA Press.

Walmsley, M. (2000). *ALMA: The Atacama Large Millimeter Array*. Memorie della Societa Astronomia Italiana **79**: p. 889.

Weglian, J.E., Olds, J.R.*, et al.* (2001). *ASPEN Revisited: The Challenge of Nuclear Propulsion for ETO*, in 37th AIAA/ ASME/SAE/ASEE Joint Propulsion Conference and Exhibit. Salt Lake City, UH.

Woods, B. (2003). *Heated Debates*. QUEST **10**(3): p. 39.

Wuchina, E., Opeka, M.*, et al.* (2004). *Designing for ultrahigh-temperature applications: The mechanical and thermal properties of HfB2, HfCx, HfNx, and alpha Hf(N)*. Journal of Materials Science **39**(19): p. 5939–5949.

CHAPTER 3
EXPERIMENTAL AND THEORETICAL MOTIVATION

3.1 Experimental and Theoretical Objectives

From a practical perspective a desirable first step is to provide a small, low power laboratory-scale proof of principle for the microwave thermal thruster that demonstrates the two key physical processes of microwave thermal propulsion: (a) To heat a refractory tube using microwaves, and (b) for the tube in turn to heat a flowing propellant.

From a theoretical perspective the ability to model these processes accurately is a necessary foundation for the design and optimization of practical and reliable microwave thermal thrusters. Standard heat exchanger design methodologies do not address such large temperature ranges, and although analytical methods were published (Bussard and DeLauer, 1958; Cooper, 1968; Knight Jr. *et al.*, 1957) to predict the convective heat transfer for application to nuclear thermal thruster design, it is unclear whether or not the assumptions they make are experimentally valid. For example, Bussard (1958) presents a quasi-1D model for predicting pressure drop and heat transfer along a channel. However, these models implicitly assume a hydrodynamically developed flow, and it is unclear to what extent factors like developing flow, propellant properties that vary with temperature, and large thermal gradients between the wall and propellant skew these predictions.

On the microwave-material interaction side, a great deal of work undertaken in the field of microwave sintering and heating of ceramics (Beatty *et al.*, 1992; Iskander *et al.*, 1996; Iskander *et al.*, 1994; Snyder, 1992; Sutton *et al.*, 1988; Terril, 1998; Yiin and Barmatz, 1995). This work can be applied to the problem of heating a ceramic tube close to its melting point using microwaves (Huang, 1969; Jackson *et al.*, 1994; Jackson *et al.*, 1995; Jackson *et al.*, 1996; Wu, 2002). In this field, several experiments and simulations of the coupled electromagnetic-conduction problem are reported (Alpert and Jerby, 1999; Ma, 1999). Some involve a moving absorber or natural convection within a thawing tube

(Basak and Ayappa, 2001), but the fully coupled problem of forced convection within a highly nonlinear absorbing microwave tube has not yet been addressed. A model of the microwave thermal thruster is incomplete without such an understanding, and a combined electromagnetic-conduction-convection model is needed.

3.2 Approach

Given the objectives of demonstrating a laboratory-scale microwave thermal thruster and comparing it to simulations, the microwave thermal thruster is reduced to the simplest form possible: A single axisymmetric channel (tube). For microwave power, a commercial 1 kW magnetron is used, similar to the ones found in most home microwave ovens, albeit operating at a frequency of 2.45 GHz instead of 140 GHz.

This change of frequency does not alter the basic physics of the microwave absorption, which for microwave thermal thrusters is material plasma resonance rather than the dipolar absorption mechanism of the water molecule responsible for the cooking of food (Metaxas and Meredith, 1983). Fig. 3-1 is calculated using the stratified layer model given in Appendix D, and the fiftyfold decrease in frequency scales linearly to a fiftyfold increase in the material resistivity at which plasma resonance occurs.

In the full-scale microwave thermal system examined in § 2.3 the heat exchanger operates in the turbulent regime with Reynolds numbers in the tens of thousands. Considering the desired ~ 2000 K exit temperature of the propellant from the tube, a flow with the same mass flow rate per unit area as that given in § 2.3 needs an unfeasibly small diameter. Instead, the flow inlet pressure is reduced to 1–5 atm, which gives a diameter on the order of a millimeter and puts the flow in the laminar regime, rather than the turbulent one. Alumina and mullite thermocouple tubes are ideally suited in this diameter range and there are corresponding compression fittings with which to attach a propellant line. Both alumina and mullite are compatible with high temperature hydrogen and have a melting point above 2000 K, depending on the grade.
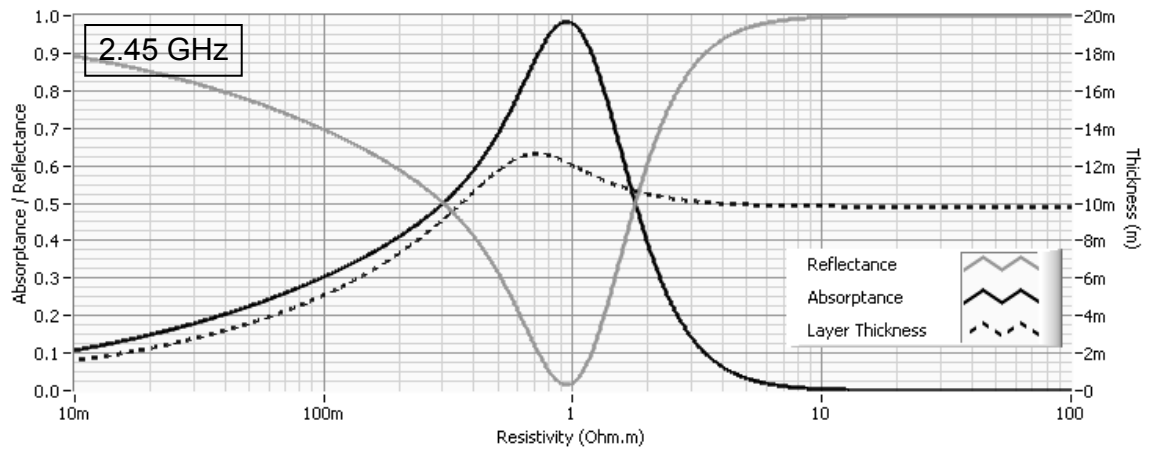
Fig. 3-1: Microwave absorption vs. resistivity at 2.45 GHz. The optimum resistivity for absorption is 100 Ω.cm, and for SiC the optimum planar layer thickness at this resistivity is 1.2 cm.

3.3   Apparatus

Both mullite and alumina are studied in the field of microwave sintering. For example, Yiin & Barmatz (1995) have demonstrated a resonant cavity arrangement (Fig. 3-2) capable of heating heat alumina rods up to their melting point.
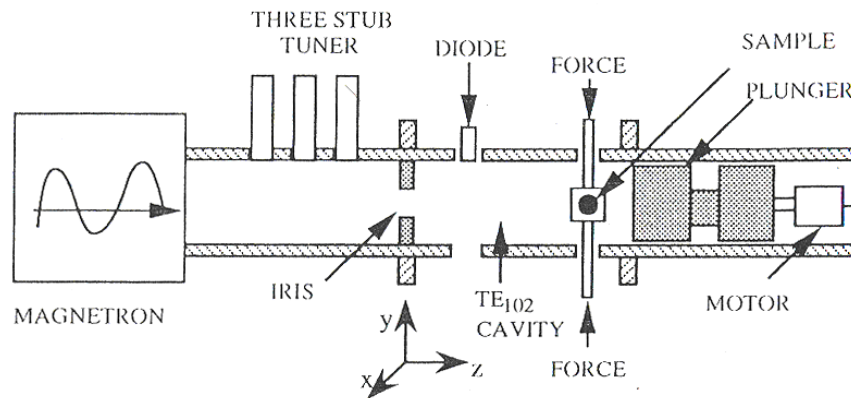
Fig. 3-2: TE$_{102}$ Resonant cavity arrangement of Yiin & Barmatz (1995).

Despite the low power of the microwave source, the resonant cavity approach raises the microwave intensity up to and beyond the 10 GW/m^2 breakdown intensity of atmospheric

pressure air, as depicted in Fig. 2-11. This is higher than the intensity of an operational microwave thermal thruster and high enough to heat alumina even though it has a room temperature resistivity on the order of 10^{14} Ω.cm, which is virtually microwave transparent and far from the resonance shown in Fig. 3-1.
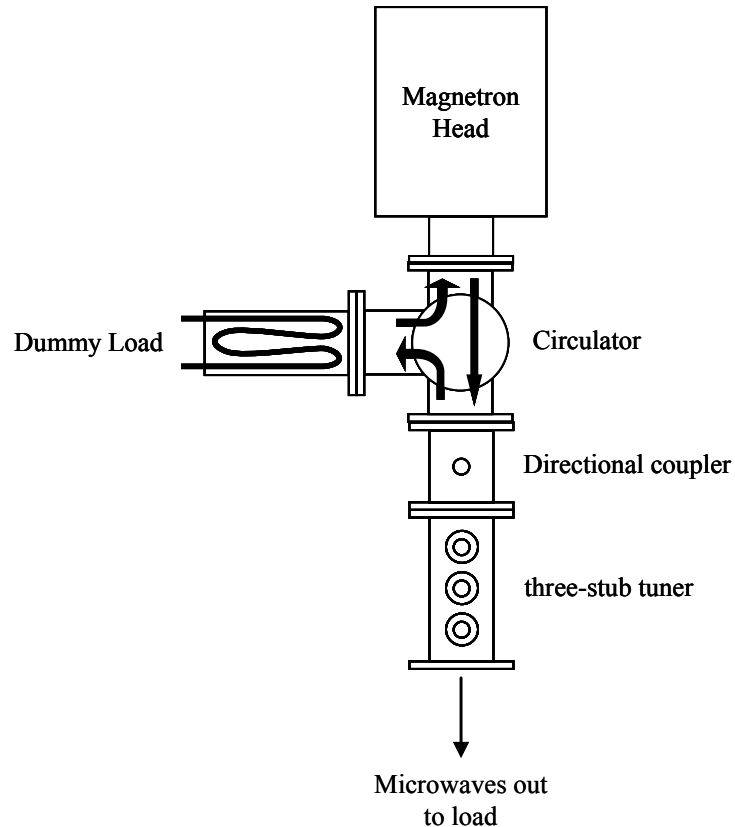
Fig. 3-3: Microwave circuit for heating.

The apparatus for generating such a resonant mode can be viewed as a microwave circuit, shown in Fig. 3-3. A microwave circulator allows power to go forward from the generator to the tuner but directs reflected power to a dummy load so as not to damage the microwave source. The three-stub tuner uses adjustable stubs that protrude into the waveguide in order to match the impedance of the resonant cavity and load with the impedance of the generator. This is analogous to the matching of impedances in a transmission line in order to maximize power transfer efficiency; there are equivalent

circuits in various degrees of complexity that can be used to model the system behavior (Meredith, 1998; Metaxas and Meredith, 1983).

At 2.45 GHz, the TE_{102} mode used by Yiin & Barmatz (1995) provides only a very short distance over which to heat a tube. A longer heating length can be achieved using a cylindrical cavity, and such a setup is depicted in Fig. 3-4.
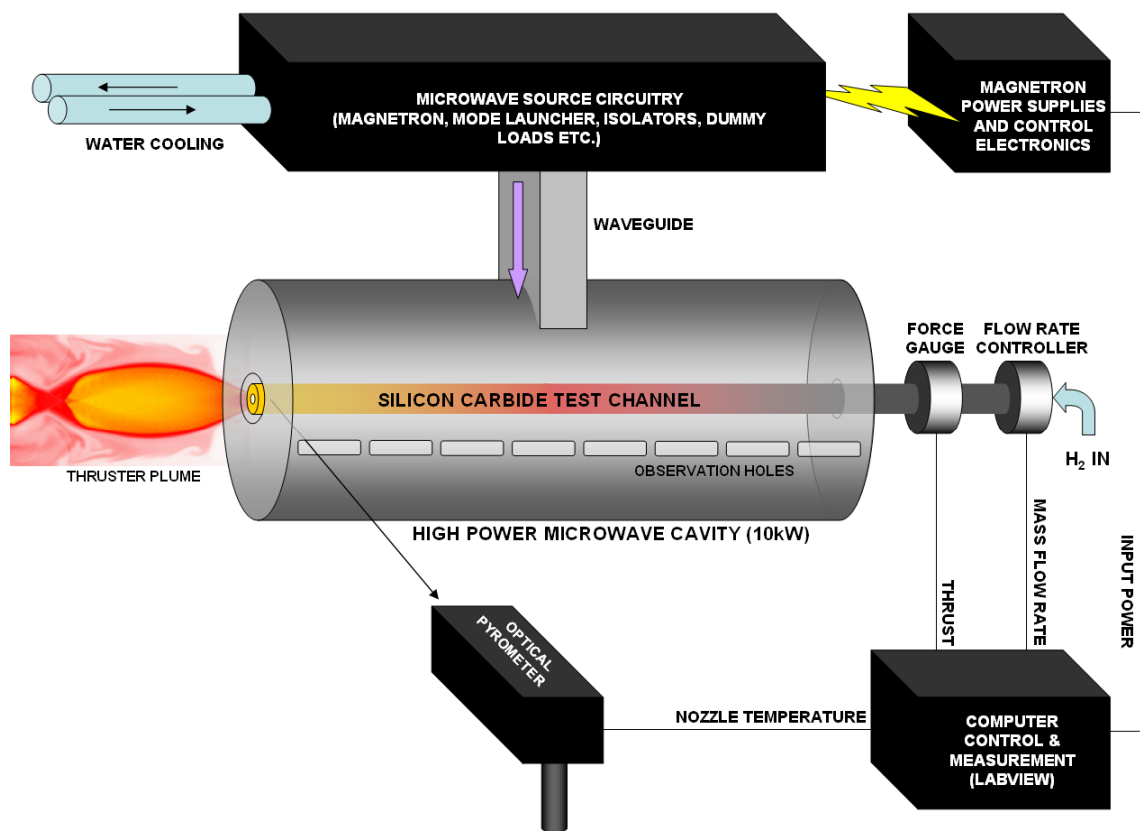
Fig. 3-4: An early concept of the experimental apparatus using a silicon carbide tube at 2.45 GHz (not to scale).

In Fig. 3-4 the waveguide is joined to the cavity using a well-known *H-H* field coupling method (Metaxas and Meredith, 1983) so that in essence a part of the magnetic field from a TE_{102} rectangular waveguide mode "leaks" through an aperture into the cylindrical

section, driving the resonant cavity mode(s) that are favored by the chosen cavity dimensions. Observation holes are used in conjunction with an optical pyrometer so that the tube temperature can be measured along its length and if necessary controlled via a feedback loop with magnetron power and/or mass flow rate.

3.4 Preliminary Sizing of Components

3.4.1 Mass Flow Controller

Given a microwave source with RF power output Q, then at most Q watts will be absorbed in the tube. Mass flow controllers are typically specified by their maximum volumetric flow rate at standard temperature and pressure, which in order to heat a propellant to ~ 2000 K can be estimated using,

$$\dot{V} = \frac{\dot{m}}{\rho_{in}} = u_{in}A \simeq \frac{Q}{\Delta h}\frac{R_g T_{in}}{1.2 P_{out}}, \tag{3.1}$$

where a 20% pressure drop along the tube is assumed. For example, a 500 W microwave source and a hydrogen propellant that exits at atmospheric pressure gives a volumetric flow rate of 12 SLPM (20 μg/s), corresponding to an inlet velocity of 250 m/s for a tube with a 2 mm inner diameter.

3.4.2 Tube

The expressions derived in the previous chapter for a uniform input flux may be used to estimate the tube length needed to provide significant heating of the channel propellant. Choosing a mass flow rate of 10 μg/s and a hydrogen propellant with an exit temperature of 1000 K, a tube on the order of 20 cm long is needed, and this length may be determined using the quasi-1D channel flow method presented in § 5.1. The difference between the inner and outer diameters is chosen to ensure there is a large enough volume of absorbing ceramic to absorb the required microwave power at the desired operating temperature, and at a field strength below the atmospheric breakdown threshold of ~ 2 MV/m for 2.45 GHz microwaves.

3.4.3 Cavity

Metaxas & Meredith (Meredith, 1998; Metaxas and Meredith, 1983) detail the industrial heating of fibers using a TM_{010} cavity mode, shown in the left of Fig. 3-5, which in theory conveys the advantage of uniform heating along the axis of the cavity. Such a uniform distribution of incident flux along the tube can considerably simplify the expressions needed to model the channel flow, and analytically derived Nusselt number correlations are available for the case of uniform flux (Kakaç *et al.*, 1987; Shah and London, 1978).

On the other hand Micci (1984) argues that the TM_{011} and TM_{012} modes (middle and right of Fig. 3-5), as opposed to the TM_{0n0} modes, are most applicable in the context of a flowing plasma. This is because the flowing plasma can readily distort the uniformity of the TM_{010} mode. A key question is therefore whether heating a thin microwave thermal heat exchanger with a flowing gas is more akin to heating a threadline, or a flowing plasma.
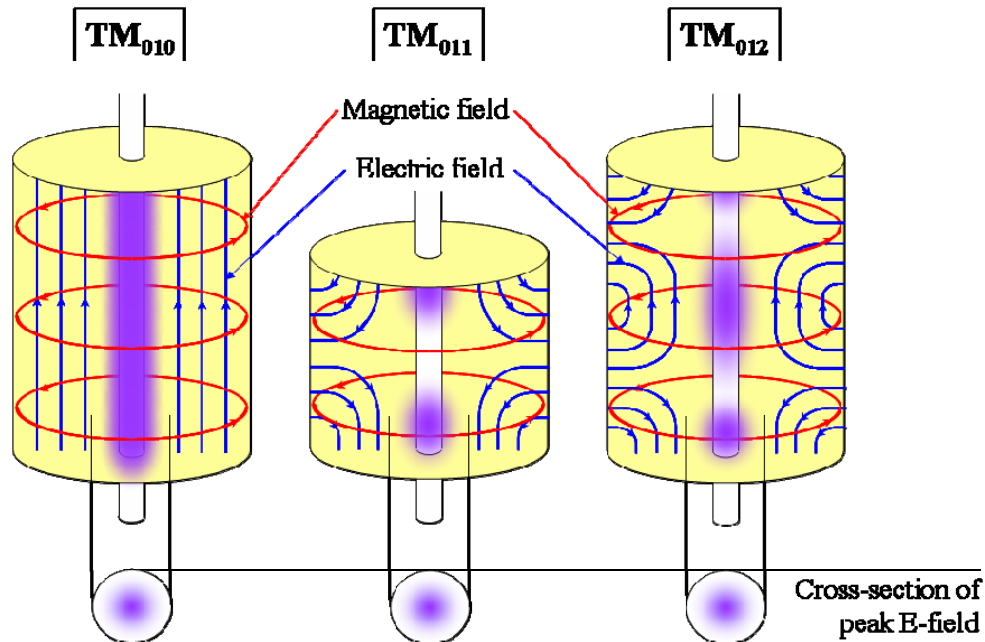
Fig. 3-5: Candidate cylindrical resonant cavity modes.

There are practical considerations for the choice of heating mode also: For the TM_{01n} class of modes the empty cavity diameter is given by,

$$D_{01n} = \frac{4.81}{\sqrt{\left(\frac{2\pi}{c}f\right)^2 - \left(\frac{n\pi}{L}\right)^2}} ,$$

(3.2)

where c is the speed of light, f is the frequency, n is the number of half wavelengths in the axial direction and L is the cavity length.

Figure 3-6 shows that the TM_{010} mode is hard to achieve because it takes a specific (non-standard) diameter of cavity to implement, whereas the others can be made with standard pipe diameters and the length is chosen such that they are tuned. Once a cavity is constructed, the TM_{01n} modes can be fine-tuned using a conducting plunger similar to the one shown in Fig. 3-2.
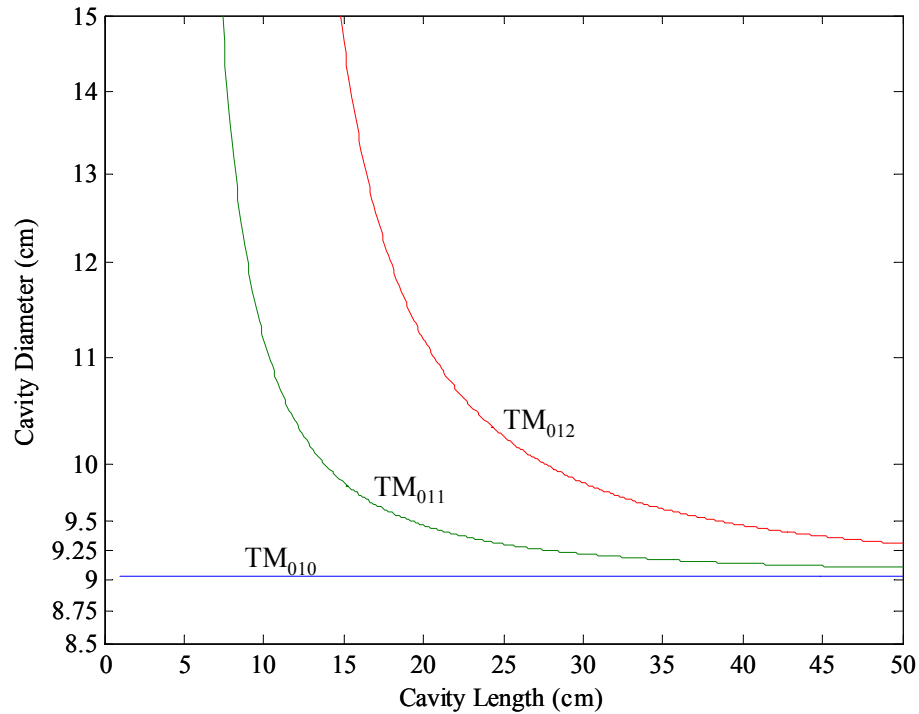
Fig. 3-6: Optimum dimensions for the cylindrical cavity TM modes.

3.5 Summary and References

A small, low power laboratory-scale proof-of-principle demonstration of the microwave thermal thruster is possible, although an exact match between the microwave frequency and high energy density turbulent flow regime of a full-scale system is not. Nevertheless, it is still possible to demonstrate the key physics of microwave thermal propulsion; namely, high flux microwave absorption, heat conduction and convection to a flowing propellant.

Apparatus and approaches developed for microwave sintering are directly applicable to this problem.   There are simplistic assumptions that can be used to size the various components.   While the cavity calculations given in § 3.4.3 are useful for preliminary sizing, they only cover empty cavity modes and the objective here is to include an axial tube. This tube in turn affects the field distribution, and has an analytical solution for the special case of self-similarity along the z-axis (along the length of the tube).

In the case of a strongly heated alumina tube, the resistivity could potentially vary over twelve orders of magnitude along its length.   In the design of practical single mode microwave cavities an effective diameter approach (Metaxas and Meredith, 1983) can also be used; however, it cannot capture the full dynamics of such a cavity, and consequently a numerical model is developed in the next chapter. In subsequent chapters this model forms the basis of the combined electromagnetic-conduction-convection code discussed in the objectives, and finally all the models are compared with measurements from the experiment proposed in the objectives and broadly outlined throughout this chapter.

Alpert, Y. and Jerby, E. (1999). *Coupled thermal-electromagnetic model for microwave heating of temperature-dependent dielectric media*. IEEE Transactions on Plasma Science **27**(2): p. 555–562.

Basak, T. and Ayappa, K.G. (2001). *Influence of internal convection during microwave thawing of cylinders*. AIChe Journal **47**(4): p. 835–850.

Beatty, R.L., Sutton, W.H. and Iskander, M.F. (1992). *Microwave processing of materials III : symposium held April 27-May 1, 1992, San Francisco, CA*, Pittsburgh, PA. Materials Research Society.

Bussard, R.W. and DeLauer, R.D. (1958). *Nuclear rocket propulsion*. McGraw-Hill series in missile and space technology, New York. McGraw-Hill.

Cooper, R.S. (1968). *Nuclear Propulsion for Space Vehicles*. Annual Review of Nuclear Science **18**: p. 203.

Huang, H.F. (1969). *A Microwave Apparatus for Rapid Heating of Threadlines*. Journal of Microwave Power **4**(4).

Iskander, M.F., Kiggans, J.O., Jr. and Bolomey, J.-C. (1996). *Microwave processing of materials V: symposium held April 8–12, 1996, San Francisco, CA*, Pittsburgh, PA. Materials Research Society.

Iskander, M.F., Lauf, R.J. and Sutton, W.H. (1994). *Microwave processing of materials IV: symposium held April 4–8, 1994, San Francisco, CA*, Pittsburgh, PA. Materials Research Society.

Jackson, H.W., Barmatz, M. and Wagner, P. (1994). *Microwave Power Absorption Profile in a Cylindrical Sample Contained in a Resonant Cylindrical Cavity*, in Microwave Processing of Materials IV: Materials Research Society.

Jackson, H.W., Barmatz, M. and Wagner, P. (1995). *Steady State Temperature Profile in a Cylinder Heated by Microwaves*. Ceramic Transactions **59**: p. 279–287.

Jackson, H.W., Barmatz, M. and Wagner, P. (1996). *Transient Temperature Distributions in a Cylinder Heated by Microwaves*, in Microwave Processing of Materials V: Materials Research Society.

Kakaç, S., Shah, R.K. and Aung, W. (1987). *Handbook of Single-Phase Convective Heat Transfer*. Wiley-Interscience.

Knight Jr., B.W., McInteer, B.B., *et al.* (1957). *A metal dumbo rocket reactor*. University of California: Los Alamos. p. 385.

Ma, F. (1999). *Electromagnetic and Thermal Modeling of Microwave Applicators using the Hybrid FDTD Techniques*. Deparment of Electrical and Computer Engineering, The University of New Brunswick, Canada.

Meredith, R.J. (1998). *Engineers' handbook of industrial microwave heating*, London, UK. Institution of Electrical Engineers.

Metaxas, A.C. and Meredith, R.J. (1983). *Industrial Microwave Heating*, London, UK. P. Peregrinus on behalf of the Institution of Electrical Engineers.

Micci, M.M. (1984). *Prospects of microwave heated propulsion*.

Shah, R.K. and London, A.L. (1978). *Laminar flow forced convection in ducts : a source book for compact heat exchanger analytical data*, New York. Academic Press.

Snyder, W.B. (1992). *Microwave processing of materials II*, Pittsburgh, PA. Materials Research Society.

Sutton, W.H., Brooks, M.H. and Chabinsky, I.J. (1988). *Microwave processing of materials : symposium held April 5-8, 1988, Reno, NV*, Pittsburgh, PA. Materials Research Society.

Terril, N.D. (1998). *Field Simulation for the Microwave Heating of Thin Ceramic Fibers*. M.S., Electrical Engineering, Viginia Polytechnic Institute and State University.

Wu, X. (2002). *Experimental and theoretical study of microwave heating of thermal runaway materials*. University Libraries Virginia Polytechnic Institute and State University.

Yiin, T. and Barmatz, M. (1995). *Microwave Induced Combustion Synthesis of Ceramic and Ceramic-Metal Composites*. Ceramic Transactions **59**.

CHAPTER 4
ELECTROMAGNETICS AND THE COUPLED EM-CONDUCTION PROBLEM

4.1   Cylindrical Axisymmetric Electromagnetic Model

The resonant cavity is modeled using FEMLab, a commercial finite element analysis package available from Comsol Inc.

4.1.1   Nomenclature

$\mathbf{E}$	Electric field intensity (vector)
$\mathbf{B}$	Magnetic flux density (vector)
$\mathbf{H}$	Magnetic field intensity (vector)
$\mathbf{D}$	Electric displacement field (vector)
$\mathbf{J}$	Current density of free charges (vector)
ρ	Density of free charge
$\tilde{\epsilon}$	Complex permittivity (absolute)
ϵ'	Real part of the complex permittivity, a.k.a the dielectric constant
ϵ''	Imaginary part of the complex permittivity, a.k.a. the loss factor
μ	Absolute permeability
ω	Angular frequency (of microwaves)
f_0	Resonant cyclic frequency
σ	Electrical conductivity
U	Energy per unit volume
Q	Cavity quality factor
P	Power
Z	Impedance
r	Radial coordinate
z	Axial coordinate
ϕ	Toroidal coordinate
β	Propagation constant

4.1.2 Governing Equations

In the presentation of the governing equations, vector quantities such as **E** and **H** are denoted in bold type, whereas scalar quantities such as μ and σ are denoted in italics. Following the FEMLab reference manual (Anon., 2004) and that of the SUPERFISH cavity code (Warren, 1987), solution of the cavity begins with Maxwell's equations:

$$\nabla \times \mathbf{E} + \partial \mathbf{B}/\partial t = 0 \qquad (4.1)$$
$$\nabla \times \mathbf{H} - \partial \mathbf{D}/\partial t = \mathbf{J} \qquad (4.2)$$
$$\nabla \cdot \mathbf{B} = 0 \qquad (4.3)$$
$$\nabla \cdot \mathbf{D} = \rho \qquad (4.4)$$

To complete the system three constitutive relations are used:

$$\mathbf{D} = \epsilon' \mathbf{E} \qquad (4.5)$$
$$\mathbf{B} = \mu \mathbf{H} \qquad (4.6)$$
$$\mathbf{J} = \sigma \mathbf{E} \qquad (4.7)$$

For the case of an axisymmetric transverse magnetic (TM) cavity mode, shown in Fig. 4-1, the magnetic field has only a φ component, and the electric field components are in orthogonal directions, so that,

$$\mathbf{H}(r,z,t) = H_\phi(r,z)\mathbf{e}_\phi e^{j\omega t}, \qquad (4.8)$$
$$\mathbf{E}(r,z,t) = (E_r(r,z)\mathbf{e}_r + E_z(r,z)\mathbf{e}_z)e^{j\omega t}. \qquad (4.9)$$

Taking the curl of Eq. (4.2) and using the constitutive relations,

$$\nabla \times \nabla \times \mathbf{H} - \nabla \times [(j\omega\epsilon' + \sigma)\mathbf{E}] = 0. \qquad (4.10)$$
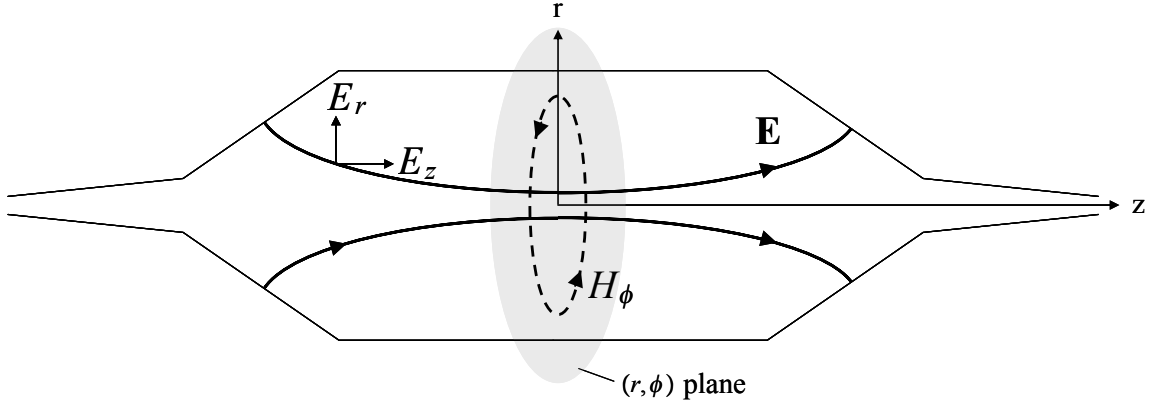
Fig. 4-1: Field lines for a transverse magnetic (TM) mode in a cylindrically symmetric cavity. Note that the electric field must be perpendicular to a conducting boundary.

Defining the complex permittivity to be

$$\tilde{\epsilon} \equiv \epsilon' + \frac{\sigma}{j\omega},$$ (4.11)

and making the relevant substitutions, a Helmholtz equation in H is obtained,

$$\nabla \times \nabla \times \mathbf{H} - \omega^2 \tilde{\epsilon} \mu \mathbf{H} = 0.$$ (4.12)

Using Eq. (4.8) this reduces to the following PDE:

$$\frac{\partial}{\partial r}\left[\frac{1}{r}\frac{\partial}{\partial r}(rH_\phi)\right] + \frac{\partial^2 H_\phi}{\partial z^2} - \omega^2 \tilde{\epsilon} \mu H_\phi = 0.$$ (4.13)

In order to avoid a loss of numerical precision due to the coordinate singularity at the axis, the substitution $u = H/r$ is made, so that,

$$r\frac{\partial}{\partial r}\left(\frac{1}{r}\frac{\partial u}{\partial r}\right) + \frac{\partial^2 u}{\partial z^2} - \omega^2 \tilde{\epsilon} \mu u = 0.$$ (4.14)

Equation (4.14) is the PDE solved by the finite element method (i.e., FEMLab).

4.2 Auxiliary Quantities

4.2.1 Power Losses on Walls

For perfectly conducting walls no power is dissipated. In practise, the walls have finite electrical resistivity ρ and the electric field has a finite skin depth in which it decays exponentially within the conductor, dissipating energy by Joule heating. Since the electric and magnetic field components are related, this heating can be written in terms of its tangential magnetic component, which is the variable solved for in TM cavity modes,

$$P_{wall} = \pi \sqrt{\frac{\mu\omega}{2\rho}} \oint_S H_\phi^2(r,z)r dz . \tag{4.15}$$

4.2.2 Quality Factor

The energy per unit volume U can be expressed in radial coordinates for a TM cavity as

$$U = \frac{\mu}{2} \frac{\int_V H_\phi(r,z)r dr dz}{\int_V r dr dz} . \tag{4.16}$$

The cavity quality factor Q is defined to be 2π times the ratio of the stored energy U to the energy loss per cycle, or equivalently,

$$Q = \frac{2\pi f_0 U}{P} = \frac{f_0}{\Delta f} , \tag{4.17}$$

where P is the power dissipated in both the wall and the load. f_0 is the resonant frequency and Δf is the bandwidth.

For a given cavity geometry and wall material each cavity mode, such as TM_{010}, has a characteristic Q value, several thousand being typical for the experimental parameters of these tests. As cavity losses decrease, the stored energy U increases and hence the Q value increases. Equation (4.16) implies that U is proportional to the square of the electric field, and broadly speaking is proportional to the power absorbed in the lossy dielectric load. Relative to heating in front of a waveguide, for example, a high Q cavity

enables almost microwave transparent materials such as high purity room temperature alumina to be heated. The disadvantage of high Q cavities is that the bandwidth of the resonance becomes narrower too, as described by Eq. (4.17), and this makes finding and maintaining the resonance as the load (tube) heats up difficult in some cases.

4.2.3   Shunt Impedance

In the equivalent circuit/transmission line theory of the microwave heating system, a shunt impedance Z with dimensions of Ω/m represents the cavity. The following crude approximation (Warren, 1987), particularly applicable for the TM_{010} mode, can be used for the purposes of impedance matching, for example in optimizing the shape of an *H-H* coupling aperture,

$$Z = \frac{E_0^2}{P/L}.$$
(4.18)

Rather than attempting to restate the equivalent circuit theory of cavity heating here I refer the reader to the excellent introductions given by Metaxas & Meredith (Meredith, 1998; 1983).

4.2.4   Mesh and Boundary Conditions

Within FEMLab*,* the computational domain is discretized into an irregular mesh of triangular elements, shown in Fig. 4-2. A quadratic Lagrange shape function formulation is used, and values of the magnetic field are interpolated between element nodes (triangle corners) using these functions. More elements are used toward the cavity drive point and dielectric tube because the field gradients can be high in these regions.

An adaptive solver is sometimes used in order to automatically refine the mesh in regions whose properties may be evolving in time. Sometimes the adaptation step is skipped in order to maximize execution speed, depending on the problem at hand and the accuracy of solution required.
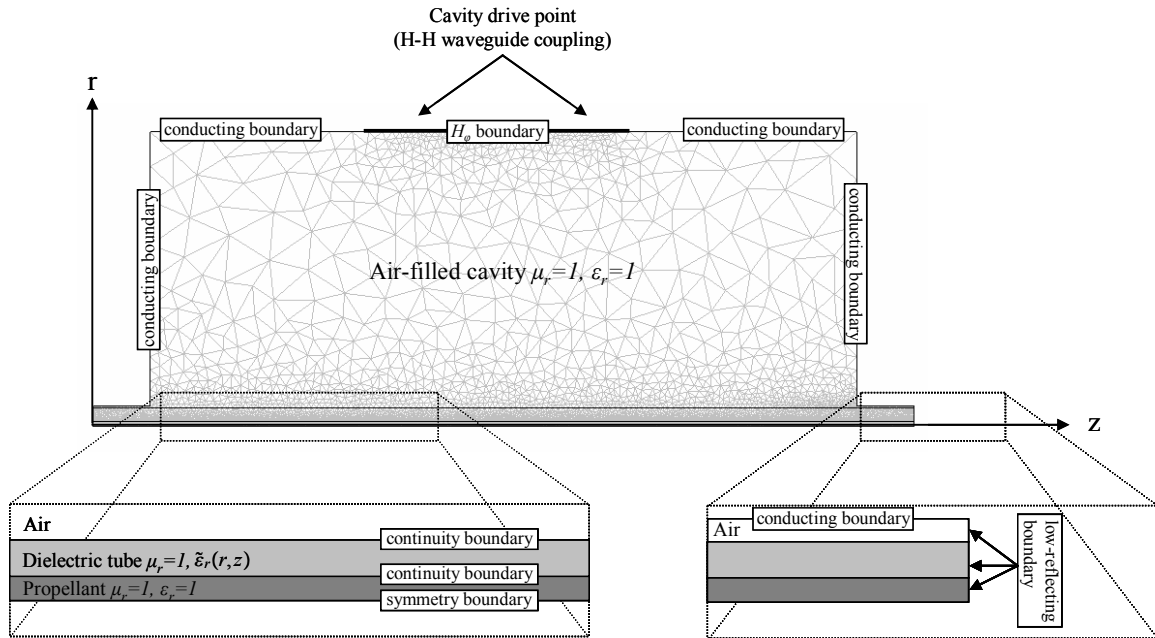
Fig. 4-2: An example mesh with volumetric and boundary conditions for the experimental setup.

The boundary conditions indicated in Fig. 4-2 are summarized in Table 4-10. Conducting boundaries represent the metal cavity walls, and within FEMLab these may be represented as perfectly conducting boundaries or by impedance boundaries, the latter allowing energy losses into the metal walls to be deduced.

Small tubes ("chokes") are used to form the cavity ends through which the dielectric tube passes and serve to reduce microwave leakage in a practical system. Low-reflecting boundaries are used to mimic microwave loss into the outside world.

The dielectric tube is modeled using continuity boundary conditions and in the volumetric sense a complex permittivity $\tilde{\varepsilon}$, the imaginary part of which is the loss factor of the tube, which is inversely proportional to the material resistivity as described by Eq. (4.11). Both the real and imaginary parts of the permittivity are a function of temperature, the imaginary part strongly so, and in general they will vary in both r and z coordinates.

Dielectric tube	Perfect magnetic conductor (PMC)	$\mathbf{n} \times \mathbf{H} = 0$
	Continuity (of tangential components of electric and magnetic fields)	$\mathbf{n} \times (\mathbf{H_1} - \mathbf{H_2}) = 0$ $\mathbf{n} \times (\mathbf{E_1} - \mathbf{E_2}) = 0$
Walls	Perfect electric conductor (PEC) Impedance	$\mathbf{n} \times \mathbf{E} = 0$

$$\sqrt{\frac{\mu}{\epsilon'}}\, \mathbf{n} \times \mathbf{H} + \mathbf{E} - (\mathbf{n} \cdot \mathbf{E})\mathbf{n} = (\mathbf{n} \cdot \mathbf{E}_s)\mathbf{n} - \mathbf{E}_s$$

Drive point — Magnetic field — Matched boundary

$$\mathbf{n} \times \mathbf{H} = \mathbf{n} \times \mathbf{H}_0$$

$$\mathbf{n} \times \nabla \times \mathbf{E} - j\beta[\mathbf{E} - (\mathbf{n} \cdot \mathbf{E})\mathbf{n}] = -2j\beta[\mathbf{E}_0 - (\mathbf{n} \cdot \mathbf{E}_0)\mathbf{n}] - 2j\beta\sqrt{\frac{\mu}{\epsilon'}}\, \mathbf{n} \times \mathbf{H}_0$$

Ends (chokes) — Low reflecting

$$\sqrt{\frac{\mu}{\epsilon'}}\, \mathbf{n} \times \mathbf{H} + \mathbf{E} - (\mathbf{n} \cdot \mathbf{E})\mathbf{n} = 2\mathbf{E}_0 - 2(\mathbf{n} \cdot \mathbf{E}_0)\mathbf{n} + 2\sqrt{\frac{\mu}{\epsilon'}}\, \mathbf{n} \times \mathbf{H}_0$$

Table 4-10: Summary of boundary conditions for the electromagnetic model.

Earlier attempts to construct a cavity model using the SUPERFISH code, which is often used to design microwave cavities for particle accelerators, met with failure because each dielectric region was assumed to have a uniform dielectric constant.   In order to approximate a tube with a spatially varying dielectric constant, the tube was partitioned into many small dielectric cells. This imposed unrealistic surface boundary conditions between adjoining cells, and the cumulative error in the field distribution became acute as the cell size was reduced. In FEMLab, this problem is avoided by specifying the tube as a single region with a complex permittivity which varies spatially throughout the volume.

4.2.5   Results

Using the parameters given in Table 4-11, the TM_{010} mode results are shown in Fig. 4-3. The empty cavity mode shown in Fig. 4-3 occurs at exactly the radius predicted earlier by the empty cavity theory in Fig. 2-2.   Although the empty cavity mode is indeed independent of length, it is highly sensitive to the effective radius of the cavity and

inserting even a thin dielectric tube detunes it. This detuning concentrates the field toward the ends in the above-cutoff case and toward the center in the below-cutoff case.

Tube parameters

Length	20.0 cm
Inner diameter	1.0 mm
Outer diameter	6.0 mm
Material	Alumina

Cavity parameters

Inner Diameter	9.367 cm
Choke end diameter	1.0 cm
Cylindrical main section length	18.0 cm
Choke length (both ends)	1.0 cm
Drive point length	34.036 mm (centered on cavity)
Frequency	2445 MHz

Table 4-11: Model input parameters for the TM_{010} mode.

$|\mathbf{E}|$ $|H_\phi|$
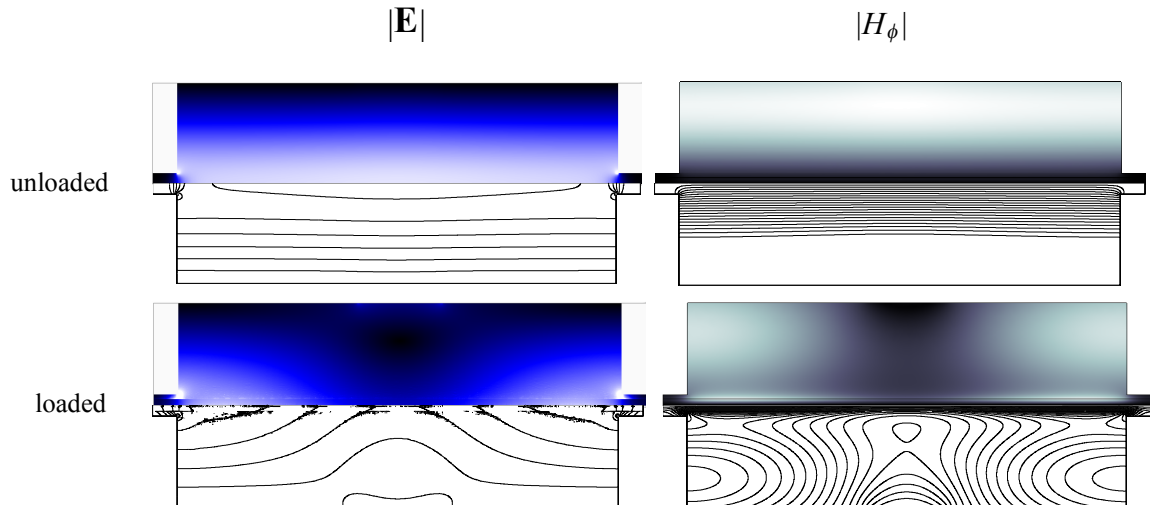
unloaded

loaded

Fig. 4-3: TM_{010} cavity electric and magnetic field distributions for the loaded and unloaded cases. The cavity geometry is as given in Fig. 4-2. The peak electric field occurs on the axis, and within the dielectric tube itself in the loaded case. The peak magnetic field occurs toward the wall; moving away from the cavity drive point in the loaded case. Note that the scale is artificially elongated in the *r* direction.

The TM_{011} and TM_{012} modes are of greater interest for practical experiments because the TM_{010} mode is highly distorted by the alumina tube and because it requires a nonstandard pipe diameter. A cavity radius of 5.08 cm corresponds to a commercially available pipe size, and the correct length for a TM_{011} mode is given in Table 4-12 using the theory given in the previous chapter.

Tube parameters

Length	19.8 cm
Inner diameter	1.59 mm
Outer diameter	3.17 mm (standard tube size)
Material	Alumina

Cavity parameters

Inner Diameter	10.16 cm (standard 4" inner diameter pipe size)
Choke end diameter	1 cm
Cylindrical main section length	15.8 cm
Choke length (both ends)	1.0 cm
Drive point length	34.036 mm (centered on cavity)
Frequency	2445 MHz

Table 4-12: Model input parameters for the TM_{011} mode.

The results in Fig. 4-4 show that the mode is changes little between the loaded (with tube) and unloaded (without tube) cases. This relative insensitivity of the mode to the effective radius of the cavity is also desirable from an experimental point of view, as it implies the mode should also be relatively insensitive as the tube heats up, further increasing the effective radius of the cavity.

|**E**| $|H_\phi|$
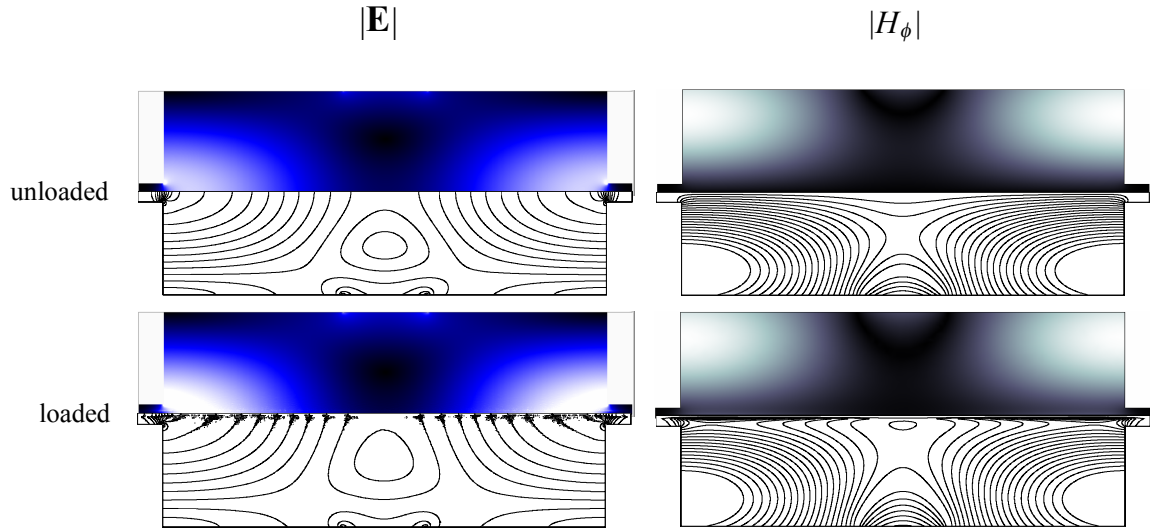
Fig. 4-4: TM$_{011}$ cavity electric and magnetic field distributions for the loaded and unloaded cases. The cavity geometry is as given in Fig. 4-2. The peak electric field occurs around the sharp corners at the cavity ends.

4.2.6 Sensitivity of the Solution to Boundary Condition Type

In this section, various boundary conditions and geometrical factors are perturbed one at a time relative to a baseline case in order to understand the sensitivity of the predicted electric field to assumptions make in the boundary conditions are real-world uncertainties in cavity fabrication. The results of this analysis are used to determine the tolerances with which to fabricate a resonant cavity and to qualitatively understand the effects of the imperfections that inevitably do arise.

Baseline Case

The baseline case is a tapered TM$_{011}$ cavity, similar to the experimental cavity shown in Fig. 7-3, with the parameters given in Table 4-13. The resulting electric field is given in Fig. 4-5. The cavity is thereafter perturbed in various ways, and Figs. 4-6 to 4-18 document the ways in which the field distribution shifts in response.

Length	36.6 cm
Inner diameter	1.19 mm
Outer diameter	1.98 mm
Material	Mullite
Input power	100 W for all cases
Tube temperature	300 K uniform

Cavity parameters

Inner Diameter	10.3 cm
Taper end diameter	2 cm
Choke end diameter	0.7 cm
Cylindrical main section length	14.7 cm
Left taper length	5.2 cm
Right taper length	5.2 cm
Choke length (both ends)	5.75 cm
Drive point length	25.527 mm (75% of waveguide height)
Offset from center of cylindrical main section	0 cm (centered)
Frequency	2440 MHz

Numerical parameters

Electromagnetic finite element mesh configuration	Adaptive, using 50,000–150,000 elements
Drive point boundary condition type	H specified only

Table 4-13: Baseline input parameters for the tapered TM_{011} sensitivity analysis.
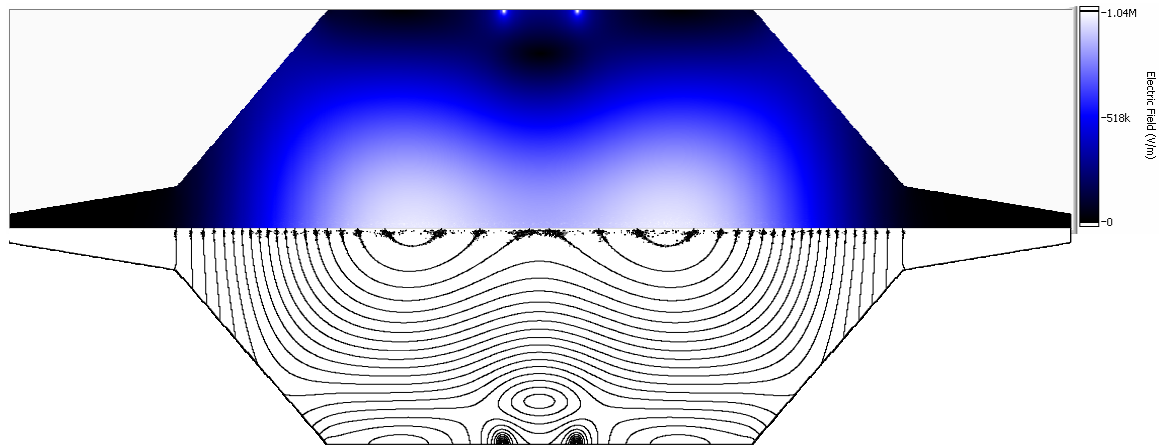
Fig. 4-5: Tapered TM_{011} cavity electric field for the parameters given in Table 4-13. In the lower contour plot, each contour represents 5% of the peak electric field near the axis. The peak electric field overall occurs at the edges of the cavity drive point (two white dots at the top of the plot).

Off-Center Drive Point
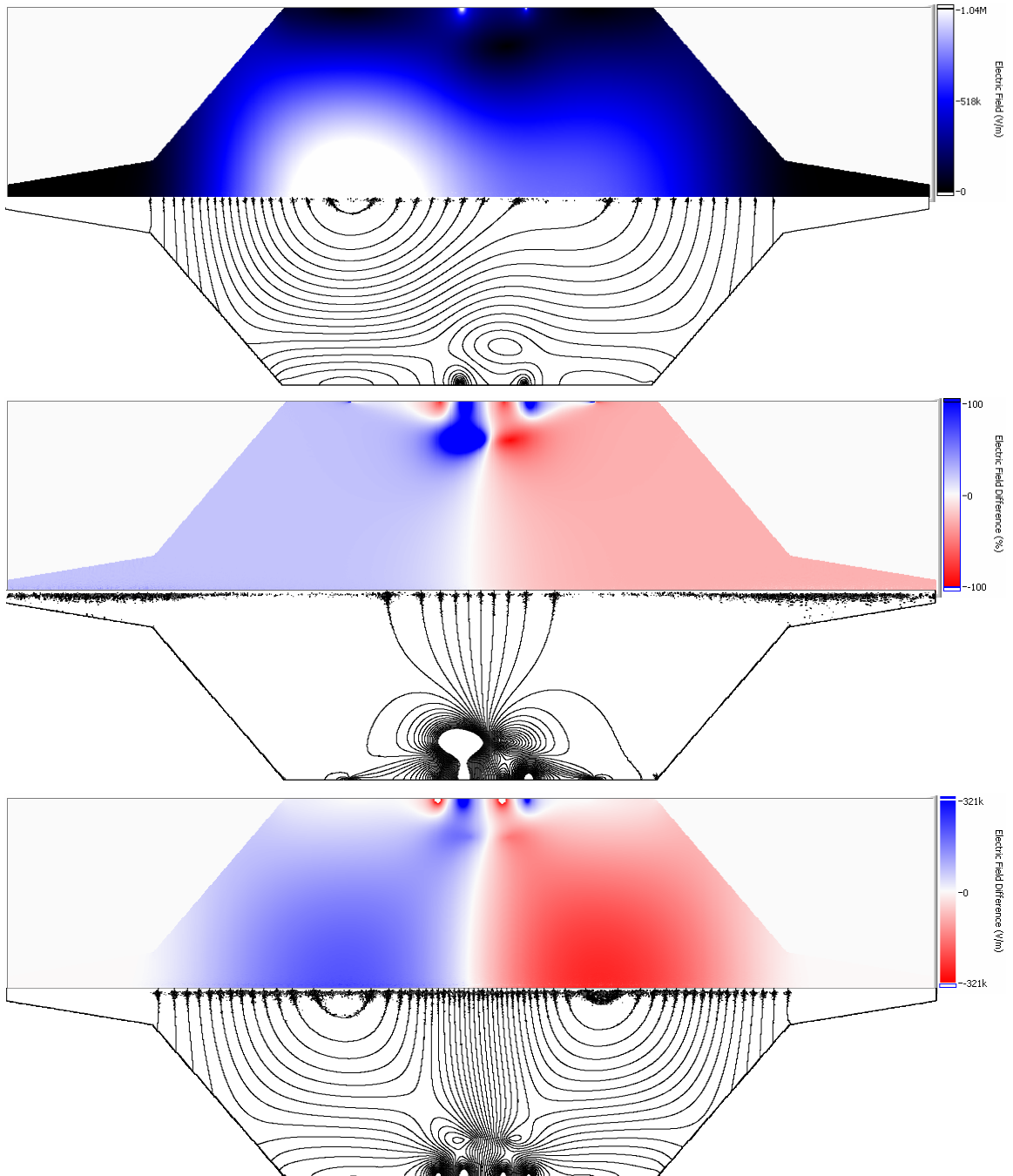
Fig. 4-6: Tapered TM_{011} cavity electric field for a drive point displaced 1 cm to the right relative to the baseline case. Contours represent 5% intervals, 5% of the maximum field in the near axis region for the top and bottom plots.

Drive Point Size
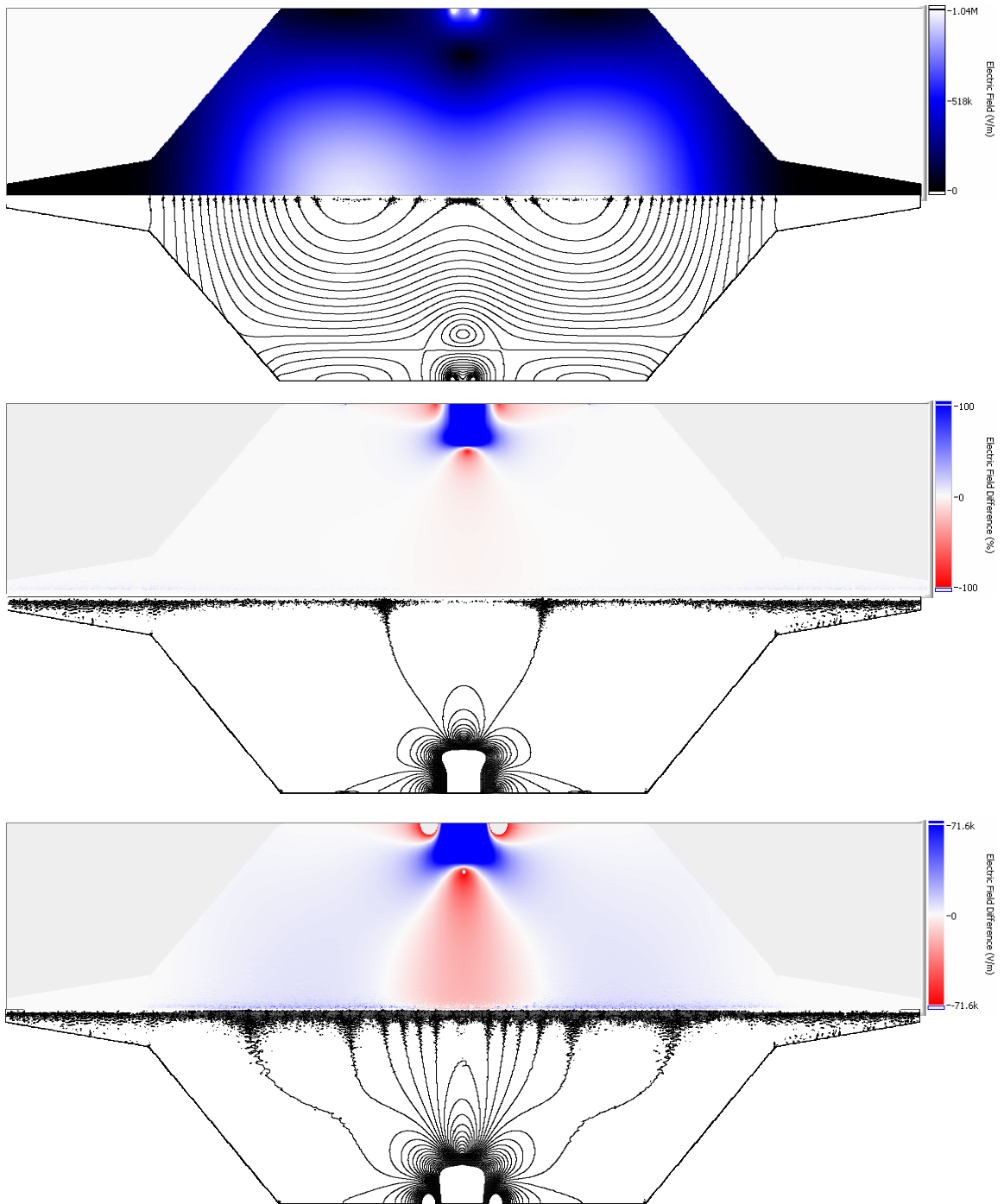
Fig. 4-7: Tapered TM_{011} cavity electric field for a drive point length 25% of maximum relative to the 75% baseline case. Contours represent 5% intervals, 5% of the maximum field in the near axis region for the top and bottom plots.
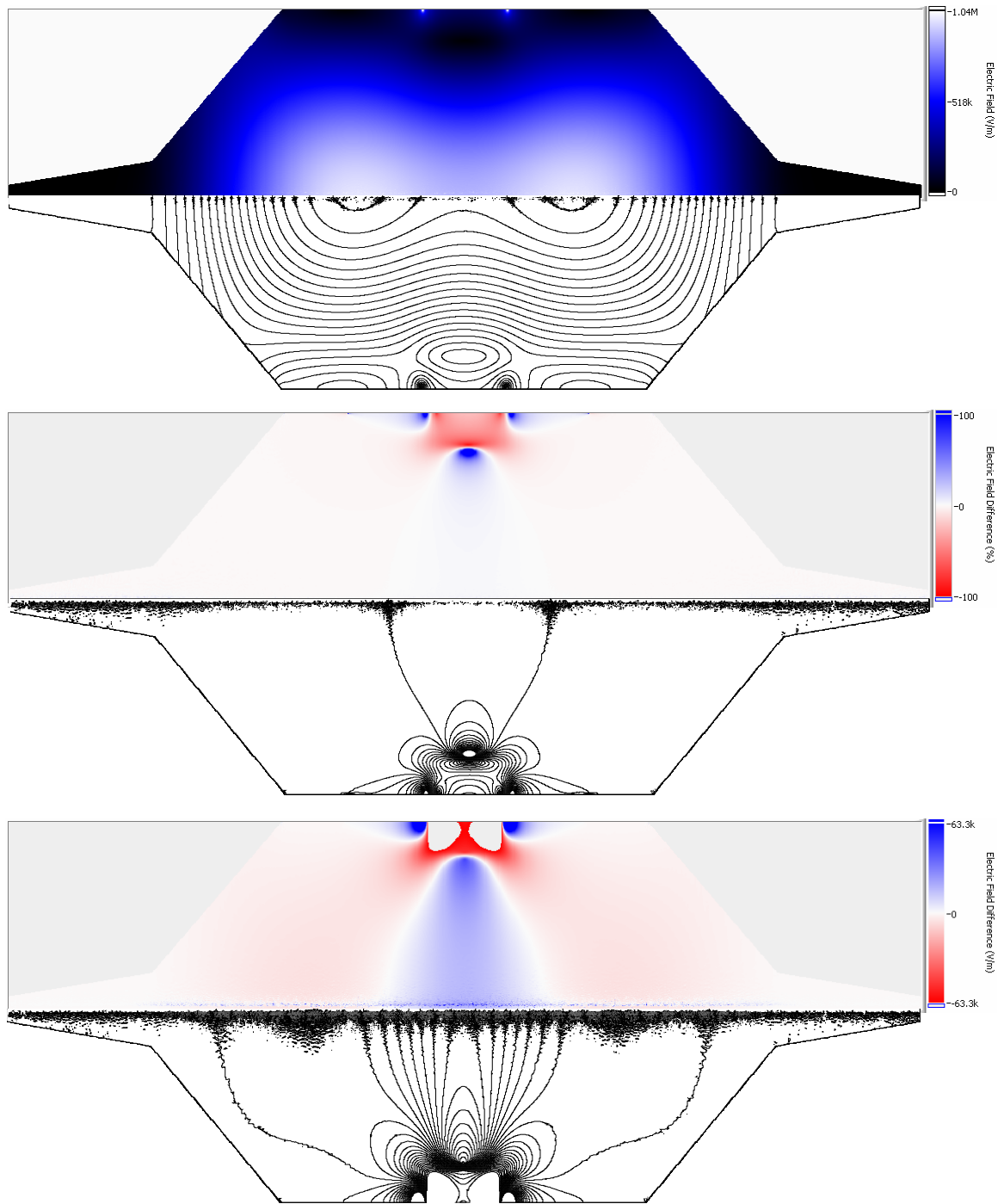
Fig. 4-8: Tapered TM_{011} cavity electric field for a drive point length 100% of maximum relative to the 75% baseline case. Contours represent 5% intervals, 5% of the maximum field in the near axis region for the top and bottom plots.

Taper End Diameter
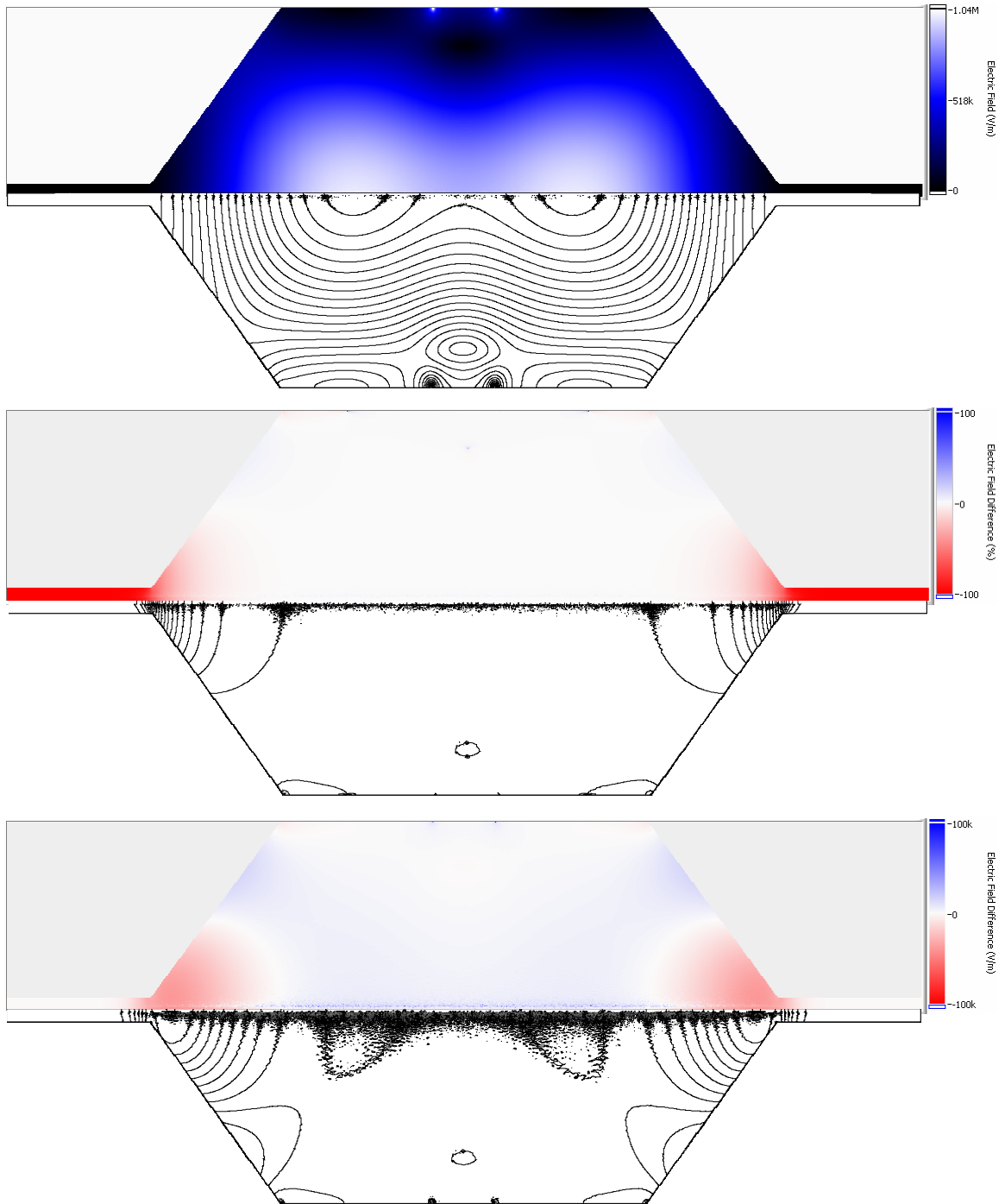
Fig. 4-9: Tapered TM_{011} cavity electric field for a taper end diameter of 0.7 cm relative to the 2 cm baseline case. Contours represent 5% intervals, 5% of the maximum field in the near axis region for the top and bottom plots.
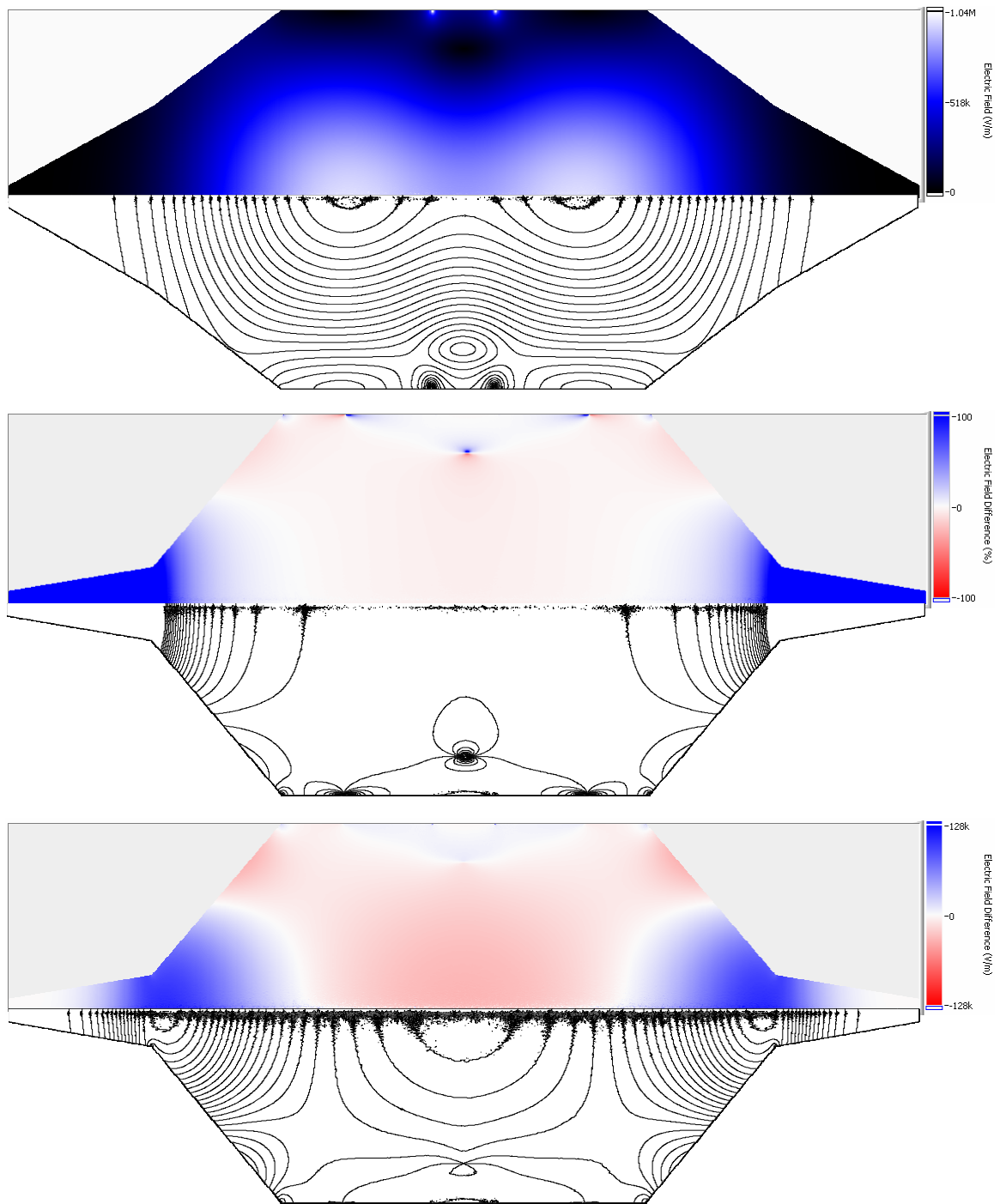
Fig. 4-10: Tapered TM_{011} cavity electric field for a taper end diameter of 5 cm relative to the 2 cm baseline case. Contours represent 5% intervals, 5% of the maximum field in the near axis region for the top and bottom plots.

Tube Radius
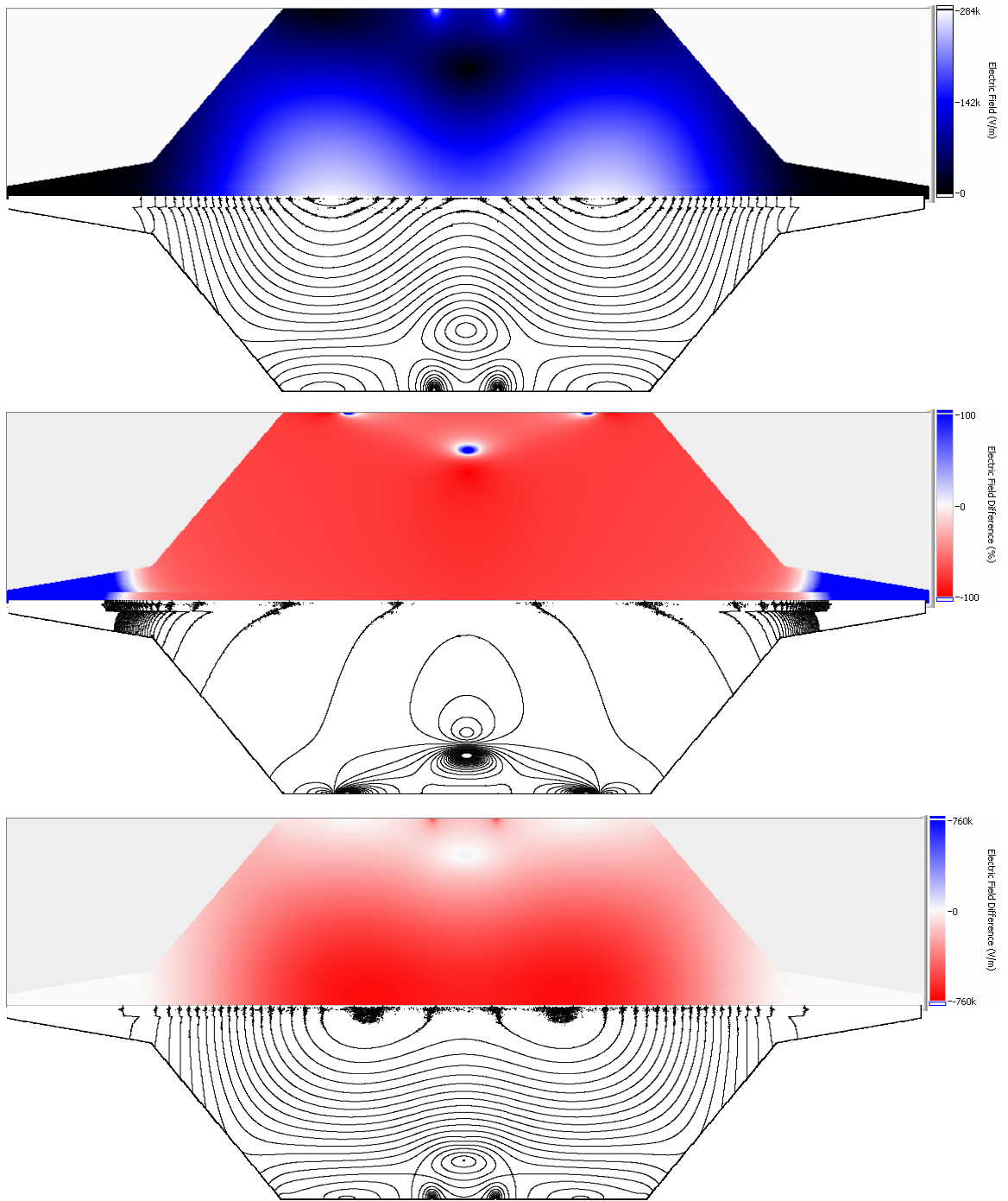
Fig. 4-11: Tapered TM_{011} cavity electric field for a mullite tube outer diameter of 6 mm relative to the 1.98 mm baseline case.   Contours represent 5% intervals, 5% of the maximum field in the near axis region for the top and bottom plots.
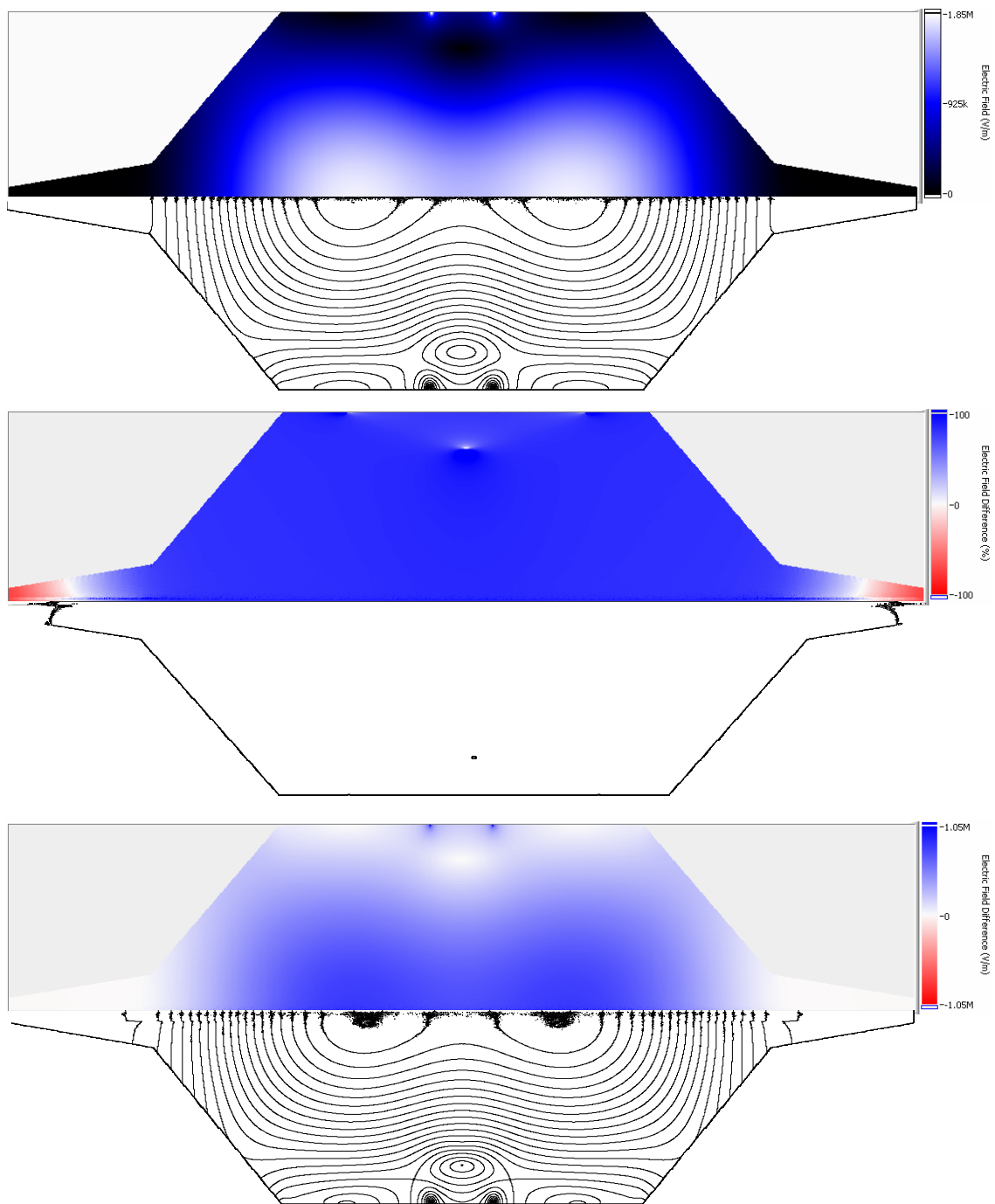
Fig. 4-12: Tapered TM_{011} cavity electric field for a mullite tube outer diameter of 1 mm relative to the 1.98 mm baseline case. Contours represent 5% intervals, 5% of the maximum field in the near axis region for the top and bottom plots.

Asymmetric Taper
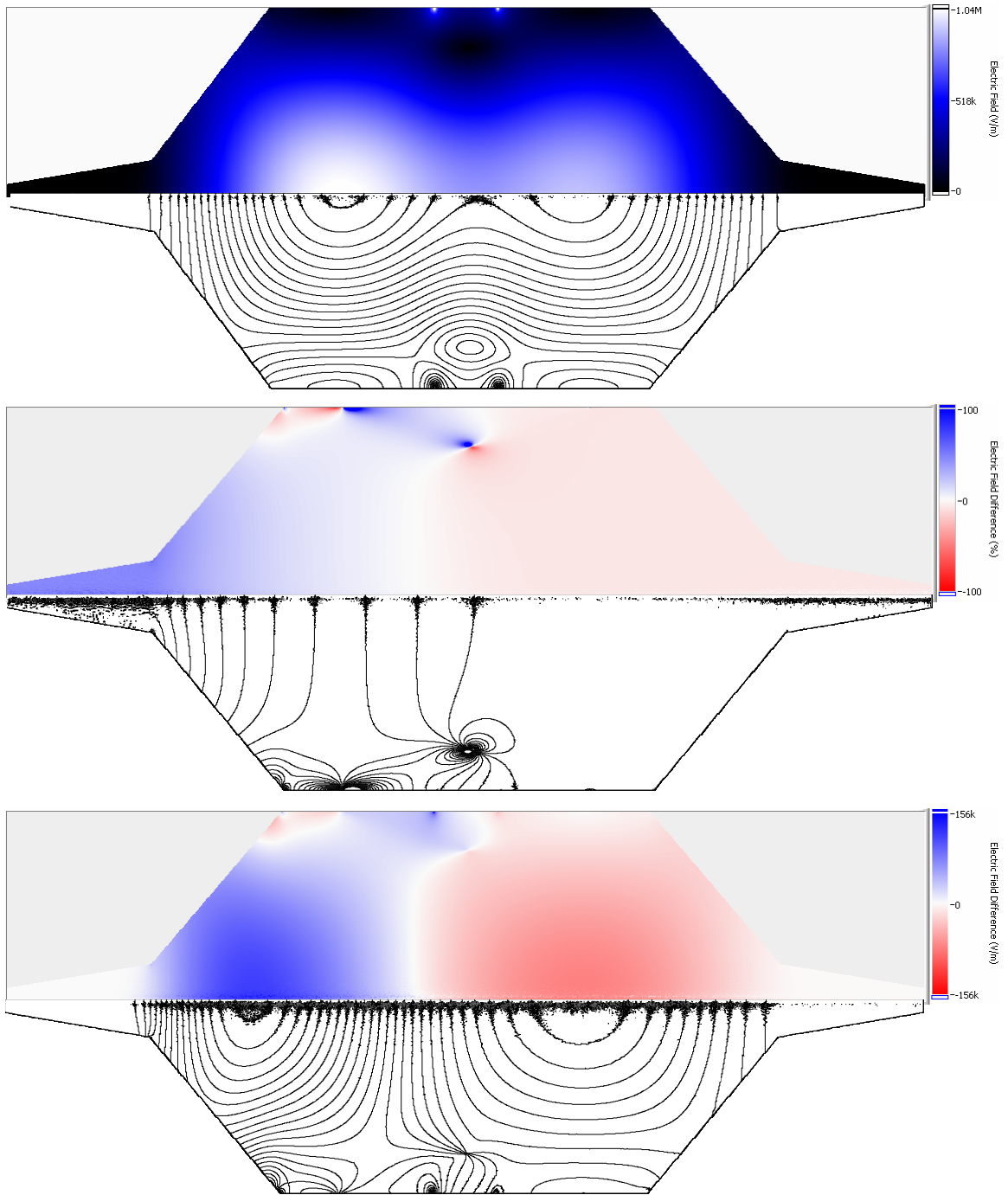
Fig. 4-13: Tapered TM_{011} cavity electric field for a left taper length of 4.8 cm relative to the 5.2 cm baseline case. Contours represent 5% intervals, 5% of the maximum field in the near axis region for the top and bottom plots.

Cavity Radius
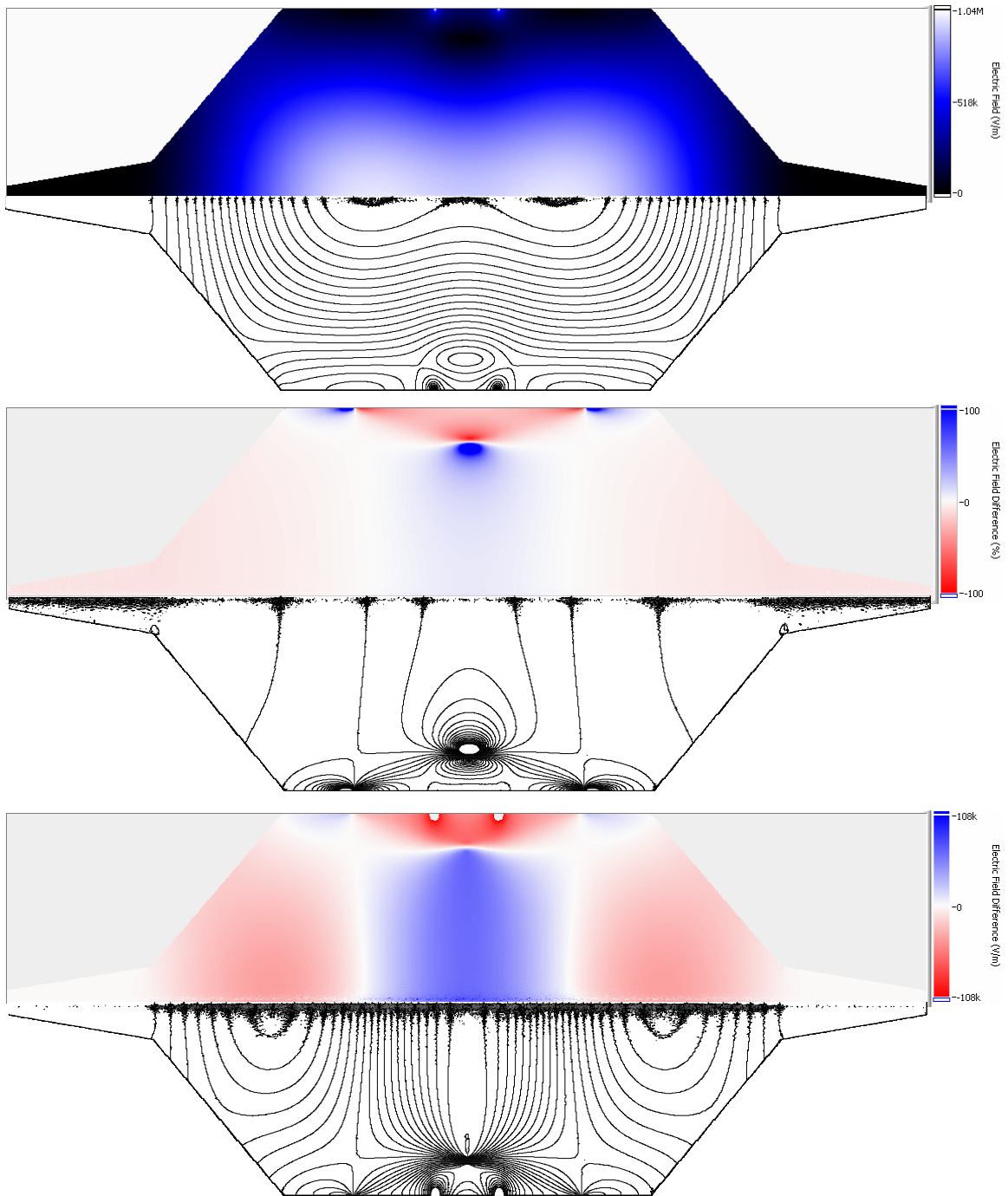
Fig. 4-14: Tapered TM_{011} cavity electric field for a cavity radius of 5.08 cm relative to the 5.15 cm baseline case. Contours represent 5% intervals, 5% of the maximum field in the near axis region for the top and bottom plots.

Perfect Magnetic Conducting Tube
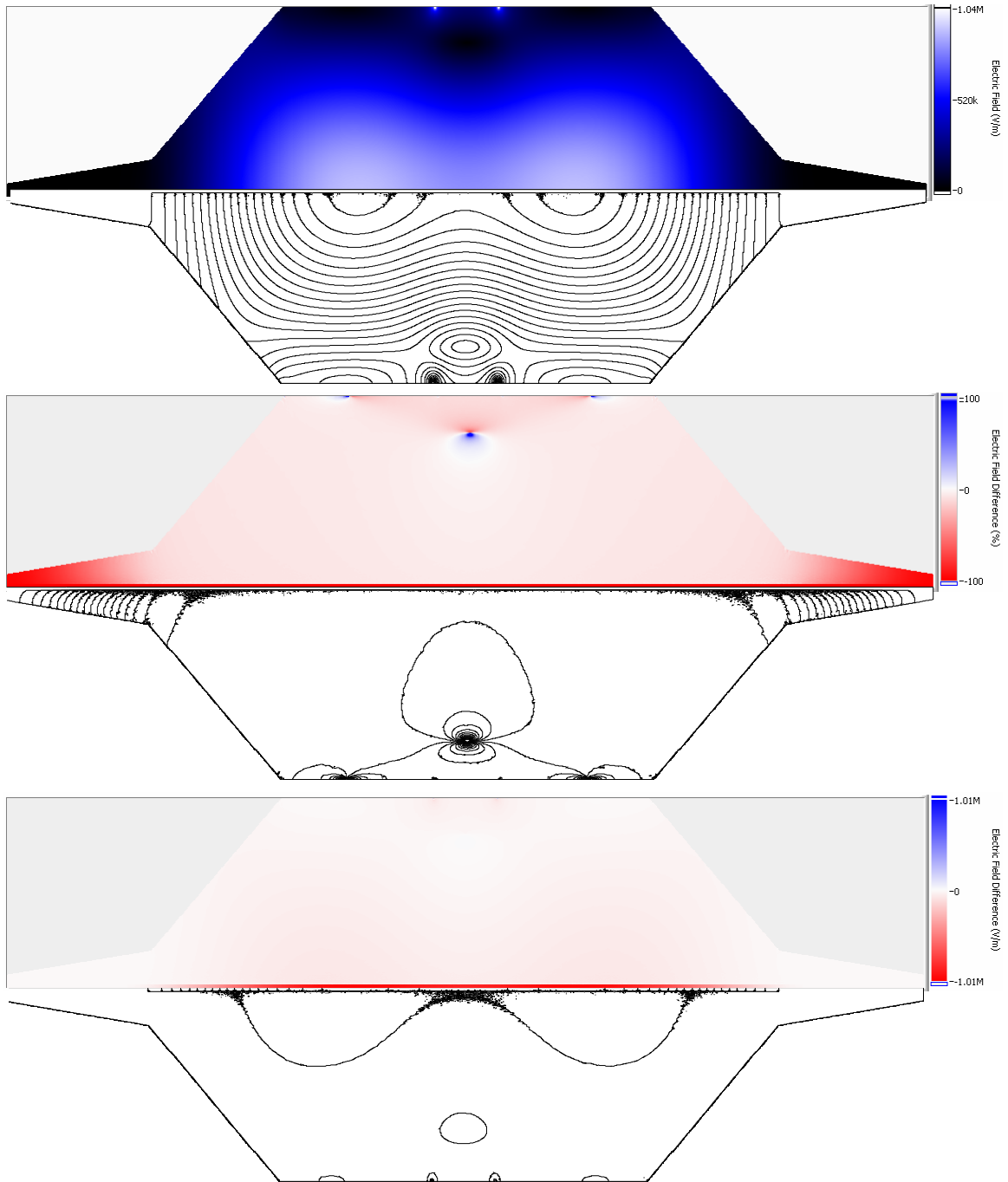
Fig. 4-15: Tapered TM$_{011}$ cavity electric field for a tube modeled as a perfect magnetic conductor (PMC) relative to the baseline case using a continuity boundary condition. Contours represent 5% intervals, 5% of the maximum field in the near axis region for the top and bottom plots.

Perfect Electric Conducting Ends
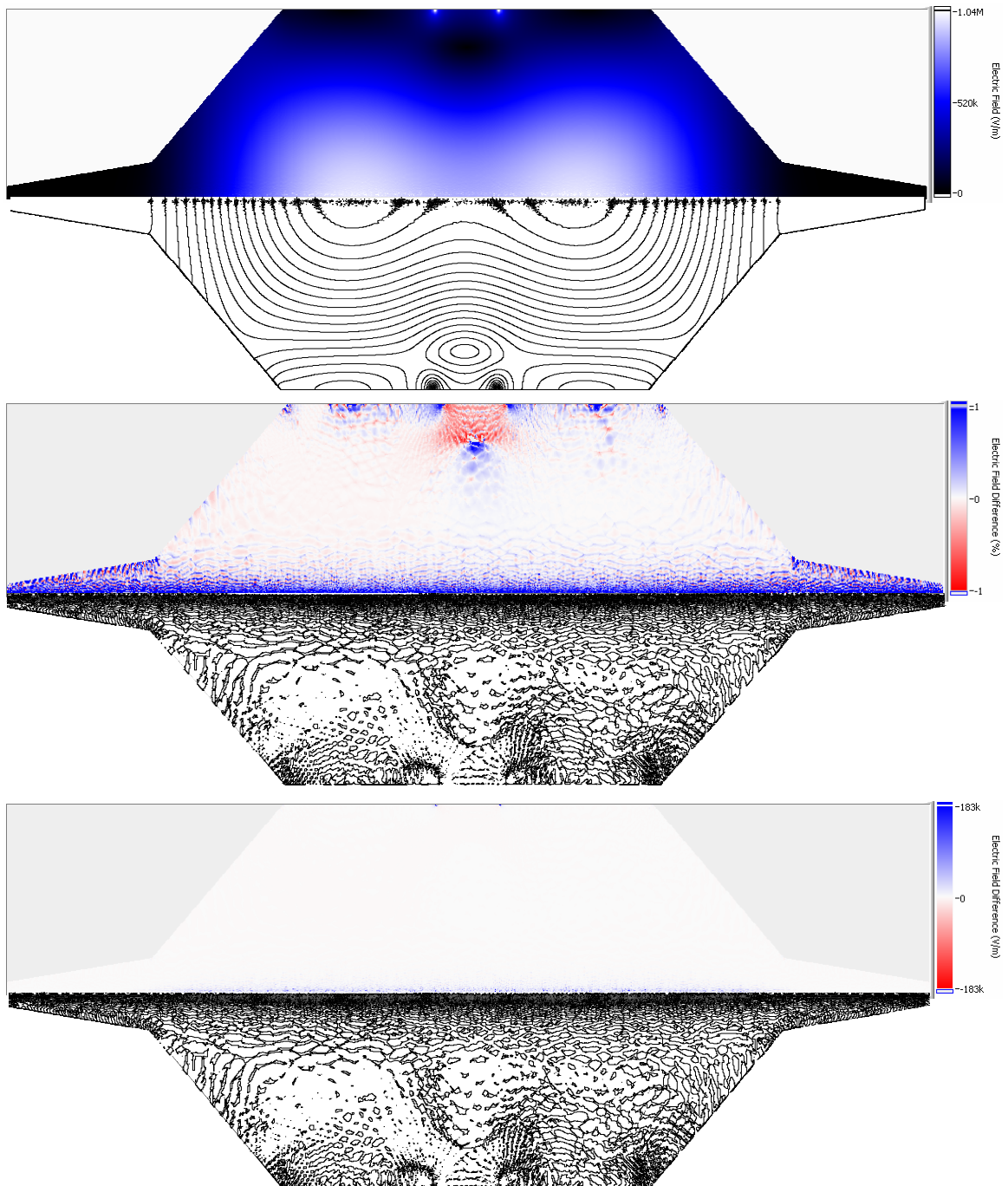
Fig. 4-16: Tapered TM_{011} cavity electric field for the case of perfect electric conducting (PEC) boundaries at either end relative to the baseline case using low reflecting boundaries to represent radiation to the outside. Contours represent 5% intervals, 5% of the maximum field in the near axis region for the top and bottom plots.

Finite Conductivity

Using an impedance boundary condition in place off all PEC boundary conditions and the conductivity of brass, there is a negligible difference in the cavity fields and the results are similar to those presented for the case of PEC ends.

Cavity Length
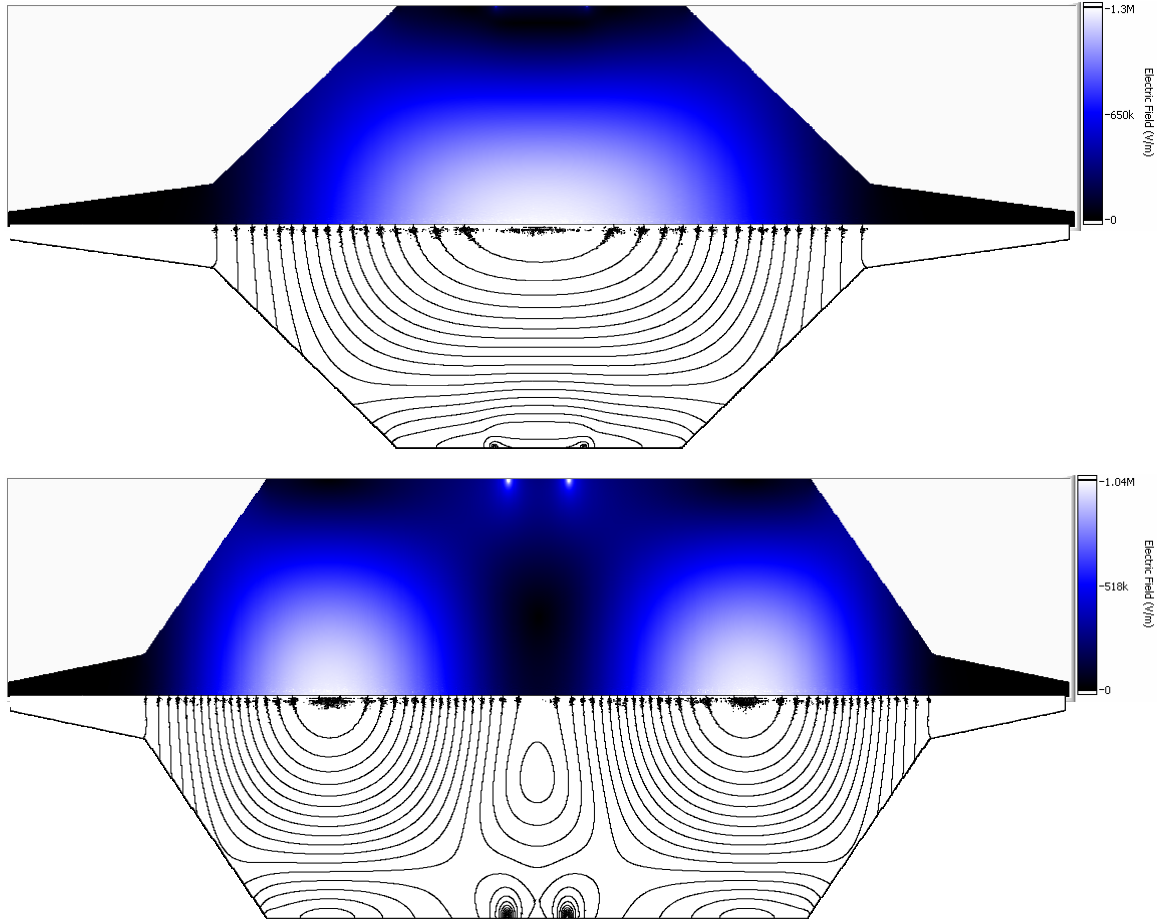
Fig. 4-17: Top: Tapered TM_{011} cavity electric field for a central section length of 8.1 cm relative to the 15.8 cm baseline case. Bottom: Tapered TM_{011} cavity electric field for a central section length of 8.1 cm relative to the 15.8 cm baseline case. Contours represent 5% of the maximum field in the near axis region.

Drive Point Boundary Condition
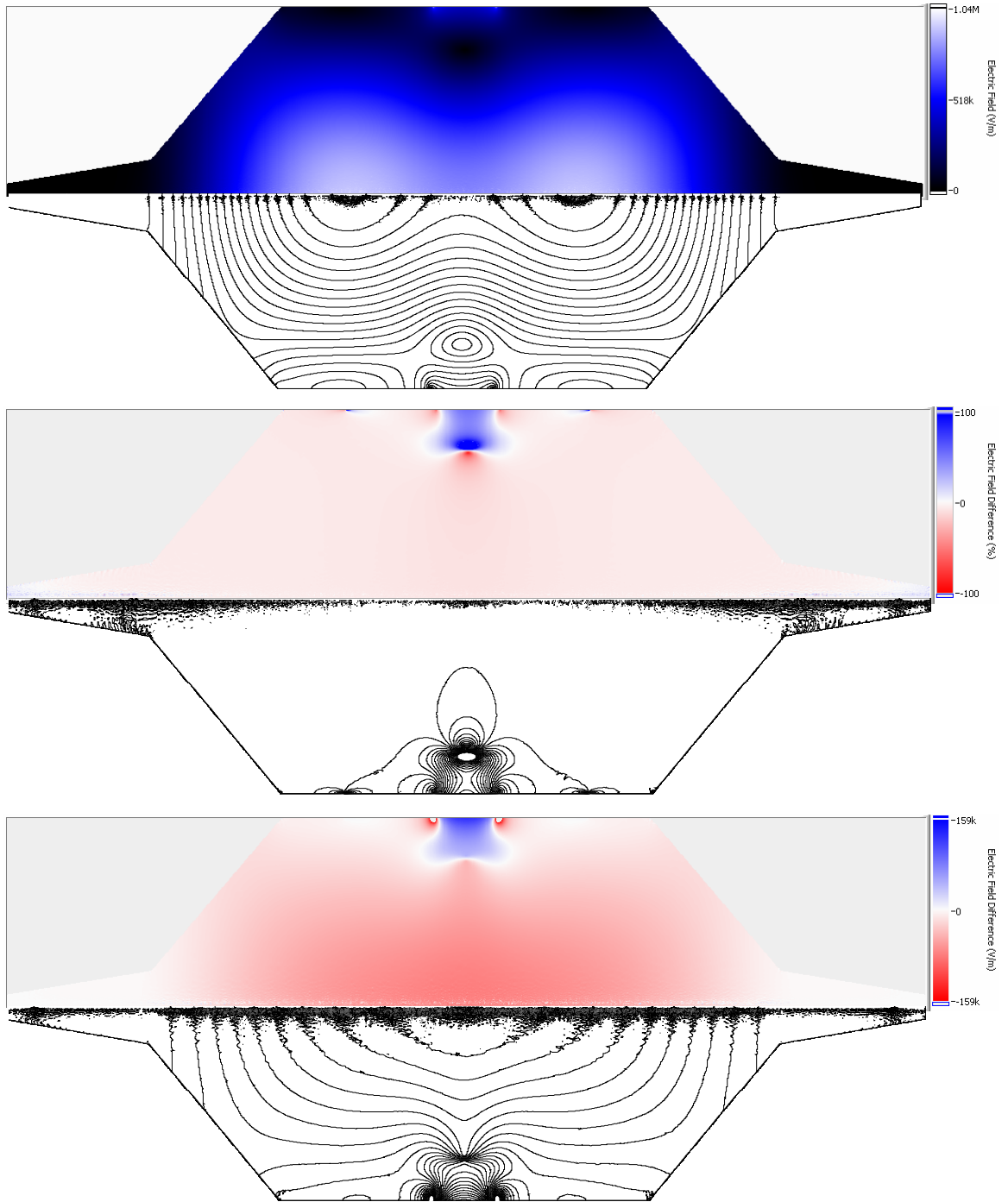
Fig. 4-18: Tapered TM_{011} cavity electric field for the case of a matched boundary with incident wave propagation constant $\beta = 32$ m^{-1} relative to the baseline case using a fixed *H* condition. Contours represent 5% intervals, 5% of the maximum field in the near axis region for the top and bottom plots.

In this test, the *H* boundary condition for the drive point replaces a matched boundary condition in which both *H* and a propagation constant for the incident mode are specified. The incident mode from the waveguide feed is assumed to be predominantly a TE_{10} mode with a commensurate propagation constant of 32 m^{-1}.

4.3   Nonlinear Conduction Model

4.3.1   Governing Equations

In general, the unsteady nonlinear conduction problem may be represented in radial coordinates as

$$\rho c_v(T)\frac{\partial T}{\partial t} = \frac{1}{r}\frac{\partial}{\partial r}\left[rk(T)\frac{\partial T}{\partial r}\right] + \frac{\partial}{\partial z}\left[k(T)\frac{\partial T}{\partial z}\right] + q_v(T), \qquad (4.19)$$

where,

$$q_v(\mathbf{E}, T) = \omega \epsilon_0 \epsilon''(T)\mathbf{E} \cdot \mathbf{E}^*. \qquad (4.20)$$

Although only the steady state solution is of interest, an iterative solution scheme is needed due the nonlinear conduction term *k(T)*. The iterative scheme used here is the false transient method (Özisik, 1994), in which the time-dependent problem is solved with a variable heat capacity such that the solution evolves toward steady state at the maximum rate permitted by the stability of the scheme. In practice, this means that the tube material behaves as if it has low thermal inertia.

For this nonlinear conduction problem, the steady state solution is in general non-unique. For example, owing to the particular nonlinear material properties of alumina (Appendix B) Jackson & Barmatz (1991) have demonstrated temperature hysteresis in an alumina sphere heated by microwaves, shown in Fig. 4-19.
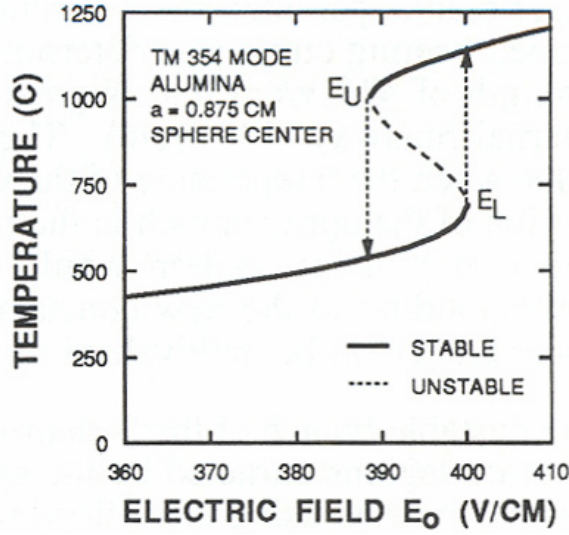
Fig. 4-19: An example of non-unique temperature behavior at the center of a microwave heated alumina sphere (Jackson and Barmatz, 1991). Solutions arising from the nonlinear conduction code would be expected to behave in a similar way.

Equation (4.19) is discretized spatially using an explicit second-order finite difference scheme and temporally by simple time marching. Because the thermal gradients can be very large, the thermal conductivity term remains inside the derivative for discretization,

$$\frac{1}{r}\frac{\partial}{\partial r}\left[rk(T)\frac{\partial T}{\partial r}\right] = \frac{1}{r}\frac{\partial}{\partial r}\left[rk_{i+1/2}\frac{T^n_{i+1,j}-T^n_{i,j}}{2dr} - rk_{i-1/2}\frac{T^n_{i,j}-T^n_{i-1,j}}{2dr}\right], \qquad (4.21)$$

where $k_{i\pm1/2}$ represents the average of the thermal conductivity between the two neighboring points. Hence, Eq. (4.19) becomes,

$$\frac{\rho c_v}{dt}\left(T^{n+1}_{i,j} - T^n_{i,j}\right) = \begin{bmatrix} \frac{k_{i+1/2,j}\left(T^n_{i+1,j}-T^n_{i,j}\right)+k_{i-1/2,j}\left(T^n_{i-1,j}-T^n_{i,j}\right)}{(dr)^2} + \frac{k_{i,j}}{a+idr}\frac{T^n_{i+1,j}-T^n_{i-1,j}}{2dr} \\ + \frac{k_{i,j+1/2}\left(T^n_{i,j+1}-T^n_{i,j}\right)+k_{i,j-1/2}\left(T^n_{i,j-1}-T^n_{i,j}\right)}{(dz)^2} \end{bmatrix} + g^n_{i,j}. \qquad (4.22)$$

Letting,

$$\alpha = \frac{k_{i,j}}{\rho C_p}, \quad \beta_r = \frac{\alpha\Delta t}{dr^2}, \quad \beta_z = \frac{\alpha\Delta t}{dz^2}. \qquad (4.23)$$

Equation (4.22) becomes,

$$T_{i,j}^{n+1} - T_{i,j}^n = \beta_r \left(\frac{k_{i+1/2,j}\left(T_{i+1,j}^n - T_{i,j}^n\right) + k_{i-1/2,j}\left(T_{i-1,j}^n - T_{i,j}^n\right)}{k_{i,j}} + \frac{dr}{a+idr}\frac{T_{i+1,j}^n - T_{i-1,j}^n}{2} \right) + \frac{\alpha \Delta t\, g_{i,j}^n}{k_{i,j}}. \quad (4.24)$$
$$+ \beta_z \frac{k_{i,j+1/2}\left(T_{i,j+1}^n - T_{i,j}^n\right) + k_{i,j-1/2}\left(T_{i,j-1}^n - T_{i,j}^n\right)}{k_{i,j}}$$

For stability,

$$\beta_r + \beta_z \leq \tfrac{1}{2}, \quad (4.25)$$

which implies a timestep of,

$$\alpha \Delta t \leq \frac{1}{2\left(\frac{1}{dr^2} + \frac{1}{dz^2}\right)}. \quad (4.26)$$

Note that this result is derived from standard linear stability analysis. For a strongly nonlinear case the stability criterion becomes a function of temperature (Richtmyer and Morton, 1967). For the false transient method a pseudo-time $\Delta t' = \alpha \Delta t$ is created, so that,

$$T_{i,j}^{n+1} = T_{i,j}^n + \Delta t' \left[\frac{1}{dr^2}\left(\frac{k_{i+1/2,j}\left(T_{i+1,j}^n - T_{i,j}^n\right) + k_{i-1/2,j}\left(T_{i-1,j}^n - T_{i,j}^n\right)}{k_{i,j}} + \frac{dr}{a+idr}\frac{T_{i+1,j}^n - T_{i-1,j}^n}{2} \right) + \frac{g_{i,j}^n}{k_{i,j}} \right]. \quad (4.27)$$
$$+ \frac{1}{dz^2}\frac{k_{i,j+1/2}\left(T_{i,j+1}^n - T_{i,j}^n\right) + k_{i,j-1/2}\left(T_{i,j-1}^n - T_{i,j}^n\right)}{k_{i,j}}$$

Equation (4.27) is iterated until steady state is reached.

4.3.2 Boundary conditions

Ghost cells implement the boundary conditions shown in Fig. 4-20, and Eqs. (4.28)–(4.31) summarize these boundary conditions. In practice, q is determined by radiative and convective heat transfer expressions at $r = b$. At the inside surface $r = a$, q is also determined by a combination of the surface temperature at the previous timestep and external factors.
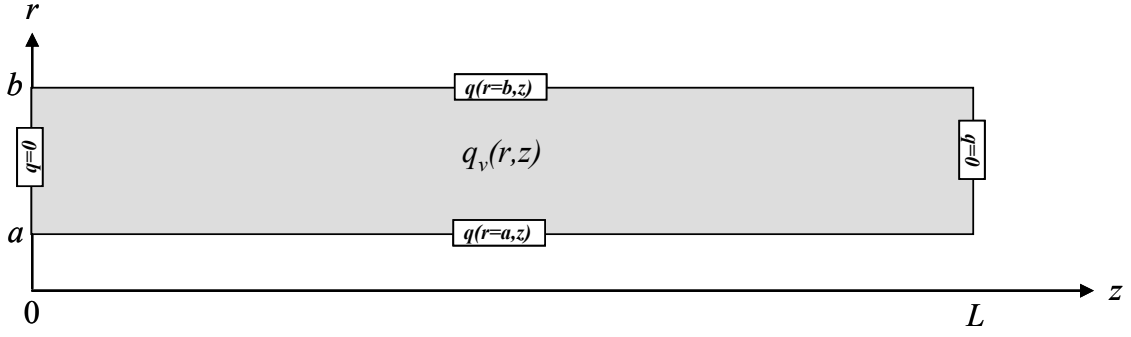
Fig. 4-20: All-flux boundary and volumetric conditions for the nonlinear conduction problem in a tubular geometry. In general, these conditions depend upon the temperature distribution $T(r,z)$ calculated at the previous timestep.

$r = a, b$:
$$k_{i,j} \frac{T_{i+1,j}^n - T_{i-1,j}^n}{2dr} = \pm q \qquad (4.28)$$

$r = a$:
$$T_{i-1,j}^n = T_{i+1,j}^n + 2dr\frac{q}{k_{i,j}} \qquad (4.29)$$

$r = b$:
$$T_{i+1,j}^n = T_{i-1,j}^n + 2dr\frac{q}{k_{i,j}} \qquad (4.30)$$

$z = 0, L$:
$$T_{i,j+1}^n = T_{i,j-1}^n \qquad (4.31)$$

4.4   Combined Electromagnetic-Conduction Model

The electromagnetic and conduction models presented separately above are now coupled via their volumetric terms. This volumetric coupling is depicted in Fig. 4-21.

In the conduction domain, the volumetric heating, calculated from the cavity electric field, is used as the internal heat generation term $g_{i,j}$. With this heat generation term the conduction model updates the temperature distribution, and using a temperature-dependent model of the tube material recalculates the complex dielectric constant over the tube. This is then used in the next recalculation of the electric field distribution.

In principle the coupled models iterate back and forth sequentially; however, the electromagnetic model is time-independent and experimentation suggests that a field recalculation every several hundred iterations of the conduction model suffices in practice for the model parameters of interest here. If the electric field recalculation is too

infrequent the solution oscillates as the temperature distribution shifts to be consistent with one field configuration and then the field changes substantially on the next update.
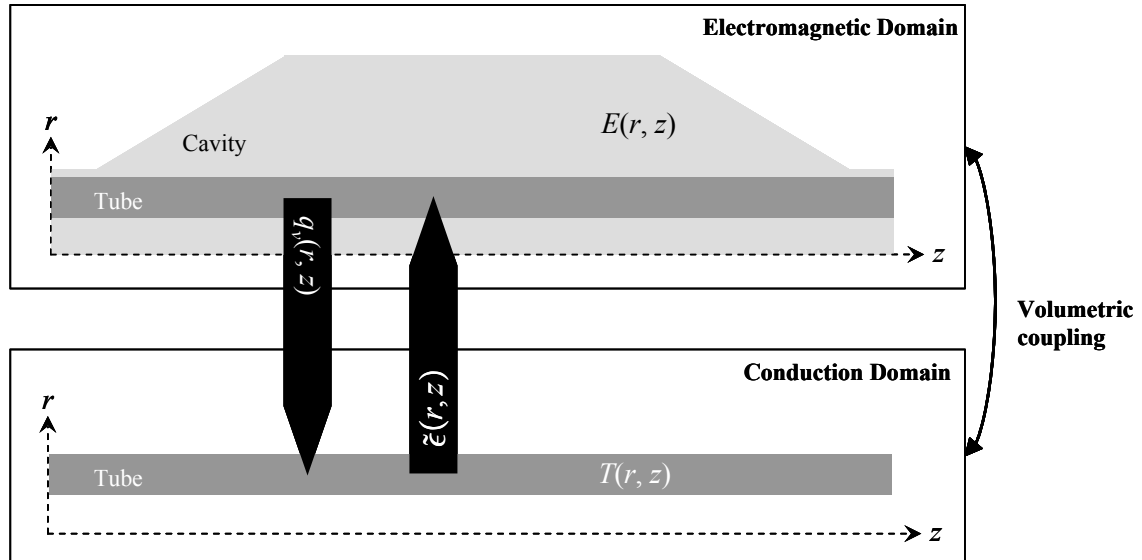
Fig. 4-21: The coupled electromagnetic-conduction problem.

To exclude the complicated problem of cavity tuning, the field is normalized on each timestep such that a specified total power is absorbed by the cavity. By using the matched boundary condition at the drive point and impedance boundary conditions for metal walls, a given input power may be specified, and its absorption in the rod and the walls or reradiation through the chokes can be monitored as the solution progresses. In the conduction model, the energy absorbed from the microwave field is in turn lost from the radiative boundary condition at the outer surface of the tube, which uses a temperature-dependent emissivity for the material chosen.

4.4.1 Results

Heating of the dielectric rod does indeed alter the field distribution and vice versa; however, for the modes presented here the fields are relatively stable as the solution proceeds. Using the parameters given in Table 4-14 the simulation evolves in pseudo-time toward a steady state solution, as shown in Fig. 4-22. The simulation itself

determines the way in which the cavity input power is partitioned between tube heating and wall heating. This partitioning of power changes as the tube heats up, causing the Q value of the tube to drop and the power absorbed in the tube to increase. Since energy is conserved, this implies that the power dissipated in the walls decreases. In turn, the extra power absorbed in tube heats it further, and in this way the tube becomes the dominating microwave load.

Tube parameters	
Length	19 cm
Inner diameter	1.59 mm
Outer diameter	3.17 mm
Material	Alumina

Cavity parameters	
Inner Diameter	10.3 cm
Choke diameter	1 cm
Cylindrical main section length	14.7 cm
Choke length (both ends)	1 cm
Drive point length	34.036 mm (100% of waveguide height)
Offset from center of cylindrical main section	0 cm (centered)
Frequency	2445 MHz
Input power	200 W

Numerical parameters	
Electromagnetic finite element mesh configuration	Adaptive, using 50,000–150,000 elements
Drive point boundary condition type	Matched using propagation constant $\beta = 32 \ \text{m}^{-1}$
(r, z) grid points for tube	(16, 1000)

Table 4-14: Input parameters for the TM_{011} EM-conduction problem.
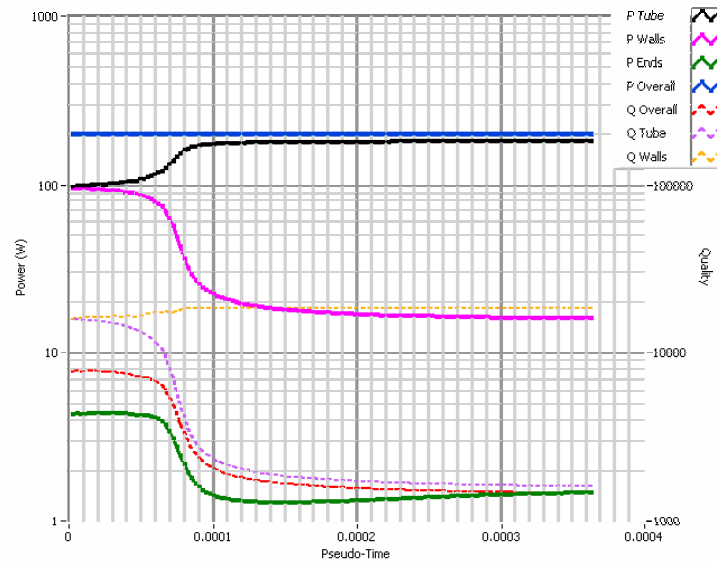
Fig. 4-22: Evolution of the TM$_{011}$ cavity toward a steady state solution.

The steady state reached is shown in Fig. 4-23. For this TM$_{011}$ cavity and in fact all cavities with flat ends, the field tends to concentrate around these ends. This is in part because of the sharp edges and in part because the field tends to concentrate around any hot region as it becomes more "conductor like," bending the electric field lines normal to its surface. The net result is a self-reinforcing cycle that favors stable thermal runaway at the cavity ends.

The heat fluxes in Fig. 4-23 show radiative energy loss at the hottest parts of the tube, and heat conduction along the tube away from the hottest regions. The thermal conductivity varies wildly, between 2 and 18 W/m/K, illustrating the importance of a nonlinear solution. Even the real part of the dielectric constant varies appreciably along the length of the cavity, and the imaginary part, represented by the loss factor, is a strong function of temperature and varies over an order of magnitude. Perhaps the greatest variation of all occurs in the volumetric heating, which is proportional to the loss factor and the square of the electric field. This triple contribution gives rise to a nine order of magnitude variation in the volumetric heating term.
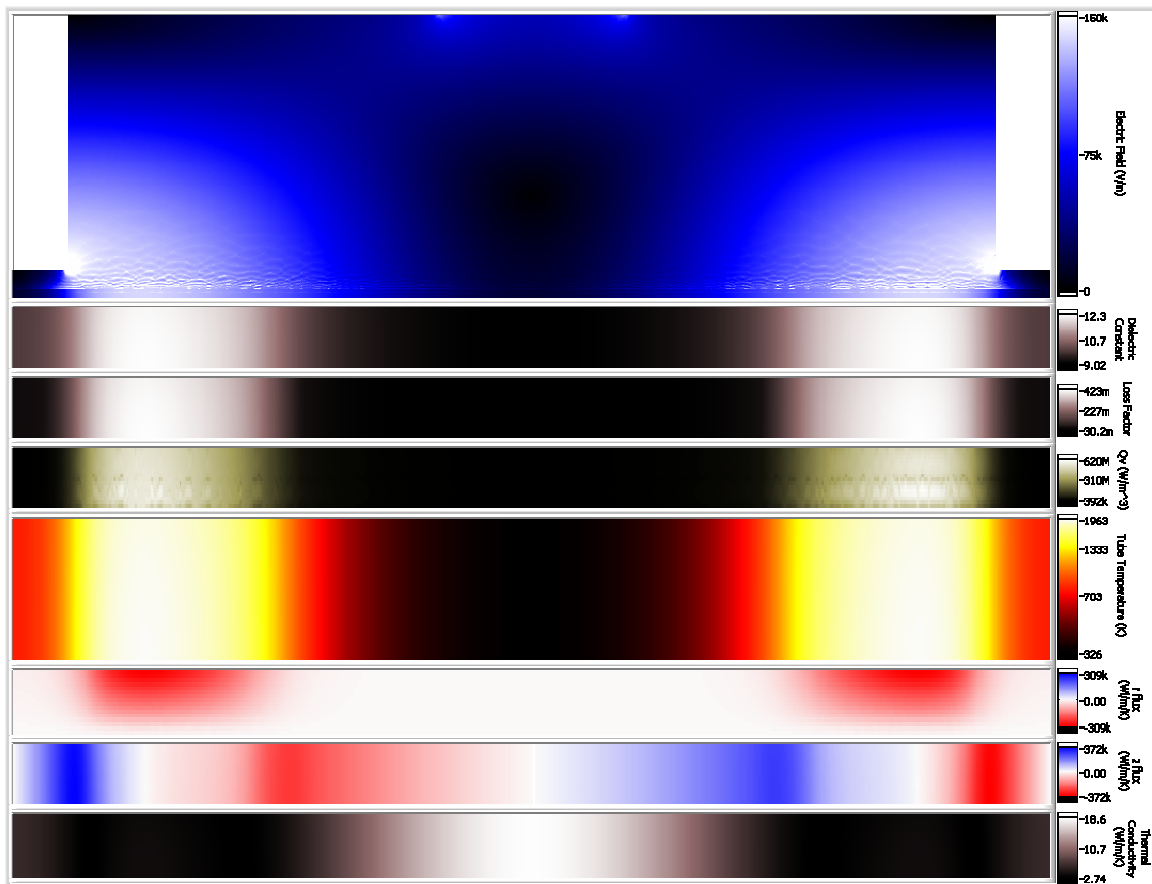
Fig. 4-23: Steady state TM$_{011}$ cavity solution with an alumina tube. For each tube quantity, the bottom edge of the intensity plot corresponds to the inner radius and the top edge corresponds to the outer radius of the tube, so as to map to the conduction domain seen in Fig. 4-21. For the electric field, the bottom edge corresponds to the axis and the top edge to the radius of the cavity, so as to map to the electromagnetic domain seen in Fig. 4-21.

In order to minimize the self-reinforcing coupling of the tube and cavity ends, as well as to provide a uniform central region of heating, a tapered TM$_{011}$ cavity is tried using the parameters given in Table 4-15. Because the electric field lines must be perpendicular to the cavity walls, the tapered ends enforce a tapered electric field toward the cavity ends. As before, the false transient technique converges toward a steady state solution, as shown in Fig. 4-24.

Tube parameters	
Inner diameter	1.59 mm
Outer diameter	4.76 mm
Material	Mullite

Cavity parameters	
Inner Diameter	4.925 cm
Taper end diameter	2 cm
Choke end diameter	0.7 cm
Cylindrical main section length	14.7 cm
Left taper length	5.2 cm
Right taper length	5.2 cm
Choke length (both ends)	5.65 cm
Drive point length	25.527 mm (60% of waveguide height)
Offset from center of cylindrical main section	0 cm (centered)
Frequency	2445 MHz
Input power	140 W

Numerical parameters	
Electromagnetic finite element mesh configuration	Adaptive, using 50,000–150,000 elements
Drive point boundary condition type	Matched using propagation constant $\beta = 32 \text{ m}^{-1}$
(r, z) grid points for tube	(16, 512)

Table 4-15: Input parameters for the tapered TM_{011} EM-conduction problem.
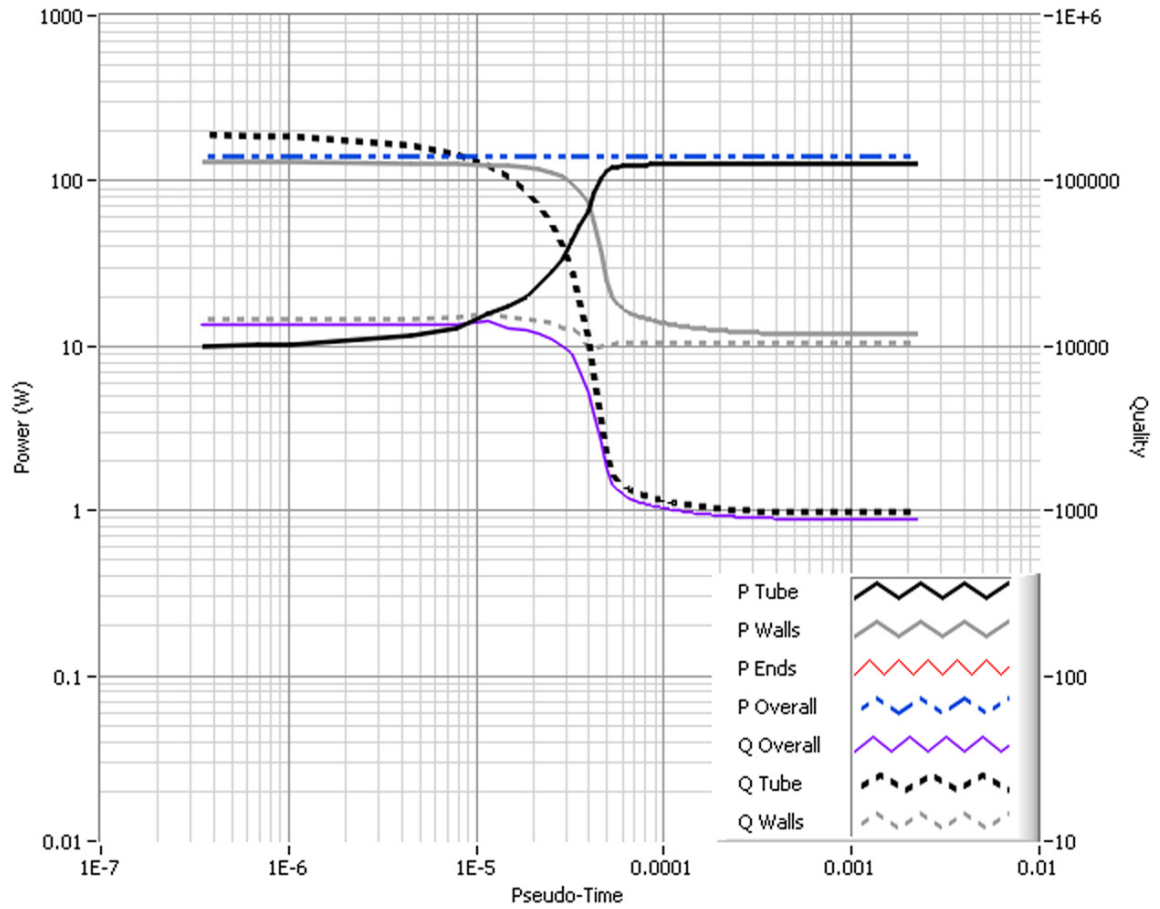
Fig. 4-24: Evolution of the tapered TM_{011} cavity toward a steady state solution.

The cavity length is carefully tuned to form a uniform region of high electric field along the axis, shown in Fig. 4-25, but unlike the TM_{010} mode, this region turns out to be stable as the tube heats up. This parameters of the cavity simulated in Fig. 4-25 are similar to the parameters of a cavity that is examined experimentally in Chapter 7. In this case, the cavity heating is symmetric. In the later case of the experimental cavity, slight asymmetric deviations are taken into account.
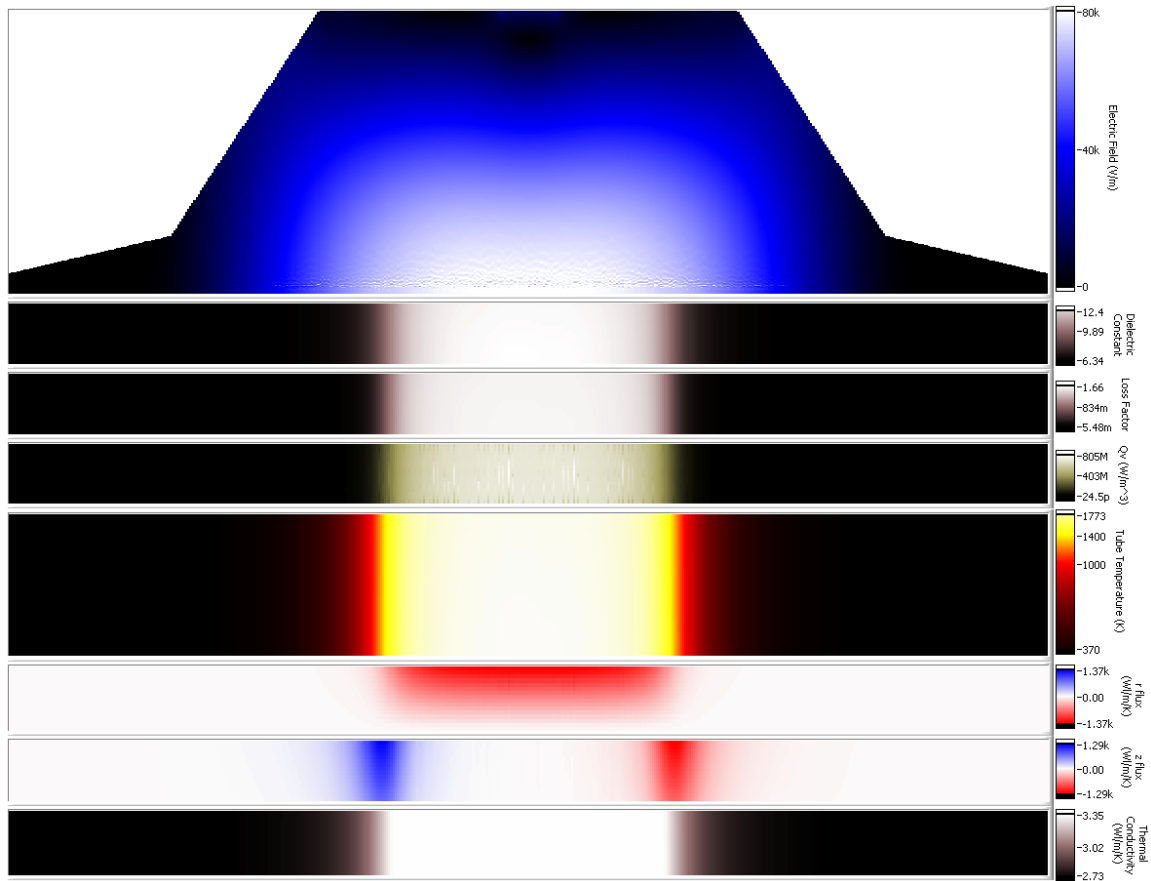
Fig. 4-25: Steady state tapered TM$_{011}$ cavity solution with a mullite tube. For each tube quantity, the bottom edge of the intensity plot corresponds to the inner radius and the top edge corresponds to the outer radius of the tube. For the electric field, the bottom edge corresponds to the axis and the top edge to the radius of the cavity.

4.5 Summary and References

The field distributions calculated by FEMLab reproduce the empty cavity modes at the dimensions predicted by theory. Adding an axial dielectric tube perturbs this mode, particularly in the TM$_{010}$ case. There is a self-reinforcing tendency for the tube to heat only at the ends, which is not desirable for tube heating purposes, and simulations suggest a tapered cavity performs better in this regard.

A stability analysis of the tapered cavity with respect to geometrical parameters indicates that the radius is the most sensitive parameter for both the dielectric tube and the cavity itself. Changing the radius is qualitatively equivalent to changing the wavelength, and such a stability analysis is useful for understanding cavity fabrication tolerances. The stability analysis also reveals that field focus may be changed by shifting the cavity drive point off-center. In general, the mode shape is insensitive to the drive point geometry, and numerically, the drive point boundary condition does not have a great effect on the field in the near axis region. Similarly, the boundary conditions chosen for the dielectric tube and cavity ends do not have a large effect on the field in the near axis region.

The coupled electromagnetic-conduction problem reveals that the peak tube temperature corresponds to the regions of peak electric field for the conventional and tapered TM_{011} cases. The tapered cavity gives a particularly uniform heating region, but a key question remains as to how stable this is once convection is introduced within the tube.

Anon. (2004). *FEMLab Reference Manual*, Röntgenlaan 19, 2719 DX Zoetermeer, Netherlands. Comsol B.V.

Jackson, H.W. and Barmatz, M. (1991). *Microwave-Absorption by a Lossy Dielectric Sphere in a Rectangular Cavity*. Journal of Applied Physics **70**(10): p. 5193–5204.

Meredith, R.J. (1998). *Engineers' handbook of industrial microwave heating*, London, UK. Institution of Electrical Engineers.

Metaxas, A.C. and Meredith, R.J. (1983). *Industrial Microwave Heating*, London, UK. P. Peregrinus on behalf of the Institution of Electrical Engineers.

Özisik, M.N. (1994). *Finite difference methods in heat transfer*, Boca Raton, FL. CRC Press.

Richtmyer, R.D. and Morton, K.W. (1967). *Difference methods for initial-value problems*. 2nd ed, New York. Interscience Publishers.

Warren, J.L. (1987). *Reference Manual for the POISSON/SUPERFISH Group of Codes, LA-UR-87-126*. Los Alamos National Laboratory.

CHAPTER 5

CONVECTION

The dimensions and operating characteristics of a heat exchange thruster are constrained by propellant gasdynamics. Heating the flow accelerates it toward sonic velocity (B. W. Knight *et al.*, 1957), yet friction within the heat exchanger channels, which is strongly related to the flow velocity, reduces the flow pressure along the channel length, increasing the work needed to "push" through a high flow rate. A balance is found between inlet conditions, exit conditions, and channel geometry that in turn determines the thruster mass, turbopump mass (to provide the required inlet pressure), specific impulse (related to the total exit temperature), and the number of channels (width) of the thruster needed to provide a given thrust.

5.1   Quasi-1D Channel Flow

5.1.1   Nomenclature

A	Area
c_p	Specific heat capacity of propellant
D_h	Hydraulic diameter of channel
f	Fanning friction factor of channel
G	Mass flow rate per unit channel area
γ	Ratio of specific heats
h	Convective heat transfer coefficient
k	Thermal conductivity of heat exchanger material
$\dot{m}$	Mass flow rate
M	Mach number
$\mathcal{M}$	Molecular mass
P	Static pressure
r	Recovery factor
R_u	Universal gas constant
ρ	Propellant density
Γ	Circumference

T	Static temperature
T_t	Total temperature
U	Propellant velocity
x	Lengthwise spatial coordinate (also denoted by z)
H	Enthalpy

5.1.2 Problem Formulation

A purely heated channel can be modeled as a Rayleigh flow, and a purely frictional channel can be modeled as a Fanno flow. The model of a heated and frictional channel flow is less straightforward but can be modeled using a semi-empirical approach described generally by Shapiro (1953) and outlined by Bussard & DeLauer (1958) for nuclear thermal systems. The approach of Bussard is extended here to predict flow properties along a constant area duct.

Beginning with a steady state control volume analysis, the mass, momentum, and energy conservation equations of the flow are derived. The control volume, shown in Fig. 5-1, is drawn about an element dx of the channel flow.
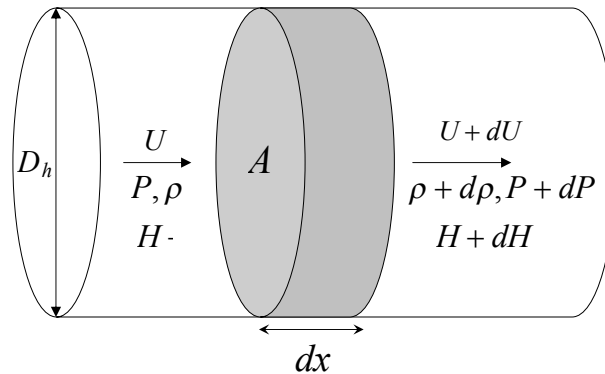
Fig. 5-1: Control volume for a fluid element within the channel.

The integral of the mass flux over the control volume is chosen to be zero since the flow is steady and there are no mass sources or sinks:

$$\oint \rho \mathbf{U} \cdot \mathbf{n} dS = 0.$$

(5.1)

Hence,

$$\rho UA = (\rho + d\rho)(U + dU)A = 0. \tag{5.2}$$

Rearranging and neglecting higher-order terms,

$$\rho dU + U d\rho = d(\rho U) = 0. \tag{5.3}$$

Integrating with respect to x, the continuity equation is obtained, where the constant of integration G is the mass flow rate per unit area.

$$G = \rho U \tag{5.4}$$

Omitting body forces, the momentum integral conservation expression is,

$$\oint_S \rho U(\mathbf{U} \cdot \mathbf{n})dS = -\mathbf{i} \cdot \oint_S P\mathbf{n}dS + \mathbf{i} \cdot \oint_S \mathbf{n} \cdot [\tau]dS. \tag{5.5}$$

Reducing each integral in turn,

$$\oint_S \rho U(\mathbf{U} \cdot \mathbf{n})dS = \rho U(-U)A + \underbrace{(\rho + d\rho)(U + dU)}_{=\rho U}(U + dU)A$$
$$= -\rho U^2 A + \rho U(U + dU)A \tag{5.6}$$
$$= \rho U A dU$$

$$-\mathbf{i} \cdot \oint_S P\mathbf{n}dS = -\mathbf{i} \cdot [-Pi A] - \mathbf{i} \cdot [(P + dP)\mathbf{i}A]$$
$$= PA - (P + dP)A \tag{5.7}$$
$$= -AdP$$

$$\mathbf{i} \cdot \oint_S \mathbf{n} \cdot [\tau]dS \simeq -\tau \Gamma dx. \tag{5.8}$$

In Eq. (5.8) viscous stresses are assumed to be significant only at the channel walls. Substituting Eqs. (5.6)–(5.8) into Eq. (5.5) yields

$$\rho UA dU = -A dP - \tau \Gamma dx$$

$$\frac{dP}{dx} = -\rho U \frac{dU}{dx} - \tau \frac{\Gamma}{A} \quad . \tag{5.9}$$

By using the definition of hydraulic diameter D_h and introducing the Fanning friction factor f,

$$D_h = \frac{4A}{\Gamma}, \tag{5.10}$$

$$f(x) = \frac{\tau}{\frac{1}{2}\rho U^2}, \tag{5.11}$$

the momentum equation is obtained:

$$\frac{dP}{dx} = -\rho U \frac{dU}{dx} - \frac{4f(x)}{D_h} \frac{1}{2}\rho U^2. \tag{5.12}$$

For energy, the integral conservation expression (omitting body forces) is

$$\oint_S \rho(H + U^2/2)(\mathbf{U} \cdot \mathbf{n})dS = -\oint_S \mathbf{q} \cdot \mathbf{n}dS + \oint_S \mathbf{n} \cdot [\boldsymbol{\tau}] \cdot \mathbf{U}dS. \tag{5.13}$$

The viscous dissipation term is dropped, hence,

$$\rho(-U)\left(H + \frac{U^2}{2}\right)A$$

$$+ \underbrace{(\rho + d\rho)(U + dU)}_{=\rho U \text{ exactly}} \left(H + dH + \frac{(U+dU)^2}{2}\right)A = q_u(x)\Gamma dx. \tag{5.14}$$

By eliminating higher-order terms,

$$dH = \frac{q_u(x)}{G}\Gamma dx - U dU, \tag{5.15}$$

which can be rearranged to yield the energy equation:

$$\frac{dH}{dx} = \frac{q_u(x)}{G}\Gamma - U\frac{dU}{dx}. \tag{5.16}$$

Note that Eq. (5.16) involves total enthalpy rather than total temperature because the specific heat capacity varies significantly in the x (longitudinal) direction. In the y direction, i.e., across the boundary layer, the temperature difference is smaller and property variations are neglected.

5.1.3 Governing Equations

General Case

The continuity, momentum and energy equations are combined with the perfect gas equation of state in order to solve the system. For convenience, the lengthwise coordinate x is nondimensionalized by the hydraulic diameter D_h.

$$G = \rho U \tag{5.17}$$

$$\frac{dP}{dx'} = -\rho U \frac{dU}{dx'} - 2f(x)\rho U^2 \tag{5.18}$$

$$\frac{dH}{dx'} = \frac{4q_u(x)}{G} - U\frac{dU}{dx'} \tag{5.19}$$

$$P = \frac{\rho R_u T}{\mathcal{M}} \tag{5.20}$$

Equations (5.17)–(5.20) are reduced to a pair of coupled first-order ODEs and solved numerically for $T(x')$ and $U(x')$ given either a temperature or flux boundary condition. Expanding into differential form, Eqs. (5.17)–(5.20) become

$$\rho dU + U d\rho = 0, \tag{5.21}$$

$$\rho U dU = -dP - 2\rho U^2 f(x) dx', \tag{5.22}$$

$$dH = \frac{4q_u(x)}{G} dx' - U dU, \tag{5.23}$$

$$\frac{dP}{P} = \frac{dT}{T} - \frac{dU}{U}, \tag{5.24}$$

$$dH = c_p dT. \tag{5.25}$$

In Eq. (5.25), the definition of specific heat capacity at constant pressure, has been added to relate enthalpy to temperature. This is an approximation because the pressure is not constant along the tube; however, for propulsion applications the thermal contribution to

enthalpy far exceeds the pressure contribution. Furthermore, the use of heat capacity here is only valid in a differential sense because it is not constant as temperature varies.

Eliminating dP, $d\rho$ and dH leaves

$$\frac{dT}{T} = \frac{\left(\frac{R_gT}{U^2}-1\right)\frac{4q_u(x)}{GU^2}+2f(x)}{\frac{R_gT}{U^2}\left[\left(\frac{R_gT}{U^2}-1\right)\frac{c_p}{R_g}+1\right]}dx', \qquad (5.26)$$

$$\frac{dU}{U} = \frac{\frac{4q_u(x)}{GU^2}-\frac{c_p}{R_g}2f(x)}{\left(\frac{R_gT}{U^2}-1\right)\frac{c_p}{R_g}+1}dx'. \qquad (5.27)$$

Given the boundary conditions $T(x_0') = T_0, U(x_0') = U_0$ and $q_u(x')$ Eqs. (5.26) and (5.27) are numerically integrated to obtain $T(x'), U(x')$. From these two quantities and G, other flow quantities such as pressure are deduced.

If the wall temperature is specified along the flow, then Eq. (5.28) is used to deduce $q_u(x')$ from the Stanton number,

$$q_u = \mathrm{St}\,G(H_w - H_{aw}), \qquad (5.28)$$

$$\mathrm{St} = \frac{\mathrm{Nu}(T)}{\mathrm{Re}(T)\mathrm{Pr}}, \qquad (5.29)$$

$$\mathrm{Re}_{D_h}(T) = \frac{GD_h}{\mu(T)}, \qquad (5.30)$$

$$10 < \mathrm{Re} < 10^6: \quad \mathrm{Nu}(\mathrm{Re}) = \left\{(4.364)^{10} + \left\{\frac{\exp[(2200-\mathrm{Re})/365]}{(4.364)^2} + \frac{1}{\mathrm{Nu}_t^2}\right\}^{-5}\right\}^{1/10}, \qquad (5.31)$$

$$\mathrm{Nu}_t = 6.3 + \frac{0.079\sqrt{\frac{f}{2}}\,\mathrm{Re}\,\mathrm{Pr}}{\left(1+\mathrm{Pr}^{4/5}\right)^{5/6}}. \qquad (5.32)$$

In double precision numerical evaluation, the above expression for Nusselt number Nu is evaluated in parts using logarithms to avoid numerical precision errors. This expression is derived by Churchill (Kakaç *et al.*, 1987) to approximate experimental correlations for the flux boundary condition spanning all flow regimes. For the transitional Nusselt number Nu_t the friction factor f is evaluated using Eq. (5.35) below.

Enthalpies are calculated using approximations for the fluid of interest. The adiabatic wall enthalpy H_{aw} is the enthalpy the bulk flow must attain for there to be no net transfer of heat. This enthalpy is calculated using an enthalpy recovery factor r (Kays *et al.*, 2005),

$$H_{aw} = H + rU^2/2, \tag{5.33}$$

$$r = \begin{cases} \mathrm{Pr}^{1/2} & \mathrm{Re} < 2400 \\ \mathrm{Pr}^{1/3} & \mathrm{Re} > 10,000 \end{cases}, \tag{5.34}$$

where H is evaluated as a function of temperature for any given fluid (Appendix A). Finally, the friction factor is given by an expression approximating experimental correlations over all flow regimes by Churchill (Kakaç *et al.*, 1987),

$$\mathrm{Re} \geq 2400: \qquad \frac{2}{f} = \left\{ \frac{1}{\sqrt{\left(\frac{8}{\mathrm{Re}}\right)^{10} + \left(\frac{\mathrm{Re}}{36500}\right)^{20}}} + \left[2.21 \log_{10}\left(\frac{\mathrm{Re}}{7}\right) \right]^{10} \right\}^{1/5}. \tag{5.35}$$

This expression exactly reproduces the more well-known expression of $f = 16/\mathrm{Re}$ in the laminar regime; however, due to the large powers it must be evaluated in parts using logarithms in the same way as the Nusselt number.

Special Cases: Frictionless, and Constant c_p

If there is no friction at the channel walls and the specific heat capacity does not vary along the channel, then Eqs. (5.26) and (5.27) become

$$\frac{dT}{T} = \frac{4q_u(x')}{Gc_pT} \frac{1}{1 + \frac{1}{\frac{RgT}{U^2} - 1}} dx', \tag{5.36}$$

$$\frac{dU}{U} = \frac{4q_u(x')}{GU^2} \frac{1}{\frac{c_p}{Rg} + \frac{1}{\frac{RgT}{U^2} - 1}} dx'. \tag{5.37}$$

These two equations are combined to produce

$$\frac{dT}{T} = \frac{\left(1-\gamma M^2\right)}{\left(1+\gamma M^2\right)} \frac{dM^2}{M^2}.$$
(5.38)

which describes a Rayleigh flow.

Special Cases: Adiabatic and Constant c_p

If $q_u = 0$ and the specific heat capacity does not vary with x then Eqs. (5.26) and (5.27) become

$$\frac{dT}{T} = \frac{U^2}{R_g T} \frac{2f(x)}{\left(\frac{R_g T}{U^2}-1\right)\frac{c_p}{R_g}+1}dx',$$
(5.39)

$$\frac{dU}{U} = -\frac{c_p}{R_g} \frac{2f(x)}{\left(\frac{R_g T}{U^2}-1\right)\frac{c_p}{R_g}+1}dx'.$$
(5.40)

Combining Eqs. (5.26) and (5.27) yields

$$c_p dT + \tfrac{1}{2}dU^2 = 0,$$
(5.41)

which describes a Fanno flow.

5.1.4   Application to a Turbulent Channel Flow

A full-scale microwave thermal channel is expected to have a hydraulic diameter on the order of a millimeter, operating at high power and H_2 pressures on the order of 100 atm. This places the flow in the turbulent regime, and the quasi-1D model is used to solve the channel flow for the case of a uniform wall flux.

All sources of energy loss, such as external radiation and convection, are neglected and the hydrogen propellant is taken to be nonparticipating.   The nonparticipating approximation is verified by referring to Appendix A: For H_2 at a pressure of 100 atm, the emissivity in Fig. A-4 decreases with increasing temperature over the range of 300 K to 3000 K. There is a low temperature region where emissivity is on the order of unity; however, at this low temperature the radiative flux is very much lower than the

convective flux. Radiative heat transfer only becomes an important transfer mechanism above around 1500 K, at which point the emissivity is on the order of 10^{-2}. The peak absorption occurs at a wavenumber of 0.04 cm^{-1}, as shown in Fig. A-5. Assuming a mean path length of 0.5 cm, the optical depth of 0.02 means that only 2% of the radiative energy is absorbed. Furthermore, the energy entering the channel via convection is much greater than the energy radiated into the channel even for a black body, so the hydrogen may be treated as non-absorbing.

The turbulent channel diameter, inlet pressure, and inlet velocity are varied such that the sonic point occurs at the desired exit temperature (thruster vacuum I_{sp}), pressure (thruster sea level I_{sp}), mass flow rate per unit area (thruster thrust-to-weight ratio), and distance from the inlet (beam footprint, channel power). The resulting parameters are given in Table 5-1.

Tube parameters

Length	1.6 m
Inner diameter	4 mm
Input power	400 kilowatts (uniform along tube length)
Cross-section geometry	Square

Flow parameters

Gas	Hydrogen
Transport properties	Temperature varying
Static temperature at inlet	300 K
Static pressure at outlet	40 atm (G iterated such that this is true)
Mean inlet velocity	80 m/s
Enthalpy recovery factor	0.89

Table 5-1: Quasi-1D turbulent gasdynamic model parameters.

The quasi-1D results are shown in Fig. 5-2. At the channel inlet, the Reynolds number is around 450,000 and decreases to around 150,000 toward the exit as the viscosity increases with temperature. As enthalpy is added, the propellant accelerates toward sonic conditions as it passes through the channel, in turn inducing a larger pressure drop, which is approximately proportional to the velocity cubed. Experimentally, sonic flow conditions occur at the end of the tube and the channel inlet conditions vary such that this

is so. The quasi-1D code implemented here becomes numerically stiff as the sonic point is approached. The inlet conditions are varied by hand such that the desired tube length is attained before the sonic point is reached.
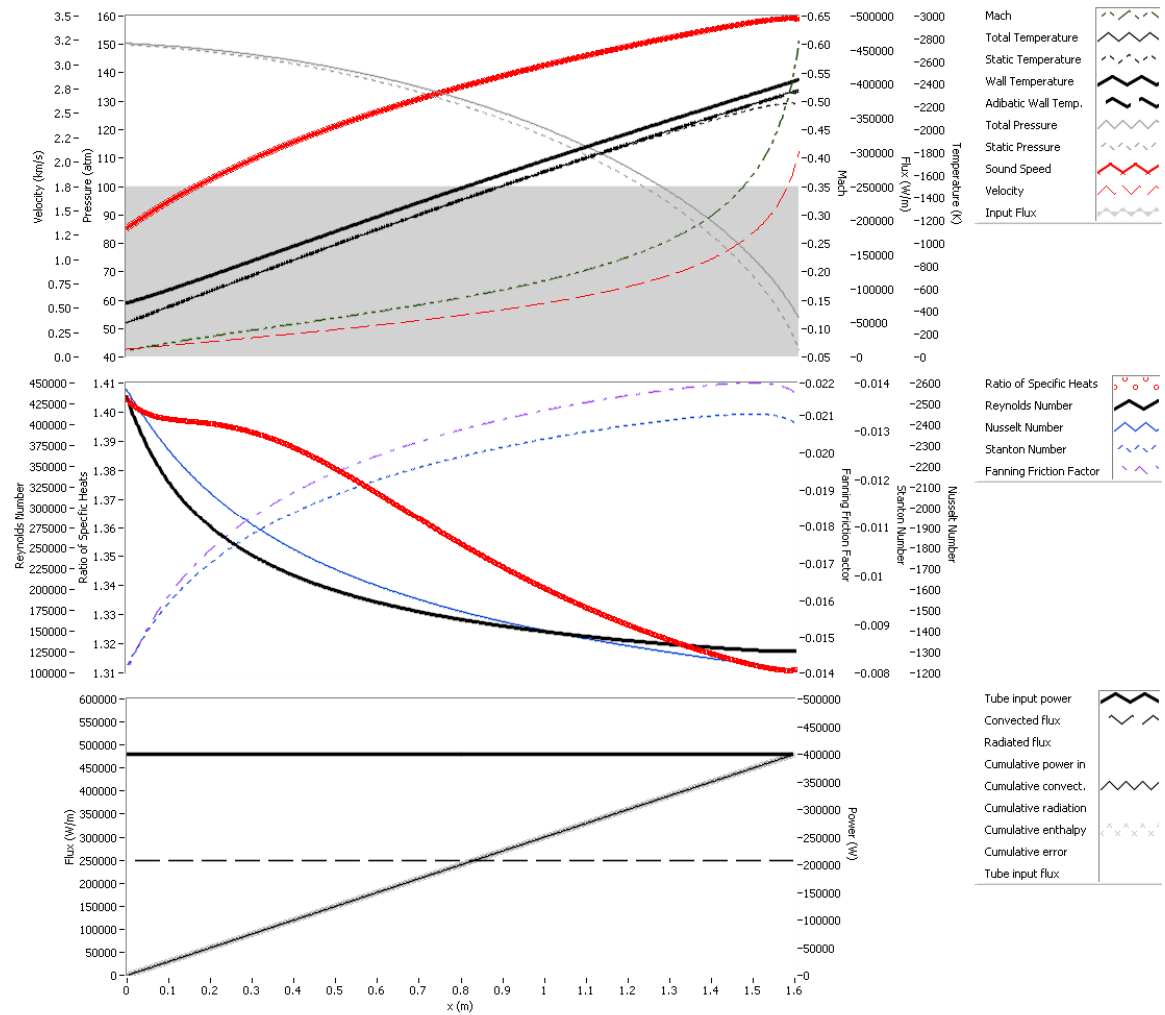
Fig. 5-2: Quasi-1D flow through a high power turbulent channel.

From a design perspective it is important to note that the location of the sonic point for any given set of inlet conditions and input energy flux constraints the channel length, and hence the geometry of the heat exchanger. In order to maximize the propellant enthalpy for a given material melting point, the wall temperature needs to be as close as possible to the propellant total temperature at the thruster exit. The results in Fig. 5-2 predict a wall

temperature that is about 250 K hotter than the propellant temperature at the channel outlet, and this bodes well for the kind of heat exchanger arrangements described in § 2.2.1.

5.1.5   Application to a Laminar Channel Flow

A laboratory-scale microwave thermal channel is expected to have a hydraulic diameter on the order of a millimeter, operating at low power with a hydrogen propellant pressure on the order of 1 atm. This places the flow in the laminar regime, and the quasi-1D model is once again used to solve the channel flow for the case of a uniform wall flux.

As before, the hydrogen propellant is taken to be nonparticipating. At low pressures, dissociation can alter the hydrogen enthalpy. Fig. A-3 shows that around atmospheric pressure and for temperatures below 2500 K the dissociation effects can be neglected.

Using the parameters given in Table 5-2, the coupled differential Eqs. (5.26) and (5.27) are integrated, starting with the initial conditions specified at $z = 0$ and proceeding until the flow becomes sonic or the designated channel length is reached. In order to attain the correct static outlet pressure, an initial value for the mass flow rate per unit area, G, is guessed and the solution iterated.

Tube parameters

Length	20 cm
Inner diameter	1.19 mm
Input power	150 watts (uniform along tube length)
Cross-section geometry	Circular

Flow parameters

Gas	Hydrogen
Transport properties	Temperature varying
Static temperature at inlet	300 K
Static pressure at outlet	1 atm (G iterated such that this is true)
Mean inlet velocity	50 m/s
Enthalpy recovery factor	0.85

Table 5-2: Quasi-1D laminar gasdynamic model parameters.

At the channel inlet on the left size of Fig. 5-3, the Reynolds number is around 625 and decreases to around 200 toward the exit because viscosity increases with temperature. In this case the channel is too short for the flow to reach its sonic point, and the relatively low energy density reduces the wall-flow temperature difference to around 100 K.

As seen from the energy balance chart at the bottom of Fig. 5-3, the input power matches the total enthalpy of the flow, indicating that energy is conserved within the simulation.
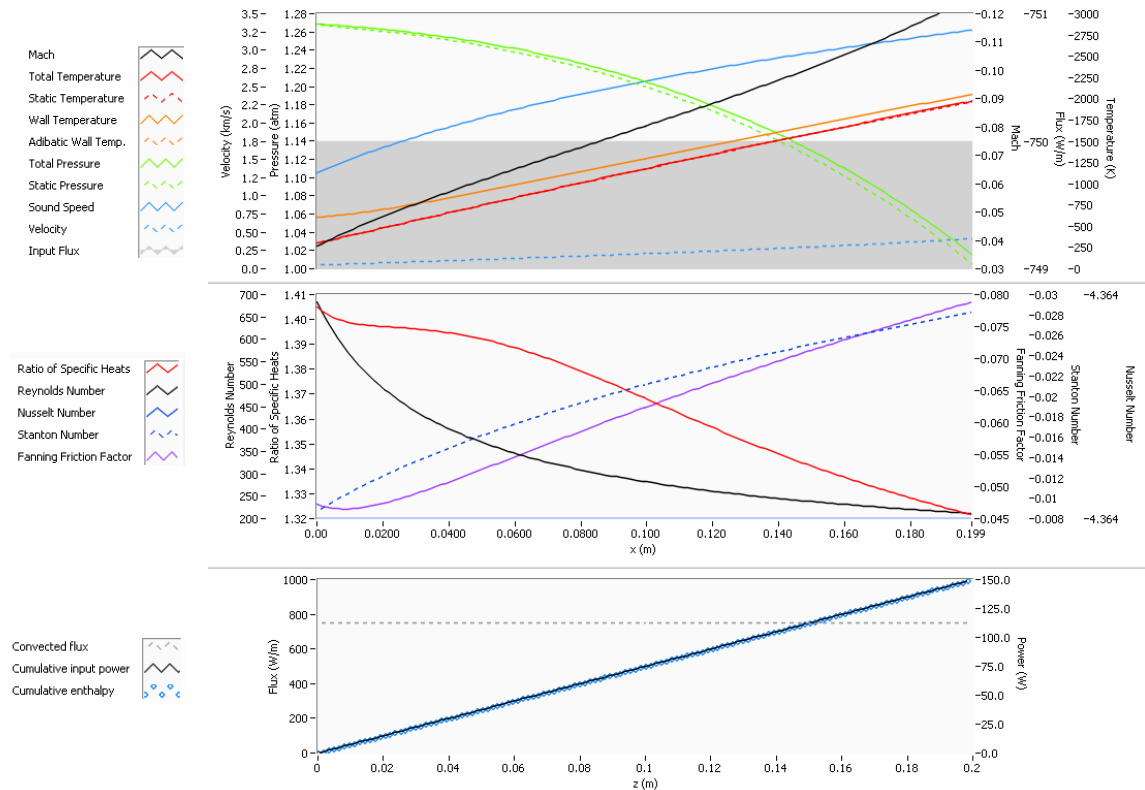
Fig. 5-3: Quasi-1D flow through a low power laminar channel.

5.2 2D Finite Difference Channel Flow

In addition to the quasi-1D flow model presented above, a finite difference model is used as an alternative and more accurate tool to forecast the evolution of the flow through a heat exchanger channel. The finite difference model presented here numerically approximates the solution of the complete time-dependent viscous compressible

axisymmetric Navier-Stokes equations in the laminar regime, including temperature-dependent fluid properties.

5.2.1 Problem Formulation

The problem formulation begins with the time-dependent Navier-Stokes equations:

$$\frac{\partial \rho}{\partial t} + \nabla \cdot (\rho \mathbf{u}) = 0 \tag{5.42}$$

$$\frac{\partial}{\partial t}(\rho \mathbf{u}) + \nabla \cdot (\rho \mathbf{u}\mathbf{u}) + \nabla \cdot (p\bar{\mathbf{I}}) = \nabla \cdot \bar{\tau} \tag{5.43}$$

$$\frac{\partial}{\partial t}\left[\rho\left(e + \frac{|\mathbf{u}|^2}{2}\right)\right] + \nabla \cdot \left[\rho\left(h + \frac{|\mathbf{u}|^2}{2}\right)\mathbf{u}\right] = \Phi + \nabla \cdot (k\nabla T) \tag{5.44}$$

In vector form these can be written as

$$\vec{u}_t + \nabla \cdot \vec{F} = G, \tag{5.45}$$

where

$$\vec{u} = \begin{pmatrix} \rho \\ \rho \mathbf{u} \\ \rho\left(e + \frac{|\mathbf{u}|^2}{2}\right) \end{pmatrix}, \vec{F} = \begin{pmatrix} \rho \mathbf{u} \\ \rho \mathbf{u}\mathbf{u} + p\bar{\mathbf{I}} \\ \rho\left(h + \frac{|\mathbf{u}|^2}{2}\right)\mathbf{u} \end{pmatrix}, G = \begin{pmatrix} 0 \\ \nabla \cdot \bar{\tau} \\ \Phi + \nabla \cdot (k\nabla T) \end{pmatrix}. \tag{5.46}$$

In radial coordinates,

$$\mathbf{u} = u\hat{\mathbf{z}} + v\hat{\mathbf{r}}, \tag{5.47}$$

$$\nabla = \hat{\mathbf{r}}\frac{\partial}{\partial r} + \hat{\mathbf{z}}\frac{\partial}{\partial z}, \tag{5.48}$$

$$\nabla \cdot \mathbf{u} = \frac{1}{r}\frac{\partial}{\partial r}(rv) + \frac{\partial u}{\partial z}, \tag{5.49}$$

$$\nabla^2 = \frac{1}{r}\frac{\partial}{\partial r}\left(r\frac{\partial}{\partial r}\right) + \frac{\partial^2}{\partial z^2}, \tag{5.50}$$

and

$$\nabla \cdot (\rho \mathbf{u}\mathbf{u}) = \left[\frac{1}{r}\frac{\partial}{\partial r}(r\rho v^2) + \frac{\partial}{\partial z}(\rho uv)\right]\hat{\mathbf{r}} + \left[\frac{1}{r}\frac{\partial}{\partial r}(r\rho uv) + \frac{\partial}{\partial z}(\rho u^2)\right]\hat{\mathbf{z}}, \tag{5.51}$$

$$\nabla \cdot (p\mathbf{I}) = \frac{\partial p}{\partial r}\hat{r} + \frac{\partial p}{\partial z}\hat{z}, \tag{5.52}$$

$$\Phi = \mu\left[2\left(\tfrac{\partial v}{\partial r}\right)^2 + 2\left(\tfrac{v}{r}\right)^2 + 2\left(\tfrac{\partial u}{\partial z}\right)^2 + \left(\tfrac{\partial v}{\partial z} + \tfrac{\partial u}{\partial r}\right)^2 - \tfrac{2}{3}\left(\tfrac{\partial v}{\partial r} + \tfrac{v}{r} + \tfrac{\partial u}{\partial z}\right)^2\right], \qquad (5.53)$$

$$\nabla \cdot (k\nabla T) = k\nabla^2 T = k\left[\tfrac{1}{r}\left(\tfrac{\partial T}{\partial r} + \tfrac{\partial^2 T}{\partial r^2}\right) + \tfrac{\partial^2 T}{\partial z^2}\right], \qquad (5.54)$$

$$\nabla \cdot \left[\rho\left(h + \tfrac{|\mathbf{u}|^2}{2}\right)\mathbf{u}\right] = \tfrac{1}{r}\tfrac{\partial}{\partial r}\left[r\rho v\left(h + \tfrac{|\mathbf{u}|^2}{2}\right)\right] + \tfrac{\partial}{\partial z}\left[\rho u\left(h + \tfrac{|\mathbf{u}|^2}{2}\right)\right], \qquad (5.55)$$

$$\nabla \cdot \bar{\bar{\tau}} = \mu\left\{\begin{array}{c}\left[\tfrac{4}{3}\left(\tfrac{\partial^2 v}{\partial r^2} + \tfrac{\partial}{\partial r}\left(\tfrac{v}{r}\right)\right) + \tfrac{\partial^2 v}{\partial z^2} + \tfrac{1}{3}\tfrac{\partial^2 u}{\partial r\partial z}\right]\hat{\mathbf{r}} \\[2mm] +\left[\tfrac{\partial^2 u}{\partial r^2} + \tfrac{1}{r}\left(\tfrac{1}{3}\tfrac{\partial v}{\partial z} + \tfrac{\partial u}{\partial r}\right) + \tfrac{1}{3}\left(4\tfrac{\partial^2 u}{\partial z^2} + \tfrac{\partial^2 v}{\partial z\partial r}\right)\right]\hat{\mathbf{z}}\end{array}\right\}. \qquad (5.56)$$

So that Eq. (5.45) simplifies to

$$\mathbf{U}_t + \mathbf{F}_r + \mathbf{F}_z = \mathbf{G}, \qquad (5.57)$$

where

$$\mathbf{U}_t = \begin{bmatrix}\tfrac{\partial \rho}{\partial t} \\[2mm] \tfrac{\partial(\rho u)}{\partial t} \\[2mm] \tfrac{\partial(\rho v)}{\partial t} \\[2mm] \tfrac{\partial}{\partial t}\left(\rho e + \rho\tfrac{u^2+v^2}{2}\right)\end{bmatrix}, \quad \mathbf{G} = \begin{bmatrix}0 \\[2mm] \mu\left[\tfrac{\partial^2 u}{\partial r^2} + \tfrac{1}{r}\left(\tfrac{1}{3}\tfrac{\partial v}{\partial z} + \tfrac{\partial u}{\partial r}\right) + \tfrac{1}{3}\left(4\tfrac{\partial^2 u}{\partial z^2} + \tfrac{\partial^2 v}{\partial z\partial r}\right)\right] \\[2mm] \mu\left[\tfrac{4}{3}\left(\tfrac{\partial^2 v}{\partial r^2} + \tfrac{\partial}{\partial r}\left(\tfrac{v}{r}\right)\right) + \tfrac{\partial^2 v}{\partial z^2} + \tfrac{1}{3}\tfrac{\partial^2 u}{\partial r\partial z}\right] \\[2mm] \Phi + k\left[\tfrac{1}{r}\left(\tfrac{\partial T}{\partial r} + \tfrac{\partial^2 T}{\partial r^2}\right) + \tfrac{\partial^2 T}{\partial z^2}\right]\end{bmatrix}, \qquad (5.58)$$

$$\mathbf{F}_r = \begin{bmatrix}\tfrac{1}{r}\tfrac{\partial}{\partial r}(\rho rv) \\[2mm] \tfrac{1}{r}\tfrac{\partial}{\partial r}(r\rho uv) \\[2mm] \tfrac{1}{r}\tfrac{\partial}{\partial r}(r\rho v^2) + \tfrac{\partial p}{\partial r} \\[2mm] \tfrac{1}{r}\tfrac{\partial}{\partial r}\left[r\rho v\left(h + \tfrac{u^2+v^2}{2}\right)\right]\end{bmatrix}, \quad \mathbf{F}_z = \begin{bmatrix}\tfrac{\partial(\rho u)}{\partial z} \\[2mm] \tfrac{\partial}{\partial z}(\rho u^2) + \tfrac{\partial p}{\partial z} \\[2mm] \tfrac{\partial}{\partial z}(\rho uv) \\[2mm] \tfrac{\partial}{\partial z}\left[\rho u\left(h + \tfrac{u^2+v^2}{2}\right)\right]\end{bmatrix}. \qquad (5.59)$$

Equation (5.57) is solved numerically until steady state is reached and all quantities of interest are derived from the resultant vector **U**.

5.2.2 Discretization

The axisymmetric flow is discretized as shown in Fig. 5-4. Radial discretization is from the axis to half the channel diameter, and axial discretization is from the inlet (left) to the outlet (right). The format of most 2D figures depicting the flow in the remaining sections follows the spatial format of this grid.
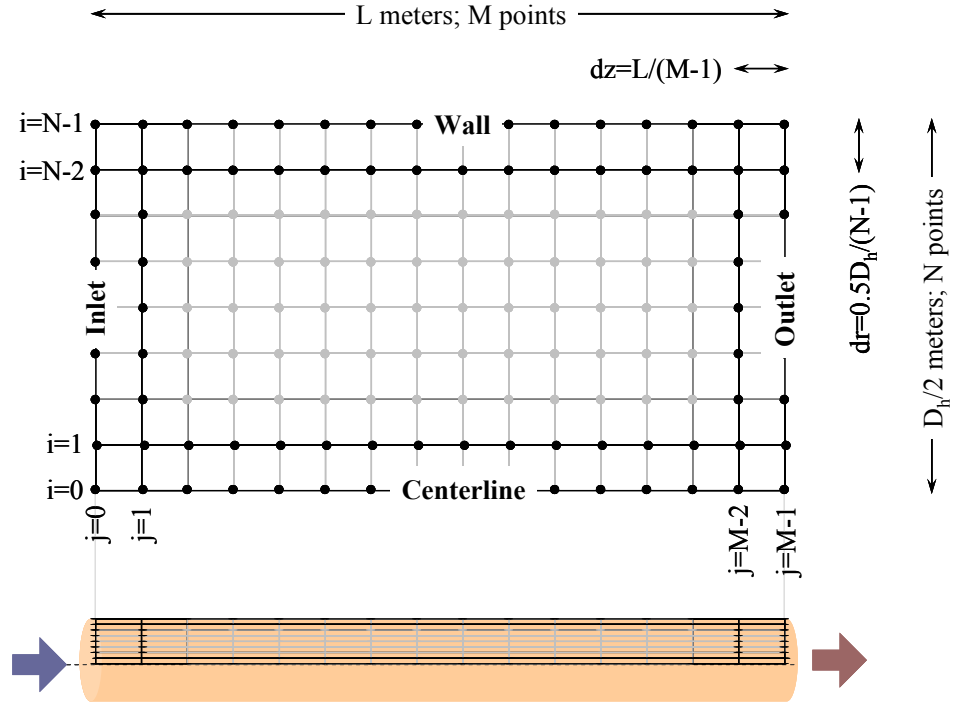
Fig. 5-4: Discretization of the flow domain for the Navier-Stokes solution.

Second-order central differences are used within the domain:

$$\frac{\partial u_{i,j}^n}{\partial r} = \frac{u_{i+1,j}^n - u_{i-1,j}^n}{2dr}, \quad \frac{\partial u_{i,j}^n}{\partial z} = \frac{u_{i,j+1}^n - u_{i,j-1}^n}{2dz} \tag{5.60}$$

$$\frac{\partial^2 u_{i,j}^n}{\partial r^2} = \frac{u_{i-1,j}^n + 2u_{i,j}^n + u_{i+1,j}^n}{(dr)^2}, \quad \frac{\partial^2 u_{i,j}^n}{\partial z^2} = \frac{u_{i,j-1}^n + 2u_{i,j}^n + u_{i,j+1}^n}{(dz)^2} \tag{5.61}$$

$$\frac{\partial^2 u_{i,j}^n}{\partial r \partial z} = \frac{1}{2dr}\left(\frac{\partial u_{i+1,j}^n}{\partial z} - \frac{\partial u_{i-1,j}^n}{\partial z}\right) = \frac{1}{2dz}\left(\frac{\partial u_{i,j+1}^n}{\partial r} - \frac{\partial u_{i,j-1}^n}{\partial r}\right) \tag{5.62}$$

First-order differences are used for boundaries:

Inlet:
$$\frac{\partial u_{i,0}^n}{\partial z} = \frac{u_{i,1}^n - u_{i,0}^n}{dz} \tag{5.63}$$

Outlet:
$$\frac{\partial u_{i,M}^n}{\partial z} = \frac{u_{i,M}^n - u_{i,M-1}^n}{dz} \tag{5.64}$$

Wall:
$$\frac{\partial u_{N,j}^n}{\partial r} = \frac{u_{N,j}^n - u_{N-1,j}^n}{dr} \tag{5.65}$$

Temporal discretization is via simple stepping or second-order Runge-Kutta (RK2) procedure.

5.2.3 Boundary Conditions

Symmetry Conditions along the Centerline

By symmetry, $v = 0$ along the centerline and $du/dr = 0$, hence there are no shear stresses along the centerline,

$$\tau_{rz} = \tau_{zr} = \mu\left(\frac{\partial v}{\partial z} + \frac{\partial u}{\partial r}\right) = 0. \tag{5.66}$$

L'Hopital's rule is used on radial quantities that vanish as r becomes small,

$$\lim_{r \to 0}\left[\frac{1}{r}\frac{\partial}{\partial r}(rf)\right] = \frac{\partial^2 (rf)}{\partial r^2}, \tag{5.67}$$

$$\lim_{r \to 0}\left[\frac{1}{r}\frac{\partial}{\partial r}\left(r\frac{\partial f}{\partial r}\right)\right] = 2\frac{\partial^2 f}{\partial r^2}. \tag{5.68}$$

Visualizing the flow either side of the axis, it is symmetric in nature, and it follows that the axis condition implements a mirroring of quantities from one side to the other such that the flow is correctly reflected (Constantinescu and Lele, 2002); Fig. 5-5. True scalar quantities such as temperature are simply mirrored, whereas for velocity $\mathbf{u} = (u, v)$ as a vector quantity, the mirror changes the sign of the v component, leaving u unchanged. The gradient of a scalar is a vector, so mirroreds in the same way as the velocity.
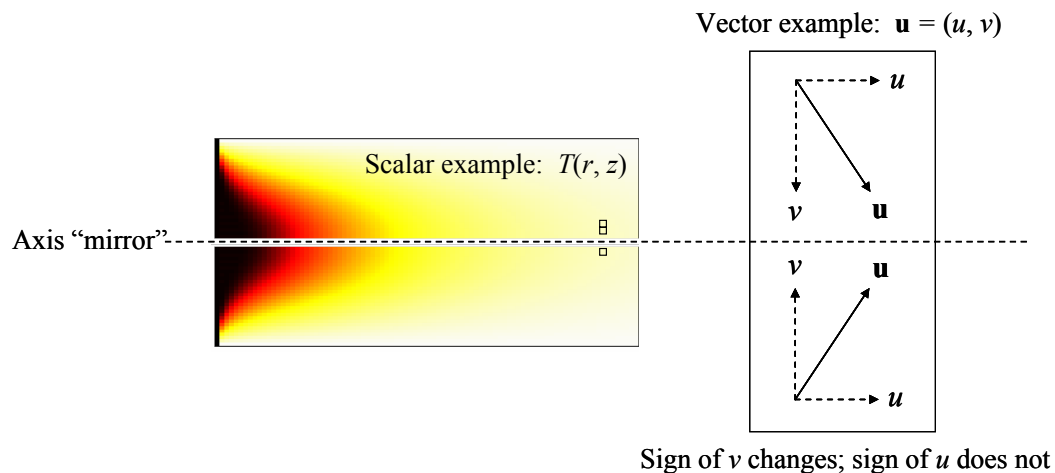
Fig. 5-5: Depiction of the axial symmetry boundary condition as a mirror. Vector quantities must be treated with care.

Navier-Stokes Characteristic Boundary Conditions (NSCBC)

For the remaining boundaries the Navier-Stokes characteristic boundary conditions suggested by Poinsot & Lele (1992) are used to ensure that all types of wave are correctly treated at the boundaries. The boundaries are treated as locally flat and inviscid in order to estimate the various wave amplitudes and reflect them.

To implement these conditions the Navier-Stokes equations are first rewritten in characteristic form,

$$\frac{\partial \rho}{\partial t} + d_1 + \frac{\partial (\rho u_2)}{\partial x_2} + \frac{\partial (\rho u_3)}{\partial x_3} = 0, \tag{5.69}$$

$$\begin{aligned} \frac{\partial (\rho E)}{\partial t} + \frac{1}{2}(u_k u_k)d_1 + \frac{d_1}{\gamma-1} + \rho(u_1 d_3 + u_2 d_4 + u_3 d_5) \\ + \frac{\partial}{\partial x_2}[(\rho E + p)u_2] + \frac{\partial}{\partial x_3}[(\rho E + p)u_3] \end{aligned} = \frac{\partial}{\partial x_i}(u_j \tau_{ij}) - \frac{\partial q_i}{\partial x_i}, \tag{5.70}$$

$$\frac{\partial (\rho u_1)}{\partial t} + u_1 d_1 + \rho d_3 + \frac{\partial (\rho u_1 u_2)}{\partial x_2} + \frac{\partial (\rho u_1 u_3)}{\partial x_3} = \frac{\partial \tau_{1j}}{\partial x_j}, \tag{5.71}$$

$$\frac{\partial (\rho u_2)}{\partial t} + u_2 d_1 + \rho d_4 + \frac{\partial (\rho u_2^2)}{\partial x_2} + \frac{\partial (\rho u_2 u_3)}{\partial x_3} + \frac{\partial p}{\partial x_2} = \frac{\partial \tau_{2j}}{\partial x_j}, \tag{5.72}$$

$$\frac{\partial (\rho u_3)}{\partial t} + u_3 d_1 + \rho d_5 + \frac{\partial (\rho u_3 u_2)}{\partial x_2} + \frac{\partial (\rho u_3^2)}{\partial x_3} + \frac{\partial p}{\partial x_3} = \frac{\partial \tau_{3j}}{\partial x_j}, \tag{5.73}$$

where,

$$\mathbf{d} = \begin{bmatrix} d_1 \\ d_2 \\ d_3 \\ d_4 \\ d_5 \end{bmatrix} = - \begin{bmatrix} \frac{\partial \rho}{\partial t} \\ \frac{\partial p}{\partial t} \\ \frac{\partial u_1}{\partial t} \\ \frac{\partial u_2}{\partial t} \\ \frac{\partial u_3}{\partial t} \end{bmatrix} = \begin{bmatrix} \frac{1}{c^2}\left[\mathcal{L}_2 + \frac{1}{2}(\mathcal{L}_5 + \mathcal{L}_1) \right] \\ \frac{1}{2}(\mathcal{L}_5 + \mathcal{L}_1) \\ \frac{1}{2\rho c}(\mathcal{L}_5 - \mathcal{L}_1) \\ \mathcal{L}_3 \\ \mathcal{L}_4 \end{bmatrix}. \tag{5.74}$$

The $\mathcal{L}_i$ are interpreted as the amplitudes of characteristic waves with characteristic velocities λ_i given by,

$$\lambda_1 = u_1 - c, \tag{5.75}$$

$$\lambda_2 = \lambda_3 = \lambda_4 = u_1, \tag{5.76}$$

$$\lambda_5 = u_1 + c, \tag{5.77}$$

Where c is the local speed of sound; λ_1 and λ_5 are the velocities of sound waves moving in the negative and positive x_1 direction. λ_2 is the convection velocity and the speed at which entropy waves travel. λ_2 and λ_2 are advection velocities in the x_1 direction for u_2 and u_3. Correspondingly,

$$\mathcal{L}_1 = \lambda_1 \left(\frac{\partial p}{\partial x_1} - \rho c \frac{\partial u_1}{\partial x_1} \right), \tag{5.78}$$

$$\mathcal{L}_2 = \lambda_2 \left(c^2 \frac{\partial \rho}{\partial x_1} - \rho c \frac{\partial p}{\partial x_1} \right), \tag{5.79}$$

$$\mathcal{L}_3 = \lambda_3 \frac{\partial u_2}{\partial x_1}, \tag{5.80}$$

$$\mathcal{L}_4 = \lambda_4 \frac{\partial u_3}{\partial x_1}, \tag{5.81}$$

$$\mathcal{L}_5 = \lambda_5 \left(\frac{\partial p}{\partial x_1} + \rho c \frac{\partial u_1}{\partial x_1} \right). \tag{5.82}$$

Referring to Eq. (5.74), u is fixed at the boundary by letting $d_3 = 0$ so that,

$$\mathcal{L}_1 = \mathcal{L}_5. \tag{5.83}$$

To assert v, let $d_4 = 0$ so that,

$$\mathcal{L}_3 = 0. \tag{5.84}$$

To assert T the expressions within Eq. (5.74) are combined to produce,

$$\frac{\partial T}{\partial t} + \frac{T}{\rho c^2} \left[-\mathcal{L}_2 + \frac{1}{2}(\gamma - 1)(\mathcal{L}_5 + \mathcal{L}_1) \right] = 0. \tag{5.85}$$

T is then fixed on the boundary by choosing,

$$\mathcal{L}_2 = \frac{1}{2}(\gamma - 1)(\mathcal{L}_5 + \mathcal{L}_1). \tag{5.86}$$

A partially reflecting pressure boundary condition is implemented by letting,

$$\mathcal{L}_1 = \frac{\sigma a}{L}(1 - \mathcal{M}^2)(p - p_\infty), \tag{5.87}$$

where M is the maximum Mach number in the flow and σ scales the pressure decay time. A high value for σ gives sudden jump of the boundary to the asserted pressure, whereas a low value for σ gives a gentler equalization that takes more time but induces smaller disturbances in the flow.

Qualitatively such boundary conditions can be visualized as "elastic" or "frictional" in that they allow deviations of the variable on the boundary, hence are more accommodating in greatly unsteady situations where exact boundary conditions produce high gradients that cause numerical instability. For solutions that begin with large transients, σ can be varied from low to high as the initial transients die away and steady state is approached. Similar expressions may be constructed for T, and u:

$$d_3 = \sigma_u \frac{c}{L}(1 - \mathcal{M}^2)(u - u_{ref}) \tag{5.88}$$

$$\mathcal{L}_2 = \sigma_T \frac{c}{L}(1 - \mathcal{M}^2)(T - T_{ref}) \tag{5.89}$$

Note that σ is negative for the temperature case due to the sign in Eq. (5.85).

Inlet: At the inlet u and T are specified, and $v = 0$ is always used. Depending on particular problem, the exact or semi-reflecting formulations are used to enforce u and T.

Wall: The wall is represented by a no-slip boundary condition with $u = v = 0$. Also, T is specified on the boundary in order to accommodate heat transfer.

Outlet: P is specified using the semi-reflecting condition in order to propagate outside pressure information back into the domain. Without such a condition, information cannot propagate into the domain and the pressure "floats" without a reference, generally increasing indefinitely.

5.2.4   Numerical stability

Due to the complexity of the compressible Navier-Stokes equations a closed form stability expression is not attempted, and instead the empirical timestep formula suggested by Tannehill (1997) is used to ensure stability, in which

$$\Delta t \le \frac{\sigma (\Delta t)_{CFL}}{1+2/\text{Re}_\Delta}. \tag{5.90}$$

where σ is a safety factor usually of ~ 0.9. The inviscid Courant-Friedrichs-Levy (CFL) condition is given by

$$(\Delta t)_{CFL} \le \left(\frac{|u|}{\Delta z} + \frac{|v|}{\Delta r} + c\sqrt{\frac{1}{(\Delta z)^2} + \frac{1}{(\Delta r)^2}} \right)^{-1}, \tag{5.91}$$

and the mesh Reynolds number is given by

$$\text{Re}_\Delta = \min(\text{Re}_{\Delta z}, \text{Re}_{\Delta r}), \tag{5.92}$$

$$\text{Re}_{\Delta z} = \frac{\rho |u| \Delta z}{\mu}, \tag{5.93}$$

$$\text{Re}_{\Delta r} = \frac{\rho |v| \Delta r}{\mu}. \tag{5.94}$$

5.2.5   Comparison with Other Solutions

Fully Developed Isothermal Compressible Flow

A closed form approximation for isothermal compressible flow is possible in the limit of a small pressure gradient, and this is used to test the correct behavior of continuity and momentum equations in the absence of temperature gradients. For hydrodynamically developed flow:

$$u(r,z) = \frac{1}{4\mu} \frac{dp(z)}{dz} (R^2 - r^2) = 2\left[1 - \left(\frac{r}{R} \right)^2 \right] u_m(z) \tag{5.95}$$

$$\frac{dp(z)}{dz} = -\frac{8\eta Q}{\pi \rho(z) R^4} \tag{5.96}$$

With a low pressure gradient such that in any short section of pipe the flow is approximately incompressible, Eq. (5.96) may be integrated over the axial distance z for a very long pipe (Landau and Lifshitz, 1989) and referenced to the imposed pressure p_b at the outlet,

$$p(z) = \sqrt{p_b^2 - \frac{16\eta Q R_g T}{\pi R^4}(z - L)}. \tag{5.97}$$

Hence, the system is written

$$p(z) = \sqrt{p_b^2 - k_2(z - L)},$$ (5.98)

$$\frac{dp(z)}{dz} = -\frac{k_2}{2p(z)},$$ (5.99)

$$u(r,z) = \frac{1}{4\mu}\frac{dp(z)}{dz}(R^2 - r^2),$$ (5.100)

where

$$k_1 = \frac{R^4}{(16\eta u_{mi})^2},$$ (5.101)

$$k_2 = \frac{1}{2k_1}\left(L + \sqrt{L^2 + 4k_1 p_b^2}\right).$$ (5.102)

Equations (5.98) and (5.100) are compared to the computed flow. To isolate just the continuity and momentum equations the conduction and viscous dissipation terms are set to zero and energy equations rearranged to enforce a zero time rate of change of temperature. If these terms are enabled the results are similar for the parameters given in Table 5-3. The results using these parameters are given in Figs. 5-6 and 5-7.

Tube parameters	
Length	5 m
Inner diameter	1 mm
Wall temperature	300 K

Numerical parameters	
Stability safety factor	0.4
Flow radial discretization	30 points
Flow axial discretization	90 points
Outlet pressure stiffness parameter	300,000
Temporal scheme	RK2
Wall boundary conditions	No slip; Temperature

Flow parameters	
Gas	Hydrogen
Transport properties	Constant
Static temperature at inlet	300 K
Static pressure at outlet	1 atm
Mean inlet velocity	25 m/s (fully developed inlet profile)

Table 5-3: Input parameters for the fully developed isothermal flow test case.

Fig. 5-6: Comparison of computed and reference (analytical) density for the isothermal test case. Computed and reference contours represent 5% of peak density; difference contours represent 0.001% each. The vertical stripes are spurious numerical waves emanating from both inlet and outlet boundary conditions. These spurious waves always occur to some extent in these nonlinear simulations and are most prevalent at a spatial period of two points for centered difference schemes (Colonius, 2004).

The error in the pressure distribution is similar to the error for the density distribution because the flow is isothermal, and the pressure and density are related through the equation of state.
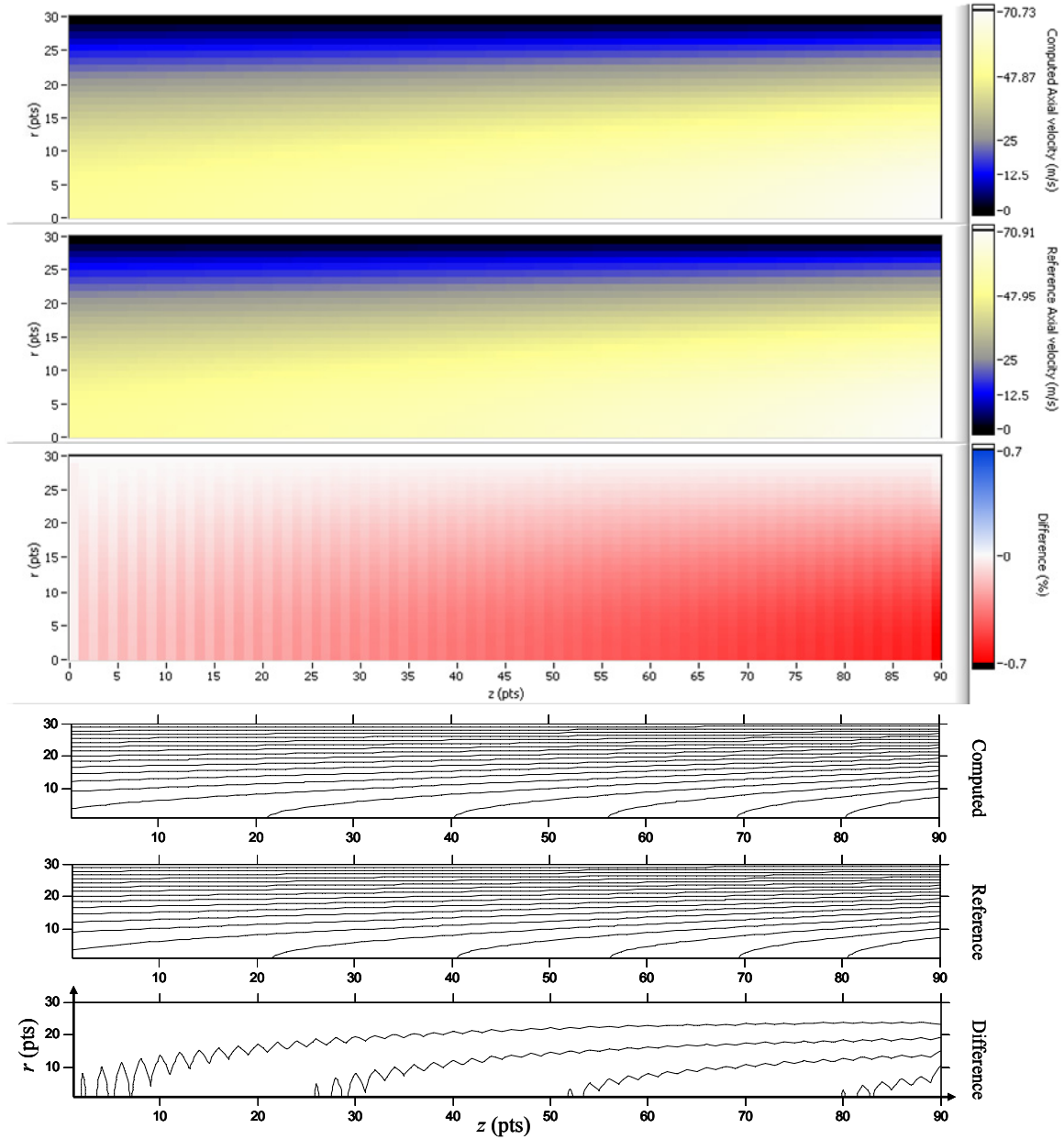
Fig. 5-7: Comparison of computed and reference (analytical) axial velocity for the isothermal test case. Computed and reference contours represent 5% of the peak velocity each; difference contours represent a difference of 0.1% each.

The comparisons given in Figs. 5-6 and 5-7 suggest that the axial velocity is most sensitive to discrepancies between computed and reference results. Experimentation with inlet velocity and tube length confirms that this error is related to the density gradient, and hence is introduced by the approximation used for the analytical isothermal compressible result. Moreover, the parameters given in Table 5-3 were chosen such that the maximum discrepancy is <1% on a coarse grid. Low inlet velocity and a long tube both reduce the pressure gradient, so both reduce error at the expense of increased convergence time.

The velocity error is normalized by the mean inlet velocity in order to deduce the percentage error. In addition to error caused by the density gradient, numerical waves unrelated to the physical solution are visible as vertical stripes. These spurious waves are a consequence of the discrete nature of the Navier-Stokes difference equations, which possess additional unphysical solutions relative to their continuous counterparts. For nonlinear simulations these waves always occur to some extent, though they decay exponentially into the domain and are most prevalent at a spatial period of two points for centered difference schemes (Colonius, 2004).

It is for this reason that first-order boundary conditions are used with a second-order interior, as the reflection coefficient for such a combination ensures that the spurious waves are not amplified.

Thermally Developing Flow

With a Prandtl number of 0.73 a hydrogen channel flow has a profile that develops both thermally and hydrodynamically at the same time. That is to say it is a simultaneously developing flow where the radial profile of u and T vary as a function of z, and for strong continuous heating do so over the entire length of the channel.

There are no closed form solutions for simultaneously developing flow suitable for direct comparison with the Navier-Stokes code, so a closed form solution for thermally

developing but hydrodynamically developed flow (equivalent to a very large Prandtl number) is used here instead (Shah and London, 1978).

Assuming that the flow has constant transport properties, and is incompressible and hydrodynamically fully developed, the temperature distribution a short distance after the inlet is given by the Graetz series:

$$\Theta(r,z) = \frac{T-T_w}{T_e-T_w} = \sum_{n=0}^{\infty} C_n R_n(r) \exp(-2\lambda_n^2 z^*) \tag{5.103}$$

$$\Theta_m(z) = \frac{T_m-T_w}{T_e-T_w} = 8\sum_{n=0}^{\infty} \frac{G_n}{\lambda_n^2} \exp(-2\lambda_n^2 z^*) \tag{5.104}$$

$$\mathrm{Nu}_{z,T} = \frac{\displaystyle\sum_{n=0}^{\infty} G_n \exp(-2\lambda_n^2 z^*)}{2\displaystyle\sum_{n=0}^{\infty} \frac{G_n}{\lambda_n^2} \exp(-2\lambda_n^2 z^*)} \tag{5.105}$$

$$\mathrm{Nu}_{m,T} = \frac{1}{4z^*} \ln\left(\frac{1}{\Theta_m}\right) \tag{5.106}$$

In this case, r is the normalized radius and z^* is the nondimensional axial distance,

$$z^* = \frac{z}{D_h \mathrm{Pe}}. \tag{5.107}$$

In turn, the Péclet number Pe is most conveniently expressed as

$$\mathrm{Pe} = \mathrm{Re}\,\mathrm{Pr}. \tag{5.108}$$

The Graetz series is evaluated using the numerical approach of Housiadas *et al.* (1999), in which the eigenfunction $R_n(r)$ is represented in terms of the confluent hypergeometric function M,

$$R(r,\lambda_n) = \exp\left(-\frac{\lambda_n r^2}{2}\right) M\left(\frac{2-\lambda_n}{4}, 1, \lambda_n r^2\right). \tag{5.109}$$

For practical computation, the confluent hypergeometric function is expanded as power and Bessel series', which are combined in a piecewise fashion to minimize the error.

$$R(r, \lambda_n) = \begin{cases} 1 & r = 0 \\ \exp\left(-\frac{\lambda_n r^2}{2}\right) \sum\limits_{m=0}^{\infty} B_m r^m J_m(\lambda_n r) & 0 < r \le 0.863 \\ \exp\left(-\frac{\lambda_n r^2}{2}\right) \sum\limits_{m=0}^{\infty} A_m (\lambda_n r^2)^m & 0.863 < r < 1 \\ 0 & r = 1 \end{cases} \tag{5.110}$$

$$A_0 = 1, \quad A_m = \frac{4m-2-\lambda_n}{(2m)^2} A_{m-1}, \quad m = 1, 2, \dots \tag{5.111}$$

$$B_0 = 1, \quad B_1 = 0, \quad B_2 = 1/2, \quad B_m = \frac{m-1}{m} B_{m-2} - \frac{\lambda_n}{2m} B_{m-3}, \quad m = 3, 4, \dots \tag{5.112}$$

These approximations are more accurate than an equivalent asymptotic series (given in the same paper) up to $n = 42$. This means that the series solutions are best used for $z^* \ge 8 \times 10^{-5}$ and the following three-term Lévêque solution is used for $z^* < 8 \times 10^{-5}$:

$$\Theta(r, z) = \Theta_0(\xi) + \eta^{1/3} \Theta_1(\xi) + \eta^{2/3} \Theta_2(\xi) \tag{5.113}$$

$$\eta = \frac{9z}{2}, \quad \xi = (1-r)\eta^{-1/3} \tag{5.114}$$

The Graetz solution assumes a developed axial velocity distribution, which is determined from Eq. (5.95) and the mean velocity, deduced at any given z using Q, the (constant) density, and the (constant) area. However, the fully developed velocity profile implies a pressure field that varies with z only, but the incompressible assumption combined with the above expression for temperature implies that the pressure varies with both r and z. The assumptions underlying the Graetz series are therefore mutually inconsistent.

Nevertheless, this inconsistency introduces only a small error provided that one relaxes the incompressibility constraint, and the density field is chosen such that the pressure varies only with z, which is the physically correct behavior. Using the parameters given in Table 5-4 the density in Fig. 5-8 is deduced from the equation of state, the Graetz solution for $T(r, z)$ in Fig. 5-9, and the pressure gradient for the fully developed incompressible case in Fig. 5-10.

Experimentation suggests that the density field obtained in this way is close to the actual density field; however, as the density is allowed to drift, so too do the pressure and

temperature fields. Since the objective is to test the energy equation, the time derivative of the density is set to equal zero to preclude this drift.

Tube parameters

Length	3 m
Inner diameter	1 mm
Wall temperature	400 K

Numerical parameters

Stability safety factor	0.4
Flow radial discretization	30 points
Flow axial discretization	90 points
Outlet pressure stiffness parameter	1,000
Temporal scheme	RK2
Wall boundary conditions	No slip; Temperature

Flow parameters

Gas	Hydrogen
Transport properties	Constant
Static temperature at inlet	300 K
Static pressure at outlet	1 atm
Mean inlet velocity	100 m/s (fully developed inlet profile)

Table 5-4:   Input parameters for the fully developed isothermal flow test case.
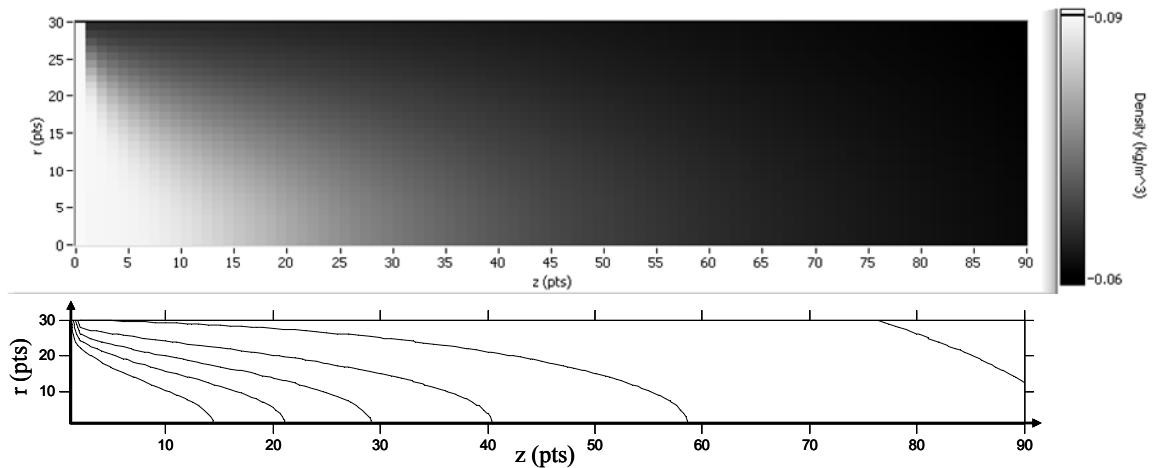
Fig. 5-8: Enforced density distribution for the thermally developing test case. Contours represent 5% of peak value.
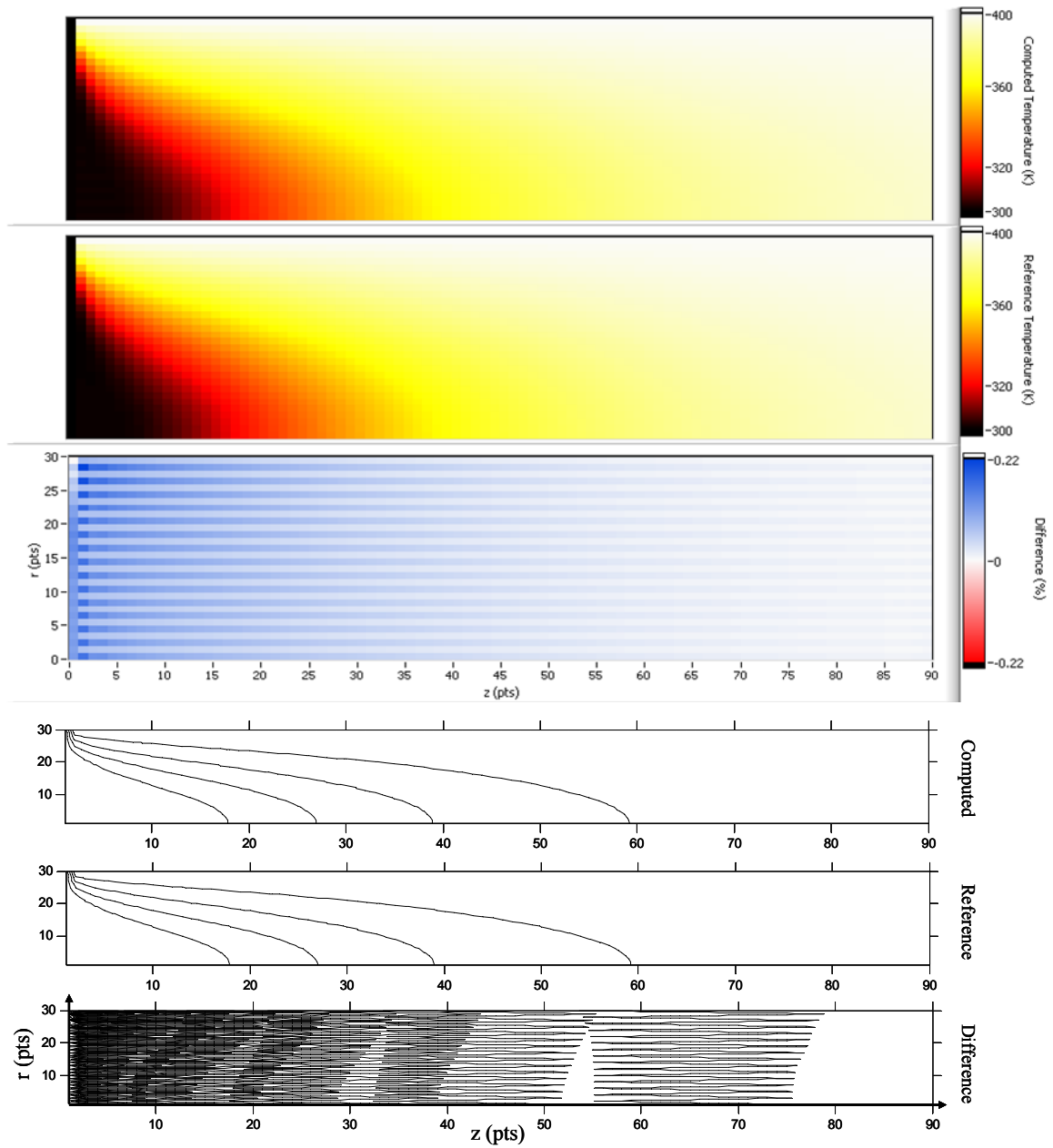
Fig. 5-9: Comparison of computed and reference (analytical) pressure for the thermally developing test case. Computed and reference contours represent 5% of the peak pressure; difference contours represent 0.01% each.
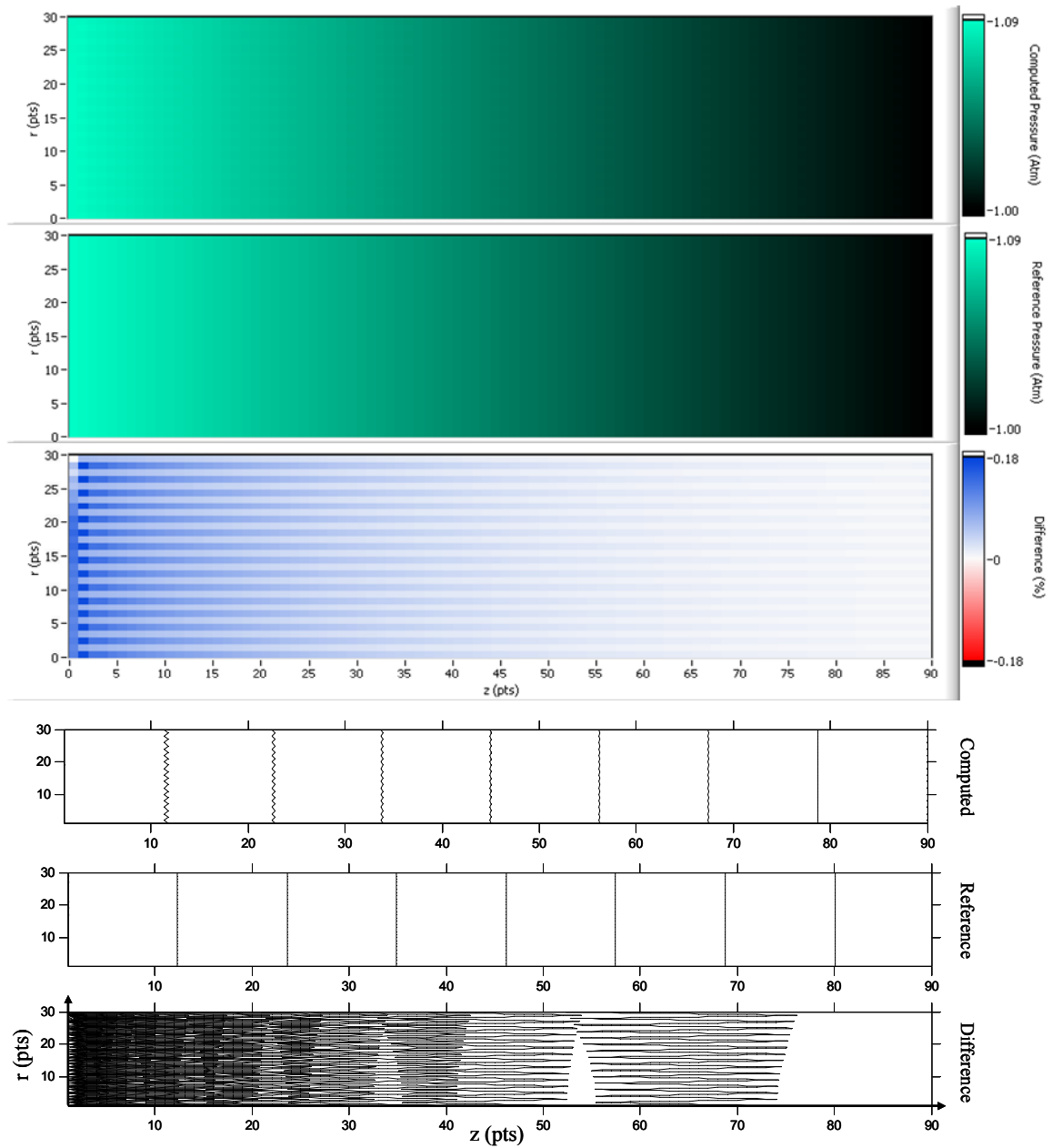
Fig. 5-10: Comparison of computed and reference (analytical) pressure for the thermally developing test case. Computed and reference contours represent 1% of the peak pressure; difference contours represent 0.01% each.

In addition to disabling the time variation of density, the thermal conductivity and viscous dissipation is also be disabled, as the simple Graetz solution presented here assumes that these terms are negligible. The results are calculated with these terms

turned on as the Peclet number for the parameters chosen is around 400, and these effects become important only below 50 or so.

Given all these assumptions, the temperature distribution in Fig. 5-9 converges to within 0.3% of the Graetz solution. The pressure distribution, shown in Fig. 5-10, converges to within 0.2%, with the uniform pressure gradient along the z direction consistent with hydrodynamically developed flow.

Due to the self-inconsistent approximations discussed above there is a 7% error in the axial velocity distribution, shown in Fig. 5-11, which causes an initial transient in the time-dependent solution. Particularly toward the inlet, the difference plot in Fig. 5-11 indicates a non-parabolic distribution, which is consistent with the idea that for a Prandtl number of 0.73 the hydrodynamic profile is in reality developing as the flow is heated.

The net effect is that while the temperature distribution is accurately predicted using the above expressions, the assumptions used introduce a modest error in the velocity distribution, which increases as the wall temperature is raised above the inlet temperature.
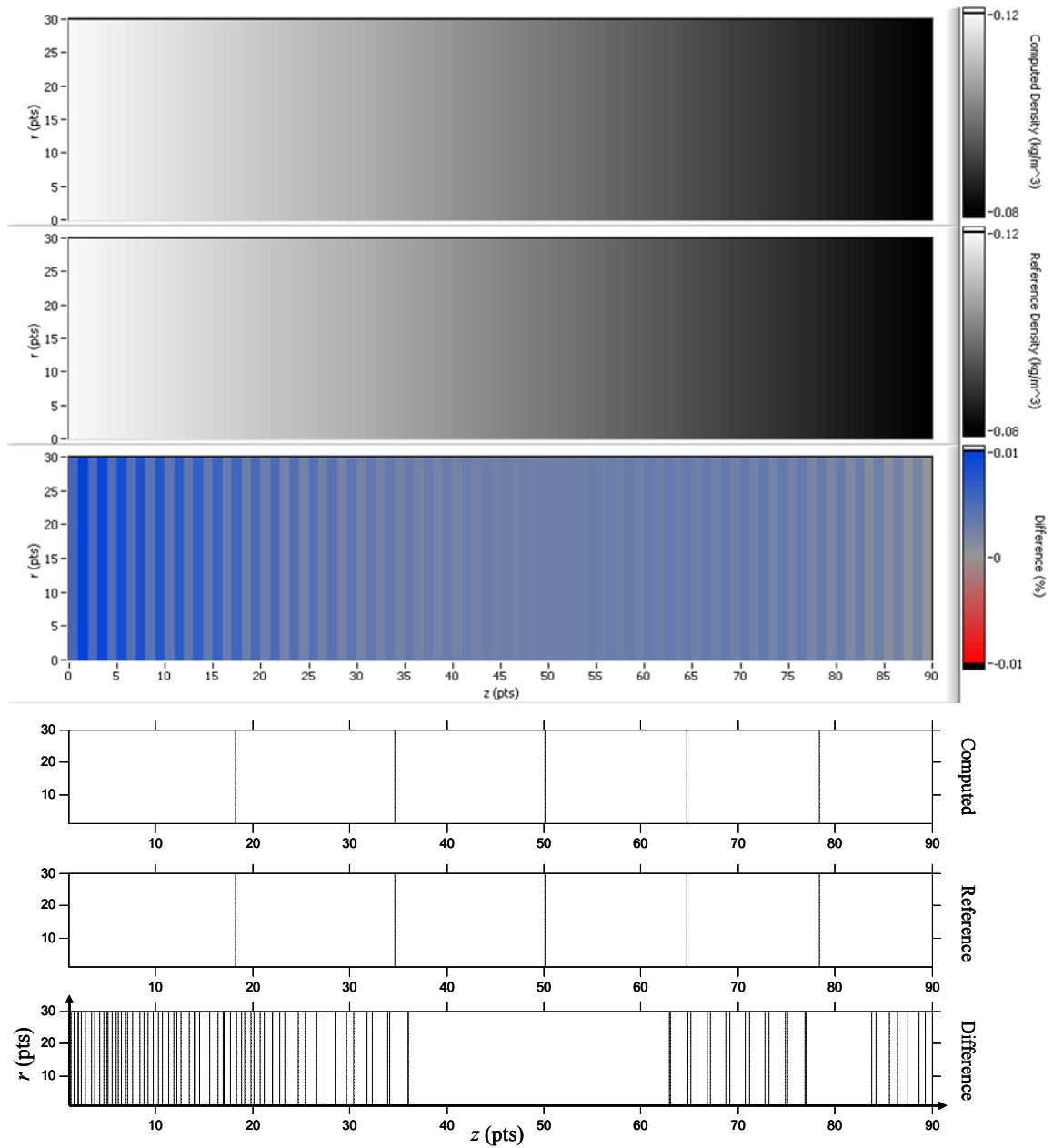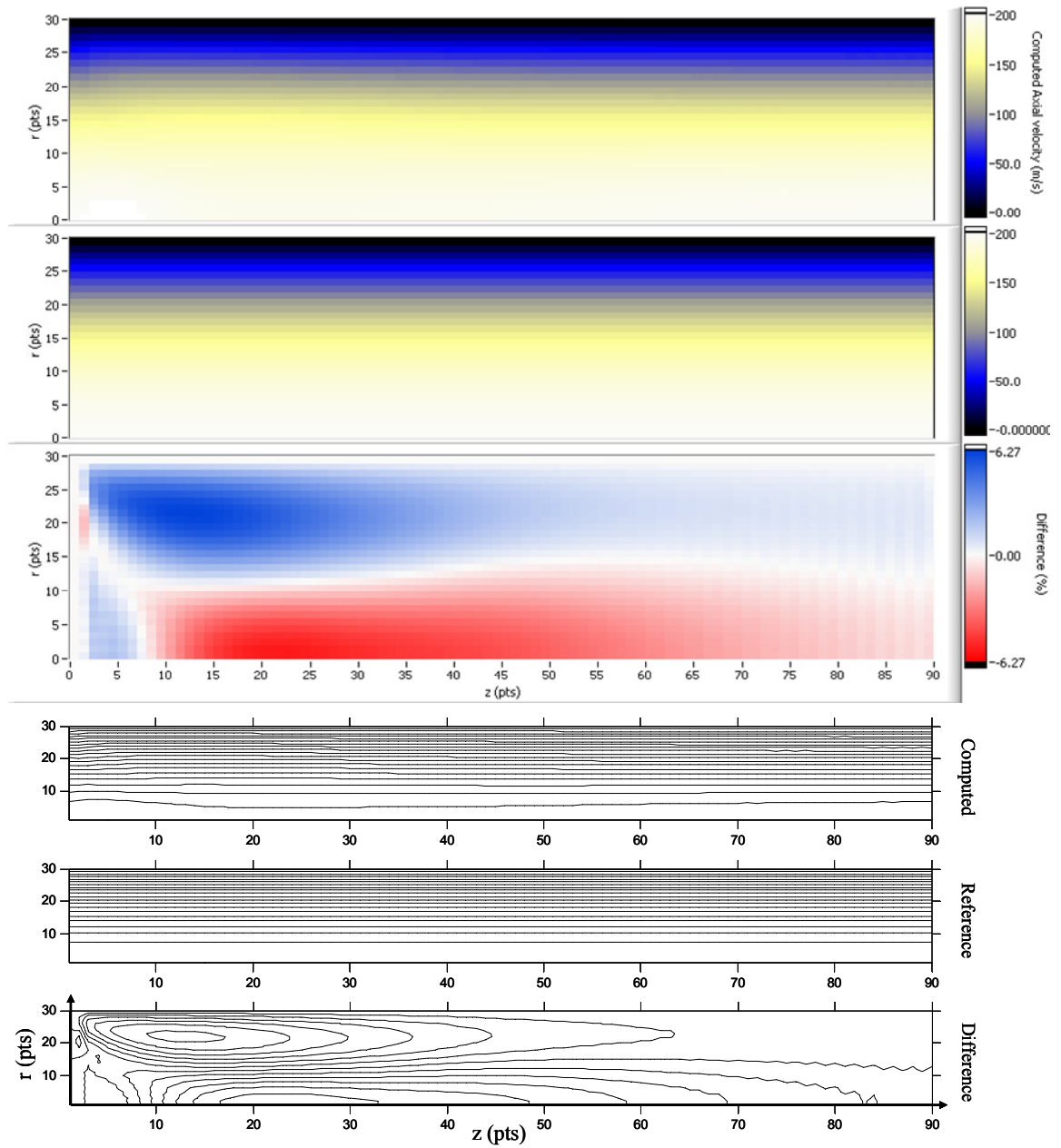
Fig. 5-11: Comparison of computed and reference (analytical) axial velocity for the isothermal test case. Computed and reference contours represent 5% of the peak velocity each; difference contours represent a difference of 0.05% each.

5.3 Comparison of Quasi-1D and 2D Results

It remains to compare the quasi-1D model results to the 2D Navier-Stokes results. The quasi-1D model is capable of modeling all quasi-1D channel geometries and flow regimes for which experimental Nusselt number correlations have been published. However, it is unclear how accurate these predictions are, given that the Nusselt correlations are usually intended for fully developed flow with a constant, linear, sinusoidal or exponentially varying wall temperature or flux.

Using the parameters given in Table 5-5 the 2D Navier-Stokes solution is iterated together with the conduction and electromagnetic model (this method is discussed in the next chapter). The electromagnetic updates are turned off within the first couple of iterations in order to isolate the flow dynamics. The solution is allowed to reach approximately steady state, and the temperature boundary condition used by the Navier-Stokes solution is used to solve the Quasi-1D model.

The results in Fig. 5-12 show good agreement between the flows predicted by the quasi-1D model and the 2D Navier Stokes model. In both simulations, the total energy convected into the flow is similar, and the resulting outlet temperatures and pressure drops, which are of primary interest for overall performance analyses, are in excellent agreement.

The convergence of the code is assessed on the basis of how well energy is conserved and and the agreement between the Navier-Stokes and quasi-1D results. In Fig. 5-12 the cumulative tube input power does not quite reach the specified tube input power in both the Navier-Stokes and quasi-1D cases shown, indicating a small energy loss. For the Navier-Stokes code, experimentation with discretization parameters indicates that this is largely, if not entirely due to discretization errors, as is the slight difference between the cumulative total enthalpy and the cumulative convection (input energy into the flow). Increasing the number of radial points improves accuracy; however, this significantly decreases the rate of convergence. The minimum discretization at which reasonable results were obtained was 16 points by 128 points. Below this number in either direction

caused the unphysical spurious waves to reflect between walls without sufficient damping, and these oscillations amplified over time until the solution collapsed.

Tube parameters	
Length	36.6 mm
Inner diameter	1.19 mm
Outer diameter	1.98 mm
Material	Mullite

Numerical parameters	
Stability safety factor	1
Flow radial discretization	16 points
Flow axial discretization	128 points
Outlet pressure stiffness parameter	100,000
Temporal scheme	RK2
Wall boundary conditions	No slip; Temperature

Flow parameters	
Gas	Hydrogen
Transport properties	Temperature variable
Static temperature at inlet	300 K
Static pressure at outlet	1 atm
Mean inlet velocity	30 m/s
Enthalpy recovery factor (quasi-1D only)	0.85 (square root of the Prandtl number)

Table 5-5: Input parameters for comparison of the quasi-1D and 2D Navier-Stokes channel flow codes.

For the quasi-1D code the discrepancy in energy values in Fig. 5-12 arises because boundary temperatures from the Navier-Stokes code are used, and given this same boundary condition the useful energy absorbed into the flow is less. This does not indicate an energy loss in the quasi-1D code (Fig. 5-2 and Fig. 5-3 indicate excellent energy conservation), rather it indicates that the quasi-1D code underpredicts the overall Nusselt/Stanton number relative to the Navier-Stokes code.
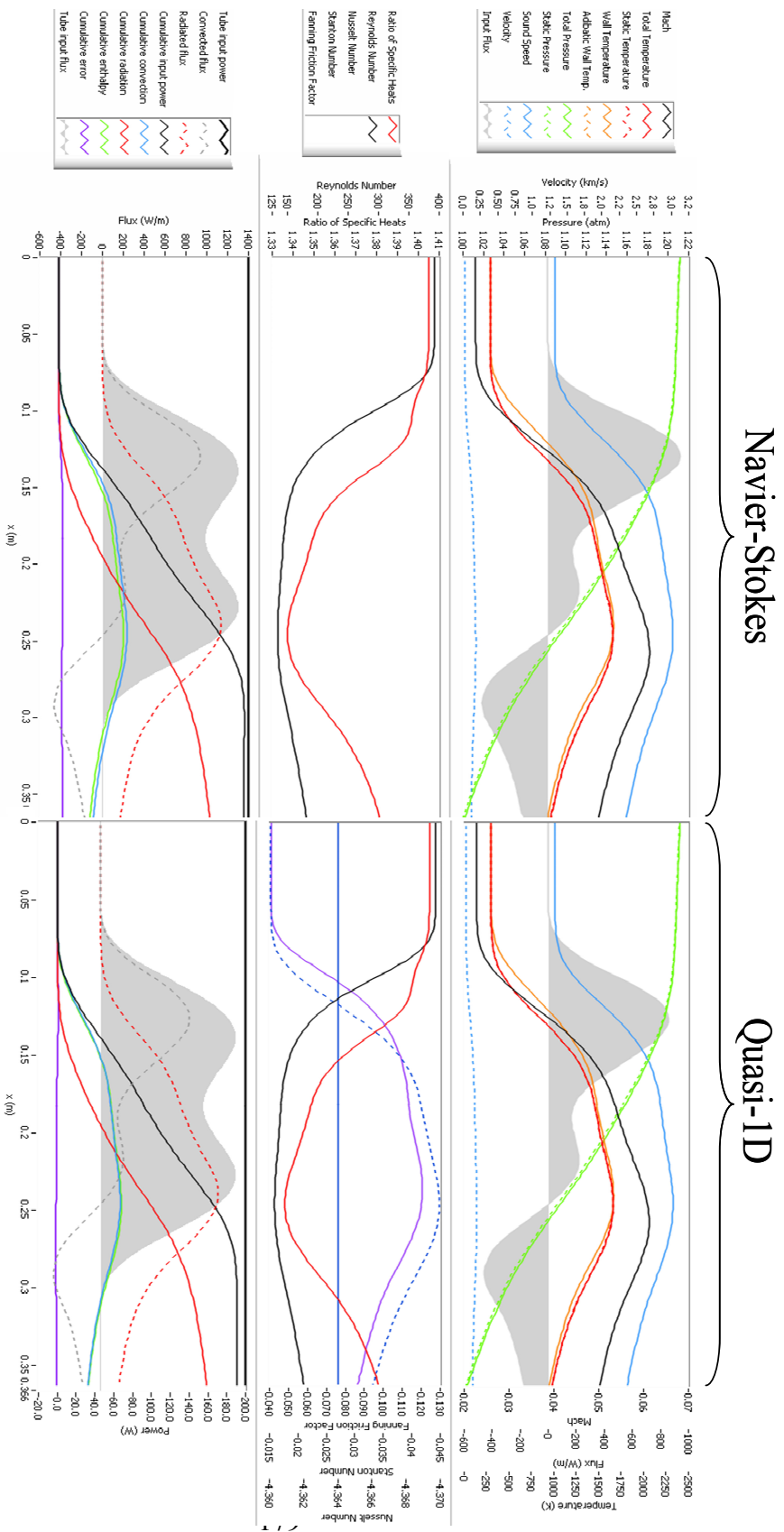
Fig. 5-12: 1D comparison of the quasi-1D and 2D Navier-Stokes channel flow codes.
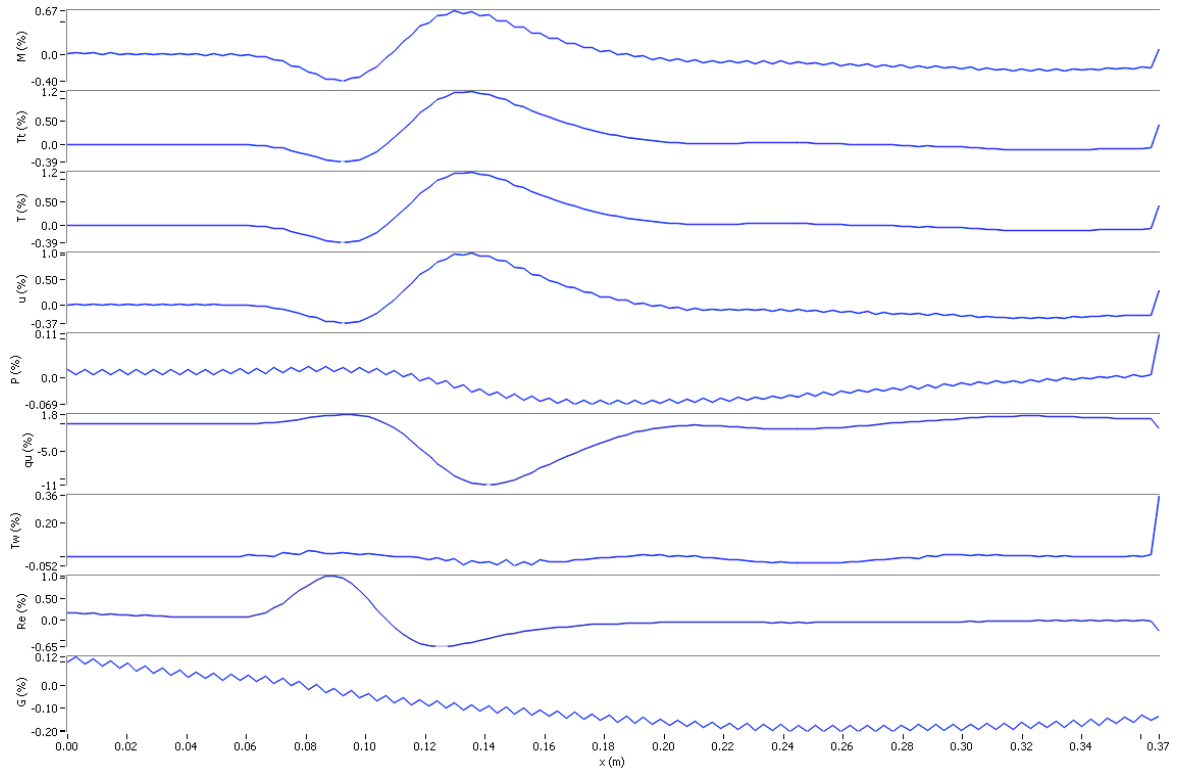
Fig. 5-13: Difference between the quasi-1D and 2D Navier-Stokes channel flow codes.

Referring to Fig. 5-13 the two models differ by less than 2% for most quantities of interest. The main disagreement is for the useful energy q_u, which is the energy convected into the flow, and this difference occurs 6–16 cm into the tube. Comparison to Fig. 5-12, shows that this coincides with the region of highest convective flux, the gray shaded area on the uppermost chart. This is consistent with a Nusselt/Stanton number this is modified by the short region of strong heating but not corrected for by the quasi-1D code.

For the purposes of simulating the flow for conceptual design, total enthalpy is conserved along the channel regardless of the Stanton number. The Stanton number instead determines the temperature (enthalpy) difference between the wall and bulk flow. This temperature difference is most important at the channel outlet, and errors in the Stanton number along the entire tube tend to average out. Similarly, the pressure gradient depends on the Fanning friction factor along the entire tube, and errors tend to average

out also. Therefore, at least in this laminar regime the hydrodynamically developing flow does not unduly affect the quasi-1D results despite the assumption of hydrodynamically developed flow, and provided that the correlations used for Nusselt number and friction factor are accurate, the quasi-1D results are accurate.

5.4   Summary and References

To understand the operation of a microwave thermal thruster entails an understanding of the simultaneously developing flow problem within each heat exchanger channel. For the purposes of thruster conceptual design an accuracy of ~ 20% is all that is needed, depending on the importance of the particular quantity, and this accuracy is more than satisfied by the quasi-1D code, whose rapid execution makes it suitable for to use within an inherently iterative design process.

For detailed design, the 2D Navier-Stokes code gives great insight into the channel flow itself and the conditions under which the quasi-1D code is in error. Indeed, the Navier-Stokes solutions can be used to generate improved Nusselt number and friction factor correlations for difficult cases provided that the flow is well enough resolved. Furthermore, time-dependent channel behavior is expected as experiments switch from single to multiple channels in parallel in the laminar regime (Bussard and DeLauer, 1958), and the Navier-Stokes solver presented here may be used in its capacity to simulate a time-dependent flow in addition to finding steady state solutions.

B. W. Knight, J., McInteer, B.B., *et al.* (1957). *A metal dumbo rocket reactor*. University of California: Los Alamos. p. 385.

Bussard, R.W. and DeLauer, R.D. (1958). *Nuclear rocket propulsion*. McGraw-Hill series in missile and space technology, New York. McGraw-Hill.

Colonius, T. (2004). *Modeling artificial boundary conditions for compressible flow*. Annual Review of Fluid Mechanics **36**: p. 315–345.

Constantinescu, G.S. and Lele, S.K. (2002). *A highly accurate technique for the treatment of flow equations at the polar axis in cylindrical coordinates using series expansions*. Journal of Computational Physics **183**(1): p. 165–186.

Housiadas, C., Larrode, F.E. and Drossinos, Y. (1999). *Numerical evaluation of the Graetz series*. International Journal of Heat and Mass Transfer **42**(15): p. 3013–3017.

Kakaç, S., Shah, R.K. and Aung, W. (1987). *Handbook of Single-Phase Convective Heat Transfer*. Wiley-Interscience.

Kays, W.M., Crawford, M.E. and Weigand, B. (2005). *Convective heat and mass transfer*. 4th ed. McGraw-Hill series in mechanical engineering., Boston. McGraw-Hill Higher Education.

Landau, L.D. and Lifshitz, E.M. (1989). *Fluid mechanics*. 2nd ed, Oxford, England; New York. Pergamon Press.

Poinsot, T.J. and Lele, S.K. (1992). *Boundary-Conditions for Direct Simulations of Compressible Viscous Flows*. Journal of Computational Physics **101**(1): p. 104–129.

Shah, R.K. and London, A.L. (1978). *Laminar flow forced convection in ducts : a source book for compact heat exchanger analytical data*, New York. Academic Press.

Shapiro, A.H. (1953). *The Dynamics and Thermodynamics of Compressible Fluid Flow*. Vol. 1, New York. The Ronald Press Company.

Tannehill, J.C., Anderson, D.A. and Pletcher, R.H. (1997). *Computational fluid mechanics and heat transfer*. 2nd ed. Series in computational and physical processes in mechanics and thermal sciences., Washington, DC. Taylor & Francis.

CHAPTER 6
THE COUPLED ELECTROMAGNETIC-CONDUCTION-CONVECTION PROBLEM

6.1   Problem Formulation

In the experimental and theoretical motivation of § 3.1 a coupled electromagnetic-conduction-convection problem is suggested for the design and optimization of practical and reliable microwave thermal thrusters.   There is equivalence between the coupled models necessary to design a microwave thermal system at full-scale and the laboratory-scale examined here.   This equivalence is seen in the montage of Fig. 6-1, which draws upon images and results given in the preceding chapters in order to show how they build toward a model and methodology for the design of future experiments and thrusters.

Both the electromagnetic field distribution over a heat exchanger and the convection within it profoundly affect the temperature distribution of the heat exchanger structure. This temperature distribution has implications for thermal stresses, thermal delamination, high temperature creep rate, dopant diffusion and radiative losses from the thruster.   It also affects absorption efficiency via the stratified layer model and indirectly the I_{sp} and thrust-to-weight ratio of the propulsion system and vehicle as a whole.   An understanding of the temperature distribution of all matter over the region of space in which high temperature materials and gases interact (the heat exchanger) in the fully coupled case is therefore central to the ability to design reliable, long life and high performance microwave thermal thrusters.

In Fig. 6-1 the most significant difference between the present model of an experimental system and the model needed for a full-scale system is that in the experimental case the macroscopic distribution of incident microwave intensity is a function of the material complex permittivity throughout the domain.   This gives rise to a number of performance reducing instabilities that will not exist in a full-scale free-space system.   These

instabilities, which arise from the nature of resonant cavity modes, were first described for the case without flow in § 4.4.1 and do indeed arise again for the case with flow.
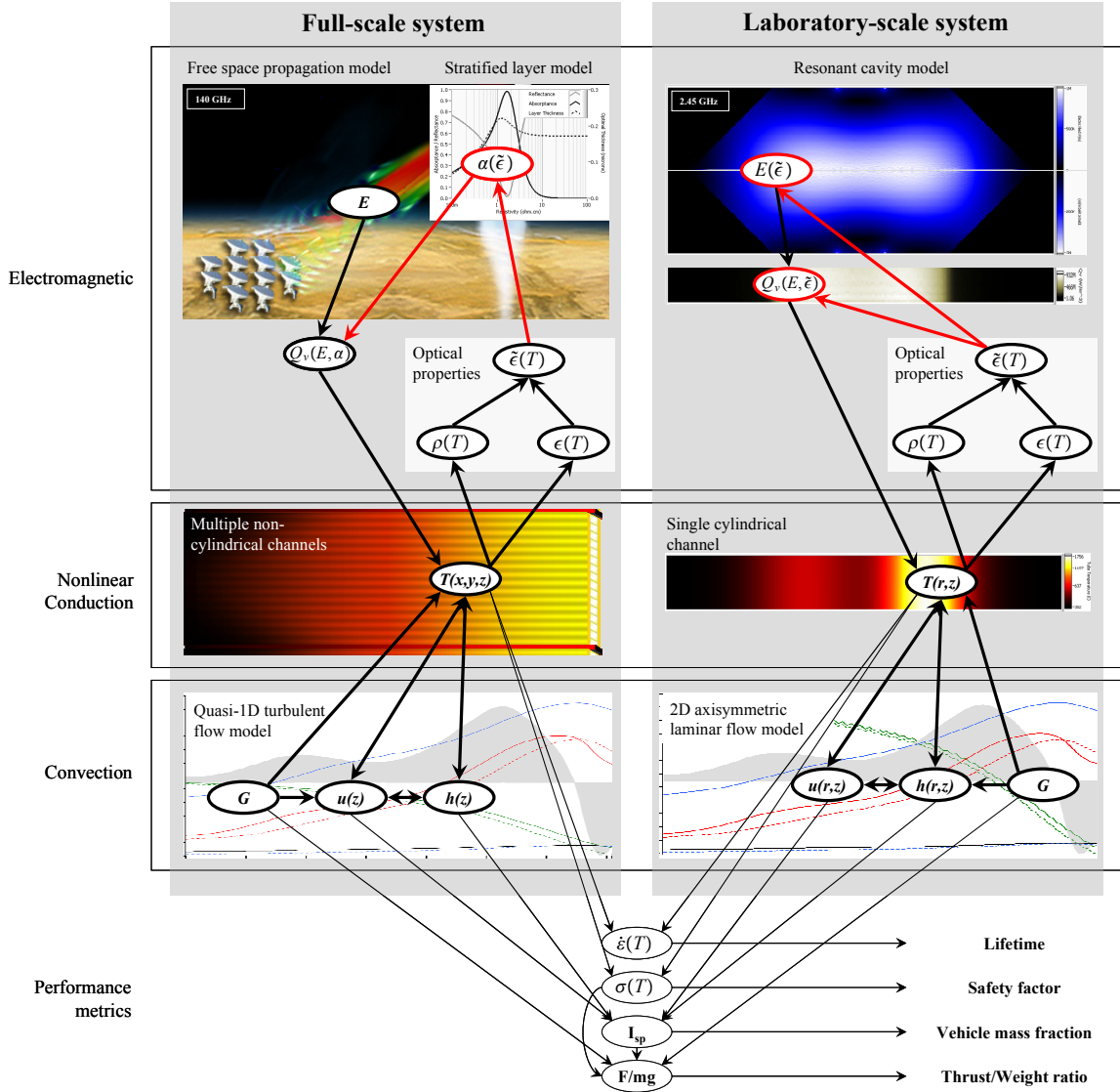
Fig. 6-1: Commonality and differences between the fully coupled performance modeling at laboratory and full-scale.

Returning to the mechanics of the numerical modeling, the coupled electromagnetic-conduction-convection problem builds upon the coupled electromagnetic-conduction

model given in Chapter 4 by adding a final convection stage to the iteration procedure, as shown in Fig. 6-2.
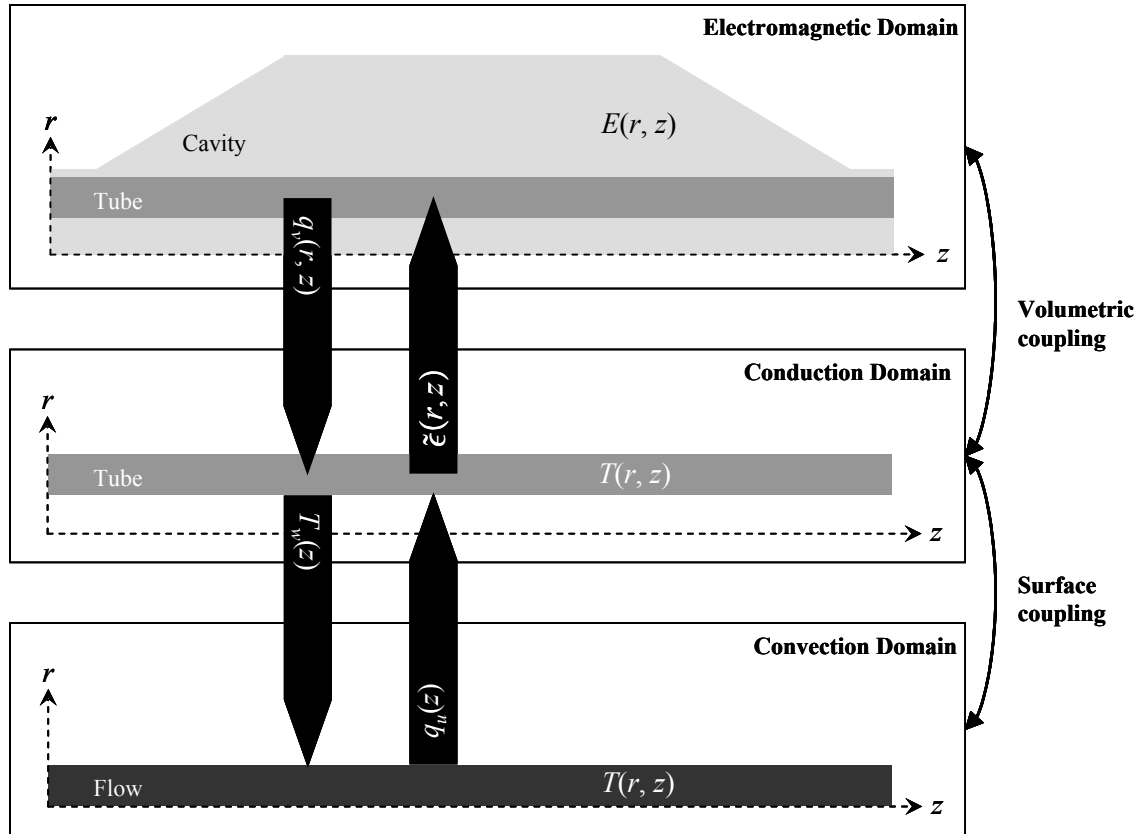
Fig. 6-2: The coupled electromagnetic-conduction-convection model.

This time, coupling is via the surface boundary conditions as opposed to volumetric conditions, whereby the surface heat flux is calculated by the convection model and returned as the inner surface flux condition for the tube in the conduction model. In previous chapters this surface was treated as adiabatic. In turn, the conduction model advances the temperature distribution another timestep and returns the inner wall temperature to the convection model. For the 2D Navier-Stokes finite difference model this temperature is the temperature of the wall nodes; for the quasi-1D model it is used to deduce wall enthalpy.

The false transient method used previously extends to encompass the convection model in this case. If the quasi-1D convection model is used, its solution is already steady state and so the conduction model becomes the rate-determining step for the solution of the fully coupled problem. Both the electromagnetic and convection models are updated together once every few hundred to few thousand iterations of the conduction model.

If the 2D Navier-Stokes convection model is used, this typically has a much shorter timestep than the conduction model timestep, and requires several hundred iterations per conduction timestep for the problem geometries of interest here. The maximum convection timestep is not known *a priori* and stepping is continued until the elapsed time reaches the same duration as the last conduction timestep. This is a matching of pseudo-time, as opposed to realtime, because of the variable effective specific heat capacity of the conduction model (the basis of the false transient method). In essence, the conduction and convection models are solved simultaneously at different timescales, which somewhat alleviates the numerical stiffness caused by the thermal inertia of the tube, at the expense of introducing potentially unphysical coupled interactions between the domains evolving on different timescales.

6.2   Quasi-1D Results

The tapered TM_{011} cavity is simulated using a conventional size of mullite thermocouple tube, about 30% of maximum magnetron power and a hydrogen gas. Initially, the quasi-1D convection model is used with the parameters given in Table 6-6 for a fast solution.

Tube parameters

Length	36.4 cm
Inner diameter	1.19 mm
Outer diameter	1.98 mm
Material	Mullite
Ambient temperature	350 K

Cavity parameters

Inner Diameter	9.85 cm
Taper end diameter	2 cm
Choke end diameter	0.7 cm
Cylindrical main section length	14.7 cm
Left taper length	5.2 cm
Right taper length	5.2 cm
Choke length (both ends)	5.65 cm
Drive point length	25.527 mm (60% of waveguide height)
Offset from center of cylindrical main section	0.075 cm (toward the right / outlet)
Frequency	2445 MHz
Input power	215 watts

Numerical parameters

Stability safety factor	1
Tube radial discretization	8 points
Tube and flow axial discretization	512 points
Electromagnetic finite element mesh configuration	Adaptive
Iteration multiplier	100 tube temperature updates per EM and convection update

Flow parameters

Gas	Hydrogen
Transport properties	Temperature varying
Static temperature at inlet	300 K
Static pressure at outlet	1 atm
Mean inlet velocity	23.86 m/s

Table 6-6: Input parameters for the quasi-1D coupled simulation.

Referring to Fig. 6-3 the simulation initially converges toward a steady state in which the Q value of the tube decreases as it heats up, so that the majority the power begins to be dissipated into the tube rather than the cavity walls. A heated region of tube develops in a similar spot to the simulations for a tube without flow, and the presence of the flow in

this case "drags" the hot region downstream toward the outlet, giving a solution similar to Fig. 6-4.
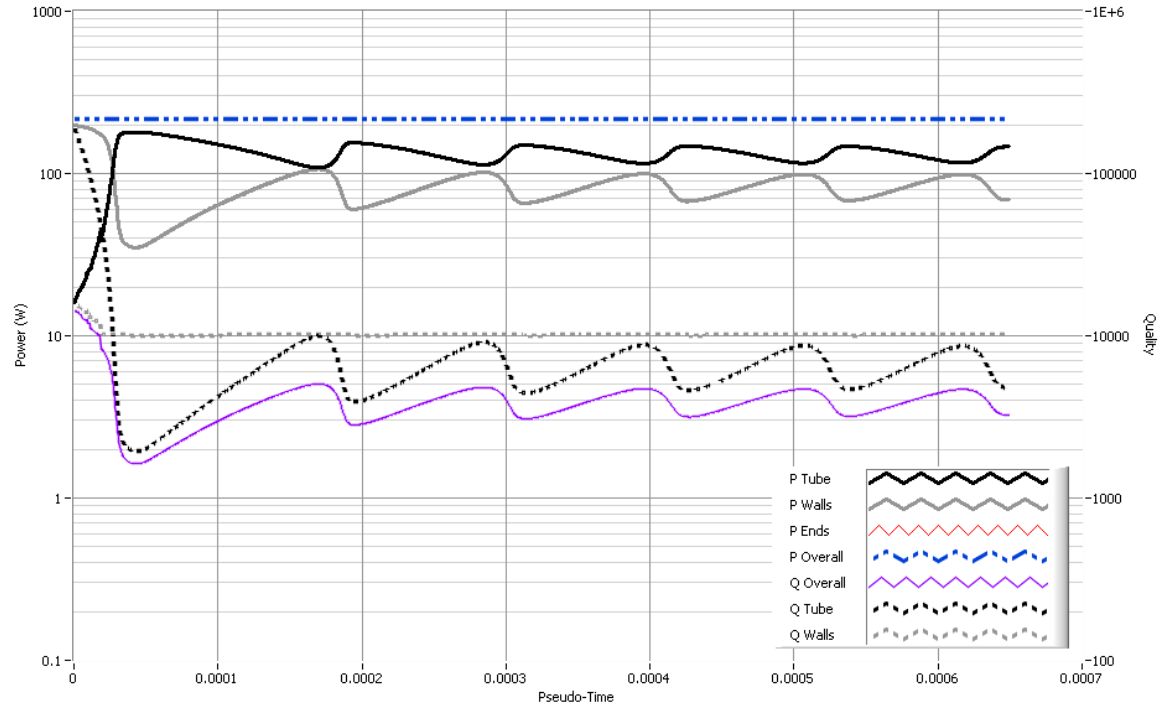
Fig. 6-3: Course of the quasi-1D coupled simulation solution.

However, instead of reaching steady state, the flow continues to drag the tube heating region into the converging section of the cavity. The converging section forces the E-field to zero, and the stable heating region is extinguished. This phase corresponds to the declining power absorbed in the tube beginning at pseudo-time $t = 5 \times 10^{-5}$ and ending at pseudo-time $t = 1.8 \times 10^{-4}$ with a minimum in the power absorbed. A region of tube upstream and ahead of the converging section of the cavity then rapidly heats, and the cycle begins again. Given that both the electromagnetic model and the quasi-1D convection model are time-independent, the source of the oscillation must logically be the conduction model.

- 188 -
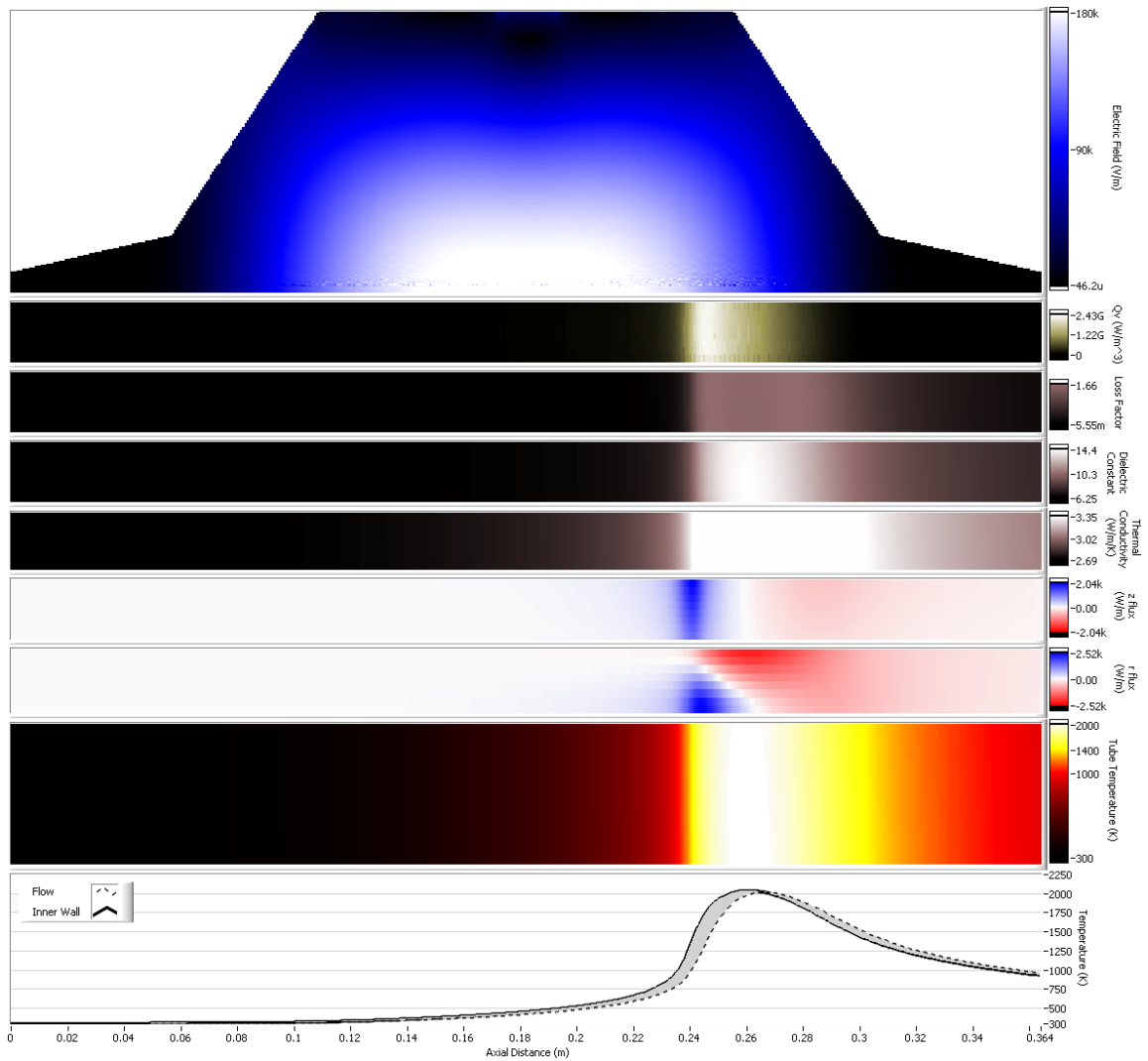
Fig. 6-4: Simulation of tube heating in the tapered TM_{011} cavity (quasi-1D convection model). For each tube quantity, the bottom edge of the intensity plot corresponds to the inner radius and the top edge corresponds to the outer radius of the tube. For the electric field, the bottom edge corresponds to the axis and the top edge to the radius of the cavity.

The oscillation continues on, with each cycle bringing the overall solution closer to steady state. For the parameters used in the present example, which correspond to experimental parameters from the next chapter, the steady state requires a probative amount of computer time. The simulation is stopped at a point where the net energy into and out of the tube is balanced, as can be seen at the bottom of Fig. 6-5 by comparing the

tube input power (calculated in the electromagnetic model) to the cumulative input power (calculated from the sum of cumulative convection and radiation).
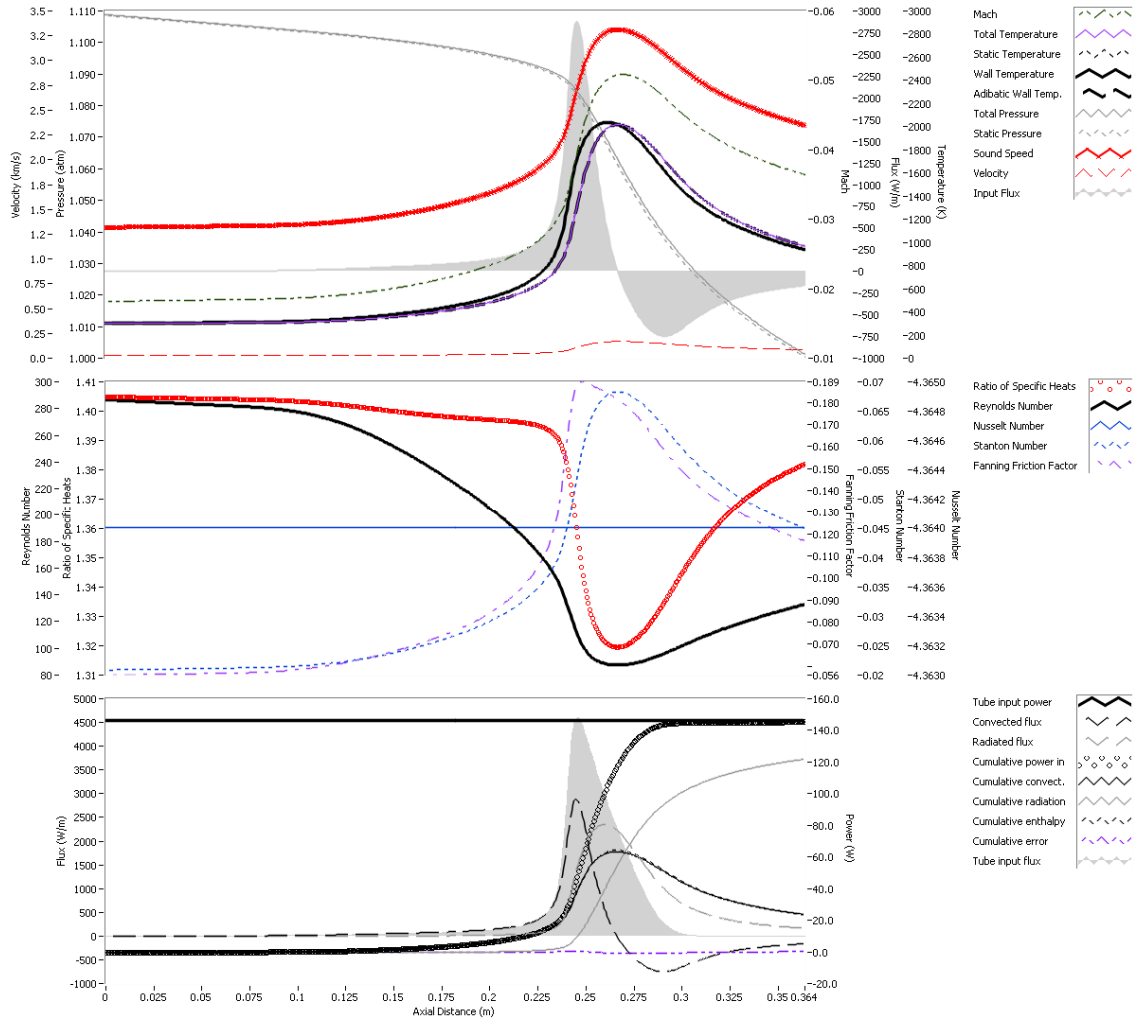
Fig. 6-5: Convective heat transfer in the tapered TM_{011} cavity (quasi-1D convection model).

The solution in Fig. 6-4 shows a heating region that has been shifted to the right by the convection with the flow and whose temperature gradient has been steepened on the left and made shallower on the right by the absorption and subsequent deposition of energy from the flow. Due to the low mass flow rate used, most of the energy convected into the

flow is subsequently lost to radiation from the tube, which is seen by comparing the cumulative convection and cumulative radiation lines in the lower chart of Fig. 6-5.

Referring again to Fig. 6-5 the hydrogen flow becomes more viscous as it heats up, bringing the Reynolds number (middle chart) down from 190 at the inlet to a minimum of 100 at a distance 27 cm downstream. The increased viscosity gives rise to a much increased pressure gradient (top chart), and in this way the pressure drop across the tube is related to the temperature of the flow within it and the length of the high temperature heating region.

The constant Nusselt number seen in the center chart of Fig. 6-5 is a consequence of the Nusselt number correlation used for the quasi-1D model. This correlation assumes a constant wall flux, which can be shown analytically to give a constant Nusselt number flow. Clearly, the convected flux (lower plot) is far from constant in this case, and a Navier-Stokes solution is used next to verify whether or not the results are accurate.

6.3   2D Navier-Stokes Results

Using the same parameters as the quasi-1D simulation in the previous section, the 2D Navier-Stokes simulation is used to verify the results. Because of the CPU time involved in the Navier-Stokes simulation, the tube input power is the specified input parameter so that the solution does not oscillate as readily. This is as opposed to specifying the cavity input power, which allows the simulation itself to determine the distribution of input energy between the tube and cavity walls. The value of 145 watts for the tube input power is determined from the lower chart of Fig. 6-5 and used together with the other input parameters shown in Table 6-7.

The stability and convergence of this coupled code was ascertained from a number of trials preceding the one presented here. Table 6-7 specifies only 16 points for radial discretization, which was necessary to produce a long enough timestep for practical computation on a desktop computer. This level of discretization balances speed with error introduced in the energy balance. Energy conservation was somewhat improved if

the first-order flux boundary condition of the Navier-Stokes model was replaced with a second-order one. The consequence of this substitution is that the unphysical spurious waves generated in the Navier-Stokes solution appeared to propagate into the conduction domain. With 128 or 256 point discretization in the axial direction the temperature in the conduction model began to spatially and temporally oscillate in the immediate viscinity of the very steep gradient encountered at ~ 25 cm along the channel. Increasing the axial discretization to 512 points eliminated this problem, provided that the iteration mulitiplier was limited to around 500 tube temperature updates per electromagnetic update.

Tube parameters	
Length	36.4 cm
Inner diameter	1.19 mm
Outer diameter	1.98 mm
Material	Mullite
Ambient temperature	350 K
Input power	148 watts

Cavity parameters	
All	As in Table 6-6

Numerical parameters	
Stability safety factor	1
Tube radial discretization	16 points
Flow radial discretization	16 points
Tube and flow axial discretization	512 points
Electromagnetic finite element mesh configuration	Adaptive, ~ 70,000 elements used
Outlet pressure stiffness parameter	1000
Iteration multiplier	500 tube temperature updates per EM update

Flow parameters	
Gas	Hydrogen
Transport properties	Temperature varying
Static temperature at inlet	300 K
Static pressure at outlet	1 atm
Mean inlet velocity	23.86 m/s

Table 6-7: Input parameters for the 2D Navier-Stokes coupled simulation.

Fixing the tube input power does indeed dampen down the cavity oscillations, as seen by the cavity Q values and powers shown in Fig. 6-6. Due to the exceptionally small

timestep involved, the cavity does not quite reach steady state in this case, and this is seen in Fig. 6-8 by the slight difference between the tube input power specified and the power transferred from the tube to the flow. This difference arises because the tube material temperature has not yet reached steady state and some of the energy is still going into heating the material.
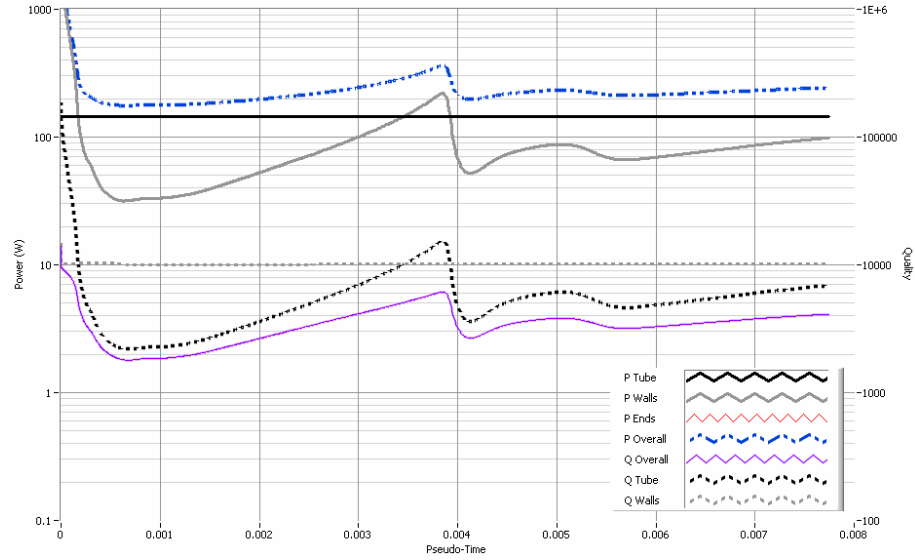
Fig. 6-6: Simulation of tube heating in the tapered TM_{011} cavity (2D Navier-Stokes convection model).

Also visible at the bottom of Fig. 6-7 is a slight difference between the cumulative convected energy (thin black line) and the cumulative enthalpy deduced directly from the flow (thin dashed black line). This difference arises from the time variation of the flow and again indicates that steady state has not yet been reached in the flow.

Additionally, discretization errors affect all these energy comparisons, and the coarse mesh used in this example exaggerates these problems. Despite this coarse mesh, the results in Fig. 6-7 are similar to those in Fig. 6-5. The main difference between these two figures is that the Nusselt number, Fanning friction factor and Stanton number are not calculated for the Navier-Stokes flow.

- 193 -
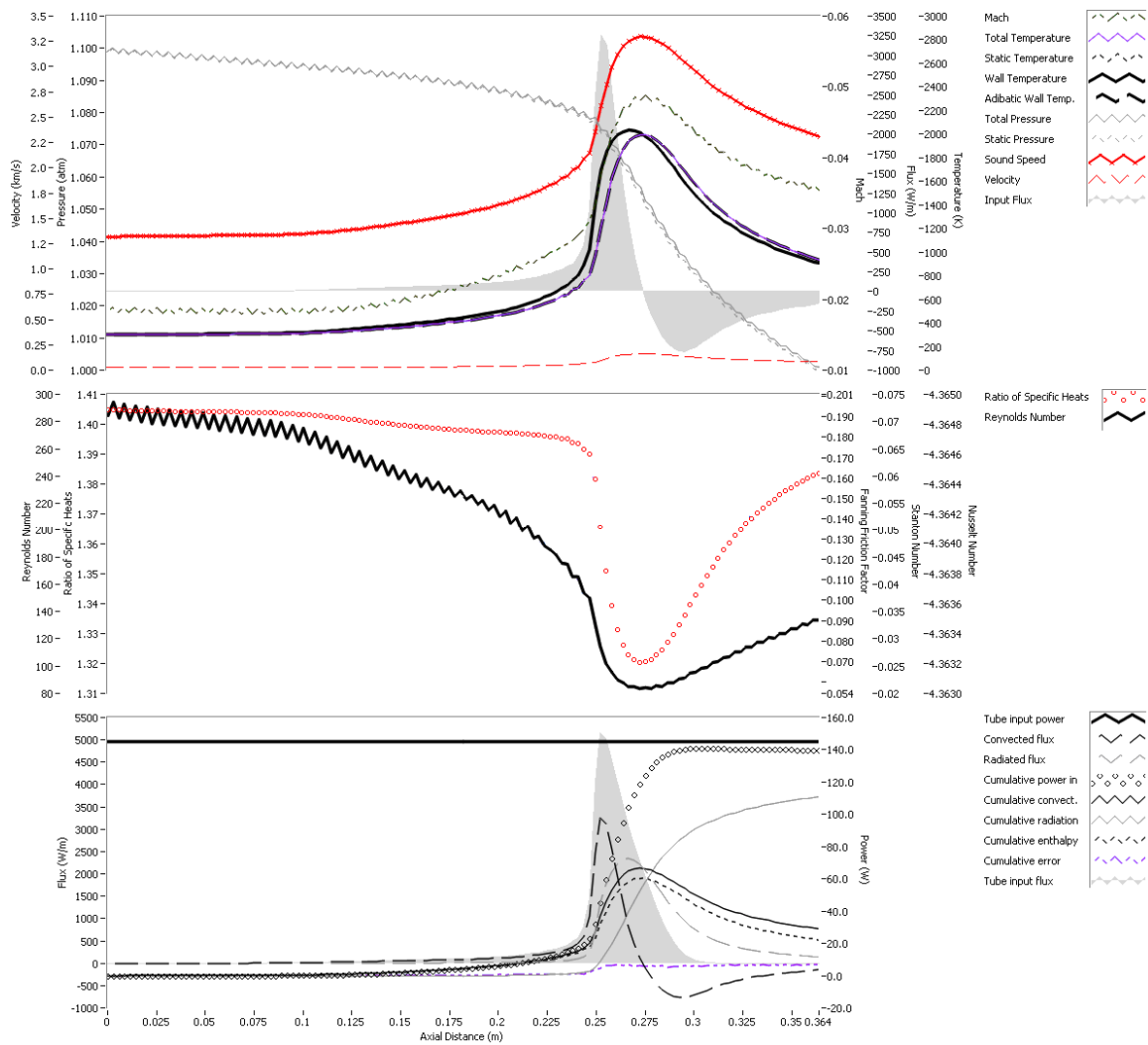
Fig. 6-7: Simulation of tube heating in the tapered TM_{011} cavity.

A composite of the complete state of the cavity, tube and flow is given Fig. 6-8. While the coarse discretization is more evident in this figure than Fig. 6-4, the Navier-Stokes code reveals the way in which the flow temperature varies in the radial direction as the propellant flows (to the right). In turn, the large flux entering the flow toward the right side of the cavity is partitioned into thermal and kinetic parts, with the kinetic energy accelerating the flow to a peak velocity of 321 m/s.
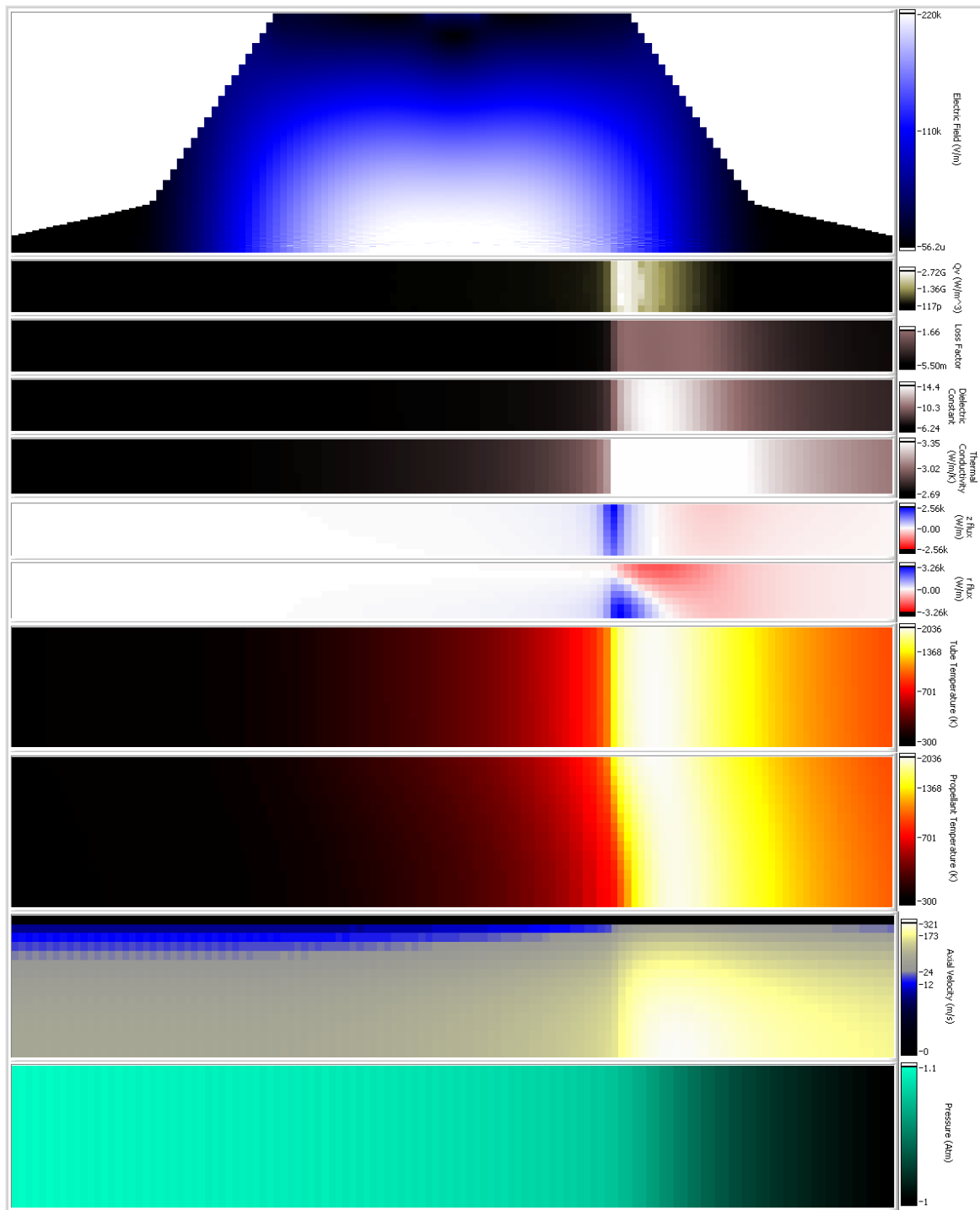
Fig. 6-8: Simulation of tube heating in the tapered TM_{011} cavity. For each tube quantity, the bottom edge of the intensity plot corresponds to the inner radius and the top edge corresponds to the outer radius of the tube. For each flow quantity, the bottom edge corresponds to the axis the top edge to the inner tube radius. For the electric field, the bottom edge corresponds to the axis and the top edge to the radius of the cavity.

As expected, the pressure gradient varies only in the axial direction, and the region of highest axial velocity corresponds to the region of highest pressure gradient. The simulation is stable, although spurious numerical waves are generated as the tube heats strongly and pressure oscillations are generated in the tube. These waves and oscillations die down relatively quickly as the flow reaches steady state, and a finer mesh reduces them considerably.

6.4 Summary and References

The fully coupled electromagnetic-conduction-convection code is suggested in § 3.1 for the design and optimization of practical and reliable microwave thermal thrusters. The coupling of these three models is successfully achieved for both the quasi-1D convection model and the 2D Navier-Stokes convection model.

Using input parameters that correspond to experiments in the next chapter, the quasi-1D variant of the fully coupled model predicts an unsteady oscillatory behavior that arguably arises due to conduction, given that the nonlinear conduction model is the only time-dependent model used in this variation of the code.

The 2D Navier-Stokes variant of the fully coupled model reproduces a similar solution to the quasi-1D solution, but in this case, the energy input to the tube is fixed so that unsteadiness in the conduction model is suppressed. This is necessary because the CPU time required for the oscillating solution with a Navier-Stokes flow solver is prohibitive. Furthermore, the mismatched conduction and convection timescales used in the false transient solution technique would otherwise complicate matters.

The mismatched timescale technique is partly justified because only the steady state solution is of interest here. However, the unexpected oscillatory solution perhaps underscores the fact that the final solution is non-unique and therefore a function of the way in which the solution evolves in time. Nevertheless, physical reasoning suggests that the dominant non-unique behavior is caused by the temperature hysteresis of the tube material, as shown by Jackson & Barmatz (1991) for the case of an alumina bead. The

dilemma of whether or not the oscillations and non-uniqueness cause the simulation to converge upon an incorrect solution is perhaps best resolved by experiment.

Finally, it is emphasized that the simulation presented here evolved very much in parallel with the experimental configuration described in the next chapter. Several hundred simulation runs similar to those presented in this chapter were used to design a series of five successive resonant cavities. The results presented in this chapter and the next pertain to only the last (and most refined) cavity that was tested.

Jackson, H.W. and Barmatz, M. (1991). *Microwave-Absorption by a Lossy Dielectric Sphere in a Rectangular Cavity*. Journal of Applied Physics **70**(10): p. 5193–5204.

CHAPTER 7
EXPERIMENTAL MEASUREMENTS OF THRUSTER TEMPERATURE AND PERFORMANCE

It is desirable as a first step to provide a small, low power laboratory-scale proof of principle for the microwave thermal thruster that demonstrates the two key physical processes of microwave thermal propulsion: (a) To heat a refractory tube using microwaves, and (b) for the tube in turn to heat a flowing propellant.

Both objectives turn out to be possible, and furthermore, some limited measurements are possible using optical pyrometers to measure the tube surface temperature. In the experiments and results documented below the limitations of optical pyrometers for this particular task become apparent; nevertheless, useful comparisons can still be made.

7.1 Apparatus

7.1.1 Summary

In the resonant cavity approach to creating a microwave thermal heat exchanger, the experimental setup shown in Fig. 7-1 can be viewed as a microwave transmission line in which the resonant cavity (the load) is impedance matched to the microwave source (the magnetron) in order to maximize the power transfer efficiency. This impedance matching is accomplished using a three-stub tuner, and the least sensitive stub is motorized for computer-controlled fine-tuning, which is needed to adjust for changes in the tube and cavity temperature.

The power absorbed in the load (the cavity and tube together) is deduced using the forward power measured by the magnetron unit itself and the reflected power measured by a microwave diode connected to the directional coupler. Power reflected by the load is redirected into the dummy load by the circulator, and the resulting heat is carried away by a water cooling system.
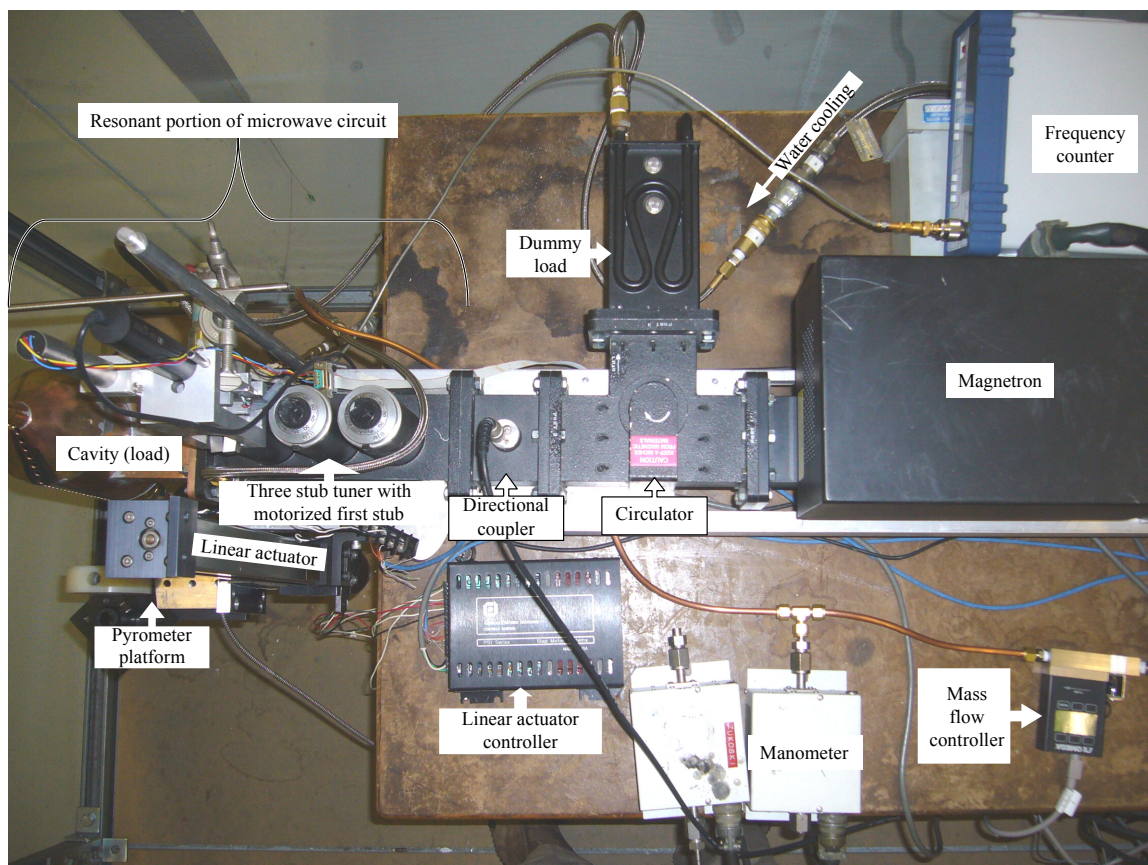
Fig. 7-1: Overview of the experimental setup.

The key equipment seen in Fig. 7-1 is summarized in Table 7-1 below. With the addition of a microwave frequency counter, it is also possible to deduce the E-field along the cavity axis, and this experiment is described shortly.

Item	Specification
Magnetron	Astex. 50–800 watts forward power. Can tolerate any voltage standing wave ratio (VSWR) without damage.
Pyrometer 1	Luxtron Accufiber M100 C. Fiber optic 950 nm single frequency
Pyrometer 2	Everest 8–14 microns bandwidth
Mass Flow Controller	Omega FMA 1600A. 0–20 SLPM; 1–10 atm pressure
Frequency Counter	BK Instruments. 0–3.5 GHz

Table 7-1: Summary of key equipment.

The surface temperature of the tube is measured using two optical pyrometers mounted on an actuated platform in order to measure tube surface temperature as a function of axial position.

For experiments with a flowing gas, a mass flow controller is used to provide and maintain a given flow rate. The particular controller used here also measures downstream pressure, another useful flow diagnostic. In order to guard against the (thankfully rare) scenario that a gas bottle regulator fails and subjects the pipes to the full bottle pressure, metal tubing and high pressure valves and fittings are used.

The experimental logistics involved in data gathering and iterating though many configurations (not presented here) toward a final experimental configuration necessitates computer automation of many aspects of the experiment, for which the *LabView* system is used. In any unforeseen scenario, software can crash and on-screen controls are cumbersome. Therefore, primary cutouts for the gas supply and the microwave system are manual, quickly operated and kept within easy reach. In addition, the mass flow controller is normally closed if power fails, and there is a microwave leakage detector and cutout system (not shown) which is backed up by a Faraday cage, described shortly.

For experiments with flowing hydrogen, the primary concern is not fire, but detonation/deflagration in the event of a hydrogen buildup. For this reason, the experiment is operated in a large and well-ventilated area. The most likely area of hydrogen buildup is within the cavity and waveguide. This would occur in the event of a leak from the ceramic tube itself or from the compression fitting at the base of the ceramic tube (and cavity) where the tube is prone to cracking. Tube sections within the microwave cavity are only prone to fail at temperatures well above the $\sim$ 900 K auto-ignition temperature of hydrogen and therefore are an immediate ignition source, and the resulting microwave-assisted hydrogen flame remains largely confined to the cavity. Typically, both mullite and alumina tubes are white hot before deformation or internal etching cause rupture.

For the case of a cracked ceramic tube within the compression fitting, which occurs more often than not with thin tubes, the crack may be heard by careful listening as the fitting is tightened, can sometimes be found using a "tug test" on the tube, but usually is undetectable except by a leakage test at very low flow rates. The checklist procedure used for these experiments therefore includes a leak test of this particular joint before every run and an operating leak detector sits near the cavity at all times during normal operation.

7.1.2 Faraday Cage

A Faraday cage is used to confine any stray microwave radiation, for example from poor waveguide connections or the observation holes in the cavity itself. This cage, shown in Fig. 7-2, is constructed from readily available steel struts and steel mesh.

Fig. 7-2: The Faraday Cage.

As a rule of thumb, the seams are electrically connected at intervals greater than about 1/8th of a wavelength in order to minimize microwave leakage (Anon., 1990). For 2.45 GHz microwaves, the corresponding wavelength is 12 cm, so the seams should electrically connect at least every 1.5 cm. In the cage shown, a far greater stitch density

was used in order to accommodate any poor electrical connections between the wire thread and mesh. For a mesh that visibly appears joined, it can still reradiate to the outside if only a poor electrical path is available to wall currents induced by stray microwaves within the cage.

The mesh shielding also extends under the cage, and the weak points are corners, the door, and any cable/pipe feedthroughs. Rubber hose is used for water cooling, and power and data cables are kept away from possible locations of high microwave intensity within the cage. Finally, in the cage shown, magnetic strips are used to seal overlapping layers of steel mesh around the door.

7.1.3   Pyrometry

Two fiber optic pyrometers are used to measure the surface temperature of the ceramic tube. Optical access to the tube inside the microwave cavity is via a line of holes drilled into the side, as shown in Fig. 7-3. The size of the holes is chosen to minimize microwave leakage while still being large enough not to excessively impinge the pyrometers' field of view.
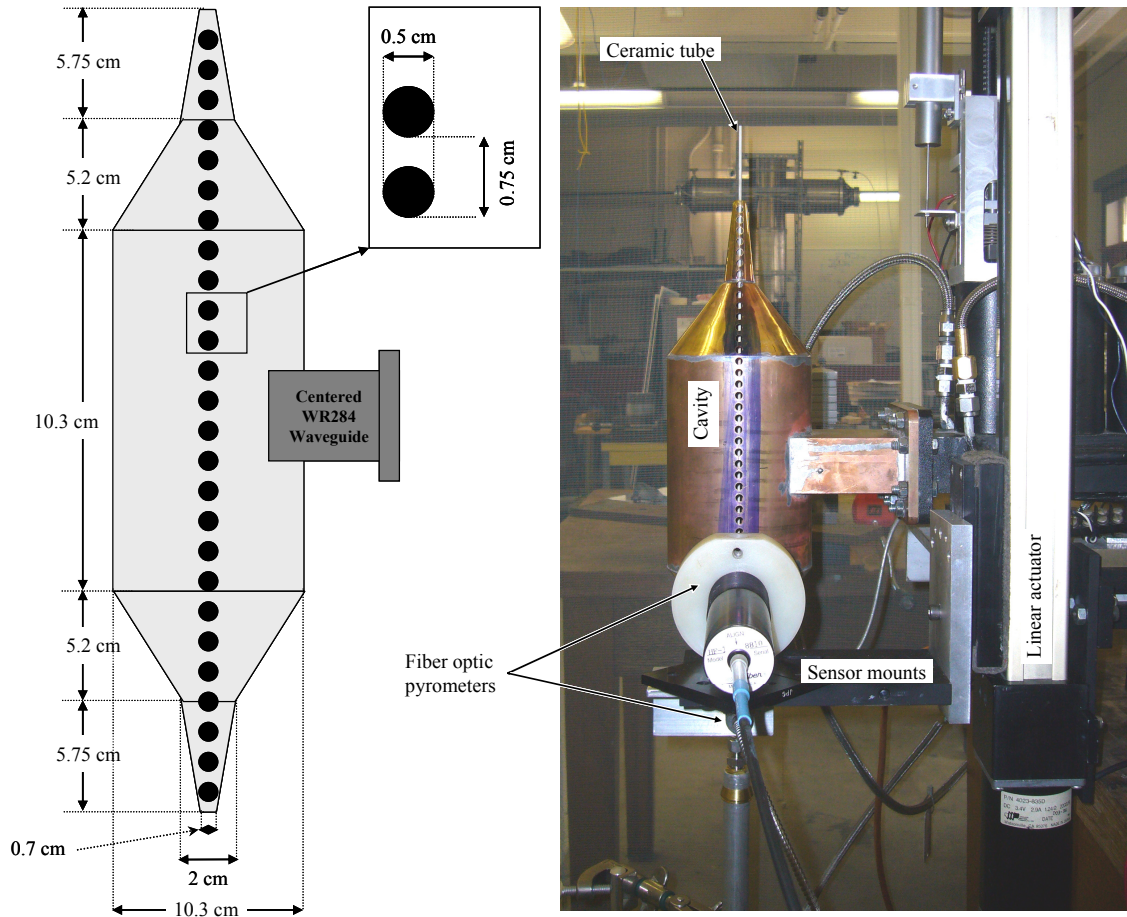
Fig. 7-3: The resonant cavity and pyrometer arrangement.

The pyrometers themselves are silicon photodetectors with a linear flux-voltage relationship. Internally, the pyrometers use a single multiplication factor obtained by calibration to convert voltage to irradiance. For a given set of focal optics and detector bandwidth the irradiance is converted to a spectral intensity and related to the temperature of the target via Planck's law for hemispherical emissive power (Siegel and Howell, 2001),

$$I_{\lambda T}d\lambda = \varepsilon_{\lambda T}\frac{2hc^2}{\lambda^5}\frac{1}{e^{hc/(\lambda k_B T)}-1}d\lambda, \qquad (7.1)$$

where $\varepsilon_{\lambda T}$ is the (known) hemispherical spectral emissivity of the target and the SI units of hemispherical emissive power are W/m^3/Sr.

The upper pyrometer as seen in Fig. 7-3 is the Luxtron model and is positioned such that its focal point is on the tube. The focal length is such that the holes do not obstruct the field of view, and alignment is accomplished by shining a white light into the fiber optic inlet. The lower pyrometer in the figure is the Everest model and its focal point is at infinity, so the holes in the cavity inevitably block a portion of the light.

A correction is made for this using a simple area ratio representing the fraction of blocked light within the field of view. For thin tubes, a further correction is made because the surface does not occupy the entire field of view through the hole. The focal spot size of the Luxtron is small enough in most cases that this correction is unnecessary; however, the Everest focuses at infinity and the correction is needed.

In practice, it is easiest to configure the pyrometers with a target emissivity of unity (black body) and make the temperature and area dependent corrections in post-processing. To simplify the algebra, for any given detector,

$$T_\lambda \equiv hc/(\lambda k_B),\qquad(7.2)$$

so that the measured temperature T_m, ambient temperature T_a, and actual surface temperature T_s may all be related to an equivalent black body intensity,

$$I_{\lambda T}d\lambda = \frac{2hc^2}{\lambda^5}\frac{1}{e^{T_\lambda/T}-1}d\lambda.\qquad(7.3)$$

An energy balance at the detector gives

$$I^m_{\lambda T}d\lambda = \alpha\varepsilon_{\lambda T_s}I^s_{\lambda T}d\lambda + (1-\alpha)I^a_{\lambda T}d\lambda,\qquad(7.4)$$

corresponding to

$$\frac{\alpha\varepsilon_{\lambda T_s}}{e^{T_\lambda/T_s}-1} = \frac{1}{e^{T_\lambda/T_m}-1} - \frac{1-\alpha}{e^{T_\lambda/T_a}-1},\qquad(7.5)$$

which is approximately independent of the detector bandwidth $d\lambda$. α is the area correction factor describing what fraction of the field of view is occupied by the target

surface. The fraction $1-\alpha$ is therefore the fraction of the field of view occupied by objects at the ambient temperature. These ambient objects are assumed to be black bodies. Rearranging Eq. (7.5) for target surface temperature,

$$T_s = \frac{T_\lambda}{\ln\left(\dfrac{\alpha\varepsilon_{\lambda Ts}}{\dfrac{1}{e^{T_\lambda/Tm}-1}-\dfrac{1-\alpha}{e^{T_\lambda/Ta}-1}}+1\right)} \, . \tag{7.6}$$

This equation is solved iteratively for T_s as the emissivity is a function of temperature. Given that the flux is proportional to the fourth power of temperature, there is a surprisingly large leeway for error in correcting the flux for emissivity and area obstructions, as a small increase in temperature corresponds to a disproportionately large increase in flux and vice versa. The downside is that a small amount of stray light from a very hot area can mask the true temperature of a cooler area.

7.2   Axial E-field

7.2.1   Theory and Procedure

The axial E-field cannot be measured directly using a probe because the conducting probe itself distorts the mode when inserted more than a small distance into the cavity. Instead, the E-field is deduced using the bead pull method (Amato and Herrmann, 1985; Goldberg and Rimmer, 1993; McDonough et al.).

In the bead pull method, a small dielectric or metallic bead is attached to a thin non-conducting thread and pulled through the cavity. As the bead or any small object passes through the cavity, it perturbs the field within it, in turn altering the resonant frequency by a small amount given by

$$-\frac{\Delta\omega}{\omega_u} = \frac{1}{4U}\left[\epsilon_0(\epsilon_r-1)\int_{\Delta V}\mathbf{E}\cdot\mathbf{E}_u dV + \mu_0(\mu_r-1)\int_{\Delta V}\mathbf{H}\cdot\mathbf{H}_u dV\right], \tag{7.7}$$

where the subscript u denotes the unperturbed cavity mode. Depending upon the geometry and other properties of the bead, the frequency shift reduces to,

$$-\frac{\Delta\omega}{\omega} = a_1 e_\parallel^2 + a_2 e_\perp^2 + a_3 h_\parallel^2 + a_4 h_\perp^2, \tag{7.8}$$

where the coefficients a_n are determined by theory or experiment for the particular bead, and

$$e^2 = \epsilon_0 E^2/4U, \tag{7.9}$$

$$h^2 = \mu_0 H^2/4U. \tag{7.10}$$

In the experimental arrangement shown in Fig. 7-4 a high purity spherical alumina bead 4.8 mm in diameter is attached to a thin cotton thread. This bead is nonmagnetic, so to first-order the fractional frequency shift is proportional to the square of the E-field. Given that U is known only by simulation, a relative measurement is made so that U need not be determined:

$$\frac{|\mathbf{E}|}{|\mathbf{E}|_{peak}} \propto \sqrt{\frac{\Delta f}{f_0}}, \tag{7.11}$$

where f_0 is the unperturbed frequency and Δf is the shift caused by the presence of the bead at any given point. For the alumina bead, the frequency shift is around 1 MHz, or about 1 part in 2500, and a microwave frequency counter is used to measure this very accurately. The frequency counter is sensitive enough to measure the frequency from outside the cavity using microwave leakage through the holes.

Early experiments using the linear actuator to pull the bead through the cavity reveal that such a small frequency shift can be lost among external factors such as poor waveguide connections and movement of the actuator itself. In fact, frequency shifts caused by the moving the position of the pyrometer platform alone correlate quite well with the field strength around the cavity walls. For this reason, a thread is passed through the wall of the Faraday cage and an external actuator used to draw the bead through the cavity so that the bead and its tensioning weight are the only moving objects within the Faraday cage. This arrangement is shown to on the right of Fig. 7-4.
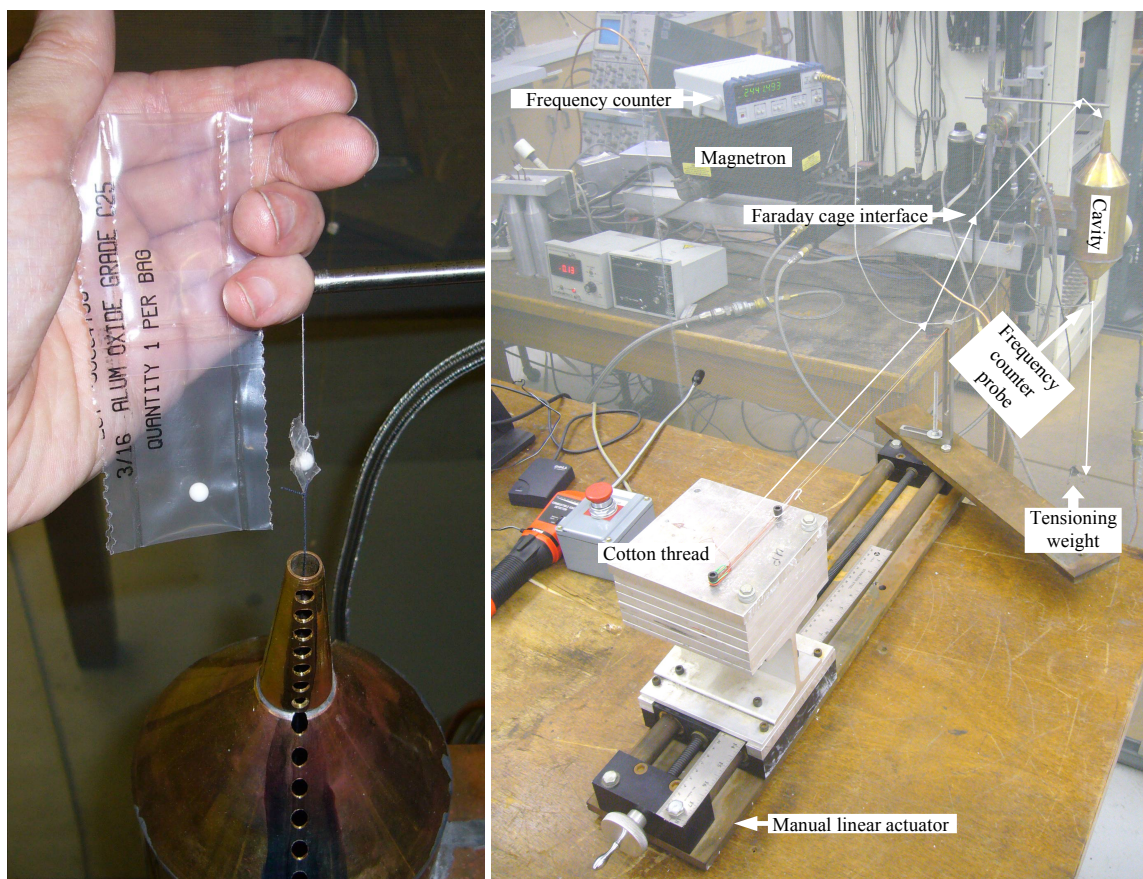
Fig. 7-4: Left: The alumina bead. Right: The cavity bead pull arrangement.

7.2.2 Results and Discussion

Given the experimental parameters in Table 7-2, the results for the loaded cavity (with tube) and the unloaded cavity (without tube) are shown in Fig. 7-5. It is clear that the computed results from the cavity show a greater separation between the two maxima of the tapered TM_{011} mode than is observed. Such a merging of these two high-field regions is achieved in the computational model by decreasing the cavity length or diameter.

Inner diameter	1.19 mm
Outer diameter	1.98 mm
Material	Mullite

Cavity parameters

Inner Diameter	9.85±0.05 cm (corrected for estimated average cavity $T = 400$ K. Diameter thermal expansion is 0.019 cm/K)
Taper end diameter	2±0.1 cm (measured)
Choke end diameter	0.7±0.1 cm (measured)
Cylindrical main section length	14.7±0.1 cm (measured)
Left taper length	5.2±0.1 cm (measured)
Right taper length	5.2±0.1 cm (measured)
Choke length (both ends)	5.65±0.1 cm (measured)
Drive point length	25.527±1 mm (60% of waveguide height; measured)
Offset from center of cylindrical main section	0.075±0.075 cm (toward the right / outlet; measured)
Input power	55±5 W (mainly dissipated in cavity walls; measured)
Frequency	2443±1 MHz (measured)

Table 7-2: Experimental parameters for the axial E-field experiment.
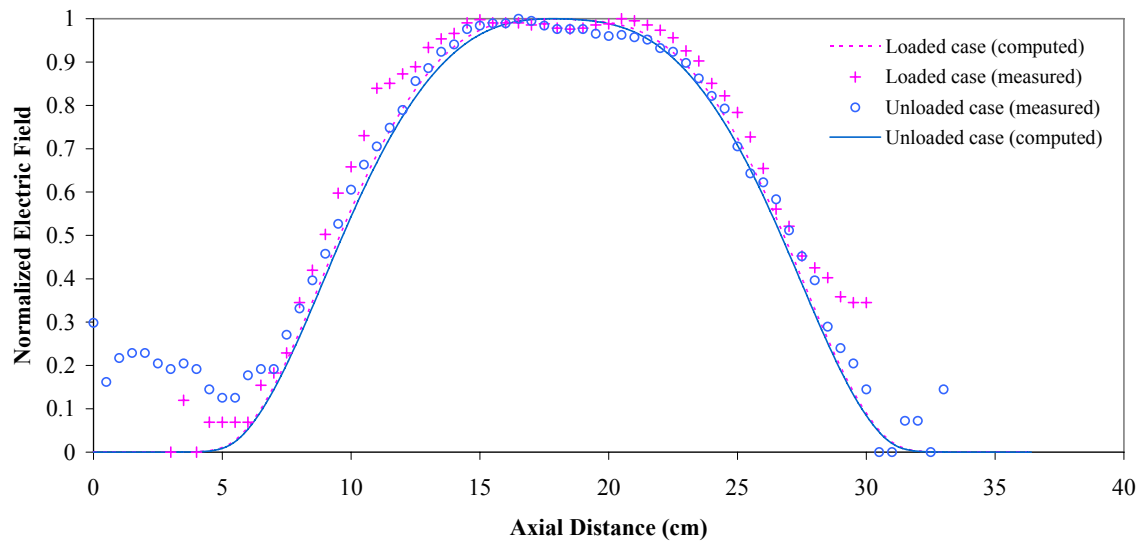
Fig. 7-5: Comparison of experimental E-field to computational models.

In Fig. 7-5 theory predicts only a slight variation of the E-field between the loaded (with tube) and unloaded (without tube) cases. The mildly decreasing trend in the measured E-field for the unloaded case suggests an asymmetry in the cavity with a larger effect than the slight offset error measured for the drive point (waveguide interface) and listed in Table 7-2. The direction of this trend is unaffected by taking bead data in the opposite direction. The possibility of error in the internal dimensions cannot be completely dismissed, given that the interior of the cavity is soldered shut. Other possible sources of this difference include poorly conducting (lead-soldered) joints, and asymmetry introduced into the cavity by various higher-order modes in the adjoining WR284 waveguide.

The difference between theory and experiment grows somewhat larger for the loaded case: The broadening of the E-field along with the central indentation is consistent with a 0.1–0.2 cm larger cavity effective diameter than predicted by the simulations. It is difficult to imagine how such a large dimensional error could arise given that the inner diameter is measured directly from tube left over from the cavity construction. Thermal expansion is insufficient to explain this error as it implies a cavity temperature of 400–500 K. The other possible cause is error in estimating the optical properties of the mullite tube, or its dimensions, or both.

Overall sources of error include thermal expansion of the cavity, interaction of leaked microwaves with moving objects within the Faraday cage, differing sensitivity of the bead to the different components of the E-field, heating of the bead, noise in the frequency counter reading caused by RF noise in the probe cable, and dimensional inaccuracies in the cavity construction.

The thermal expansion of the cavity causes a small trend upwards or downwards with axial distance. Since the cavity is cooled only via its adjoining waveguide, this source of error is minimized by waiting for the cavity to reach steady state, so that the frequency drift is small in comparison to the bead effect over the timescale of a single pass. In addition, data is taken in both directions to verify that this source of error is small.

Heating of the bead is also an insignificant source of error, as verified by taking multiple passes is opposite directions at differing rates. Furthermore, the bead temperature can be checked by hand shortly after a pass. However, it is not possible to monitor the bead temperature using the pyrometers as any movement of the pyrometer platform to track the bead disturbs the resonant frequency.

Noise in the frequency counter readings is responsible for the noisy readings in the low E-field at either end of the cavity and can be seen in Fig. 7-5. This noise can be minimized by careful impedance matching of the cable, by minimizing the cable length, and by integrating many readings or over a longer period. The latter method proves sufficient for the experimental arrangement examined here.

As already discussed, the resonant frequency is also affected by any microwave leakage combined with the movement of any object within the Faraday cage. Data from multiple passes suggest that this is not a significant source of error for the external actuator arrangement shown in Fig. 7-4.

Finally, dimensional inaccuracies in the cavity construction comprise the majority of the error and the qualitative effect of many different inaccuracies is presented in § 4.2.6.

It is concluded that the discrepancies between theory and experiment are most likely a symptom of the approximations used in the cavity simulation, particularly around the area of the drive point. This is despite the fact that these discrepancies can mostly be explained by dimensional inaccuracies, and that a better fit to the experimental data can be obtained using dimensions slightly different to those measured.

7.3   Tube Temperature (No Flow)

7.3.1   Theory and Procedure

A mullite tube is heated without a flowing gas in order to compare theory and experiment without the added complication of convection. Adiabatic behavior is preferable to isothermal behavior, so the Biot number Bi determines difficulty of heating to an extent,

$$\text{Bi} \ = \ \frac{hL_c}{k} \,, \tag{7.12}$$

where h is the convective heat transfer coefficient, k is the thermal conductivity and L_c is a characteristic length scale. Tubes of a higher Biot number can be easier to heat, but this metric is not the complete picture as the absorption properties of the tube and the variation with temperature tend to dominate in determining whether or not the tube will reach the "magic" temperature of around 700 K, which qualitatively is a tipping point for thermal runaway. Above this temperature, the loss factor increases rapidly, causing the cavity Q value to drop and bandwidth to increase. This leads to more stable and controllable heating up to the material melting point.

Mullite tubes are used in these experiments because the microwave absorption characteristics of alumina are determined by the impurities within the material, usually from the particular "binder" compounds used to bind alumina the powder together, and so the heating characteristics of similar alumina grades tend to vary widely between manufacturers. 95% purity alumina tubes can be heated quite easily; however, thin 99.9% alumina tubes (low Biot number) can prove extraordinarily difficult to heat without adding an artificial contaminant.

Experimentation with a graphite layer rubbed onto the outside of tubes proves that even thin high purity alumina tubes can achieve thermal runaway; however, the graphite sometimes oxidizes away before the underlying tube can be sufficiently heated, so the results are not easily repeatable. A more satisfactory approach was found in which a thin copper layer was rubbed onto the outside of the tube, forming a susceptor layer. The susceptor layer strongly absorbs microwaves and the copper does not so readily oxidize as graphite; however, the high temperature copper permanently infiltrates the alumina structure, leaving it a brown color and undoubtedly changing its absorption and emission characteristics in ways that require extra modeling.

Typically, ad hoc adjustments are made to both tuning and power input in order to find and maintain a steady state. With the present experimental setup, the adjustments (especially tuning) require a great deal of trial and error to perfect. As a general strategy,

an effective method is to detune the setup very slightly using the stub tuner so that the cavity gradually drifts into resonance as the tube heats up. However, the cavity itself has a similar behavior and the operator must determine whether any slow decay in the reflected power is due to the gradual heating of the cavity, the gradual lead into the thermal runaway within the tube, or the gradual lead into resonance without thermal runaway. As resonance approaches, the tube can sometimes overheat on a rapid timescale, and "meltdown" can occur faster than the operator can respond for thin tubes or at high power.

7.3.2   Results and Discussion

In the experiment presented here a mullite tube of intermediate diameter is heated using the parameters given in Table 7-3, and the cavity is fine tuned using the motorized stub of the three-stub tuner. For the diameter of tube used in this example, the heating characteristics are relatively easy to master and any overheating occurs on a timescale of several seconds.

Tube parameters	
Inner diameter	1.59 mm
Outer diameter	4.76 mm
Material	Mullite (Omega)

Cavity parameters	
Inner Diameter	9.85±0.05 cm (measured and corrected for estimated average cavity $T = 400$ K) (diameter thermal expansion is 0.019 cm/K)
Taper end diameter	2±0.1 cm (measured)
Choke end diameter	0.7±0.1 cm (measured)
Cylindrical main section length	14.7±0.1 cm (measured)
Left taper length	5.2±0.1 cm (measured)
Right taper length	5.2±0.1 cm (measured)
Choke length (both ends)	5.65±0.1 cm (measured)
Drive point length	25.527±1 mm (60% of waveguide height; measured)
Offset from center of cylindrical main section	0.075±0.075 cm (toward the right / outlet; measured)
Input power	(134 ± 5) W (measured, varies according to tuning)

Table 7-3: Experimental parameters for tube heating with no flow.

Earlier simulation of this cavity configuration in § 4.4.1 suggests that symmetric heating of this cavity is unstable, and that the heating region on either the left or right side predominates after some time. Based on the sensitivity analysis in § 4.2.6, the small offset of the cavity drive point should favor the bottom of the cavity seen in Fig. 7-6 (left side in Fig. 7-7). However, Fig. 7-6 shows that the heating region stabilizes in the top side of the cavity. Rotating the cavity and rerunning the experiment reveals that the top side of the cavity is still favored, therefore eliminating geometric asymmetry of the cavity itself as a possible explanation. Indeed, in earlier testing, the lower (left) side of the tube briefly glows, only to be overtaken in the end by the (right) side.

Fig. 7-6: Steady state microwave heating of a mullite tube (no flow).

There are two theories as to why the heating region always stabilizes at the top side of the cavity. The first is that the orientation of the three-stub tuner causes an asymmetry of the input mode, and the second is that natural convection sets up a vertical temperate gradient within the cavity that favors heating at the top. Inverting the three-stub tuner is not

possible in the present setup, and the second explanation is verified by feeling the temperature of the top and bottom of the cavity by hand shortly after testing.

The temperature distributions measured by the two optical pyrometers are given in Fig. 7-7. Based on Fig. 7-6 the Luxtron pyrometer data is clearly in error, and as discussed in the next section this is thought to be caused by internal cavity reflection that predominates in the near visual range where the Luxtron is sensitive and the Everest is not. Turning to the Everest data, which is taken in the far infrared, higher than predicted temperatures between 7 and 17 cm along the cavity are consistent with a tube that is somewhat heated by light reflected from the hottest region onto the brass cavity walls and back onto the rest of the tube. Given that the Everest data does not show unusually large temperatures at the 30 cm position whereas the Luxtron does, it is inferred that cavity reflection is not great in the far infrared spectrum, and that the temperatures indicated are indeed close to the true tube temperature for the Everest pyrometer.
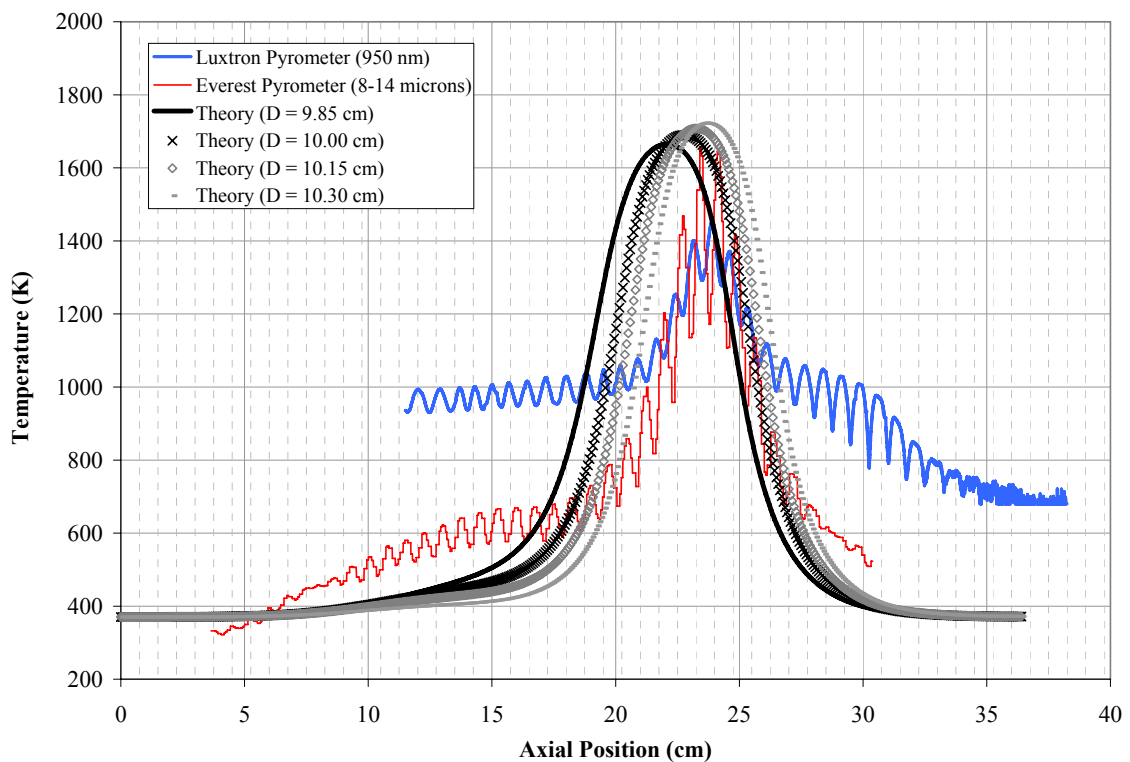
Fig. 7-7: Comparison of theory and experimental results for a mullite tube with no flow.

Theory predicts the left side of the cavity reaches thermal runaway due to the slight perturbation of the cavity drive point offset. A model of natural convection within the cavity and the resulting temperature gradients and thermal expansions is beyond the scope of the present work. It is assumed in this work that the net effect of the convection is simply to perturb the field and/or tube temperature by a small amount large enough to favor heating on the right, but not large enough to alter the resulting shape and position of the peak heating region.

Given this assumption, the sign of the small drive point offset is negated to represent a small perturbation equivalent to convection that biases thermal runaway to the right. As described by the sensitivity analysis in § 4.2.6, the drive offset primarily affects the magnitude of the peak field on either side of the drive point and has relatively little effect on the shape of the mode or the position of the E-field peaks. It remains to compare the resulting theoretical curves with the pyrometer data.

The peak Everest temperatures compare favorably to the peak temperatures predicted by the theory at all the various cavity diameters calculated; however, there is a ~ 2 cm disagreement over the position of the peak and the predicted width is approximately double that measured by both pyrometers. The measured cavity diameter is 9.85 cm; however, the E-field measurements for the loaded cavity in the previous section are consistent with a greater cavity diameter. None of the calculated curves up to diameters of 10.3 cm are fully consistent with the measured data, though there is fairly good agreement for 10 cm and 10.15 cm diameters on the right side of the peak heating region.

It is concluded that any uncertainty over the effective diameter of the cavity, owing to dimensional inaccuracies or errors in estimating the dielectric constant of the tube, are insufficient to explain the difference between theory and experiment in Fig. 7-7. The anomalous heating on the left side of the cavity is most likely caused by cavity reflections close to visible wavelengths. On this basis of available data, it is not possible to infer the cause of the narrower than predicted heating region, and the two most likely candidates

are direct effects of the natural convection and asymmetric shifts in the cavity dimensions due to the thermal gradients established by the natural convection.

7.4   Tube Temperature (Hydrogen Flow)

7.4.1   Theory and Procedure

Even without a flowing gas, achieving thermal runaway can be difficult. The addition of flow cavity tuning and stable heating of the tube akin to a balancing act, which becomes harder with decreasing tube size, increasing flow rate and increasing input power.

Because hydrogen gas is both explosive and flammable, extra precautions are taken to ensure that "meltdown" does not occur at a high flow rate. Hydrogen flames have a low emissivity and they are difficult to see. The heat from even a large flame nearby is not easy to feel on the skin as it is for a hydrocarbon flame. In order to make the flame more visible the tube outlet is dipped in brine before the experiment begins. The sodium D-lines emit strongly and color the flame bright orange even at very low concentrations.

Before microwave power is applied, the hydrogen flame is lit at a minimal flow rate, giving a tiny flame at the top of the tube. Then, cavity resonance is found at the lowest power possible. The power is increased and the cavity tuned accordingly until thermal runaway is achieved in the tube. Contrary to the earlier approach of letting the tube drift into a cavity resonance, it is best in this case to keep the tube on the other side of the resonance so that any sharp increase in temperature moves the cavity farther away from resonance and decreases the absorbed power in the tube.

Tube power and flow rate are increased incrementally, so that the tuning dynamics at each successive power level can be gauged. Once the cavity is operating at high power and the cavity response with changing flow rate is well understood, the flow rate is decreased so that thermal runaway can occur very slowly. The pyrometers, the frequency counter and the reflected power readings are all used as real-time diagnostics in order to control this process.

7.4.2 Results and Discussion

A stable operating point is achieved using the experimental parameters given in Table 7-4. The thin tube is chosen in order to maximize the ratio of convective conductance to radiative conductance, i.e., to cause absorbed energy to favor convection over radiation. This thin tube makes cavity tuning difficult as the Q value remains quite high.

Tube parameters	
Length	36.4 cm
Inner diameter	1.19 mm
Outer diameter	1.98 mm
Material	Mullite (Coorstek)
Cavity parameters	
Dimensions	As given in Table 7-3
Frequency	(2445.39 ± 0.1) MHz (measured, varies according to tuning)
Input power	(215 ± 15) W (measured, varies according to tuning)
Flow parameters	
Gas	Hydrogen
Static temperature at inlet	(300.5 ± 0.1) K (measured)
Pressure drop across tube	(0.104 ± 0.005) atm (measured)
Mean inlet velocity	23.86 m/s (corresponds to Reynolds number of)

Table 7-4: Experimental parameters for tube heating with a hydrogen flow.

The result corresponding to the above parameters is shown on the right of Fig. 7-8. Initially, thermal runaway is achieved at low flow rate (left) and the cool flow produces an invisible hydrogen flame at the outlet. As the tube temperature increases, the flame becomes yellow due to the sodium (middle). The flow rate is once again increased and the final stable operating point is attained (right). The increased flow rate carries with it more energy from the tube, moving the glowing region further into the thin cavity choke region.
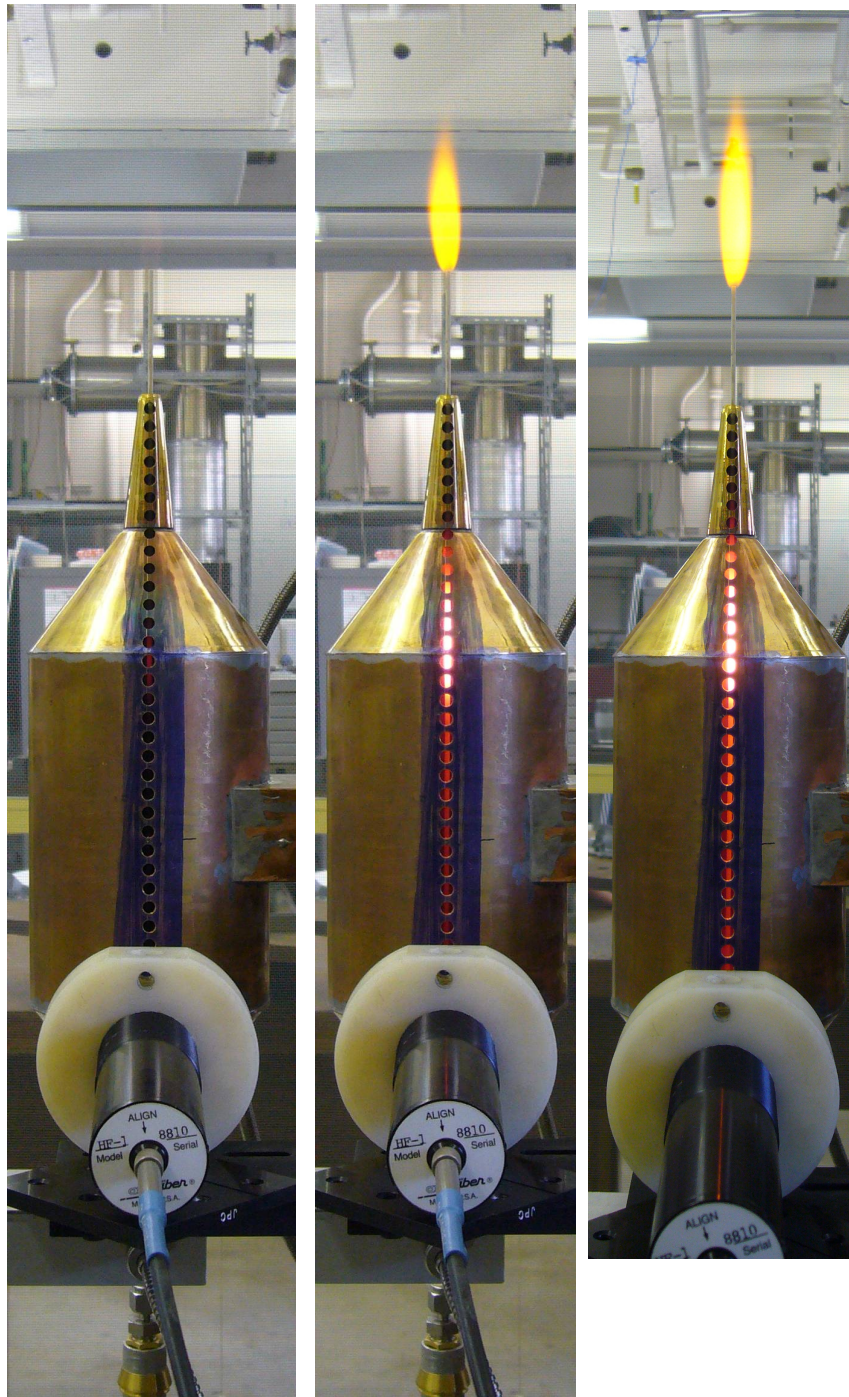
Fig. 7-8: Stable operation of the microwave thermal channel with a hydrogen gas. Left: The mullite tube at dull red heat produces a clear hydrogen flame. Middle: The same tube a short time later at white heat produces a bright yellow flame due to deliberate sodium contamination. Right: The same tube at a higher flow rate glows dull red in the narrow choke region.

The pyrometers used to scan the surface temperature presented in Fig. 7-9 can be seen in their parked position at the bottom of Fig. 7-8, with the Luxtron on top and the Everest below. Based on image comparisons alone there is good qualitative agreement between theory and experiment, which agree on the position of peak temperature to within a centimeter or so. The simulations presented in the previous chapter suggest that the Reynolds number varies between 300 (at low T) and 80 (at high T) in the tube, with the temperature variation of viscosity causing this variation.
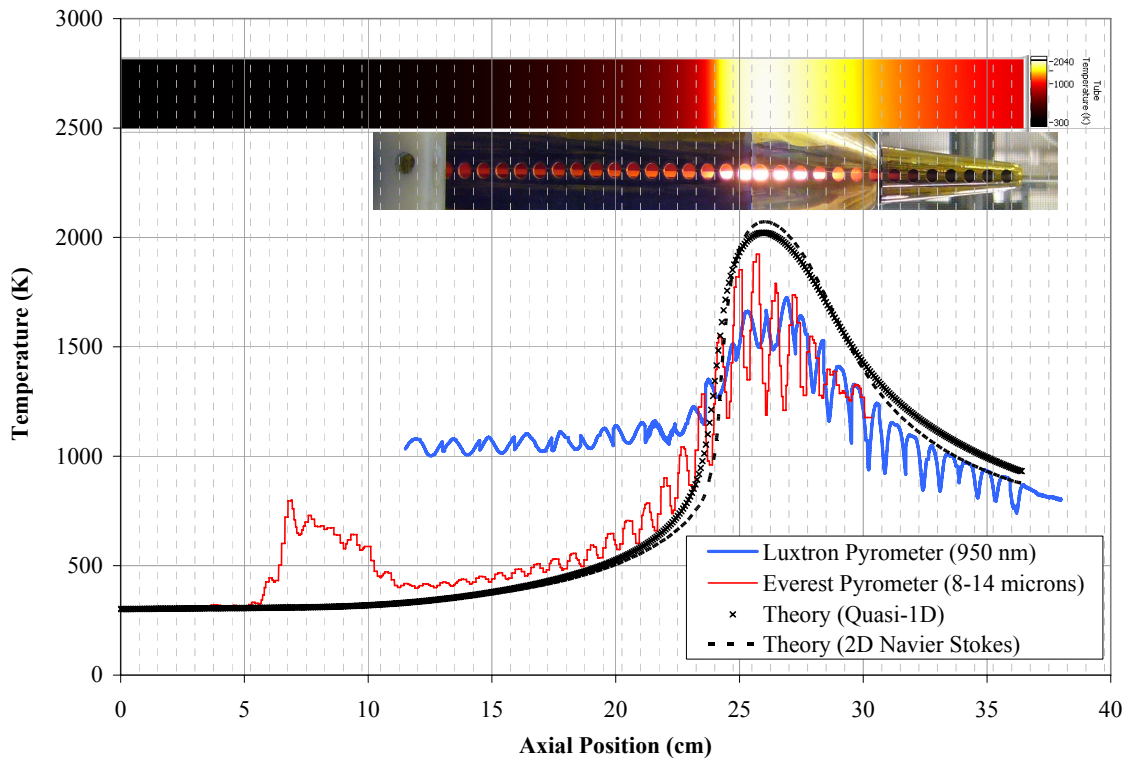
Fig. 7-9: Comparison of theory and experimental results for a mullite tube with flowing hydrogen.

The pyrometer data requires more careful interpretation; however, it is clear from this data that the theory correctly predicts the position of the peak temperature to within a centimeter and the variation in cooling rate of the hydrogen as it passes through the narrow choke region of the cavity.

Less clear from the pyrometer data is the exact peak temperature, and the way in which the temperature rises to its peak. The Luxtron temperature readings are clearly in error to the left of the peak, and given the agreement with theory on the right of the peak it is logical to conclude that this false reading is due to reflection within the cavity. Comparing the apparent tube temperature in the image with the measured tube temperature to the left and right of the temperature peak, there is clearly a discrepancy in the visible wavelength range. A ~ 1100 K temperature toward the tube exit is not visibly glowing, whereas the ~ 1100 K temperature along the entire left side of the tube, according to the Luxtron, does appear to be glowing.

It is therefore concluded that the cavity reflects well in the visible range, and this logically affects the visible images and the Luxtron pyrometer in the near infrared while not affecting the Everest pyrometer to a great degree in the far infrared. It is further inferred that the anomalous temperature peak on the left side of the tube in the Everest data is in fact a real hot spot caused by light reflected from the right cone into the left cone and onto the tube. This transfer of energy from the right to left cone then explains why both numerical models underpredict the heating before the peak, and over predict the peak temperature and subsequent temperatures as the flow cools.

A final corroborating factor is the pressure drop across the tube. The quasi-1D theory predicts a pressure drop of 0.109 atm across the tube as measured from the cavity inlet to the cavity outlet. The 2D Navier-Stokes theory predicts a pressure drop of 0.1 atm over this same region. The pressure drop across the tube and including the small length of extra tube beyond the cavity outlet is measured at 0.104 atm by the pressure transducer on the outlet side of the mass flow controller.

7.5   Unsteady Behavior (Nitrogen Flow)

A new type of unsteady behavior is observed in Fig. 7-10 using the parameters given in Table 7-5. The unsteady behavior is present at the flow rate of 8 SLPM; however, operation is stable when the flow rate is reduced to 3 SLPM. A qualitative comparison of

this behavior to that of the quasi-1D simulations in § 6.2 suggests that there is a common mechanism at work, in which a heating region begins in the region of the peak E-field and travels downstream until the diminishing E-field caused by the converging cavity walls extinguishes it.

Tube parameters	
Inner diameter	1.59 mm
Outer diameter	4.76 mm
Material	Mullite (Omega ORM-11618-24)
Cavity parameters	
Dimensions	As given in Table 7-3
Input power	(200± 15) W (measured, varies according to tuning)
Flow parameters	
Gas	Nitrogen
Static temperature at inlet	(297.2 ± 1) K (measured)
Mean inlet velocity	25.3 m/s (stable), 67.4 m/s (unstable)

Table 7-5: Experimental parameters for tube heating with a nitrogen flow.

Although the simulations of the previous chapter are for a hydrogen flow, they display similar behavior in that the oscillation grow worse as the flow rate is increased, even in the laminar regime. Correcting the pseudo-time for density and specific heat capacity, the timescale of the simulation instability is also on the order of seconds.

The lower flow rate in Table 7-5 is in the laminar regime, and the upper flow rate is in the transitional regime. The unsteady nature of transitional flow is not thought to directly cause the oscillation observed here, because the timescale of this oscillation is very long. Again, it is noted that the simulations reproduce similar behavior even in the laminar regime.
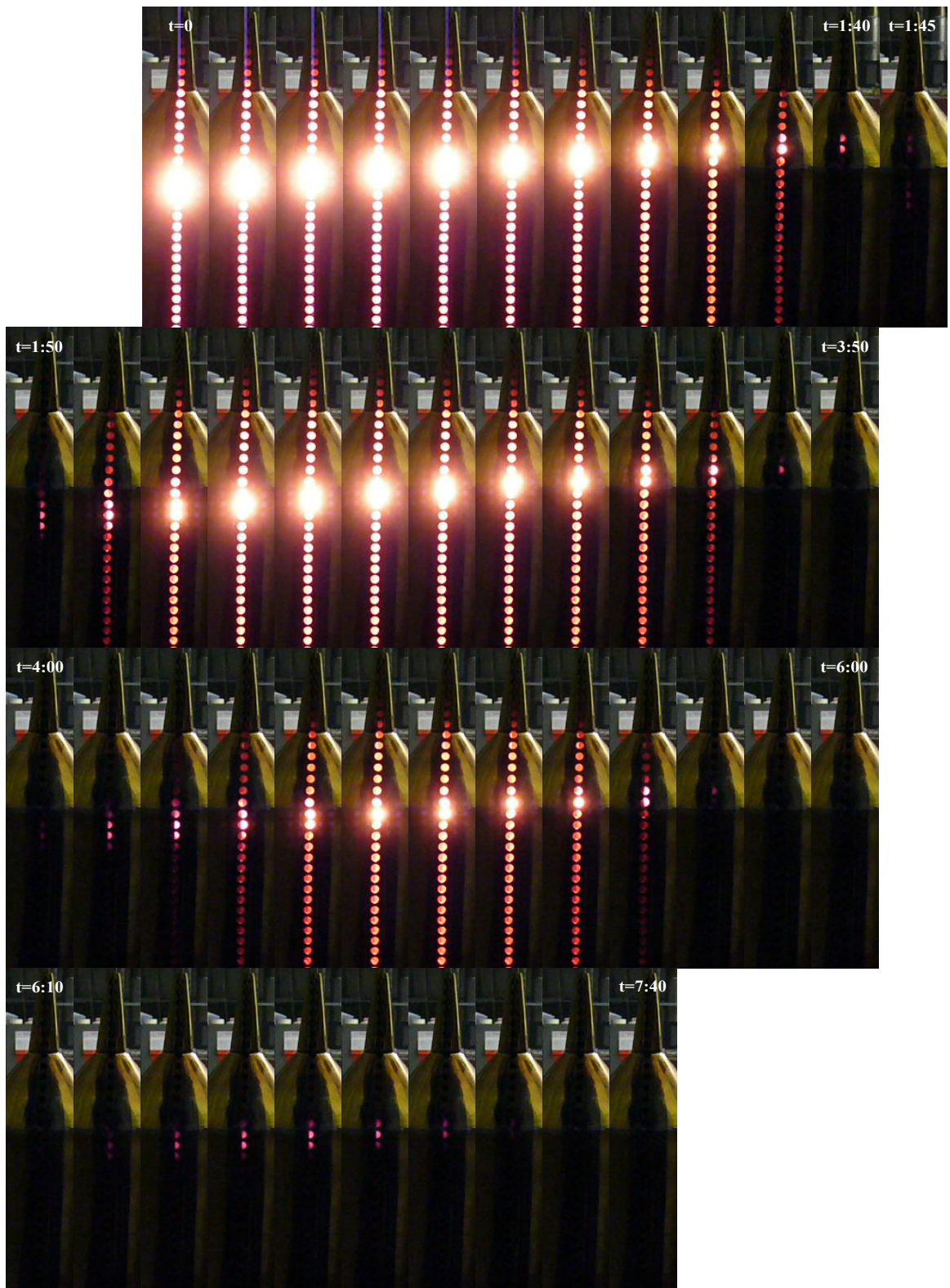
Fig. 7-10: Unsteady behavior of the microwave thermal channel with a nitrogen flow.

7.6   Summary and References

Despite the experimental complications of natural convection and cavity reflection, it is concluded that the coupled electromagnetic-conduction-convection code successfully captures the leading-order behavior of the microwave thermal channel.

Without flow, the subtle effects of natural convection appear to distort the dynamics of the resonant cavity to a significant extent. Study of this aspect is beyond the scope of the present work, and it evidently does not affect the cavity dynamics in a major way when the microwave thermal channel is operating.

In addition to investigating ways to prevent light reflection within the cavity, it is recommended that future studies consider using a network analyzer to better find and track cavity resonances. A thermal imaging camera can be used to determine the cavity temperature distribution, and a spectropyrometer (Felice, 2003) or alternative instrument can be used to eliminate much of the uncertainty over the true high temperature emissivity of the materials involved.

Finally, the unexpected oscillatory behavior for a nitrogen flow may explain the difficulty in finding a stable operating point for the hydrogen flow investigated earlier in this chapter. An investigation of this phenomenon is also beyond the scope of the present work; however, it is noted that the simulations in § 6.2 appear to capture the dynamics of this process. If the oscillatory behavior does indeed play a role in the regimes of interest then future resonant cavity experiments at higher power and mass flow rate may need to consider it when implementing any automatic control, for example, of the peak tube temperature.

Amato, J.C. and Herrmann, H. (1985). *Improved Method for Measuring the Electric-Fields in Microwave Cavity Resonators*. Review of Scientific Instruments **56**(5): p. 696–699.

Anon. U.S. Army Corps of Engineers (1990). *Electromagnetic Pulse (EMP) and Tempest Protection for Facilities.* Chapter 5 — Facility Design.

Felice, R.A. (2003). *The Spectropyrometer – A Practical Multi-wavelength Pyrometer.* AIP Conference Proceedings: p. 711–716.

Goldberg, D.A. and Rimmer, R.A. (1993). *Automated bead-positioning system for measuring impedances of RF cavity modes.* Proceedings of the Particle Accelerator Conference: p. 871–873.

McDonough, C., Barmatz, M. and Jackson, H.W. *Application of the Boltzmann-Ehrenfest Principle to Containerless Microwave Processing in Microgravity.* Ceram. Trans. **36**: p. 581–590.

Siegel, R. and Howell, J.R. (2001). *Thermal radiation heat transfer.* 4th ed, New York. Taylor & Francis.

CHAPTER 8

CONCLUDING REMARKS

8.1   Experimental Demonstration

As a first step on the path to a microwave thermal rocket, a laboratory-scale facility was proposed in § 3.1 and constructed in order to demonstrate the key physics of microwave absorption, conduction, and subsequent convection into a flowing hydrogen propellant, together and at high energy density. This demonstration has been successful (Fig. 8-1).
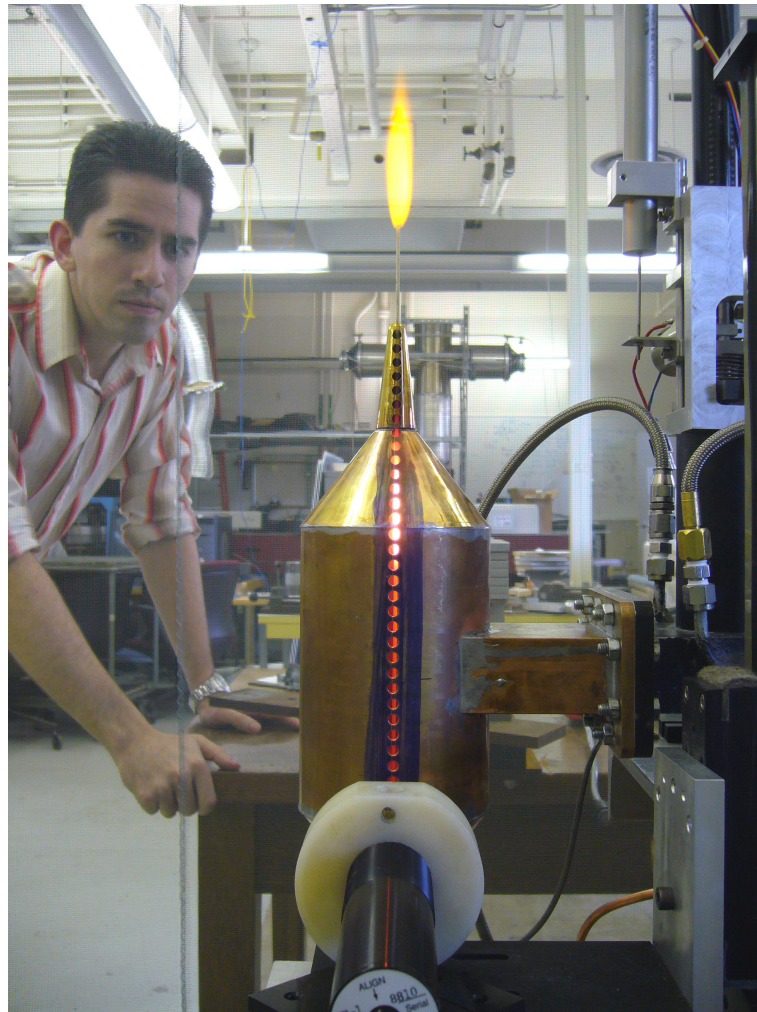
Fig. 8-1: Key elements of the microwave thermal thruster brought together and operating at laboratory-scale (§ 7.4.2).

The laboratory-scale experiment uses a cylindrical axisymmetric geometry about a single circular tube in order to enable a low-cost resonant cavity approach to heating. This is different from the free-space propagation and absorption envisaged for the full-scale launch system and the cavity approach displayed some unexpected time-dependent oscillations, which by the very particular nature of the experiment have not been observed before. These oscillations are thought to arise from an extra coupling between the tube heating pattern and the tube temperature. This coupling would not exist in a free-space (non-resonant) system.

The limited data available suggests that stable operation of this experiment, as seen in Fig. 8-1, becomes unstable as the gas flow rate is increased. Indeed, to extend the resonant cavity approach to higher flow rates and power levels in future experiments, control of the cavity tuning and input power will need to be automated, as the timescales involved become too small for human control. This automated control may require a greater understanding of the unsteady cavity dynamics, though this is by no means a certainty given the very limited data gathered on this phenomenon so far.

8.2 Theoretical Modeling

A theoretical modeling capability for the microwave thermal heat exchanger was proposed in § 3.1 in order to pave the way for future investigations and development. Over subsequent chapters, a coupled electromagnetic-conduction-convection code was formed in order to simulate the behavior of the single microwave thermal heat-exchanger channel seen in Fig. 8-1.

This model is the first to combine the three domains of electromagnetics, conduction, and convection to solve for the heat transfer characteristics of a microwave absorbent channel. In addition to apparently capturing the time-dependent oscillatory behavior of the cavity, even using a time-independent convection code (Chapter 6), the model convincingly reproduces the surface temperature distribution along the heat exchanger. This temperature distribution is readily evident in Fig. 8-1, and the comparison is made

using surface temperature measurements taken from two optical pyrometers that scan the length of the tube, as well as by visual comparison with images and video. A further confirming factor is that the gas pressure drop across the tube is similar in both theory and experiment, and itself varies approximately with the energy absorbed by the flow.

The design of future experiments and full-scale thrusters will require the simultaneous modeling of two or more microwave thermal channels without the simplification of an axisymmetric geometry, which enables a 2D simulation instead of a 3D one. For this task, the quasi-1D convective heat transfer model is ideally suited; however, care will need to be taken in selecting the Nusselt number correlations and friction factor expressions used.

For a single channel, the Navier-Stokes convection model given in § 5.2 has been valuable in verifying the predictions of the quasi-1D model and the circumstances under which it is in error. For future experiments, the Navier-Stokes model may be used to generate Nusselt number and friction factor correlations for unusual situations or heating patterns, and these correlations may in turn be used in the quasi-1D models, which are time-independent and several orders of magnitude faster to execute.

Future experimental multichannel microwave thermal heat exchangers operating in the laminar regime are expected to encounter laminar flow instabilities (Bussard and DeLauer, 1958), and this is an avenue in which theory and experiment can advance together, perhaps using an array of coupled quasi-1D models with heat transfer correlations generated from the single-channel Navier-Stokes model.

A full-scale microwave thermal thruster is presently envisaged to operate in the turbulent regime, as did the NERVA nuclear thermal demonstrations, and this regime is thought to be stable with respect to multichannel flow instabilities. It is a simple matter to adapt the quasi-1D model given in § 5.1 to turbulent noncircular channels; however, it is not so simple to extend the Navier-Stokes code to a turbulent non-circular channel. Perhaps the most careful thought of all will need to go into how to simplify and model the

temperature of the exchanger material structure when hundreds of somewhat coupled channels are contained within it.

8.3   A Short-term View of the Future

8.3.1   Economics and Conceptual Design

Simple back-of-the envelope calculations given in § 2.3 highlight key trades for the conceptual design of microwave thermal systems; however, the key economic questions surrounding microwave thermal rocketry remain:

- How cheap will the whole system be ($/kg of payload)?

- What is the initial infrastructure cost, and what is the payload size at which this is minimized?

- In what logistical regime (payload, flight rate) is microwave thermal launch superior to other approaches?

As discussed in § 2.3 simple parametric modeling is unsatisfactory because the answers to these questions need to be quantified with a known confidence, such as 10%, 50% and 90% confidence intervals. There are various approaches to the probabilistic treatment of design inputs (Thunnissen, 2005) and one or more of these will be needed to establish the logistical regime in which microwave thermal launch is superior enough relative to existing systems to warrant the initial investment, and to produce dependable cost estimates spanning that regime.

8.3.2   Engineering

Analysis of the microwave thermal rocket concept, preliminary experiments and feedback from experts in several disciplines has highlighted the expected future challenges for a microwave thermal launch system, which include:

Material Creep Rate (§ 2.2.3): At high temperatures, heat exchanger materials such as silicon carbide become ductile and have a finite strain rate, allowing a high temperature propellant to push through the channel walls at their hottest point (this was indeed observed in experiments with alumina). On the other hand, this effect helps to reduce stress concentrations arising from thermal expansion, which may otherwise be a problem with multimaterial thrusters and square channels. This effect needs to be better integrated into the design reasoning process.

Optical properties (§ 2.2.3): The loss factor (resistivity) of materials varies by many orders of magnitude over the temperature range of interest. Data on these properties is scarce at very high temperatures and often varies from batch to batch of a given material. A way should be found to characterize these materials and control or otherwise compensate for uncertainties in their optical properties. If resistivity gradients are used to make a heat exchanger robust to such material variations, then the effect of high temperature operation on these gradients should be checked, for example if dopants are used, and the electromagnetic performance stability of these gradients should be modeled.

Thruster Dynamic Response: It is desirable for an operational thruster to reach operating temperature quickly and to be robust to interruptions in the microwave beam. This requires a control system, for example to reduce propellant flow rate in the event of beam interruption (for example by an aircraft wandering too close to the beam) in order to maintain the heat exchanger temperature and avoid thermal shock, which may otherwise rupture the heat exchanger.

Heat Exchanger Fabrication (§ 2.2.3): There are many possible approaches to constructing a heat exchanger, depending on scale, materials used, number of materials, the type of joining required, channel geometry (circular or square), the possible need for functionally graded materials and whether the heat exchanger is designed for low-cost, single use, easy replacement or long life and reliable performance. The joint where the

high temperature end of the heat exchanger meets a pipe may also require some thought, depending on the materials used.

Heat Exchanger-Aeroshell Integration: The way in which a heat exchanger is structurally and thermally coupled to the aeroshell needs further thought. If the heat exchanger is to be used as part of a re-entry heat shield there are re-entry loads to consider and alternative options for sacrificing it upon re-entry or building it for reuse or refurbishment. If necessary, the heat exchanger may form part of an active cooling system upon re-entry. If the propellant tank uses autogenous pressurization (self-pressurization) then a hot structure approach may be desirable, with the thermal load entering the tank controlled by the radiative and conductive coupling between the heat exchanger and the rest of the structure.

Phase Locking of Microwave Sources (§ 2.2.4): High power phase locking has been achieved with large numbers of magnetrons and klystrons, but not yet gyrotrons. From informal evidence there is every indication that gyrotrons phase lock in the same way as all the other vacuum microwave sources; however, it would be prudent to demonstrate this, initially at small scale.

Feed System Breakdown: This has been a problem for coupling high power microwave sources to parabolic dishes in the past, and a specific feed system design will need to address this issue explicitly.

High Power Phase Shifters: This has been a problem for more conventional phased arrays in the past. At millimeter wavelengths, there are many possible ways to alter the optical path between the microwave source and each array element, as the beam is quasi-optical. For example using a series of reflective plates at the Brewster angle can be used to adjust the path length of the beam. Again, this is an issue a detailed design may need to address explicitly.

Beam steering: For small angles of ~ 10 degrees, a phased array of fixed dishes can be electronically steered by introducing systematic phase differences between each dish.

For large angles, the phased array is mechanically steered, leading to the possibility of mechanical deformation and vibrations causing inintended phase shifts. The extent of this problem needs to be quantified, and ways to passively or actively compensate for the potential phase errors need to be identified.

Electromagnetic Propagation (§ 2.2.6): While ideal beam propagation (with margin) is considered in § 2.2.6, the progagation of the wavefront needs to be modeled in order to obtain a more accurate estimate of propagation efficiency. This model should include propagation at an angle from a phased array of parabolic dishes (with gaps), propagation through pockets of water vapor in the lower atmosphere, and the effects (if any) of ionospheric striations in the upper atmosphere. Although it has never been observed microwave absorption by water vapor near the phased array could set-up a site-specific local atmospheric circulation that draws in more water vapor and gives rise to a characteristic atmospheric phase stability. This effect may become important if, for example, 5% of a 300 MW beam is absorbed.

Vehicle Tracking: The phased array is effectively a high power millimeter radar, and one beam-steering approach might use a closed-loop control system using the reflected portion of the beam, which may also provide real-time diagnostic information on the state of the heat exchanger. An alternative is an open-loop system which would track the heat exchanger optically in the infrared, for example.

8.4 Overall Concept

The launch problem is in essence a problem of economics and low-flight rate that is perpetuated by the technical insufficiency of conventional rockets. This problematique exists in a metastable state: The economic potential of space can only be realized at a launch price an order of magnitude below the present payload price of $10,000 per kilogram delivered to low earth orbit. The new price of ~ $1,000 per kilogram can only be reached by economies of scale that cannot and do not exist today, and are supported by demand from new industries once the key price of $1,000 per kilogram or less has

been sustained for several years. The past 40 years of launch price data suggests that there is no evolutionary path between the two states. If a trend akin to Moore's law (1975) can be discerned from the launch price data at all, it suggests that $1,000 per kilogram will not be reached for another 50 to 100 years at least.

There are but two ways out of this quandary: The first is to increase launch demand substantially, bringing into play economies of scale that lower launch prices, stimulating new and sustainable demand from space applications that only become possible at such low prices. The second is to improve substantially the launch technology itself, making a resolution of the launch problem possible without such a large artificial (or real) boost in demand.

This thesis offers a technological solution to the launch problem by proposing a new (Parkin, 2006) launch concept based upon directed energy. Directed energy launch was first suggested by Tsiolkovsky (1924), and by leaving the rocket energy source on the ground a world of new design possibilities emerge. For the microwave thermal rocket, which can be viewed as an adaptation of the nuclear thermal propulsion principle, this results in a nuclear thermal-class specific impulse (I_{sp}) of 700–900 seconds in a propulsion subsystem whose overall thrust-to-weight ratio (T/W) is 50–150 (§ 2.3.4). In contrast, the T/W of much less than 10 for nuclear thermal thrusters precludes their use for space launch, and the I_{sp} of less than 460 seconds for convectional chemical rockets precludes the kind of structural margins necessary for low-cost manufacturing and reusability at the present and historical market size.

For microwave thermal rockets, the first and most important simplification is that a single high performance propellant such as hydrogen can be used, leading to a rocket with only one fuel tank, one turbopump, and a propulsion system that operates at lower temperatures than conventional thrusters (~ 2500 K versus ~ 3500 K) yet achieves twice the I_{sp} (~ 800 seconds versus ~ 450 seconds). Via the exponential nature of the rocket equation this has a profound effect on the vehicle mass fraction, substantially reducing the engineering difficulty of launch, which in detailed design translates to lower

complexity and cost via increased engineering margins and safety factors. The low density of liquid hydrogen is a traditional concern for rocket and airbreathing launch concepts as it implies greater vehicle drag losses during ascent; however, the ascent trajectory analysis in § 2.3.2 shows that this concern is unfounded.

In the past, microwave directed energy launch concepts were economically unattractive due to the hardware cost of the beam facility. This hardware cost is a function of microwave power and aperture area, the latter in turn being a function of frequency and maximum range. Given the new short range (150 km vs. 1000+ km) ascent trajectory suggested in § 2.3.2 combined with the higher frequency beam that Benford (1995) points out is possible from a high altitude site (140–300 GHz vs. 2.4–35 GHz); the aperture diameter required for a beam facility is reduced by orders of magnitude, though still requires a phased array with a diameter on the order of 250 meters.

The higher microwave frequency of 94–300 GHz enables gyrotron microwave sources to be used, the price of which has fallen by six orders of magnitude over the past 40 years (§ 2.2.4). A commercially available gyrotron plus its support equipment presently costs \$2M–5M/MW, and is still falling. This is far lower than the cost of an equivalent laser system, and the hardware costs of gyrotrons and aperture area together now account for about \$100 per kilogram of payload over the expected lifetime of the components. This is on the order of the energy cost of launch, and is plausible provided that the engineering complexity and lifetime of the beam facility is comparable with the engineering complexity and lifetime of the turbines, transformers and distribution system used to generate and provide electricity.

Given a low beam facility cost amortized over its expected lifetime, the key metric becomes the minimum initial investment for which microwave thermal launch is possible. This entails a probabilistic cost analysis that is beyond the scope of the present work, but will be needed to ascertain the regime in which microwave thermal launch is economically advantageous to other systems. At present, the drive to minimize the initial investment required for directed energy launch systems generally has led to studies that

predominantly address the payload regime of 1–1000 kg. However, the heavy launch analyses in § 2.3.3 reveal no inherent physical reason why the microwave thermal approach cannot scale up to a payload weighing many hundreds of tons into orbit. Microwave thermal launch scales in such a way the atmospheric breakdown is not a limiting factor. The price of directed energy heavy launch should at least scale linearly with payload unless it begins to stress the availability of any particular resource.

8.5   References

Benford, J. and Dickinson, R. (1995). *Space Propulsion and Power Beaming Using Millimeter Systems*, in Intense Microwave Pulses III. Also published in Space Energy and Transportation, 1, p. 211.

Bussard, R.W. and DeLauer, R.D. (1958). *Nuclear rocket propulsion*. McGraw-Hill series in missile and space technology, New York. McGraw-Hill.

Moore, G.E. (1975). *Progress in digital integrated electronics*, in Proceedings of the 1975 International Electron Devices Meeting. Piscataway, NJ.

Parkin, K. (2006). *Microwave heat-exchange thruster and method of operating the same*, USPTO Patent 6993898. California Institute of Technology.

Thunnissen, D.P. (2005). *Propagating and mitigating uncertainty in the design of complex multidisciplinary systems*. Ph.D., Division of Engineering and Applied Science, California Institute of Technology.

Tsiolkovsky, K.E. (1924). *Spaceship, 1924, in Izbrannye Trudy, Compiled by Vorob'ev, B.N., Sokol'skii, V.N., General Editor Acad. Blagonravov, Izdatel'stvo Akademii Nauk SSSR, Moscow, Russia, 1962, 222 (in Russian). Edited Machine Translation prepared by Translation Division, Foreign Technology Division, WP-AFB, Ohio, on May 5th, 1966, 307.*

Appendix A   HYDROGEN PROPERTIES

Constants

The Prandtl number Pr of 0.73 and molecular mass M_r of 2.016 g/mol are approximated to be constant for molecular hydrogen in the temperature range 90–3000 K.

Specific Heat Capacity

Specific heat capacity is calculated using (Chase, 1998)

$$C_p(\text{J kg}^{-1}\,\text{K}^{-1}) = A + Bt + Ct^2 + Dt^3 + E/t,$$
(A.1)

where $t = T(Kelvin)/1000$, C_p=heat capacity (J/mol/K), and the coefficients A–E are given in Table A-1. This function is shown graphically in Fig. A-1.

Temperature (K)	298–1000	1000–2500	2500–6000
A	16401.87401	9207.878472	21534.50397
B	-5636.615575	6080.038194	-2129.503472
C	5671.039683	-1418.544643	631.1646825
D	-1375.433532	133.0545635	-48.05357143
E	-78.64980159	981.1458333	-10185.44742
F	-4950.792163	-569.1656746	-19104.74107

Table A-1: Constants used in the calculation of hydrogen enthalpy and specific heat capacity. Adapted from the values of Chase (1998).
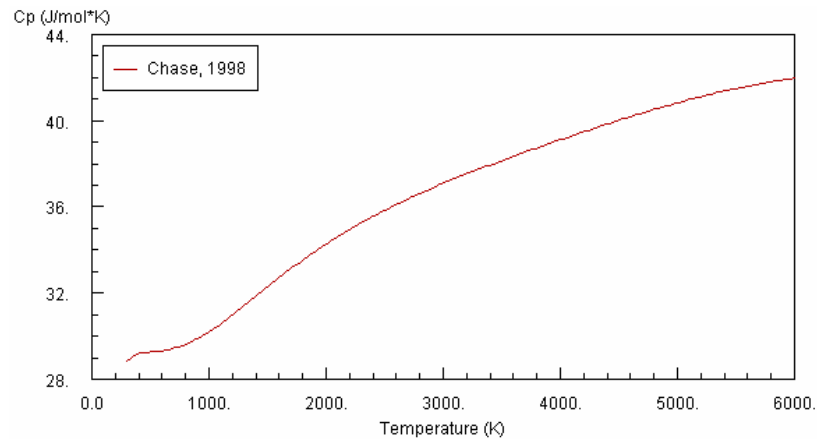
Fig. A-1: Specific heat capacity of H_2 vs. temperature (Chase, 1998).

Ratio of Specific Heats

This ratio changes substantially in the temperature range of interest, as seen in Fig. A-2.
It is calculated from the temperature-dependent specific heat capacity using

$$\gamma(T) = \frac{c_p(T)}{c_p(T)-R}. \tag{A.2}$$

Equation (A.2) implicitly assumes an ideal gas. If the units of specific heat capacity are
J/mol/K then R is the universal gas constant (8.3145 *J/mol/K*).
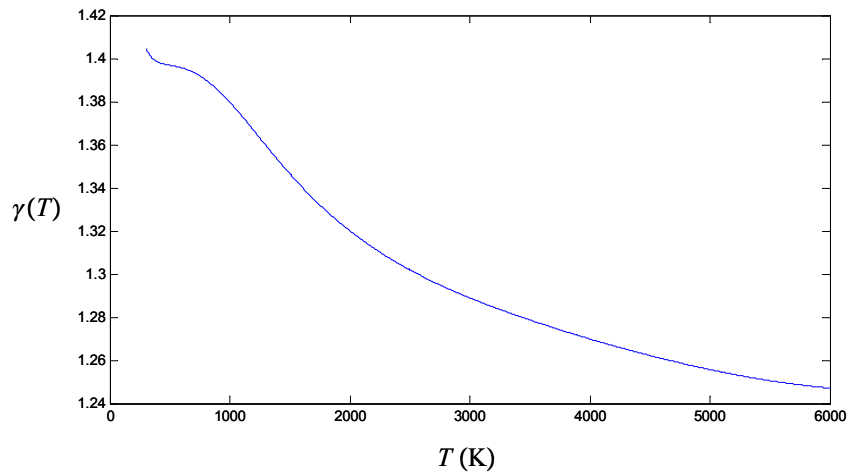
Fig. A-2: Ratio of specific heats vs. temperature for H_2.

Bulk Viscosity

Bulk viscosity μ is calculated using Sutherland's law,

$$\mu(T) = \mu_0 \left(\frac{T}{T_0}\right)^{1.5} \frac{T_0+S}{T+S}, \tag{A.3}$$

where the relevant constants for H_2 are $T_0 = 273\,\text{K}$, $\mu_0 = 8.411 \times 10^{-6}\,\text{N s / m}$, and
$S = 97\,\text{K}$ (White, 1991).

Thermal Conductivity

Thermal conductivity K is deduced by rearranging the definition of Prandtl number Pr,

$$K(T) = \frac{\mu(T)C_p(T)}{\text{Pr}}, \qquad\qquad\qquad (\text{A.4})$$

and using the known value of Pr in conjunction with the temperature-dependent expressions for bulk viscosity and specific heat capacity given above.

Enthalpy and Dissociation

Neglecting pressure and dissociation effects, the enthalpy h is calculated using (Chase, 1998),

$$h(\text{J kg}^{-1}) = At + Bt^2/2 + Ct^3/3 + Dt^4/4 - E/t + F, \qquad\qquad (\text{A.5})$$

where $t = T(Kelvin)/1000$ and the coefficients A–F are given in Table A-1. This expression neglects the effects of dissociation, which is shown in Fig. A-3.
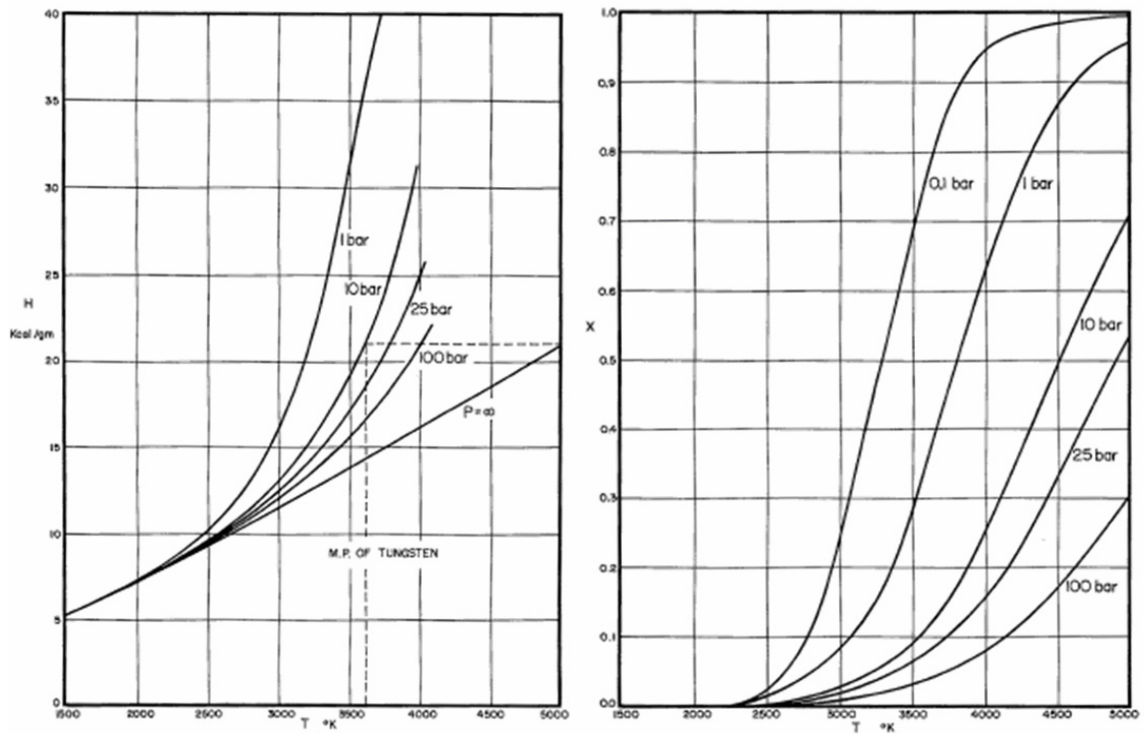
Fig. A-3: Left: The variation of hydrogen enthalpy with temperature and pressure. Right: The dissociation fraction of hydrogen as a function of temperature and pressure (Knight Jr. *et al.*, 1957).

- 237 -

Absorption and Emission

For heat transfer calculations Figs. A-4 and A-5 are used to determine whether or not the hydrogen may be treated as a non-participating gas.
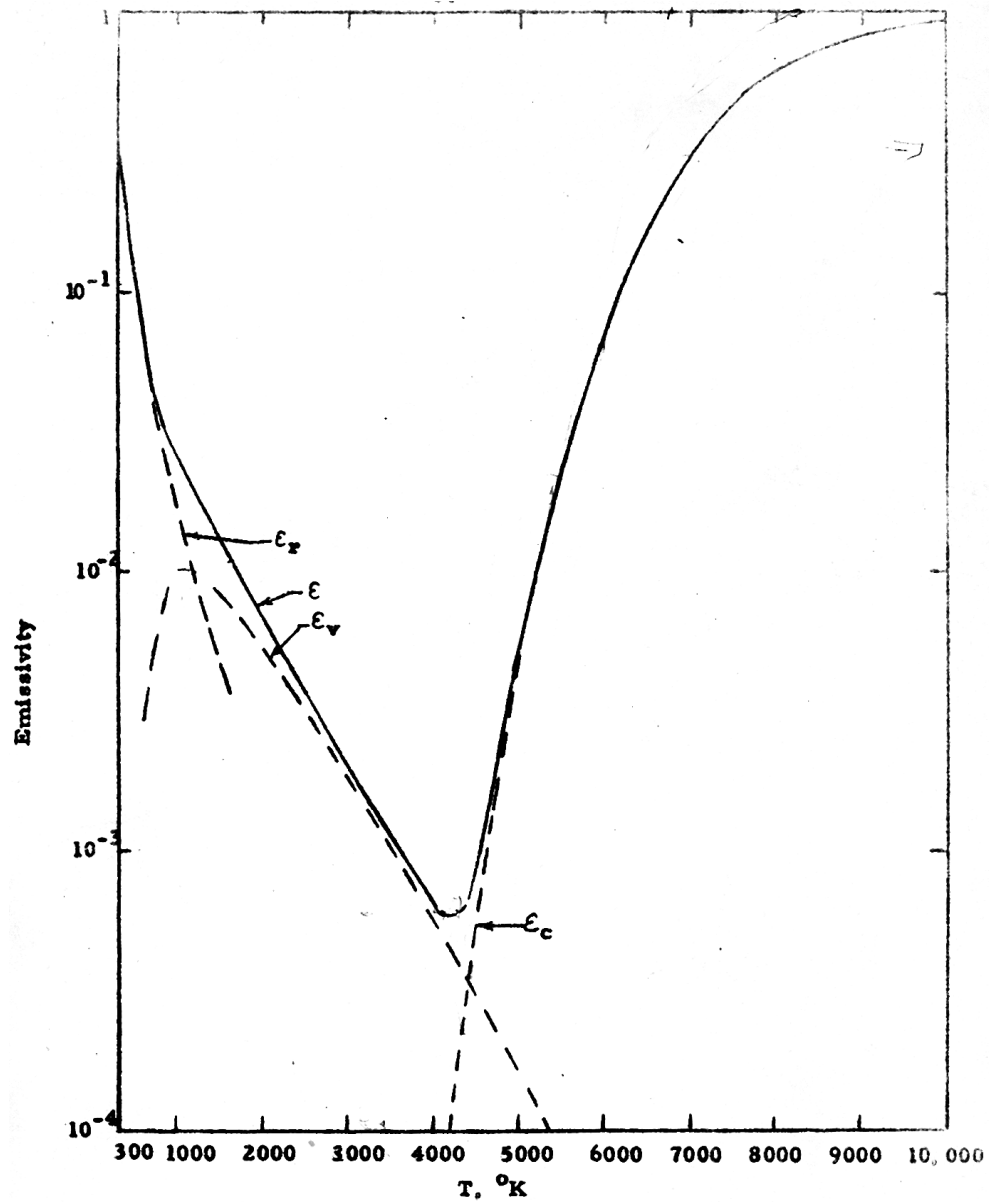
Fig. A-4: The total emissivity ε of a hydrogen plasma at 100 atm through a mean path length of 30 cm. The dashed lines indicate emissivity contributions from the pressure-induced rotational lines ε_r, the fundamental band $\varepsilon_{y'}$, and from the continuum spectrum ε_c (Olfe, 1960).
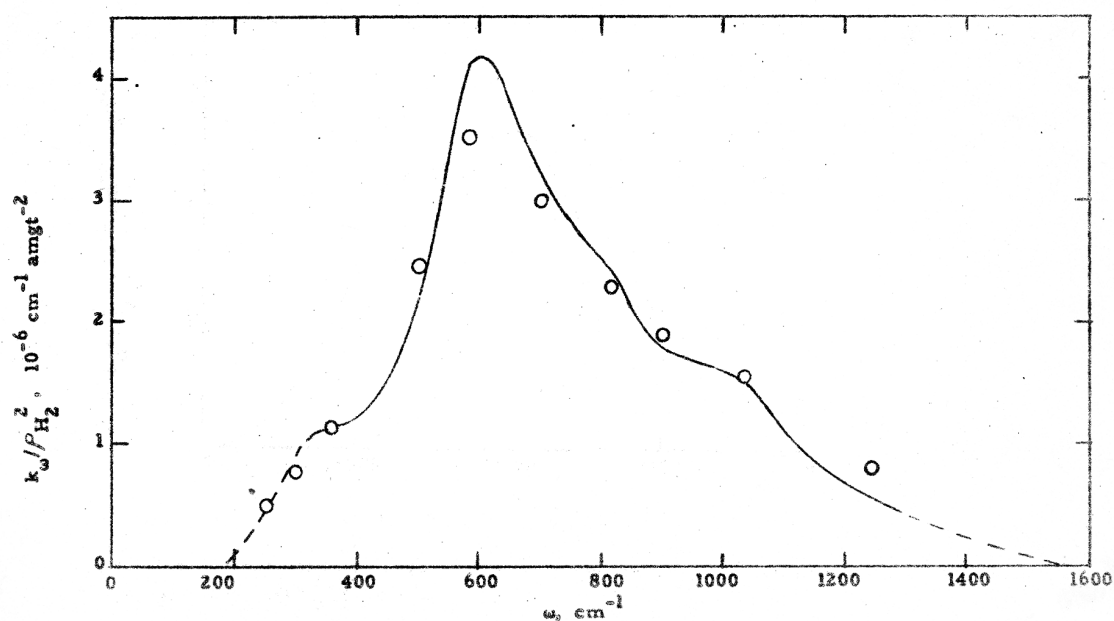
Fig. A-5: The pressure-induced absorption coefficient vs. wavenumber for the rotational lines of H_2 at 300 K (Olfe, 1960).

References

Chase, M.W. (1998). *NIST-JANAF Themochemical Tables*. J. Phys. Chem. Ref. Data **Monograph 9**: p. 1–1951.

Knight Jr., B.W., McInteer, B.B., *et al.* (1957). *A metal dumbo rocket reactor*. University of California: Los Alamos. p. 385.

Olfe, D.B. (1960). *Equilibrium emissivity calculations for a hydrogen plasma at temperatures up to 10,000 K*, Pasadena. Daniel and Florence Guggenheim Jet Propulsion Center, California Institute of Technology.

White, F.M. (1991). *Viscous fluid flow*. 2nd ed. McGraw-Hill series in mechanical engineering, New York. McGraw-Hill.

Appendix B   MATERIAL PROPERTIES

Mullite

Hemispherical total emissivity is approximated to the normal emissivity, which is interpolated from the values used by Goodson (1997) and tabulated in Table B-1.

T (K)	K (W/m/K)
300	0.960
400	0.933
500	0.900
600	0.840
700	0.773
800	0.713
900	0.653
1000	0.610
1100	0.560
1200	0.533
1300	0.507
1400	0.473
1500	0.460
1600	0.437
1700	0.423
1800	0.410
1900	0.400

Table B-1: Tabulated normal emissivity of mullite (Goodson, 1997).

For the real part of the dielectric constant ϵ',

$$\epsilon'(T) = 2 \times 10^{-6}\, T^2 + 6.0633, \qquad\qquad (B.1)$$

where T is measured in Kelvin. The loss factor ϵ'' is calculated using a polynomial fit to the data of Xi & Tinga (1991),

$$\epsilon''(T) = -2.2578 \times 10^{-6}\, T^2 + 8.5382 \times 10^{-3}\, T - 7.5642. \qquad (B.2)$$

The thermal conductivity k is interpolated from the values calculated by Goodson (1997) and tabulated in Table B-2.

T (Celsius)	k (W/m/K)
25	5.68
100	5.21
200	4.73
300	4.26
400	4.15
500	4.00
600	3.75
700	3.55
800	3.48
900	3.39
1000	3.35
1100	3.42
1200	3.47
1300	3.47
1400	3.41
1500	3.35

Table B-2: Tabulated thermal conductivity of mullite (Goodson, 1997).

Alumina

For alumina, material properties are calculated with the expressions used by McConnell (1999),

$$\varepsilon_T = \begin{cases} 0.78 & T < 400\,\text{K} \\ -3.4546 \times 10^{-4}\,T + 0.9182 & 400\,\text{K} \le T < 1500\,\text{K} \\ 0.4 & T \ge 1500\,\text{K} \end{cases}, \tag{B.3}$$

$$\epsilon'(T) = 2 \times 10^{-3}\,T + 8.3712, \tag{B.4}$$

$$\epsilon''(T) = \begin{cases} 0.03\left(1 + \sqrt{\frac{T-273}{600}}\right) & T \le 873\,\text{K} \\ -0.14 + 3.3333 \times 10^{-4}(T - 273) & T > 873\,\text{K} \end{cases}, \tag{B.5}$$

$$k(T) = 0.55\left(\frac{6788}{T-125} + 3.562 \times 10^{-33}\,T^{10}\right), \tag{B.6}$$

- 241 -

where T is measured in Kelvin, ε_T is the normal emissivity, ϵ' is the real part of the dielectric constant, and ϵ'' is the imaginary part of the dielectric constant (loss factor). As before, pyrometer measurements assume a gray body in the absence of an expression for spectral emissivity, and so (B.3) is used in place of the hemispherical spectral emissivity.

Silicon Carbide

For the alpha form of silicon carbide, useful expressions for a number of properties at high temperature are given by Munro (1997),

$$\text{FS(MPa)} = 359 + \frac{87.9}{1+208600e^{-0.012T}}, \quad 0\,°\text{C} \ \le T \le 1500\,°\text{C}, \tag{B.7}$$

$$C_p(\text{J kg}^{-1}\,\text{K}^{-1}) = 1110 + 0.15T - 425e^{-0.0003T}, \quad 0\,°\text{C} \ \le T \le 2000\,°\text{C}, \tag{B.8}$$

$$k(\text{W m}^{-1}\,\text{K}^{-1}) = \frac{52{,}000e^{-1.25\times10^{-5}T}}{T+437}, \quad 0\,°\text{C} \ \le T \le 2000\,°\text{C}, \tag{B.9}$$

where FS is flexural strength and k is thermal conductivity. Note that T is measured in Celsius in the above expressions.

In Fig. B-1 Munro (1997) also examines the key issue of high temperature creep rate, and the model from which this figure is derived is also used to deduce the maximum SiC thruster temperature of 1900 K in § 2.2.3.
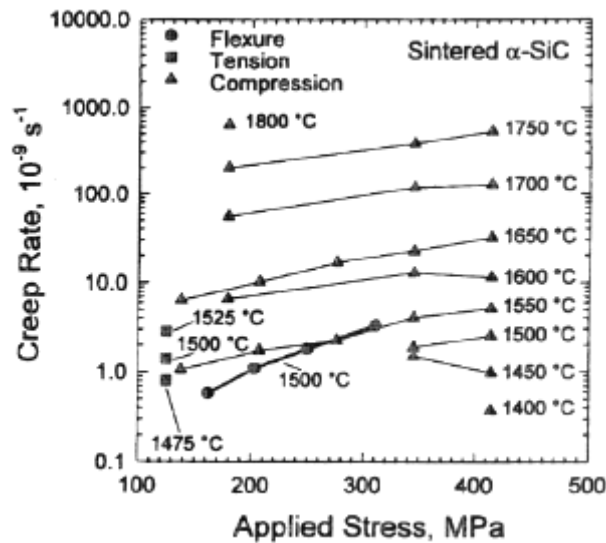
Fig. B-1: High temperature creep rate of sintered α-SiC (Munro, 1997).

References

Goodson, C.C. (1997). *Simulation of Microwave Heating of Mullite Rods*. Masters Thesis, Department of Mechanical Engineering, Virginia Polytechnic Institute and State University.

McConnell, B.G. (1999). *A Coupled Heat Transfer and Electromagnetic Model for Simulating Microwave Heating Of Thin Dielectric Materials in a Resonant Cavity*. Masters Thesis, Department Of Mechanical Engineering, Virginia Polytechnic Institute and State University.

Munro, R.G. (1997). *Material properties of a sintered alpha-SiC*. Journal of Physical and Chemical Reference Data **26**(5): p. 1195–1203.

Xi, W. and Tinga, W.R. (1991). *A High Temperature Microwave Dielectrometer*. Ceramic Transactions **21**: p. 215–224.

Appendix C ASCENT TRAJECTORY MODEL

While the rocket equation analysis indicates the feasibility of the microwave thermal rocket concept, an ascent trajectory analysis is used to confirm this finding by modeling the performance of a particular design, in this case a 1 ton launcher with X-33 type aeroshell.

Trajectory

Ascent trajectory equations are derived from a non-inertial control volume analysis in the radial coordinate system shown in Fig. C-1.
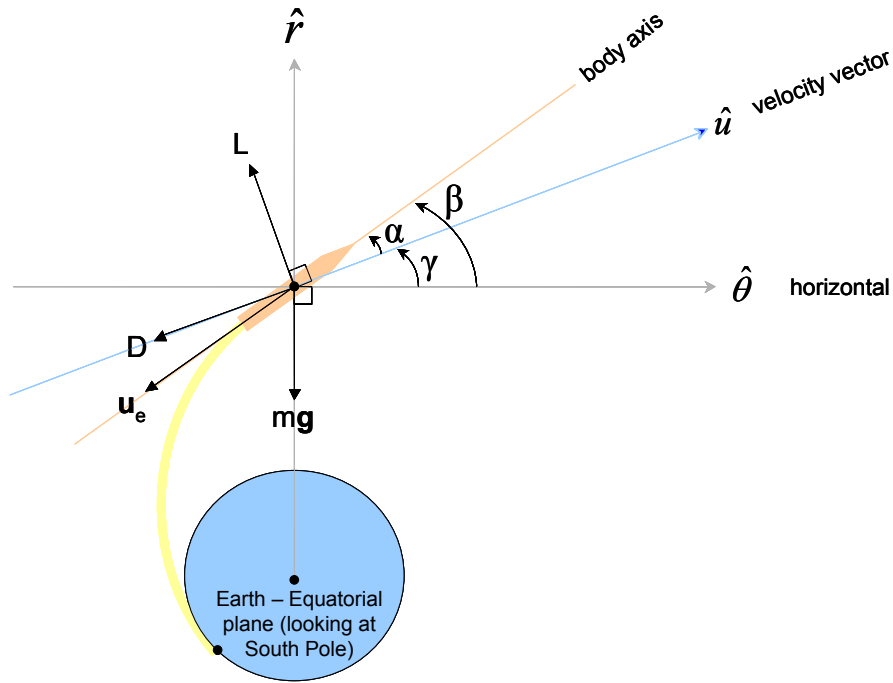
Fig. C-1: The ascent trajectory coordinate system.

The unit vectors are:

$$\hat{r} = \hat{x}\cos\theta + \hat{y}\sin\theta$$
$$\hat{\theta} = -\hat{x}\sin\theta + \hat{y}\cos\theta$$

(C.1)

Unlike Cartesian unit vectors, radial ones vary with time,

$$\frac{\partial \hat{r}}{\partial t} = \dot{\theta}\hat{\theta}, \quad \frac{d\hat{\theta}}{dt} = -\dot{\theta}\hat{r}. \tag{C.2}$$

Hence,

$$\mathbf{r} = r\hat{r}, \tag{C.3}$$

$$\dot{\mathbf{r}} = \mathbf{u_r} = \frac{\partial}{\partial t}(r\hat{r}), \tag{C.4}$$

$$\ddot{\mathbf{r}} = \dot{\mathbf{u}}_{\mathbf{r}} = (\ddot{r} - r\dot{\theta}^2)\hat{r} + (2\dot{r}\dot{\theta} + r\ddot{\theta})\hat{\theta}. \tag{C.5}$$

With these prerequisites established, the analysis begins with the continuity and momentum equations,

$$\dot{m} = -\dot{m}_p, \tag{C.6}$$

$$m\dot{\mathbf{u}}_{\mathbf{r}} = \mathbf{T} - \mathbf{D} + m\mathbf{g}. \tag{C.7}$$

Referring to Fig. C-1, forces are introduced about the (point mass) launch vehicle, as well as the velocity angle γ, angle of attack α, and rocket velocity u_r velocity in the direction of motion, given by

$$\gamma = \tan^{-1}(\dot{r}, r\dot{\theta}), \tag{C.8}$$

$$\alpha = \beta - \gamma, \tag{C.9}$$

$$u_r = \sqrt{\mathbf{u_r} \cdot \mathbf{u_r}} = \sqrt{\dot{r}^2 + (r\dot{\theta})^2}, \tag{C.10}$$

where β is a trajectory steering angle that is chosen for any given trajectory. u_r is needed to calculate lift and drag,

$$L = \rho u_r^2 A C_L / 2, \quad D = \rho u_r^2 A C_D / 2. \tag{C.11}$$

Forces on the diagram are resolved into orthogonal components along the $(\hat{r}, \hat{\theta})$ unit vectors:

$$\mathbf{g} = -\frac{m\mu}{r^2}\hat{r} \tag{C.12}$$

$$\mathbf{D} = D(u_r)\left(-\hat{\theta}\cos\gamma - \hat{r}\sin\gamma\right) \qquad (C.13)$$

$$\mathbf{L} = L(u_r)\left(\hat{r}\cos\gamma - \hat{\theta}\sin\gamma\right) \qquad (C.14)$$

$$\mathbf{T} = T\left[\hat{\theta}\cos(\alpha + \gamma) + \hat{r}\sin(\alpha + \gamma)\right] \qquad (C.15)$$

$$\mathbf{u_e} = u_e\left[-\hat{\theta}\cos(\gamma + \alpha) - \hat{r}\sin(\gamma + \alpha)\right] \qquad (C.16)$$

Putting Eqs. (C.12) to (C.16) into Eq. (C.7), neglecting the unsteady and relative acceleration terms, then grouping by unit vectors, the momentum equations are obtained along the $\left(\hat{r}, \hat{\theta}\right)$ unit vectors, respectively:

$$\hat{r}: \qquad m(\ddot{r} - r\dot{\theta}^2) = T\sin(\alpha + \gamma) - D(u_r)\sin\gamma + L(u_r)\cos\gamma - mg \qquad (C.17)$$

$$\hat{\theta}: \qquad m(2\dot{r}\dot{\theta} + r\ddot{\theta}) = T\cos(\alpha + \gamma) - D(u_r)\cos\gamma - L(u_r)\sin\gamma \qquad (C.18)$$

The unknowns to be integrated are (m, r, θ), representing mass, radius, and angular displacement, respectively. Thrust T and propellant mass flow rate $\dot{m}$ are calculated from the propulsion model; lift L and drag D are calculated from the aerodynamic model. $\mu = 3.9863 \times 10^{14} \, m^3 s^{-2}$ for earth. In the limit $T \rightarrow 0, L \rightarrow 0, D \rightarrow 0$, Eqs. (C.17) and (C.18) reduce to Kepler's equation,

$$\ddot{\mathbf{r}} + \frac{\mu}{r^3}\mathbf{r} = \mathbf{0}. \qquad (C.19)$$

Beam Tracking

For the design of a phased array the range to target S and slew angle λ are of interest, in addition to their time rates of change. Based on Fig. C-2 the range to target and slew angle are written

$$S = \sqrt{r_e^2 + (r_e + h)^2 - 2r_e(r_e + h)\cos\theta}, \qquad (C.20)$$

$$\lambda = \sin^{-1}\left[\frac{(r_e + h)\sin\theta}{S}\right], \qquad (C.21)$$

where r_e is the radius of the Earth and h is altitude. For the range rate (C.20) is differentiated, giving

$$\dot{S} = \frac{\dot{r}(r - r_e\cos\theta) + r\dot{\theta}r_e\sin\theta}{S}. \qquad (C.22)$$
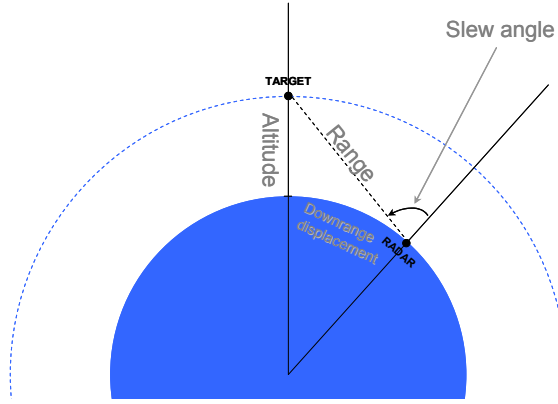
Fig. C-2: The beam tracking coordinate system.

For the slew rate, (C.21) is differentiated

$$\dot{\lambda}\cos\lambda = \frac{\dot{h}\sin\theta}{S} + \frac{(r_e+h)\dot{\theta}\cos\theta}{S} - \frac{\dot{S}(r_e+h)\sin\theta}{S^2},$$

(C.23)

and after some substitutions and rearrangements,

$$\dot{\lambda} = \frac{\frac{\dot{r}}{r}+\dot{\theta}\cot\theta-\frac{\dot{S}}{S}}{\sqrt{\frac{S^2}{r^2\sin^2\theta}-1}}.$$

(C.24)

Propulsion

Atmospheric density $\rho(r)$ is calculated from a 1976 standard atmosphere and A is the aeroshell frontal area, obtained by scaling the aeroshell geometry based on LH_2 density. The lift and drag coefficients are obtained from the launcher aerodynamic model. In this case, a zero angle of attack is assumed for the atmospheric portion of flight, and the coefficient of drag is approximated using Mach 0.6 to 1.8 drag data (Whitmore and Moes, 2000) from SR-71 testing of the LASRE X-33 aeroshell model:

$$C_{D_0} = \begin{cases} 0.3 & M < 0.9 \\ 6M - 5.1 & 0.9 \leq M < 1 \\ -1.1667M + 2.0667 & 1 \leq M < 1.3 \\ 0.55 & 1.3 \leq M \end{cases}$$

(C.25)

In the propulsion model, a throttle factor η is specified for the trajectory,

$$T = g\dot{m}_p I_{sp}, \quad P_j = \dot{m}_p \left(gI_{sp}\right)^2/2, \quad \dot{m}_p = \eta\left(\dot{m}_p\right)_{\max}, \tag{C.26}$$

where $g = 9.81$ m/s^2, P_j is jet power, and $\left(\dot{m}_p\right)_{\max}$ is a chosen maximum propellant mass flow rate. Finally, the variation of I_{sp} with altitude is

$$I_{sp} = \frac{1}{g}\sqrt{2c_p\left(T_t^*\right)T_t^*\left(1-\frac{p_a}{p_t^*}\right)^{\gamma-1/\gamma}}, \tag{C.27}$$

where T_t^*, P_t^* are wall temperature and total pressure at the channel exit, respectively. Since the sonic point is the highest temperature point in the thruster, T_t^* is chosen to be 2800 K, and P_t^* is conservatively chosen to be 20 atm. P_a is the ambient atmospheric pressure, obtained from the atmospheric model at any given altitude.

References

Whitmore, S.A. and Moes, T.R. (2000). *Base-drag-reduction experiments on the X-33 Linear Aerospike SR-71 flight program*. Journal of Spacecraft and Rockets **37**(3): p. 297–303.

Appendix D   HIGH POWER MICROWAVE BREAKDOWN MODEL

Microwave frequency determines the maximum beam energy density via the constraint of atmospheric breakdown. Free-space atmospheric breakdown is an electron avalanche process leading to a plasma whose characteristic dimension is very large, hence breakdown occurs when

$$\frac{dn_e}{dt} = n_e v_i - n_e v_a - n_e v_r \geq 0, \tag{D.1}$$

where n_e is the number of free electrons and v_i, v_a, v_r are the ionization, attachment and recombination collision frequencies, respectively. Ionization due to the incident beam generates free electrons, whereas attachment and recombination removes them. Hence the stability limit is

$$v_i = v_a + v_r. \tag{D.2}$$

Letting $\xi = \dfrac{E_e}{P}, Y_x = \dfrac{v_x}{P}$,

$$\Upsilon_i(\xi) - \Upsilon_a(\xi,h) - \Upsilon_r(\xi,f) = 0, \tag{D.3}$$

where using the expressions of Liu *et al.* (1997),

$$\Upsilon_i(\xi) = \begin{cases} (1.32 + 0.054\xi) \times 10^7 e^{-\frac{208}{\xi}} & 30 \leq \xi \leq 54 \\ (5.0 + 0.19\xi) \times 10^7 e^{-\frac{273.8}{\xi}} & 54 < \xi \leq 120 \\ 54.08 \times 10^6 \sqrt{\xi}\, e^{-\frac{359}{\xi}} & 120 < \xi \leq 3000 \end{cases} , \tag{D.4}$$

$$\Upsilon_a(\xi,h) = \frac{8.3 \times 10^6 e^{-\frac{6.7}{T_e(\xi)}} + 2335\rho(h)}{T_e^{3/2}(\xi)}, \tag{D.5}$$

$$\Upsilon_r(\xi,f) = \left(4.8 \times 10^{-8} T_e(\xi)^{-0.39} + 2.1 \times 10^{-8} T_e(\xi)^{-0.63}\right) n_e(f), \tag{D.6}$$

$$T_e(\xi) = \begin{cases} 0.1\xi^{1.43} & 1 \leq \xi \leq 5 \\ 0.4\xi^{0.577} & 5 < \xi \leq 54 \\ 2.17\xi^{0.15} & 54 < \xi \leq 150 \\ 0.18\xi^{0.65} & 150 < \xi \leq 500 \end{cases} , \tag{D.7}$$

$$n_e(f) = 12.36 \times 10^{-3} f^2. \tag{D.8}$$

Equation (D.3) is solved iteratively for ξ given a known frequency f and altitude h. This value of ξ is then used in Eq. (D.9) to find the breakdown electric field, and hence the breakdown intensity at any given frequency and altitude. The resulting curves of breakdown intensity threshold vs. altitude are shown in Fig. 2-11.

$$E_{rms}(\xi,f) = \xi \sqrt{\left(\frac{2\pi f}{\Upsilon_m(\xi)}\right)^2 + 1} \tag{D.9}$$

$$I = c\varepsilon_0 E_{rms}^2 = 2.65 \times 10^{-3} E_{rms}^2 \tag{D.10}$$

$$\Upsilon_m(\xi) = \begin{cases} \dfrac{2.35 \times 10^9 \xi}{1+0.58\xi} & 1 \le \xi \le 30 \\[2mm] \dfrac{3.24 \times 10^8 \xi}{1+0.04\xi} & 30 < \xi \le 54 \\[2mm] \dfrac{2.93 \times 10^8 \xi}{1+0.041\xi} & 54 < \xi \le 120 \\[2mm] 5.2 \times 10^8 \sqrt{\xi} & 120 < \xi \le 3000 \end{cases} \tag{D.11}$$

The results predict that breakdown occurs more easily at low frequencies, ionizing air into a plasma that can distort and reflect the incoming beam. The beam frequency has a disproportionate effect on the breakdown intensity; for example a 300 GHz beam can achieve 1000 times the power density of a 3 GHz beam, assuming that it is constrained at the altitude of minimum breakdown intensity. By moving to higher frequency in this way, the energy density can enter the energetic regime needed for space launch.

References

Liu, G., Liu, J., *et al.* (1997). *The study of high power microwave (HPM) air breakdown.* SPIE **3158**.

Appendix E   PLANAR STRATIFIED LAYER MODEL

The fraction of incident microwave energy absorbed or reflected by a planar thruster can be analytically estimated using a stratified layer model (Born and Wolf, 1999), representing electromagnetic propagation within an idealized layered-structure thruster. In addition to demonstrating the optical performance of a thruster design, this model can be used to predict the layer thicknesses needed for optimal microwave absorption at the conceptual design stage.

Governing Equations

The governing equations for the stratified layer model are Eqs. (E.1) to (E.8).   The approximation used for the material properties is given separately in Eq. (E.9) and completes the overall set of equations used to predict thruster optical performance. Overall, the governing equations pertain to a planar layered structure, for example the one shown in Fig. E-1, where a microwave beam is incident at some angle onto the surface.
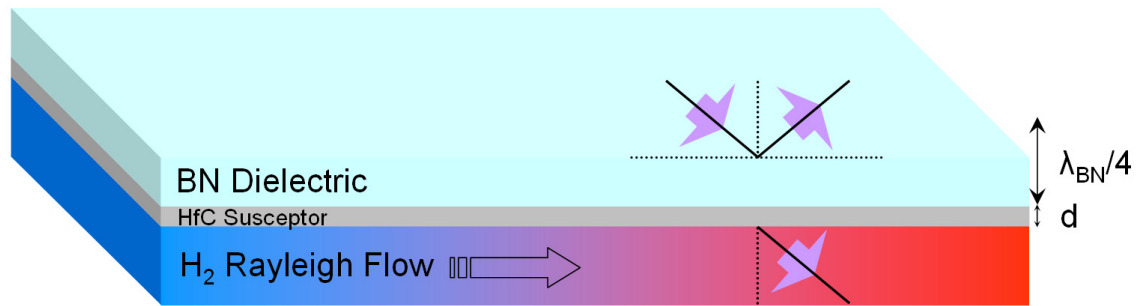
Fig. E-1: An idealization of the microwave thermal channel flow using an HfC susceptor with a boron nitride (BN) supporting structure.

Equations (E.1) and (E.2) are the energy reflection, transmission, and absorption coefficients, which are calculated from the electric field reflection and transmission coefficients given by Eqs. (E.3) and (E.4). The angle of incidence and wave polarization enters through Eq. (E.5). The transverse direction is orthogonal to the plane of incidence;

hence the electric field component of a transverse electric (TE) wave would oscillate out of the plane of the paper in Fig. E-1. Material properties also enter through Eq. (E.6), and are assembled into a "characteristic" matrix for each layer of material, numbered $l = 1$ to $N - 1$, in Eq. (E.7), where $l = 0$ corresponds to the incident medium and $l = N$ corresponds to the transmitted medium, both of which are usually free-space not counted as a layer. Multiplying the characteristic matrix of each layer by the next, an overall characteristic matrix is formed, from whose elements the complex reflectivity and transmissivity are calculated in Eqs. (E.3) and (E.4).

$$R = |r|^2, \qquad T = \frac{p_0}{p_N}|t|^2 \tag{E.1}$$

$$A = 1 - R - T \tag{E.2}$$

$$r = \frac{(M_{11} + p_N M_{12})p_0 - (M_{21} + p_N M_{22})}{(M_{11} + p_N M_{12})p_0 + (M_{21} + p_N M_{22})} \tag{E.3}$$

$$t = \frac{2p_0}{(M_{11} + p_N M_{12})p_0 + (M_{21} + p_N M_{22})} \tag{E.4}$$

$$p = \left. \begin{array}{l} \hat{n}n_0 \cos\theta \\ (1/(\hat{n}n_0))\cos\theta \end{array} \right\} \begin{array}{l} TE \\ TM \end{array} \tag{E.5}$$

$$\beta = 2\pi \frac{\hat{n}h}{\lambda_0} \cos\theta \tag{E.6}$$

$$M = \prod_{l=1}^{N-1} m_l \tag{E.7}$$

$$m_l = \begin{bmatrix} \cos\beta_l & -(i/p_l)\sin\beta_l \\ -ip_l \sin\beta_l & \cos\beta_l \end{bmatrix} \tag{E.8}$$

To solve for the reflection and transmission coefficients, the complex refractive index $\hat{n}$ is specified. The complex refractive index $\hat{n}$ is related to widely available DC material properties via the Drude model in Eq. (E.9). The dielectric constant is assumed to remain at its DC value throughout the microwave frequency range. n_0 is the absolute refractive index of free-space, f is microwave frequency in Hz, and σ is conductivity in S/m. At these relatively low microwave frequencies, the material properties are approximated to their DC values.

$$\hat{n} = \sqrt{\mu\left(\varepsilon_{DC} + i\frac{18\times10^9\,\hat{\sigma}}{f}\right)}, \quad \hat{\sigma} = \frac{\sigma_{DC}}{1 - i\dfrac{f\varepsilon_{DC}}{2\sigma_{DC}}} \qquad\qquad (E.9)$$

Susceptor Absorption: Hafnium Carbide Thruster

As described in § 2.2.1, incident microwaves can be absorbed in a single semiconducting layer. An alternative approach that can utilize very thin layers of ultra-refractory metals is now given.

A good conductor efficiently reflects energy, and a good insulator efficiently transmits it. Between these two extremes, a poor conductor absorbs energy by Joule heating. This effect is optimized by tailoring the thickness of the poorly conducting layer; such a layer is called a susceptor (Buffler, 1991). Hafnium carbide (HfC) is one of the poorest electrical conductors of the ultrarefractory metal alloys, and also the most refractory (heat resisting) material known, with a melting point of 4200 K (380 K above that of diamond).

An idealization of the inner surface of a microwave thermal channel employing an HfC susceptor is shown in Fig. E-1. The thin susceptor absorbs no more than 50% of the incident energy; however this efficiency is increased by the boron nitride dielectric layer acting as an anti-reflection coating. The free-space wavelength at 140 GHz is 2.14 mm, and so within the boron nitride (BN) layer the wavelength is 1 mm. By maintaining the thickness at an odd number of quarter wavelengths (0.25 mm) within reasonable tolerance, the BN layer can achieve this anti-reflection property in practice.

Even with the poor conductivity of HfC, the optimum susceptor absorption of 80% at 140 GHz requires a layer only 6 nm thick, as seen in the upper chart of Fig. E-2. Using this 6 nm thickness, the off-normal incidence profile is shown in the lower chart of Fig. E-2. In this case, the TE-polarized wave is absorbed more efficiently as the source tilts even 65 degrees off-normal.   In the ascent trajectory, this means that peak absorption efficiency would correspond to the initial and final stages of horizontal acceleration,

above the atmosphere, when one might intuitively expect the poorest absorption efficiency.
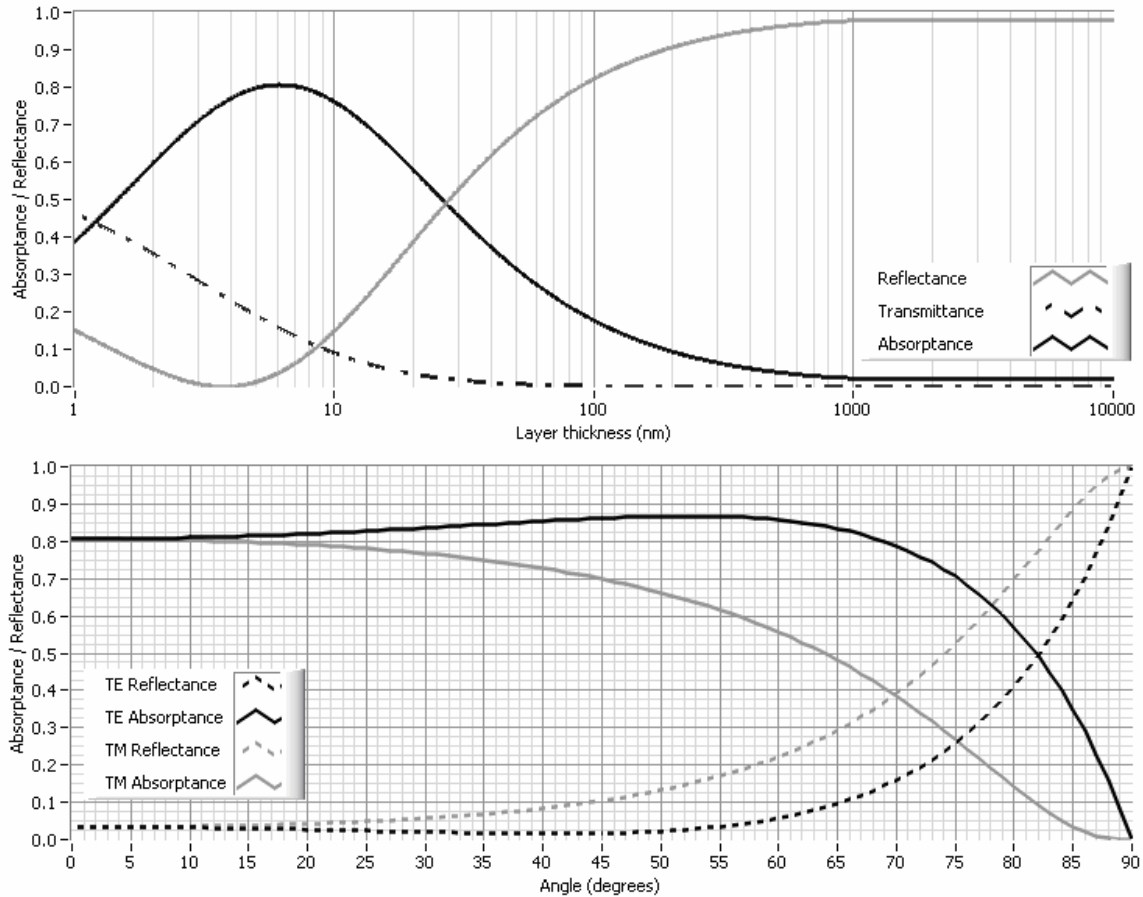
Fig. E-2: Optical performance of the HfC-BN microwave thermal channel calculated from the stratified layer model. Top: HfC susceptor performance at 140 GHz, 45 µΩ.cm. Bottom: 6 nm HfC susceptor off-normal response at 140 GHz, 45 µΩ.cm.

However, an HfC layer only 6 nm thick cannot survive in a high temperature channel flow. It could also be difficult to realize the full temperature capability of an HfC susceptor because it would have to bond with a material of lower melting point, such as BN, to contain the high-pressure propellant flow. The absorption fraction of a thin layer susceptor varies with the product of conductivity and thickness, rather than either quantity individually, and this means that an HfC refractory foam of 100 times lower conductivity could be 100 times thicker. A practical susceptor approach at present would

be to accept lower temperature operation and embed the susceptor within the BN layer, thereby protecting it from the hydrogen flow.

References

Born, M. and Wolf, E. (1999). *Principles of Optics: Electromagnetic Theory of Propagation, Interference and Diffraction of Light*. 7th ed.

Buffler, C.R. (1991). *A Simple Approach to the Calculation of Microwave Absorption, Transmission and Reflection of Microwaves from a Susceptor Film*. Microwave World **12**(3): p. 5–7.

Appendix F   CONCEPTUAL DESIGN MODEL

There are many ways to solve for an integrated conceptual design depending on what aspects of the system are known initially and what the designer wishes to solve for. The model presented here follows to a great extent the methodology of Humble *et al.* (1995), so this treatment omits many more standard details of the idealized isentropic gasdynamic analysis and emphasizes the design aspects that are peculiar to microwave thermal rockets.

Rocket Equation

The analysis in this case begins with the rocket equation (as opposed to the ascent trajectory simulation given above) and has three top level inputs:

- I_{sp}: This is a key determinant of both system performance and the temperature and pressure regime the propulsion system endures.
- Δv: Mission specific, includes margin for drag and gravity loss.
- Peak acceleration a_{max}: This occurs at cutoff and for a short-range ascent trajectory is in the range of 20 g's.
- Vehicle wet mass m_0: Payload mass is then a variable that is solved for. One may also specify payload mass and solve for wet mass.

Given I_{sp} and Δv the rocket equation is used to obtain the mass fraction c,

$$ c \equiv \frac{m_0}{m_f} = e^{-\frac{\Delta v}{g I_{sp}}} , \tag{F.1} $$

where m_f is the final mass (dry mass), equal to the wet mass m_0 minus the propellant mass m_{pro}. Given that the wet mass is specified this implies known values for m_f and m_{pro}. Still unknown are the payload and structural masses.

Using m_f and a_{max} the vehicle thrust T is deduced to be,

$$ T = m_f g a_{max} . \tag{F.2} $$

Assuming a cylindrical tank, an initial propellant tank diameter D_{tank} is guessed and passed to the propulsion subsystem below, which is iterated with the tank subsystem below until the tank diameter and heat exchanger width are equal. This is the top-level design iteration and, once converged, the tank and propulsion subsystems are defined. Together, the tank mass and propulsion mass are combined with a number of other structural overheads to give the overall structural mass m_{str}. Given the structural mass, it remains to deduce the payload mass from the wet mass,

$$m_{pay} = m_0 - m_{pro} - m_{str}. \tag{F.3}$$

From here it is a simple matter to obtain the key metrics of payload fraction and propulsion system thrust-to-weight ratio.

Propellant Tank

Once the volume of the tank is determined from the propellant requirements and leaving adequate ullage, the tank diameter D_{tank} and tank mass m_{tank} is calculated using

$$D_{tank} = \sqrt[3]{\frac{V_{tank}}{\frac{\pi}{4}(B+1/3)}}, \tag{F.4}$$

$$A_{tank} = \pi D_{tank}^2 (B+0.69), \tag{F.5}$$

$$t_{tank} = \frac{f_s P_{tank} D_{tank}}{2\sigma_{tank}}, \tag{F.6}$$

$$m_{tank} = \rho_{tank} A_{tank} t_{tank}, \tag{F.7}$$

where B is the length to diameter ratio of the tank, P_{tank} is the pressure, σ_{tank} is the ultimate yield stress of the tank material, f_s is the safety factor (including corrections for welds, etc.,) and ρ_{tank} is the density of the tank material.

Propulsion: Nozzle

An initial total pressure $(P_t)_{noz}$ is guessed. In this approach the expansion ratio is calculated based on an assumed exit Mach number M_e,

$$\varepsilon = \frac{1}{M_e}\left[\left(\frac{2}{\gamma+1}\right)\left(1 + \frac{\gamma-1}{2}M_e^2\right)\right]^{\frac{\gamma+1}{2\gamma-2}}.$$ (F.8)

The ratio of specific heats γ is unknown and so the ideal exit velocity U_e, deduced from the I_{sp} and nozzle thrust efficiency, is divided by M_e to give the speed of sound. The speed of sound is used to solve iteratively for the static exit temperature T_e. Given T_e and M_e a total temperature T_{te} is deduced using well-known isentropic relations, and assuming adiabatic expansion this is equal to the total temperature at the nozzle throat and heat exchanger exit.

In order to deduce the mass of the nozzle something the pressure must be specified at one point in the system. Hence the total pressure $(P_t)_{noz}$ combined with a Mach number defines the static pressure at any given point between the heat exchanger exit and the nozzle exit. These pressures then define the thickness t of the nozzle at the exit and throat. Given a chosen cone angle θ_{cn} and the expansion ratio calculated above the diameters D and radii r of the nozzle are combined with the thicknesses and material density ρ to deduce the nozzle mass m_n.

$$m_n = 2\pi\rho L_n\left[\tfrac{1}{3}f_1 f_2 L_n^2 + \tfrac{1}{2}(f_1 r_t + f_2 t_t)L_n + r_t t_t\right]$$ (F.9)

$$f_1 = \frac{t_e - t_t}{L_n}, \quad f_2 = \frac{r_e - r_t}{L_n}$$ (F.10)

$$t = \frac{f_s r P}{F_{tu}}$$ (F.11)

$$D_e = \sqrt{\frac{4\varepsilon A_t}{\pi}}$$ (F.12)

$$L_n = \frac{D_e - D_t}{2\tan\theta_{cn}}$$ (F.13)

Finally, the propellant mass flow rate is calculated from the ideal thrust T_{ideal} and U_e, and the jet power P_j is calculated from the mass flow rate and U_e,

$$\dot{m} = \frac{T_{ideal}}{U_e},$$ (F.14)

$$P_j = \tfrac{1}{2}\dot{m}U_e^2.$$ (F.15)

These two quantities are used next in the solution of the heat exchanger model.

Propulsion: Heat Exchanger

For the purposes of modeling an elastically scaling propulsion system, the width of the heat exchanger is taken to equal the tank diameter or some multiple thereof. An aspect ratio is chosen for the heat exchanger based on how many segments will be arranged on the underside of the launcher and in what way.

For purely performance reasons, a key objective is to minimize the temperature difference between the wall and flow at the exchanger outlet, as this maximizes I_{sp} for any given maximum wall temperature, which is limited by material creep rate. This objective is most easily achieved by choosing a single segment heat exchanger with the channels aligned in the direction of motion. On the other hand this can imply a very large single segment heat exchanger, which may be impractical to fabricate and handle, so for larger launchers, performance is sacrificed a little for multiple segments such as the eight segment arrangement shown on the vehicle to the right of Fig. 2-1. This eight segment arrangement consists of two sets of four opposing heat exchangers. Propellant flows towards the center for each pair of heat exchangers, causing the peak temperature to occur in this region.

It is assumed that the power flux absorbed by the heat exchanger is uniform, and furthermore that this absorbed flux translates to a wall flux that is evenly distributed about the circumference of each heat exchanger channel. This is of course an idealization to be revisited in more detailed design.

Given the known length and width of each heat exchanger segment, a hydraulic channel diameter D_h is chosen, along with the Mach number at the heat exchanger exit. The higher the (subsonic) exchanger exit Mach number is, the higher the mass flow rate per unit area of the heat exchanger, and hence the higher the thrust-to-weight ratio. This all comes at the expense of a greater pressure drop along the channel, which must be overcome by bleeding off more of the heated flow to power the turbopump. This extra energy expenditure can be taken into account in the overall exchanger power requirement

by iterating a few times; the hydrogen flow used to power the turbopump is assumed to be recycled into the turbopump inlet.

The total combined channel exit area is deduced from Eq. (F.16) using the known mass flow rate, heat exchanger outlet Mach, and the total temperature and pressure, known from the nozzle solution and indirectly determined by the I_{sp}.

$$\frac{\dot{m}}{A} = pM\sqrt{\frac{\gamma(T)}{R_g T}} \tag{F.16}$$

The area of each individual channel is known from the hydraulic diameter, so the total number of channels needed is deduced. Assuming square channels for the sake of clarity, a sidewall thickness between each channel is specified as a fraction of D_h. Given the wall thicknesses and channel diameter a total exchanger width is implied, which may or may not be consistent with the chosen exchanger geometry. The total pressure, initially guessed for the nozzle, is adjusted and the intervening steps iterated such that the widths are consistent. Note that for square channels a corner stress concentration factor is used in calculating the structural safety factor.

The power transferred into the propellant per unit channel length is the product of the convective heat transfer coefficient H and the temperature difference between the bulk flow and channel wall at any given point along the channel,

$$\frac{dP}{dL} = H(T)\Gamma(T_w - T). \tag{F.17}$$

Given the known geometry at this stage the channel circumference Γ is known, as is the power density dP/dL. Given also the bulk static flow temperature T, which is deduced from the total temperature and the exchanger exit Mach number, Eq. (F.17) is solved for the peak wall temperature T_w, a key design constraint.

If the channel flow is fully turbulent with a Reynolds number Re above 10,000, the convective heat transfer is approximated in nondimensional form by the experimental Nusselt number correlation,

$$Nu = 0.023(Re)^{0.8}(Pr)^{1/3}, \qquad\qquad\qquad\text{(F.18)}$$

where the Nusselt, Reynolds, and Prandtl numbers are given by

$$\text{Nu}(T) = \frac{H(T)D}{K(T)}, \quad \text{Pr} = \frac{\mu(T)c_p(T)}{K(T)}, \quad \text{Re}(T) = \frac{\dot{m}}{A}\frac{D}{\mu(T)} \qquad\qquad\text{(F.19)}$$

For H_2 in the range of 300–3000 K, $\text{Pr} \sim 0.73$ is assumed for an H_2 propellant. Equations (F.19) are rearranged to find the heat transfer coefficient in terms of the channel geometry and hydrogen properties,

$$H(T) = \frac{K(T)}{D}0.023\,\text{Re}^{0.8}\,\text{Pr}^{1/3}. \qquad\qquad\qquad\text{(F.20)}$$

For a channel of square cross-section, rather than circular, this heat transfer coefficient is multiplied by 0.76 (Levenspiel, 1998). $\mu(T)$ is calculated using Sutherland's law and relevant constants for H_2 (Wilcox, 2000). $c_p(T)$ is calculated from polynomial approximations (Chase, 1998), and $K(T)$ is deduced from these values and the Prandtl number.

References

Chase, M.W. (1998). *NIST-JANAF Themochemical Tables*. J. Phys. Chem. Ref. Data **Monograph 9**: p. 1–1951.

Humble, R.W., Henry, G.N. and Larson, W.J. (1995). *Space propulsion analysis and design*. 1st ed. Space technology series, New York. McGraw-Hill.

Levenspiel, O. (1998). *Engineering flow and heat exchange*. Rev. ed. Plenum chemical engineering series., New York. Plenum Press.

Wilcox, D.C. (2000). *Basic fluid mechanics*. Second ed.